

Copyright
by
Michael David Harmon
2016

The Dissertation Committee for Michael David Harmon
certifies that this is the approved version of the following dissertation:

**Numerical Algorithms Based On Galerkin Methods For
The Modeling Of Reactive Interfaces In
Photoelectrochemical Solar Cells**

Committee:

Irene M. Gamba, Co-Supervisor

Kui Ren, Co-Supervisor

Clint Dawson

Omar Ghattas

Graeme Henkelman

**Numerical Algorithms Based On Galerkin Methods For
The Modeling Of Reactive Interfaces In
Photoelectrochemical Solar Cells**

by

Michael David Harmon, B.A. MATH.; M.S. C.A.M.

DISSERTATION

Presented to the Faculty of the Graduate School of
The University of Texas at Austin
in Partial Fulfillment
of the Requirements
for the Degree of

DOCTOR OF PHILOSOPHY

THE UNIVERSITY OF TEXAS AT AUSTIN

August 2016

Dedicated to my family for their courage, support and unyielding love.

Acknowledgments

I first want to thank my mother and father who, without this work would not have been possible. They instilled in me a passion for science and showed me what strength, hardwork and dedication could achieve. I want to thank my sister Beth and her husband Ian for always being there for me and supporting me. Thank you to my coach David Ginsberg for always pushing me past my limits and helping me achieve what I never thought possible.

I am deeply indebted to my advisors Dr. Gamba and Dr. Ren. I truly appreciate of their kindness, patience and guidance. I also have to thank my committee members for their assistance. I learned a great deal from Dr. Dawson's finite element course and am thankful for the time he took to answer my questions on the LDG method. Thank you to Dr. Ghattas, from whom I gained deep insight to scientific computing. It seems that every time I talked to him my code ran faster. Finally, thank you to Dr. Henkleman for pushing me to better understand semiconductor-electrochemistry and science in general.

While they are not on my committee, I would also like to thank Dr. Bard and Dr. Bangerth. It was a honor to learn from Dr. Bard, one of the foremost experts in semiconductor-electrochemistry. I gained tremendous amount of knowledge from him and am thankful he took the time to answer all my questions. I am also thankful to Dr. Bangerth, not only because he

started the deal.II library which made this work possible, but also because of his dedication to teaching scientific computing. I learned a great deal from his online lectures and reading his discussions on forums.

Thank you to Kent Van Vels, I really enjoyed working with you and learned a lot you. This work would not be possible without the support of Elena Nirlo, you helped me in so many ways and I cannot thank you enough. Thank you to Omar Al Hinai for being a great person and explaining the mixed method to me a billion times. Thomas Kirschenmann is an inspiration to me, he overcame great adversity and I'm thankful he showed me the ropes of graduate school. I had not taken Chemistry since high school and I'm very grateful that Naomi Choodnovskiy took the time to explain basic concepts to me over and over again. Thank you to Talea Mayo, who is an amazing person and great scientist! Thank you to Kathryn Maupin for all the talks, walks, and rides to the airport. And thank you to Ju Liu for being my friend and for all the conversations we had.

Thank you to UT students and staff: Timothy Povich, Mathias Taus, Truman Ellis, Corey Bryant, Jonathan Young, Juan Diego Rodriguez, Jose Morales, Craig Michoski, Gary Gold, Yaniv Brick, Sam Aminfard, Stephanie Rodriguez, Andee Kaplan, and Arielle Mimouni.

Thank you also to my non-UT friends who kept me sane in Austin: Jeff Rockwell, Robert Dembeck, Jose Portillo, Sam Edminson, John Torres, Hinlan Wong, Andre Denson, Dan Reibstein, Guy Feldman and Rabbi Zev Johnson.

Numerical Algorithms Based On Galerkin Methods For The Modeling Of Reactive Interfaces In Photoelectrochemical Solar Cells

Publication No. _____

Michael David Harmon, Ph.D.
The University of Texas at Austin, 2016

Co-Supervisors: Irene M. Gamba
Kui Ren

Large-scale utilization of photovoltaic (PV) devices, or solar cells, has been hampered for years due to high costs and lack of energy storage mechanisms. Photoelectrochemical solar cells (PECs) are an attractive alternative to conventional solid state PV devices because they are able to directly convert solar energy into hydrogen fuel. The hydrogen fuel can then be used at a later time to generate electricity. Photoelectrochemical solar cells are able to produce fuel through chemical reactions at the interface of a semiconductor and electrolyte when the device is illuminated. In this dissertation, we focus on the modeling and numerical simulation of charge transport in both the semiconductor and electrolyte region as well as their interaction through a reactive interface using the drift-diffusion-Poisson equations.

The main challenges in constructing a numerical algorithm that produces reliable simulations of PECs are due to the highly nonlinear nature of

the semiconductor and electrolyte systems as well as the nonlinear coupling between the two systems at the interface. In addition, the evolution problem under consideration is effectively multi-scale in the sense that the evolution of the system in the semiconductor and the corresponding one in the electrolyte evolve at different time scales due to the quantitative scaling differences in their relevant physical parameters. Furthermore, regions of stiffness caused by boundary layer formation where sharp transitions in densities and electric potential occur near the interface and pose severe constraints on the choice of discretization strategy in order to maintain numerical stability.

In this thesis we propose, implement and analyze novel numerical algorithms for the simulation of photoelectrochemical solar cells. Spatial discretizations of the drift-diffusion-Poisson equations are based on mixed finite element methods and local discontinuous Galerkin methods. To alleviate the stiffness of the equations we develop and analyze Schwarz domain decomposition methods in conjunction with implicit-explicit (IMEX) time stepping routines. We analyze the numerical methods and prove their convergence under mesh refinement. Finally, we present results from numerical experiments in order to develop a strategy for optimizing solar cell design at the nano-scale.

Table of Contents

Acknowledgments	v
Abstract	vii
List of Tables	xii
List of Figures	xiii
Chapter 1. Introduction	1
1.1 Background and Motivation	1
1.2 Literature Review	6
1.2.1 Photoelectrochemical Solar Cells	6
1.2.2 Numerical Approximations	9
1.3 Summary of Contributions	15
1.4 Outline of Dissertation	17
Chapter 2. Modeling Of Photoelectrochemical Solar Cells	18
2.1 Domain Decomposition Of The Model Problem	19
2.2 Charge Transport In Semiconductors	20
2.3 Semiconductor-Electrochemistry	32
2.3.1 Charge Transport In Electrolytes	32
2.3.2 Semiconductor-Electrolyte Interface Reactions	37
2.3.3 Relationship Of Interface Conditions To Other Models In Electrochemistry	45
2.3.3.1 Butler-Volmer Model	45
2.3.3.2 Schottky Model	47
2.3.4 Photoelectrochemical Solar Cells	49
2.4 Summary Of Mathematical Model	52

Chapter 3. Numerical Approximations To Model Problem	56
3.1 Preliminaries	56
3.1.1 Non-Dimensional Formulation	56
3.1.2 Preliminary Notation	58
3.2 Mixed Finite Element Method (MFEM)	63
3.3 Local Discontinuous Galerkin (LDG) Method	66
3.4 Implicit/Explicit (IMEX) Time Stepping Algorithms	70
3.4.1 The Implicit-Implicit-Explicit Alternating Schwarz Scheme	72
3.4.2 The Implicit-Explicit-Explicit Alternating Schwarz Scheme	77
3.4.3 The Implicit-Explicit-Explicit Parallel Schwarz Scheme .	79
3.4.4 The Two-Scale Implicit-Explicit-Explicit Parallel Schwarz Scheme	81
3.5 Overview of Numerical Software	83
3.5.1 One Dimensional Code	85
3.5.2 Two Dimensional Code	86
Chapter 4. Analysis Of Local Discontinuous Galerkin Methods	87
4.1 Preliminaries	87
4.1.1 Model Properties	87
4.1.2 Identities and Theorems	92
4.2 Primal Form	96
4.3 Consistency Of Primal Form	99
4.4 Continuity and Coercivity of Bilinear Forms	104
4.5 Error Estimates	109
Chapter 5. Numerical Results	127
5.1 Study On Discretizations Convergence Rates	127
5.1.1 One Dimensional Results	128
5.1.2 Two Dimensional Results	129
5.1.2.1 Decoupled Tests	131
5.1.2.2 Coupled MFEM-LDG-IMEX Test	134
5.1.2.3 Coupled LDG Reactive Interface Test	135
5.2 Studies On Computational Performance	138

5.2.1	Study On The Performance Of Time Stepping Algorithms	138
5.2.2	Parallel Implementation	142
5.3	Numerical Experiments	146
5.3.1	One Dimensional Simulations	148
5.3.1.1	Effect Of Device Size	148
5.3.1.2	Impact Of Interfacial Charge Transfer Rates	150
5.3.1.3	Impact Of The Doping Profile	154
5.3.1.4	Comparison With The Schottky Approximation	158
5.3.2	Two Dimensional Simulations	162
5.3.2.1	Boundary Conditions Case 1	164
5.3.2.2	Boundary Conditions Case 2	166
5.3.2.3	Boundary Conditions Case 3	167
Chapter 6.	Concluding Remarks And Future Developments	178
Appendices		180
Appendix A. Appendix		181
A.1	LDG Analysis Appendix	181
A.1.1	Lipschitz Property of Recombination	181
A.1.2	Derivation Of Primal Form Of LDG Method	182
Bibliography		187
Vita		207

List of Tables

5.1	Time in seconds spent in the subroutines of each Schwarz method.	139
5.2	Run times and speedup ratio of two dimensional code on Stampede. The number of degrees of freedom (DOFS) was 31,040 for the MFEM and 15,360 for each LDG system for a total of 92,480 DOFS.	145
5.3	Run times and speedup ratio of two dimensional code on Stampede using the reduced MFEM. The number of degrees of freedom (DOFS) was 7,840 for the MFEM and 15,360 for each LDG system for a total of 69,280 DOFS.	146
5.4	Physical constants	147
5.5	Bulk silicon properties	147
5.6	Bulk redox properties	147
5.7	D-I & D-II parameter values.	149
5.8	D-III & D-IV parameter values (left) and performance (right).	149
5.9	Performance of D-III (left) & D-IV (right) with various k_{ht} values.	152
5.10	D-V (left) parameter values & performance (right).	156
5.11	D-VI (left) & D-VII (right) parameter values.	160
5.12	Parameter values for the two dimensional simulations.	164
5.13	D-VIII (left) & D-IX (right) domains.	165

List of Figures

1.1	Typical set up of a photoelectrochemical solar cell. Here $h\nu$ is a photon, e^- and h^+ are the photo-generated electron-hole pair, and A/A^- are the redox species [99].	2
1.2	Comparison of photon absorption and carrier collection in planar (A) and nanowire (B) solar cells [144].	3
2.1	Domain decomposition of model problem.	19
2.2	a.) The various energy levels of a n-type semiconductor in equilibrium, adapted from [25]. b.) Quasi Fermi-levels under local excitation, adapted from [111].	22
2.3	a) The energy levels of the redox couple. Note here $E_{F,el}$ is the reference Fermi level of electrolyte. b) The density of states for redox couples. [111]	36
2.4	Energy levels in a semiconductor-electrolyte interface, here e stands for the charge of an electron, $\Delta\Phi_{SC}$, $\Delta\Phi_H$ are the space charge region and Helmholtz potentials respectively; χ^{el} , Φ^{el} are respectively the surface dipole contribution and work function of the electrolyte which we will not discuss further. [111]	38
2.5	Potential drops across the double layer in the electrolyte. V_{SC} , V_H , V_G are the SCR, Helmholtz and Gouy layer potentials respectively. [122]	39
2.6	Energy levels of the semiconductor and electrolyte under an applied biases. Source: [111]	42
2.7	Dynamics of a n-type semiconductor PEC solar cell under illumination. [4]	49
2.8	Solar cell current-voltage curve. Here I , U are the current and applied voltage respectively; I_s , U_{ph} are the short circuit current and open circuit respectively. [111]	51
5.1	1D L^2 error plots for (a) MFEM on Poisson's equation and (b) LDG on the drift-diffusion equation.	129
5.2	L^2 error plots for steady-state electron densities.	130
5.3	2D L^2 error plots for MFEM for the problem (5.1.3).	132

5.4	2D L^2 error plots for the LDG-IMEX method for the problem (5.1.6)	134
5.5	2D L^2 error plots for the MFEM-LDG method for the problem (5.1.6)	136
5.6	2D L^2 error plots for the LDG-PS-IMEXEX method for the problem (5.1.15) and (5.1.16) for (a) $k = 1$ and (b) $k = 2$	138
5.7	Run time performance results provided by GRVY.	139
5.8	Percentage of runtime in subroutines from Table 5.1.	142
5.9	Run time performance results of key subroutines provided by the deal.II library using one core on Stampede.	144
5.10	Steady state characteristics of D-I in the the dark.	150
5.11	Steady state characteristics of D-I in under illumination.	151
5.12	Steady state characteristics of D-II in the the dark.	152
5.13	Steady state characteristics of D-II in under illumination.	153
5.14	Illuminated current-voltage curves for D-III & D-IV.	154
5.15	Illuminated current-voltage curves for D-III with varying minority transfer rate.	155
5.16	Illuminated current-voltage curves for D-IV with varying minority transfer rate.	155
5.17	Illuminated currents of D-V with different doping profiles.	157
5.18	Electric field values of D-V with different doping profiles.	158
5.19	Current density as computed with full system and Schottky approximation.	161
5.20	Illuminated current-voltage curves for device D-VII.	161
5.21	The domain for two dimensional nanowire simulations.	162
5.22	Densities of charge carriers in D-VIII (parallel interface with case 1 boundary conditions) with (a) $\Phi_{app} = 0.0$ [V] and (b) $\Phi_{app} = 0.0$ [V]. Note: Densities are in 10^{17} [cm $^{-3}$].	168
5.23	Carrier currrents in device D-VIII (parallel interface with case 1 boundary conditions) with $\Phi_{app} = 0.0$ [V] for D-VIII.	169
5.24	Carrier currrents in device D-VIII (parallel interface with case 1 boundary conditions) with $\Phi_{app} = 0.5$ [V].	170
5.25	The potential distribution of D-VIII (parallel interface with case 1 boundary conditions) with different applied biases.	171

5.26 Densities of charge carriers in device D-IX (oblique interface with case 1 boundary conditions) with (a) $\Phi_{app} = 0.0$ [V] and (b) $\Phi_{app} = 0.0$ [V]. Note: Densities are in 10^{17} [cm^{-3}].	172
5.27 Carrier currents for device D-IX (oblique interface with case 1 boundary conditions) with $\Phi_{app} = 0$ [V]	173
5.28 Carrier currents for device D-IX (oblique interface with case 1 boundary conditions) with $\Phi_{app} = 0.5$ [V].	174
5.29 The potential distribution of device D-IX (oblique interface with case 1 boundary conditions) with different applied biases.	175
5.30 Results from D-VIII (parallel interface with case 2 boundary conditions).	176
5.31 Electron densities for D-VIII (parallel interface with case 3 boundary conditions). Note: The density is in 10^{16} [cm^{-3}].	177

Chapter 1

Introduction

1.1 Background and Motivation

Large-scale utilization of photovoltaic (PV) devices, or solar cells, has been hampered for years due to high costs and lack of energy storage mechanisms. Photoelectrochemical solar cells (PECs), also known as semiconductor-electrolyte solar cells, are an attractive alternative to conventional solid state PV devices. PECs such as those depicted in Figure 1.1 are able to directly convert solar energy into hydrogen fuel. The hydrogen fuel can then be used at a later time to generate electricity. In the typical setup depicted in Figure 1.1, a PEC consists of four main components: the solid semiconductor electrode, the liquid electrolyte component, the semiconductor-electrolyte interface and the counter (metal or semiconductor) electrode. When sunlight shines on the semiconductor component, photons are absorbed and generate electron-hole pairs. These electrons and holes are separated by a built-in electric field within the semiconductor. The separation of the electrons and holes leads to an electrical current in the cell and the accumulation of charges at the semiconductor-electrolyte interface. At the interface, the photo-generated electrons or holes induce a chemical reaction at the semiconductor electrode. A similar chemical reaction also occurs at the counter electrode. These chemical

reactions create or eliminate reductant-oxidant (redox) species in the electrolyte. The transport of the produced redox pairs through the electrolyte results in a continuous current across the device.

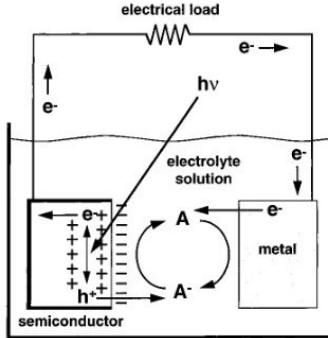


Figure 1.1: Typical set up of a photoelectrochemical solar cell. Here $h\nu$ is a photon, e^- and h^+ are the photo-generated electron-hole pair, and A/A^- are the redox species [99].

Research on PECs has traditionally focused on planar cell designs, but recently there has been interest in cell designs that use thin nanostructured wires such as those depicted in Figure 1.2. In a planar device (Figure 1.2 A), photo-generated electrons and holes are collected in directions parallel to photon absorption. In order for PECs' to achieve sufficient energy conversion efficiencies to be commercially viable the electron/hole diffusion length (L_D) (the average distance an electron/hole can travel without being eliminated) must be larger than the absorption length ($1/\alpha$) (the average distance a photon will penetrate the semiconductor crystal before generating an electron-hole pair). This constraint necessitates the use of expensive, high quality crystals that either have large diffusion lengths or small absorption lengths. In PECs

that use a nanowire design (Figure 1.2 B) the electron/hole collection and photon absorption directions are decoupled, thereby alleviating the need for high quality crystals to attain sufficient energy conversion efficiencies.

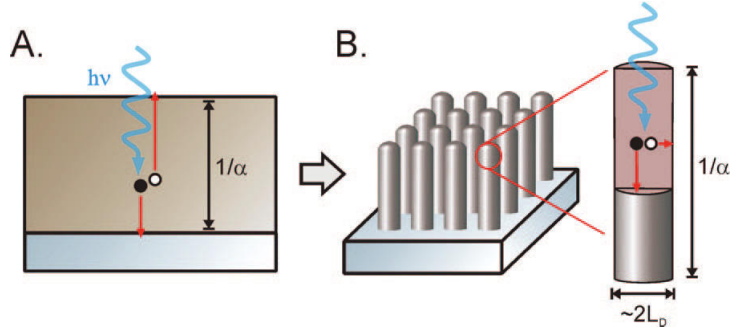


Figure 1.2: Comparison of photon absorption and carrier collection in planar (A) and nanowire (B) solar cells [144].

The physical mechanisms of charge creation, elimination and transport in the semiconductor and the electrolyte components are well-understood. The most popular mathematical model used to describe these processes is a macroscopic reactive-flow-transport system of partial differential equations. In the semiconductor community this system is known as the drift-diffusion-Poisson equations [108], while in the electrochemistry community it is called the Plank-Nernst-Poisson equations [24]. The physics of charge transfer between the components of the PEC is far less understood, and the appropriate mathematical model to describe the chemical reactions is still under debate [29, 94, 99, 111]. However, it is well-documented that the overall performance of photoelectrochemical solar cells is highly dependent on the chemical reactions at the solid-liquid interface [99]. Therefore a through understanding of

the dynamics of charge transfer at the semiconductor-electrolyte junction is essential for designing efficient photoelectrochemical solar cells.

The standard model of the interfacial reactions uses the product of electron-oxidants and hole-reductant densities at the interface. The nonlinear coupling of electron-hole pairs and reductant-oxidant pairs across the interface poses serious challenges from the mathematical and computational perspective. In most previous studies of PECs, researchers avoided the complications of the coupled nonlinear interface conditions by using the so-called “Schottky approximation.” In this approximation, one linearizes the interface conditions by treating the density of reductants and oxidants as constants. Simulations based on this procedure, while valid in some instances, have been shown to produce results which deviate from the results produced by simulations that use the nonlinear coupled interface conditions [84]. In order to accurately quantify the performance of PECs simulations that use the coupled nonlinear reactive interface conditions need to be conducted.

The main challenges in constructing a numerical algorithm that produces a reliable simulation of PECs are due to the nonlinearities arising, not only, from the coupling of the corresponding drift diffusion (transport) equations to the Poisson equation in both the semiconductor region and the electrolyte region, respectively, but also, with the nonlinear reactive interface conditions on semiconductor-electrolyte interface. While there have been many contributions in the last forty years on the approximations to solution of a single drift-diffusion-Poisson system in the semiconductor region, there is no

previous work, to the best of our knowledge, that deals with the whole coupled system that incorporates the nonlinear interface conditions for photoelectrochemical solar cells. In addition, the evolution problem under consideration is effectively multi-scale in the sense that the evolution of the system in the semiconductor and the corresponding one in the electrolyte evolve at different time scales due to the quantitative scaling differences in the relevant physical parameters such as mobilities or characteristic charge densities. The nonlinearity and multi-scale nature of the semiconductor-electrolyte interface place severe constraints on our choice of discretization strategy.

In particular, in order to ensure computational stability, the size of the time step (chosen for any time discretized scheme) is dominated by the value in the fast-varying component, that is, the semiconductor component. Using small time steps in the numerical simulations for the problem in the whole domain results in regions of stiffness caused by boundary layer formation where sharp transitions in densities and electric potential occur (i.e. near interfaces). This problem can be tackled by using fine enough meshes around the interface that would resolve these boundary layers. Such considerations limit even further the time step sizes on the employed computational method.

In this dissertation we propose, implement and analyze numerical algorithms for the simulation of semiconductor-electrolyte solar cells on the mathematical model developed in [84]. To simplify the presentation we neglect the dynamics of the counter electrode and only consider the interaction of the semiconductor and the electrolyte. Spatial discretizations of the drift-diffusion-

Poisson equations are based on local discontinuous Galerkin (LDG) methods and mixed finite element methods respectively. To alleviate the stiffness of the equations we develop and analyze implicit-explicit (IMEX) time stepping routines. We then analyze our numerical approximations and prove their convergence under mesh refinement. Finally, we present results from numerical experiments in order to develop a strategy for optimizing solar cell design at the nano-scale. In the next section we briefly review previous studies in this research domain.

1.2 Literature Review

1.2.1 Photoelectrochemical Solar Cells

The first modern (silicon) solar cell was invented in the 1954 by Chapin, Fuller and Pearson [114], however, research in using solar cells for terrestrial energy production remained minimal until the energy crisis of the 1970's. Since that time the field of photovoltaics has been greatly boosted by the research of semiconductor devices and the simulations tools developed to analyze them. The majority of these simulations have used the drift-diffusion-Poisson equations to model the transport of electrons and holes in semiconductors. The drift-diffusion-Poisson equations was first proposed by Van Roosbeck in 1950 [142] and has remained the standard model for semiconductor devices since it represents a good balance between accuracy and computational efficiency [108]. However, the drift-diffusion-Poisson equations still pose many challenges from the computational perspective. Indeed the system is notorious for

its stiffness, nonlinearity, and the locality of its physical behavior [38, 108, 130]. With the introduction of VLSI-circuits and the decreasing size of solid state devices, there has been a increased need for more complicated models which incorporate quantum effects [91, 108, 143]. However, the inclusion of quantum effects through more advanced models is not necessary for most photovoltaic devices [114].

The first solid-liquid junction solar cell was invented by Becquerel in 1839 and consisted of platinum electrodes and silver chloride dissolved in a acidic solution [114]. Electrochemical systems such as the one developed by Becquerel were later analyzed by Helmholtz Gouy, Debye, Stern and Chapman by treating them as electrical circuits and fitting model parameters with experimental results [24, 29, 111, 115]. In this theory, the formation of boundary layers of charge in the electrolytes are treated as parallel-plate capacitors. While this discovery produced great insight into the basic properties of electrochemical systems, models that require less ad-hoc assumptions were desired. Researchers now model the transport of ions in electrolytes by using the Planck-Nernst-Poisson (PNP) equations [31, 65, 86, 117]. Since the PNP equations are equivalent to the drift-diffusion-Poisson equations they share many of the same mathematical and computational difficulties. Additionally, in electrochemical systems there is still debate on how to appropriately describe the chemical reactions at the electrode-electrolyte interface as boundary conditions to the PNP equations [29, 94, 99, 111].

The chemical reactions at electrode-electrolyte interfaces involve the

transfer of electrons between the solid and liquid. The classical theory of electron transfer between electrodes and electrolytes was developed in the 1960’s by Marcus [105, 106], Hush [87], and Geirscher [74, 75]. In the early 1970’s Honda and Fujishima performed the first study to demonstrate that a semiconductor (in this case TiO_2) can be used to perform electrolysis on water [68]. This discovery sparked interest in utilizing semiconductor-electrodes to produce hydrogen fuel from water. In the last few decades there has been substantial effort to better understand the fundamental science of electron transfer at semiconductor electrode-liquid interfaces [72, 73, 76, 97–99, 116, 120, 134].

Parallel to the research in electron transfer theory has been the effort to develop semiconductor-electrolyte (photoelectrochemical) solar cells that directly convert solar energy into hydrogen fuel. Numerous device designs which use various semiconductor materials and electrolytes have been pursued [24, 67, 80, 90, 110, 111]. Recent theoretical efforts in semiconductor-electrochemistry have focused on modeling and simulation of devices using the drift-diffusion-Poisson equations with the goal of optimizing device performance. Particular interest has been focused on using nanostuctured wires to enhance carrier collection and therefore energy conversion efficiency [61, 67, 93, 110, 113, 127, 147]. In most of these studies the investigators used the Schottky approximation which neglects the interaction of the semiconductor with the electrolyte altogether. The first study to perform simulations using the fully coupled nonlinear semiconductor-electrolyte interface was completed by He. et. al. [84]. In this study the authors demonstrated that using the Schottky

approximation produces discrepancies when the concentration of redox species is comparable to the density of electron and holes. The model that the authors introduce in [84] is the model we shall adopt in this dissertation and will be discussed in Chapter 2.

1.2.2 Numerical Approximations

The drift-diffusion-Poisson equations are an example of a more general class of mathematical problems called reactive-flow-transport systems. Over the last few decades significant effort has been invested in the numerical discretization of these problems. In addition to research in semiconductor and electrolytes, such systems play an active role in research of oil-recovery, contaminant transport and air-quality. There are numerous discretization schemes that have been investigated on reactive-flow-transport problems [9, 23, 28, 43, 44, 58, 64, 70, 88, 125, 138]. In this dissertation we will approximate solutions to our mathematical model using a hybrid spatial discretization. To be specific we use a mixed finite element method (MFEM) to solve the Poisson equation and a discontinuous Galerkin (DG) method to solve the drift-diffusion equations. In [58], the authors show that such a choice of numerical discretizations is a compatible choice of algorithms. Compatibility of algorithms implies that the numerical method are locally mass conservative. This is an extremely important property for numerical methods to have when simulating reactive-flow-transport problems [58, 126]. DG methods and the MFEM both belong to a class of numerical methods called finite elements methods (FEM). Finite ele-

ment methods have been used extensively throughout science and engineering to approximation solutions to mathematical models involving partial differential equations [30, 89, 107, 135]. The finite element method relies on a weak formulation of the partial differential equation and the introduction of a mesh for the computational domain. Approximations to solutions of the weak formulation are obtained by expressing the solution as a linear combination of polynomials that are local to each element in the mesh.

The mixed finite element method (MFEM) is used to approximate solutions of Poisson’s equation where both the primary variable and its gradient are needed. This is achieved by rewriting the second order differential equation as two first order equations and introducing a weak formulation. The MFEM is an appealing method since it is mass conservative and produces approximations to gradients that are more accurate than solving for the primary variable using a traditional FEM and post processing to approximate its gradient [33, 35, 58]. The existence of solutions to the weak formulation of the mixed method is guaranteed by the Babuska-Brezzi or *inf-sup* condition [20, 34]. However, it is well known that stability of the continuum problem does not guarantee stability of the finite element approximation [32, 33]. Stable approximations to solutions of the Poisson equation by a mixed finite element method were first proposed by Raviart and Thomas [123]. In their study, the authors used the Raviart-Thomas elements to approximate the gradient and discontinuous polynomials elements to approximate the primary variable. In addition, they proved that this choice of function spaces results in $\mathcal{O}(h^{k+1})$

(where h is the maximum diameter of a mesh element) convergence rates for the approximation of both variables. Since their initial discovery, mixed finite element methods have been used extensively in modeling subsurface flow and computational fluid dynamics [9, 11, 32, 35, 63, 79].

Discontinuous Galerkin (DG) methods were first proposed by Reed and Hill [124] as a method for solving the neutron transport problem and later analyzed by Lesaint and Raviart [96]. The application of DG methods to more general hyperbolic problems was investigated by Cockburn and Shu in the seminal works on Runge-Kutta DG methods [16–19]. The discontinuous Galerkin method is similar to the traditional finite element method (FEM) in its use of a weak formulation. However, traditional FEM uses polynomial basis functions that are continuous across elements, while, DG methods use local polynomial basis functions that are discontinuous across elements in the mesh. Due to the discontinuous nature, DG approximations are essentially double valued on the element edges. The uniqueness of DG approximations is enforced through the introduction of flux terms to the weak formulation. The numerical fluxes also have the advantage of enhancing the stability and accuracy of the method [85]. DG methods have many desirable qualities including being locally mass conservative, the ability to capture sharp gradients and also have high order accuracy [39, 85, 126]. Additionally, they are suitable for parallel implementation and can easily handle complex geometries. One drawback of DG method compared to the traditional FEM is that DG methods have an increase in the number of unknowns or degrees of freedom.

The local discontinuous Galerkin (LDG) method is a numerical discretization which approximates higher order differential equations by rewriting them as systems of first order equations. In this way the LDG method is similar to the mixed finite element method. The key difference between the two methods is that the LDG method uses discontinuous polynomials basis functions for all the variables one is approximating. The solution's regularity is enforced by penalizing the discontinuities in the solution across element faces. The first application of the local discontinuous Galerkin method to parabolic problems was implemented on the Navier-Stokes equations by Bassi and Rebay [27]. This method was later analyzed by Cockburn, Shu, Dawson and others for the general case of convection-diffusion equations [42, 48, 50, 51]. It was shown that in multiple dimensions the LDG method provides approximations to densities (or more general primary variables) that converge with the rate $\mathcal{O}(h^k)$ [48]. The LDG method is particularly useful for the case of convection dominated transport where there are step gradients in the solution. In such instances, traditional Galerkin finite element methods produce spurious oscillations in the computed solutions while DG methods remain stable [89].

The extension of the LDG method from parabolic problems to elliptic problems was proposed soon after its initial introduction [40, 41, 49, 92]. For elliptic problems, the convergence of approximations to variable gradients was proven to have a rate of $\mathcal{O}(h^k)$. The convergence rate of approximations to the primary variable was shown to depend on the penalty parameter. For the case where the penalty is of $\mathcal{O}(1)$ and $\mathcal{O}(h^{-1})$ the convergence rates were

proven to be $O(h^{k+1/2})$ and $\mathcal{O}(h^{k+1})$ respectively [40]. The LDG method was subsequently unified with the so-called primal DG methods for solving general elliptic equations in the seminal work of Arnold et. al. [12]. The LDG method shares many of the attractive qualities of traditional DG methods. In addition to these, for the case of transport of charge carriers the LDG method provides approximations to both the charge carrier densities and their current fluxes.

Numerical methods which have a large number of unknowns, such as the MFEM and LDG method, require efficient computational routines for solving large systems of equations. Many numerical methods have been proposed to speed-up traditional computations. The two methods we investigate in this dissertation are non-overlapping domain decompositions and implicit-explicit (IMEX) time stepping techniques. The first domain decomposition method was introduced by Schwarz in 1870 [129] for solving an elliptic problem on an irregular domain. Schwarz partitioned the domain into two overlapping subdomains. He solved the original problem by iteratively solving the solution on each subdomain and passing information between the two subdomains. Such techniques are called Schwarz methods and have received much investigation in their application to parallel computations [71, 109, 112, 121].

In the late 1980's and early 1990's Lions investigated the theoretical foundation of Schwarz methods and their application to parallel computations. He was able to prove the convergence of overlapping Schwarz methods for linear elliptic problems [102, 103] and later extended this work to non-overlapping Schwartz methods [104]. Since the 1990's interest in using domain decompo-

sition methods for parallel computations has been replaced by the utilization of distributed linear solvers [140]. However, domain decomposition methods still remain useful as preconditioners [71, 140] as well as in applications to partitioned analysis in multiphysics problems such as fluid-structure interaction [37, 77, 78] and fluid-fluid interaction [52, 53].

Implicit-explicit (IMEX) or semi-implicit time stepping methods have been traditionally applied to convection-diffusion equations [13, 14, 95, 141]. The choice of underlying spatial discretization of the differential equation is of little consequence to the time marching procedure. However, the use of IMEX time stepping in conjunction with LDG spatial discretizations on convection-diffusion equations was recently introduced by H. Wang et. al. [145, 146]. The theory of IMEX time stepping is based on the observation that the time step required for stability of explicit methods on convective problems is $\Delta t = \mathcal{O}(h)$. In contrast, the time step for stability of explicit methods on diffusive problems is $\Delta t = \mathcal{O}(h^2)$. A constraint of $\mathcal{O}(h^2)$ is quite severe, especially for problems that have boundary layers and where locally refined meshes are required. In order to alleviate the constraint of using small time steps for convection-diffusion equations, one often treats the diffusive term using implicit time stepping and the convective term with explicit time stepping. This allows one to use time steps that are on the order of $\mathcal{O}(h)$ for the convection-diffusion problems and can substantially reduce over all CPU run time of simulations. Furthermore, in convection-diffusion systems, the convection field is often a nonlinearly coupled term. We will show in Chapter 5 that for our problem significant savings

in CPU time can be achieved by treating the convective term explicitly instead of implicitly our in time stepping routines.

The extension of IMEX methods from convection-diffusion equations to problems involving the decomposition of parabolic problems across multiple domains was proposed by Dawson, et. al. [59, 60]. The authors utilized an overlapping domain decomposition where the overlapping portion was updated using explicit time stepping. The non-overlapping portions of the domain decomposition were then updated utilizing implicit time stepping. IMEX decoupling procedures using non-overlapping domain decompositions for linearly coupled parabolic problems was investigated by Connors et. al. [52]. This work was later extended to nonlinear coupled Navier-Stokes equations for fluid-fluid interaction [53]. We adopt similar time stepping routines to [52] as well as techniques developed for the simulation of two-phase flow [45–47, 131, 136] to the simulation of semiconductor-electrolyte interfaces. In Chapter 3 we will further review these methods and introduce new improvements for our application problem.

1.3 Summary of Contributions

This dissertation discusses the modeling and simulation of the transport and the transfer of charges across a semiconductor-electrolyte interface. Software is developed in one dimension using the Eigen numerical linear algebra library and in two dimensions using the deal.II library. Both codes are designed for easy of use and utilize shared-memory parallelization to speed-

up computations. Analysis of the underlying numerical approximations is performed and both codes are verified using a test-suite. Specifically in this dissertation we will discuss the following contributions:

- Derivation and discussion of the mathematical modeling of charge transport and transfer in photoelectrochemical solar cells. The relationship between the macroscopic model used for computation and the Geirscher model of electron transfer in terms of energy levels is fully explained.
- Development of local discontinuous Galerkin methods and mixed finite element methods for the spatial discretization of drift-diffusion-Poisson systems which are coupled through a reactive interface.
- Development and analysis of specifically tailored implicit-explicit-Schwarz time stepping routines to alleviate the stiffness of the model system. We remark that the utilization of non-iterative techniques was necessitated in order to guarantee existence and uniqueness of solutions.
- Theoretical analysis of the local discontinuous Galerkin (LDG) method applied to transport problems with reactive interfaces. Specifically, we introduce the primal form of the LDG method and prove its consistency as well as the coercivity and continuity of its bilinear forms. We then use these properties to prove semidiscrete error estimates for the LDG method in primal form.

- We perform numerical experiments to discover the dependence of solar cell performance on device parameters and develop a strategy to maximize power output for nanoscale devices.

1.4 Outline of Dissertation

The rest of this dissertation is as follows. A review and discussion of the mathematical model of photoelectrochemical solar cells is provided in Chapter 2. In Chapter 3 we introduce the numerical methods and code base used to simulate the dynamics of the reactive semiconductor-electrolyte interface in photoelectrochemical solar cells. In Chapter 4 we analyze the local discontinuous Galerkin (LDG) approximations to the drift-diffusion equations and prove semidiscrete error estimates. In Chapter 5 we conduct studies on the convergence of our numerical approximations and discuss the performance of our algorithms. Additionally, we present results of some numerical experiments to analyze the performance of PECs under various scenarios. Finally, in Chapter 6 we review the completed work and offer some directions for future research projects.

Chapter 2

Modeling Of Photoelectrochemical Solar Cells

In this chapter we discuss the mathematical model of semiconductor-electrolyte interfaces that is used to simulate photoelectrochemical solar cells. We shall focus on the reactive charge dynamics of the semiconductor-electrode-liquid junction and neglect any interaction with other electrodes. The macroscopic model we adopt was introduced in [84]. This model is based on a drift-diffusion-Poisson system and approximates the transport behavior of delocalized electrons and holes in a semiconductor as continuum charge densities. Adopting this model requires several mathematical and physical assumptions that shall be discussed. The drift-diffusion-Poisson model for PECs is attractive from a computational point of view, however, it circumvents any discussion of the energetics of the reactions between electron-hole pairs and redox species. Indeed, most of the classical theories of electron transfer across an electrode-electrolyte interface have been described in terms of energy levels of the individual carriers [25, 111, 122, 134]. We therefore carefully derive the mathematical model in [84] and relate the chemical reactions at the interface in terms of the energy levels of the electrons, holes, oxidants and reductants. Additionally, in Section 2.3.3 we remark on the relationship of this model to other models traditionally used in electrochemistry. Finally, in Section 2.4 we

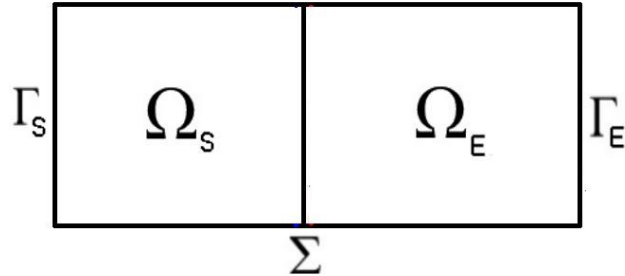


Figure 2.1: Domain decomposition of model problem.

summarize the mathematical model and the underlying assumptions for its physical validity.

2.1 Domain Decomposition Of The Model Problem

We first introduce the domain decomposition of the semiconductor-electrolyte interface. In Figure 2.1, the solid semiconductor region is Ω_S and will contain electrons and holes. The liquid electrolyte region is Ω_E and will contain reductants and oxidants. The electrons, holes, reductants and oxidants reside within their respective material domains. The interaction of electron/holes with the redox species only occurs at the interface of the solid and liquid. The domain of the device is,

$$\Omega := \Omega_S \cup \Omega_E. \quad (2.1.1)$$

The interface of the semiconductor and electrolyte, Σ , is defined as,

$$\Sigma := \overline{\Omega}_S \cap \overline{\Omega}_E. \quad (2.1.2)$$

We stress that other than at the interface, the two domains do not intersect,

$$\Omega_S \cap \Omega_E = \emptyset. \quad (2.1.3)$$

The unit normal vector pointing from the semiconductor to the electrolyte is labeled \mathbf{n}_{Σ^S} . The unit normal vector pointing from the electrolyte to the semiconductor is \mathbf{n}_{Σ^E} . The boundary of the semiconductor that is not the interface is labeled Γ_S and the boundary of the electrolyte that is not the interface is labeled Γ_E . The exterior boundary of the domain, Γ , is then,

$$\Gamma := \Gamma_S \cup \Gamma_E, \quad (2.1.4)$$

and the total boundary of our device is defined to be the sum of interface and the semiconductor and electrolyte boundaries,

$$\partial\Omega := \overline{\Omega_S \cup \Omega_E} \setminus \Omega_S \cup \Omega_E = \Sigma \cup \Gamma_S \cup \Gamma_E. \quad (2.1.5)$$

Finally, the exterior boundary Γ can be decomposed into portions where carriers have Dirichlet conditions, $\Gamma_{S,D}$ and $\Gamma_{E,D}$, and where carriers have insulating Neumann conditions, $\Gamma_{S,N}$ and $\Gamma_{E,N}$.

2.2 Charge Transport In Semiconductors

A semiconductor is a solid crystalline material with electrical conductivity that is between an insulator and conductor. Electrons that can generate an electrical current are called free electrons. Electrons that are bound to atoms in the semiconductor lattice are called bound electrons. Electrons in

semiconductor crystals have continuous energy levels within finite intervals called energy bands. Free electrons have energies in the conduction band(s), labeled E_C [eV]. Bound electrons have energies in the valance band(s), labeled E_V [eV]. Due to the periodic nature of crystal lattices, electrons have certain energies that they cannot attain. The band gap, E_g [eV], is defined as these “forbidden” energy levels (see Figure 2.2 a.)). The band gap also separates the lowest conduction band from the highest valance band. It is defined as,

$$E_g := E_C - E_V. \quad (2.2.1)$$

The set of all the energy levels and band gaps is called the bandstructure. The Fermi level, E_F [eV], is the energy level in the bandstructure where an electron has occupation probability of one half. In a semiconductor the Fermi level naturally lies within the band gap. Therefore the valance band is nearly full of electrons and the conduction band is nearly empty. There are a small number of electrons that are able to be promoted from the valance band to the conduction band by absorbing thermal energy through a process called thermal excitation. The resulting electron density is called the intrinsic density (ρ_i [cm⁻³]) and has energy E_i [eV].

The electrical conductivity of a semiconductor can be increased though a process called doping. Doping a semiconductor is the process of introducing impurities into the crystal lattice. Adding donors (with density $N_D(\mathbf{x})$ [cm⁻³]) involves replacing a normal semiconductor atom with an atom that has more electrons. Adding acceptors (with density $N_A(\mathbf{x})$ [cm⁻³]) means replacing a

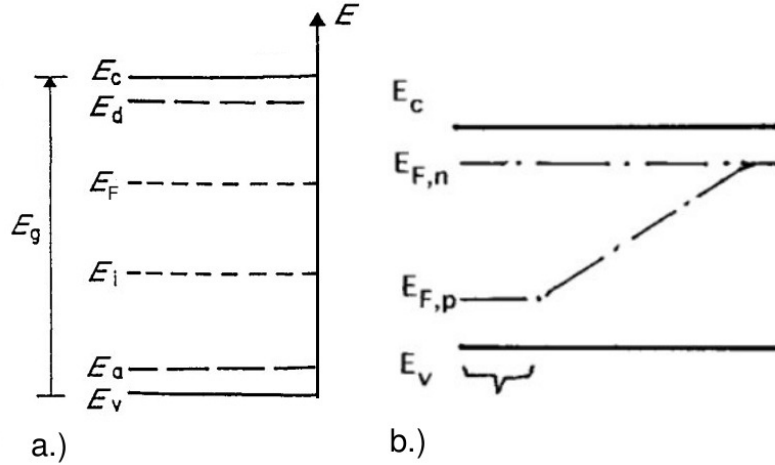


Figure 2.2: a.) The various energy levels of a n-type semiconductor in equilibrium, adapted from [25]. b.) Quasi Fermi-levels under local excitation, adapted from [111].

normal semiconductor atom with an atom that has less electrons. We define the doping profile, $C(\mathbf{x})$ [cm^{-3}], as the total fixed background charge density,

$$C(\mathbf{x}) := N_D(\mathbf{x}) - N_A(\mathbf{x}). \quad (2.2.2)$$

Donor electrons have energy E_d [eV] that is very close to the conduction band and are often ionized through thermal fluctuations in their energy [139] (see Figure 2.2 a.)). Ionization of the donors gives rise to conduction band electrons (we will refer to them as just electrons from now on). Through a similar process, ionization of acceptors with energy E_a [eV] gives rise to charge carriers called holes (see Figure 2.2 a.)). Holes are positively charged quasi-particle that represent a missing electron in the periodic crystal structure. Holes have energies levels that are in the valance band. We label the electron density $\rho_n(\mathbf{x}, t)$ [cm^{-3}] and the hole density $\rho_p(\mathbf{x}, t)$ [cm^{-3}].

Doping a region with more donors than acceptors moves the Fermi level of the semiconductor closer to the conduction band and increases the density of electrons. The resulting semiconductor is then called “n-type.” In a n-type semiconductor electrons are called majority carriers and holes are called minority carriers. Similarly, doping a region with more acceptors than donors moves the Fermi level of the semiconductor closer to the valance band and increases the density of holes. The resulting semiconductor is called “p-type.” In a p-type semiconductor electrons are called minority carriers and holes are called majority carriers. The electron affinity, denoted by χ^{SC} [V], is the energy needed to move an electron from the conduction band to the surface of the semiconductor divided by the charge of an electron. The surface of the semiconductor is also known as the vacuum level and has an energy level denoted by E_{VAC} [eV]. Finally, the work function of a semiconductor, denoted by Φ^{SC} [V], is defined as the energy need to move an electron from the Fermi-level to the surface E_{VAC} divided by the charge of the electron. The relation of electron affinity and work function in terms of the semiconductor energy levels are displayed in Figure 2.4.

In non-degenerate semiconductors (semiconductors where the Fermi level is below the conduction band) and normal temperatures (around 300K), the densities of electrons and holes in equilibrium are approximated using Boltzmann statistics [139],

$$\rho_n^e = N_C e^{-(E_C - E_F)/k_B T}, \quad \rho_p^e = N_V e^{-(E_F - E_V)/k_B T}. \quad (2.2.3)$$

The terms N_V , N_C [cm⁻³] are the effective densities of states for the conduction band and valance band respectively. k_B [J/K] is the Boltzmann constant and T [K] is temperature. The densities of electrons and holes in equilibrium can also be related to the intrinsic density through the equations [139],

$$\rho_n^e = \rho_i e^{(E_F - E_i)/k_B T}, \quad \rho_p^e = \rho_i e^{(E_i - E_F)/k_B T}. \quad (2.2.4)$$

In equilibrium the product of the density of electrons and holes is related to the intrinsic density through the so-called “law of mass” [139],

$$\rho_n^e \rho_p^e = \rho_i^2. \quad (2.2.5)$$

Using equations (2.2.1), (2.2.3), and (2.2.5) we obtain a relation for the intrinsic density,

$$\rho_i = \sqrt{N_C N_V} e^{-E_g/2k_B T}. \quad (2.2.6)$$

Remark 2.2.1. In equilibrium the Fermi level of a semiconductor is constant. This implies,

$$\nabla E_F = 0 \quad (2.2.7)$$

A semiconductor device can be driven out of equilibrium by an excitation event such as an applied voltage bias or photon absorption. A semiconductor under local excitation like that depicted in Figure 2.2 b.) no longer has a constant Fermi level. Therefore, we can no longer describe the densities of electrons and holes in the device by the equations of (2.2.3) or (2.2.4). When the excitation of electrons and hole is not too great, the semiconductor

device can be said to be in quasi-equilibrium. The densities of electrons and holes in quasi-equilibrium can then be described by [114],

$$\rho_n = N_C e^{-(E_C - E_{F,n})/k_B T}, \quad \rho_p = N_V e^{-(E_{F,p} - E_V)/k_B T}. \quad (2.2.8)$$

The terms $E_{F,n}(\mathbf{x})$ [eV] and $E_{F,p}(\mathbf{x})$ [eV] are the quasi-Fermi levels of electrons and holes respectively. The difference in the quasi Fermi-levels is equal to the energy of the excitation event $\Delta\mu$ [eV] [114],

$$E_{F,n} - E_{F,p} = \Delta\mu, \quad (2.2.9)$$

When a semiconductor is driven out of equilibrium by an excitation event then an electric current density is produced as a response. The electric current density \mathbf{J} [A cm^{-2}] is composed of two parts, the first being due to the transport of electrons and is called the electron current density (\mathbf{J}_n [A cm^{-2}]). The second component is due to the transport of holes and is called the hole current density (\mathbf{J}_p [A cm^{-2}]). The electron and hole current densities are related to the gradients of the quasi-Fermi levels by [114],

$$\mathbf{J}_n = \mu_n \rho_n \nabla E_{F,n}, \quad \mathbf{J}_p = \mu_p \rho_p \nabla E_{F,p}. \quad (2.2.10)$$

The terms μ_n [cm^2/Vs] and μ_p [cm^2/Vs] are the electron and hole mobility respectively. Solving (2.2.8) for $E_{F,n}$ and $E_{F,p}$ and taking the gradients we obtain,

$$\begin{aligned} \mathbf{J}_n &= \mu_n \rho_n \nabla E_C + \mu_n k_B T \nabla \rho_n - \nabla (k_B T \ln(N_C)) + k_B \ln(\rho_n) \nabla T, \\ \mathbf{J}_p &= \mu_p \rho_p \nabla E_V - \mu_p k_B T \nabla \rho_p + \nabla (k_B T \ln(N_V)) - k_B \ln(\rho_p) \nabla T. \end{aligned} \quad (2.2.11)$$

If our semiconductor is compositionally invariant then N_C and N_V are constants. Additionally, this also implies that gradients in the conduction and valance band energies are only due forces on the charges by the electric field \mathbf{E} [V/cm] within the semiconductor [114]. If we make the reasonable assumption that the electrons and holes will be the same temperature as the semiconductor lattice, then the temperature T is constant [114]. With these two assumptions (2.2.11) reduces to,

$$\begin{aligned}\mathbf{J}_n &= q\mu_n \mathbf{E} \rho_n + \mu_n k_B T \nabla \rho_n, \\ \mathbf{J}_p &= q\mu_p \mathbf{E} \rho_p - \mu_p k_B T \nabla \rho_p,\end{aligned}\tag{2.2.12}$$

where, q [C] is the charge of an electron. Under low biases, we can relate the mobility of the carriers to their diffusivity D [cm² s⁻¹] through the Einstein relation [139],

$$D = \mu U_T,\tag{2.2.13}$$

where U_T [V] is the thermal voltage. The thermal voltage is defined as,

$$U_T := \frac{k_B T}{q}\tag{2.2.14}$$

Substituting the Einstein relation (2.2.13) into (2.2.12), we obtain the drift-diffusion equations for the current densities of electrons and holes,

$$\begin{aligned}\mathbf{J}_n &= q\mu_n \mathbf{E} \rho_n + qD_n \nabla \rho_n, \\ \mathbf{J}_p &= q\mu_p \mathbf{E} \rho_p - qD_p \nabla \rho_p.\end{aligned}\tag{2.2.15}$$

Remark 2.2.2. Under large electric fields semiconductors exhibit a so-called “velocity saturation” effect. With small electric fields the electron and hole

drift velocity v_n^{dr} , v_p^{dr} [cm/s] [130],

$$v_c^{\text{dr}} := \mu_c \mathbf{E} \cdot \frac{\mathbf{J}_c}{|\mathbf{J}_c|}, \quad \text{for } c = \{n, p\}. \quad (2.2.16)$$

increases linearly. However, at a certain applied bias a saturation in the drift velocity is reached and further increases in the electric field do not yield increases in the drift current. Instead, the energy from the applied potential is absorbed by the crystal lattice as phonons (phonons are quasi-particles that represent quantized vibrational modes of the crystal lattice) and dissipated as heat. Velocity saturation effects are modeled using electric field dependent mobilities [107, 108, 130, 139]. One such example for silicon is [130],

$$\mu_c(\mathbf{E}) := \frac{2\mu_c}{1 + \sqrt{1 + (2\mu_c|\mathbf{E}|/v_{\text{sat}}^c)^2}}, \quad (2.2.17)$$

where v_c^{sat} [cm s^{-1}] for $c = \{n, p\}$ is the saturation velocity.

The time evolution of electron and hole densities is determined by the conservation of charge,

$$-q \frac{\partial \rho_n}{\partial t} - \nabla \cdot \mathbf{J}_n = -qG(\mathbf{x}) + qR(\rho_n, \rho_p), \quad (2.2.18)$$

$$q \frac{\partial \rho_p}{\partial t} + \nabla \cdot \mathbf{J}_p = qG(\mathbf{x}) - qR(\rho_n, \rho_p). \quad (2.2.19)$$

The functions $G(\mathbf{x})$ [cm $^{-3}s^{-1}$] and R [cm $^{-3}s^{-1}$] are the generation and recombination functions respectively. When sunlight shines on an semiconductor photons with energy larger than the band gap E_g will be absorbed and excite an electron from the valance band to the conduction band. The

promotion of an electron to the conduction band will generate a corresponding hole in the valence band. The generation of electrons and holes therefore occur in pairs and is modeled using the macroscopic source function [84, 114],

$$G(\mathbf{x}) := \begin{cases} \alpha(\mathbf{x}) G(\mathbf{x}_0) \exp\left(-\int_0^s \alpha(\mathbf{x}_0 + s' \boldsymbol{\theta}_0) ds'\right) & \mathbf{x} = \mathbf{x}_0 + s \boldsymbol{\theta}_0 \\ 0 & \text{otherwise} \end{cases} \quad (2.2.20)$$

The point \mathbf{x}_0 is the photon's incident location and $\boldsymbol{\theta}_0$ is the incident direction. $\alpha(\mathbf{x})$ [cm^{-1}] is the photon absorption coefficient. The absorption coefficient has been averaged over all energy values of light that generate free carriers, i.e. all photons with energy greater than or equal to the band gap. The term $G(\mathbf{x}_0)$ [$\text{cm}^{-2} \text{s}^{-1}$] represents the surface photon flux (averaged over wavelengths) at \mathbf{x}_0 .

Remark 2.2.3. We have assumed here that photons will travel in a straight line and will not be scattered throughout the crystal. For more complicated models see [114].

Remark 2.2.4. We have neglected any discussion on whether our material is a direct or indirect band gap semiconductor. Any knowledge of the bandstructure is implicitly known through the function $\alpha(\mathbf{x})$. See [114] for more detailed discussion of the optical excitation of semiconductors.

Recombination is the process in which a conduction band electron interacts with a hole and results in a valence electron. Thus it is a process in which the electron/hole pair are eliminated. Recombination coincides with a loss of energy, most often in the form of light or heat. While there are

many different mechanisms for recombination in a semiconductor, we shall only incorporate Shockley-Read-Hall (SRH) recombination or “trap assisted recombination” [132]. This recombination mechanism arises from localized impurities or defects in the semiconductor crystal that capture electrons and holes and cause them to recombine. SRH recombination is the most dominant recombination mechanism in real materials and is extremely important near material boundaries or interfaces as the concentration of defects is higher in those regions [114]. Other effects such as Auger and radiative recombination may be important in other semiconductor devices, but are never the dominate recombination mechanism in photovoltaic devices [114, 130]. SRH recombination is modeled using the nonlinear sink functional,

$$R(\rho_n, \rho_p) := \frac{\rho_n \rho_p - \rho_i^2(\mathbf{x})}{\tau_p(\mathbf{x}) (\rho_n + \rho_n^t(\mathbf{x})) + \tau_n(\mathbf{x}) (\rho_p + \rho_p^t(\mathbf{x}))}. \quad (2.2.21)$$

The terms $\rho_n^t(\mathbf{x})$ [cm^{-3}] are the $\rho_p^t(\mathbf{x})$ [cm^{-3}] are the density of traps for electrons and holes respectively. The functions $\tau_n(\mathbf{x})$ [s] and $\tau_p(\mathbf{x})$ [s] are the recombination times for electrons and holes respectively. They represent the average lifetime of electrons or holes before they are eliminated. We choose a single trap center at the middle of the band gap and therefore replace the trap densities with the intrinsic density: $\rho_n^t = \rho_p^t = \rho_i$ [135].

Remark 2.2.5. We remark that the generation and recombination functions are the same for both electrons and holes and this enforces the assumption that electrons and holes are always created and eliminated in pairs. We also note that SRH recombination can also be a source of electron-hole pairs through the process of thermal excitation.

The electric potential Φ [V] and electric field \mathbf{E} [V/cm] in a semiconductor are related to the densities of electrons and holes through Poisson's equation,

$$-\nabla \cdot (\epsilon_S \nabla \Phi) = \frac{q}{\epsilon_0} (C(\mathbf{x}) - (\rho_n - \rho_p)), \quad (2.2.22)$$

$$\mathbf{E} = -\nabla \Phi. \quad (2.2.23)$$

The constants, ϵ_S , ϵ_0 [$\text{C V}^{-1} \text{ cm}^{-1}$] are the semiconductor dielectric constant and vacuum permittivity constant respectively. The presence of the doping profile in Poisson's equation plays a critical role in the ability of a solar cell to convert sunlight into electricity. In traditional solid state solar cells the doping profile contains charge asymmetries that result in a potential and a corresponding electric field across the device. This electric field is responsible for producing a current by separating the photo-generated electrons and holes before they can recombine. This will be discussed in greater detail in Section 2.3.2.

All semiconductor devices require metal contacts where charges can flow into or out of the device. Ohmic contacts are non-rectifying metal contacts that allow charge flow in either direction [139]. At Ohmic contacts (labeled $\Gamma_{S,D}$), the electron and holes obtain their equilibrium densities [107],

$$\rho_n(\mathbf{x}, t) = \rho_n^e(\mathbf{x}), \quad \rho_p(\mathbf{x}, t) = \rho_p^e(\mathbf{x}) \quad \text{on } \Gamma_{S,D} \quad (2.2.24)$$

Semiconductors that are in equilibrium must satisfy charge neutrality condition [107, 139],

$$C(\mathbf{x}) - \rho_n^e + \rho_p^e = 0. \quad (2.2.25)$$

Using (2.2.25) and (2.2.5) we can solve for ρ_n^e and ρ_p^e to obtain,

$$\rho_n^e = \frac{1}{2} \left(C + \sqrt{C^2 + 4\rho_i^2} \right), \quad \rho_p^e = \frac{1}{2} \left(-C + \sqrt{C^2 + 4\rho_i^2} \right) \quad \text{on } \Gamma_{S,D}. \quad (2.2.26)$$

Insulating contacts (labeled $\Gamma_{S,N}$) are usually formed by an oxide or glass layer [107] and have the following conditions on the current densities and electric field,

$$\mathbf{n} \cdot \mathbf{J}_n(\mathbf{x}, t) = 0, \quad \mathbf{n} \cdot \mathbf{J}_p(\mathbf{x}, t) = 0, \quad \mathbf{n} \cdot \mathbf{E}(\mathbf{x}, t) = 0 \quad \text{on } \Gamma_{S,N}. \quad (2.2.27)$$

The values of the potential on the Ohmic contact will be discussed in the next section.

Remark 2.2.6. The validity of the drift-diffusion-Poisson system is dependent on the size of the active area or characteristic length of the device. For devices where the characteristic length is larger than the mean free path the drift-diffusion-Poisson equations is a valid model for electron/hole transport in semiconductors. When the characteristic length is comparable to or smaller than the mean free path more accurate models must be used; see [91, 108, 114, 130] for more details. Silicon, the semiconductor material most often used in terrestrial photovoltaic devices, is a poor absorber of light. This property necessitates that silicon based solar cells need to be a few hundreds of microns in thickness in order to produce sufficient currents [114]. On this length scale the drift-diffusion-Poisson system can accurately capture the physics of the problem [143] and more complicated models need not be pursued.

2.3 Semiconductor-Electrochemistry

2.3.1 Charge Transport In Electrolytes

An electrolyte is a liquid that consists of ions dissolved in a solvent. Electric currents in the electrolyte are due to the transport of ions/charge carriers as well as the chemical reaction they are involved in. The charge carriers that we model are called reductants and oxidants. We define a reductant, or reducing agent, as the chemical species that donates electron(s) during a chemical reaction. Reduction is therefore a process in which a chemical substance gains electron. Similarly, the oxidant, or oxidizing agent, is chemical species that accepts electron(s) during a chemical reaction. Therefore oxidation is a process in which a chemical substance losses an electron. We label the density of reductants ρ_r [cm⁻³] and the density of oxidants ρ_o [cm⁻³].

We shall only consider the transport of reductants and oxidants (redox) in the electrolyte due to migration from the electric field as well as by diffusion. The current density equations for the reductants (\mathbf{J}_r [A cm⁻²]) and oxidants (\mathbf{J}_o [A cm⁻²]) are then the drift-diffusion equations,

$$\begin{aligned}\mathbf{J}_r &= \alpha_r q \mu_r \mathbf{E} \rho_r - q D_r \nabla \rho_r, \\ \mathbf{J}_o &= \alpha_o q \mu_o \mathbf{E} \rho_o - q D_o \nabla \rho_o.\end{aligned}\tag{2.3.1}$$

The constants α_r and α_o are the charge numbers of the redox species [84]. In this context we have ignored any forced convection of the electrolyte or redox species. Convective forces do not play a vital role in the interface reactions and their incorporation into our model would necessitate solving the Navier-Stokes equations for the fluid flow [24, 84]. The time evolution of reductants

and oxidants is governed by the conservation of charge,

$$\begin{aligned} \alpha_r q \frac{\partial \rho_r}{\partial t} + \alpha_r \nabla \cdot \mathbf{J}_r &= 0 \\ \alpha_o q \frac{\partial \rho_o}{\partial t} + \alpha_o \nabla \cdot \mathbf{J}_o &= 0 \end{aligned} \quad (2.3.2)$$

We note that the lack of generation/recombination functions reflects the fact that reductant and oxidants are only generated/eliminated by the chemical reactions at the interface. Therefore we limit our model to include only heterogeneous reactions which occur at the interface [24]. We will not discuss homogeneous reactions (e.g. autoionization of water) that occur throughout the electrolyte domain, see [84] for more information on modeling homogeneous reactions.

Often additional ions are added to the electrolyte to improve its conductivity, but are not involved in the electrode reactions [111]. These additional ions are called the supporting electrolyte. In our model we do not consider any additional ions in the electrolyte besides those involved in the heterogeneous reactions; for details on the impact of supportive electrolytes on PECs see [24, 84]. Thus, besides the charges of the redox species, we assume our electrolyte is charge neutral. The charge neutrality of the electrolyte is incorporated as a lack of doping profile in Poisson's equation for the potential and electric field. Therefore the Poisson equation for the electrolyte is,

$$-\nabla \cdot (\epsilon_E \nabla \Phi) = \frac{q}{\epsilon_0} (\alpha_r \rho_r + \alpha_o \rho_o), \quad (2.3.3)$$

where ϵ_E is the electrolyte dielectric constant.

We assume that our semiconductor-electrode is isolated from any other electrode. This implies that the boundary of the electrolyte can only be decomposed into a Dirichlet portion ($\Gamma_{E,D}$) and an insulating portion ($\Gamma_{E,N}$). On the Dirichlet portion the reductants and oxidants take on their bulk values [24],

$$\rho_r(\mathbf{x}, t) = \rho_r^\infty(\mathbf{x}), \quad \rho_o(\mathbf{x}, t) = \rho_o^\infty(\mathbf{x}) \quad \text{on } \Gamma_{E,D}. \quad (2.3.4)$$

On the insulating insulating portion of the electrolyte we have,

$$\mathbf{n} \cdot \mathbf{J}_r(\mathbf{x}, t) = 0, \quad \mathbf{n} \cdot \mathbf{J}_o(\mathbf{x}, t) = 0, \quad \mathbf{n} \cdot \mathbf{E}(\mathbf{x}, t) = 0 \quad \text{on } \Gamma_{E,N}. \quad (2.3.5)$$

Additionally, we mention that the potential and the so-called displacement electric field must remain continuous across the semiconductor-electrolyte interface [84],

$$\Phi|_{\Sigma^S} = \Phi|_{\Sigma^E} \quad \text{and} \quad \mathbf{n}_{\Sigma^S} \cdot \epsilon_S \nabla \Phi + \mathbf{n}_{\Sigma^E} \cdot \epsilon_E \nabla \Phi = 0. \quad (2.3.6)$$

Before we discuss the chemical reactions at the interface of the semiconductor and electrolyte we discuss the redox species in terms of their energy levels. The Nernst equation,

$$\Phi_{\text{redox}} = \Phi_{\text{redox}}^0 + U_T \ln \left(\frac{\rho_o}{\rho_r} \right), \quad (2.3.7)$$

relates the potential of a redox couple, Φ_{redox} [V], to their respective concentrations. Φ_{redox} is always defined with respect to the reference potential Φ_{redox}^0 [V] (see Remark 2.3.1). The Nernst equation is useful because it allows

us introduce the concept of a redox couple's Fermi level [111]. The Fermi-level E_F^{redox} [eV] of a redox couple in equilibrium is defined with respect to the reference Fermi-level, $E_F^{0,\text{redox}}$ [eV], as,

$$E_F^{\text{redox}} = E_F^{0,\text{redox}} - k_B T \ln \left(\frac{\rho_o}{\rho_r} \right). \quad (2.3.8)$$

Remark 2.3.1. The reference potential and reference Fermi-levels will be assumed to be known and coincide with the vacuum level to be consistent with the semiconductor. In electrochemistry the reference potential is traditionally chosen to coincide with the reference electrode, however, the difference between the two choices is a measurable constant [24, 25, 111, 122].

Geirscher [74–76] developed a model for non-adiabatic electron transfer using the energy levels of the semiconductor and the redox couple. In this framework, an oxidant represents an unoccupied energy state in the electrolyte, while a reductant represents an occupied energy state. Normally the redox pairs would have discrete energy levels, however, their interaction with the electrolyte solvent results in a broadening of their energy levels (see Figure 2.3). The density of states for reductants and oxidants therefore follow the Gaussian distributions [111],

$$\begin{aligned} D_r(E) &= \rho_r W_0^{-1} e^{-(E-E_{\text{Red.}}^0)^2/W_0^2}, \\ D_o(E) &= \rho_o W_0^{-1} e^{-(E-E_{\text{Ox.}}^0)^2/W_0^2}. \end{aligned} \quad (2.3.9)$$

The constant $W_0 = 2\sqrt{k_B T \lambda_{\text{reorg.}}}$ [eV] is an energy for normalization and $\lambda_{\text{reorg.}}$ [eV] is the solvent reorganization energy. The “oxidant energy level”

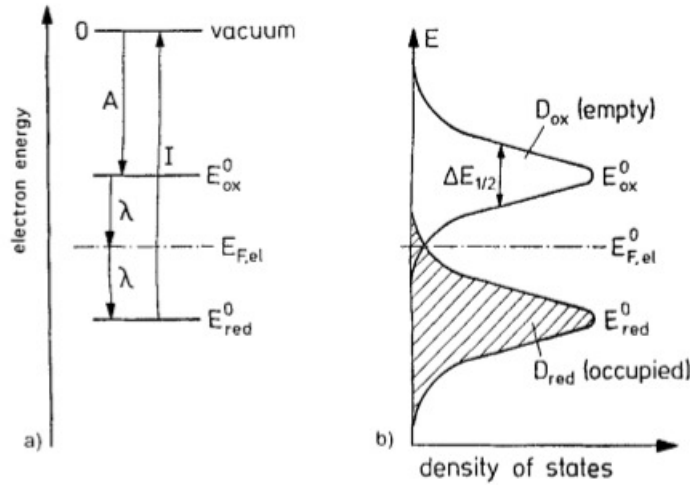


Figure 2.3: a) The energy levels of the redox couple. Note here $E_{F,el}$ is the reference Fermi level of electrolyte. b) The density of states for redox couples. [111]

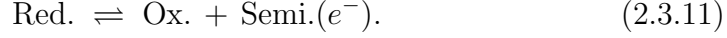
E_{Ox}^0 [eV] and “reductant energy level” $E_{Red.}^0$ of the electrolyte are related to the redox Fermi level by the solvent reorganization energy,

$$E_{Ox.}^0 = E_F^{0,\text{redox}} - \lambda_{\text{reorg.}} \quad E_{Red.}^0 = E_F^{0,\text{redox}} + \lambda_{\text{reorg.}} \quad (2.3.10)$$

The energy levels of the electrolyte are depicted in Figure 2.3 a). These definitions allow us to discuss the chemical reactions at the interface in terms of the energy levels of the individual charge carriers in both the semiconductor and electrolyte.

2.3.2 Semiconductor-Electrolyte Interface Reactions

When a semiconductor and electrolyte are brought into contact there will be a transfer of electrons across the interface through the process,



This process continues until equilibrium is achieved and there is no net current flowing through the interface. The conditions for equilibrium require that Fermi-levels of the semiconductor and the electrolyte be equal [111, 122] (see Figure 2.4). The transfer of charge across the interface involves mostly majority carriers in the semiconductor. This is because without illumination there is an insufficient density of minority carriers to contribute to the reactions [111]. After the majority carriers are transferred to the electrolyte they leave behind their ionized cores which are bound to the lattice. The presence of the ionized cores results in a build-up of charge in a region of the semiconductor called the “space charge region” (SCR). This build-up of charge gives rise a electric potential called the SCR potential (see Figure 2.5) and is denoted Φ_{SCR} [V]. The SCR potential creates an electric field which forces majority carriers away from the interface. The value of the SCR potential can be quantified by solving Poisson’s equation [84, 139],

$$\Phi_{\text{SCR}} = U_T \ln \left(\frac{\rho_n^e \rho_p^e}{\rho_i^2} \right). \quad (2.3.12)$$

Remark 2.3.2. We remark that under illumination, minority carriers will be generated in the semiconductor. If they are able to diffuse into the SCR

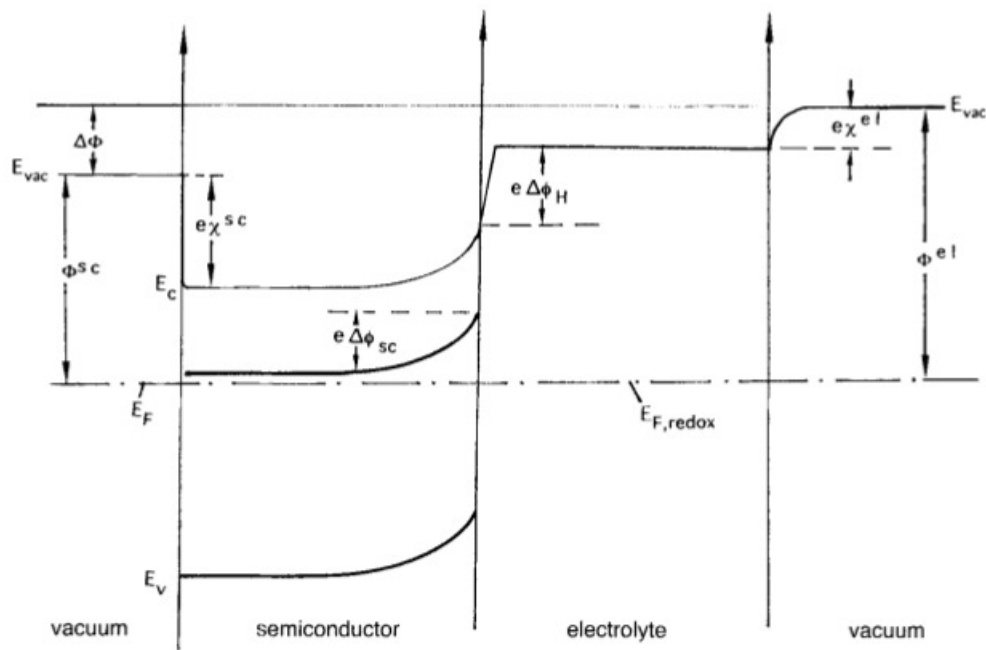


Figure 2.4: Energy levels in a semiconductor-electrolyte interface, here e stands for the charge of an electron, $\Delta\Phi_{SC}$, $\Delta\Phi_H$ are the space charge region and Helmholtz potentials respectively; χ^{el} , Φ^{el} are respectively the surface dipole contribution and work function of the electrolyte which we will not discuss further. [111]

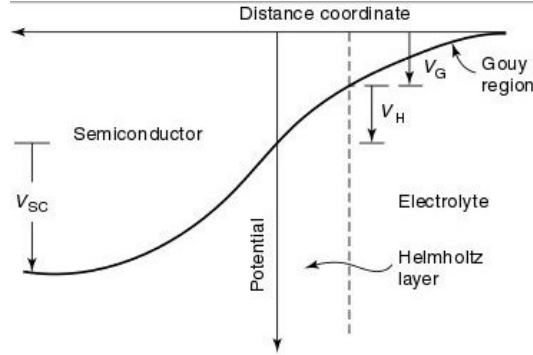


Figure 2.5: Potential drops across the double layer in the electrolyte. V_{SC} , V_H , V_G are the SCR, Helmholtz and Gouy layer potentials respectively. [122]

before recombining, then the electric field will force them toward the interface and generate chemical reactions [111, 114]. The chemical reactions due to the photo-generated minority carrier lead to a continuous current throughout the device called the “illuminated current.”

Remark 2.3.3. The SCR potential corresponds to the so called “built-in” potential in a solid state solar cell.

In the electrolyte region there will be two potentials build-ups that form the so-called “double layer” (see Figure 2.5). The potential that is closest to the interface is called the Helmholtz potential. The Helmholtz potential occurs across the Helmholtz layer and is labeled Φ_H [V]. The second potential layer extends from the Helmholtz layer into the bulk of the electrolyte in a region called the “Gouy layer.” The potential across the Gouy layer is labeled Φ_G [V]. In our model we neglect the effect of the Gouy potential as is often done [111]. The Helmholtz potential gives rise to an electric field that forces one redox

species towards the interface and the other away from it through a process called absorption [24].

When a potential bias is applied across a photoelectrochemical solar cell the resulting potential drop usually occurs in the space charge region [111]. This effect is modeled on the Ohmic contact as,

$$\Phi(\mathbf{x}, t) = \Phi_{\text{SCR}}(\mathbf{x}) + \Phi_{\text{app}}(\mathbf{x}) \quad \text{on } \Gamma_{S,D}. \quad (2.3.13)$$

On the other hand, the potential across Helmholtz layer Φ_H usually remains unchanged under applied biases [111]. This effect manifests in our model as the potential attaining its constant bulk value on the electrolyte boundary [84],

$$\Phi(\mathbf{x}, t) = \Phi^\infty(\mathbf{x}) \quad \text{on } \Gamma_{E,D}. \quad (2.3.14)$$

The fact that an applied potential only occurs over the space charge region has lead to the concept of “band edge pinning” [111]. This is when the value of the conduction and valance band at the interface remain fixed and applied voltages move the semiconductor Fermi-level E_F^{semi} up or down. The movement of E_F^{semi} subsequently induces the movement of the conduction and valance band in the bulk of the semiconductor as shown in Figure 2.6. The movement of the bands in the bulk of the semiconductor is called “band bending” [111]. Applying voltages to the device therefore either enhances or reduces the band bending. We depict the three cases of band bending in a n-type semiconductor-electrolyte interface in Figure 2.6.

In equilibrium the Fermi-levels of the semiconductor and electrolyte are equal,

$$E_F^{semi.} = E_F^{\text{redox}}, \quad (2.3.15)$$

and no net charge transfer occurs. When we apply a bias to the semiconductor-electrolyte solar cell Φ_H remains unaltered; this implies the redox Fermi-level E_F^{redox} will be unchanged [111, 122]. However, the potential change in the semiconductor is $\Phi_{\text{SCR}} \rightarrow \Phi_{\text{SCR}} + \Phi_{\text{app.}}$. This implies, as previously mentioned that the semiconductor Fermi-level will move up or down depending on the bias. An anodic bias moves the semiconductor Fermi-level lower such that,

$$E_F^{semi.} < E_F^{\text{redox}}. \quad (2.3.16)$$

Anodic currents involve electron transfer from the an occupied state in the electrolyte (reductant) to either the conduction band or valance band. Similarly, a cathodic bias moves the semiconductor Fermi-level higher such that,

$$E_F^{semi.} > E_F^{\text{redox}}. \quad (2.3.17)$$

Cathodic currents involve electron transfer from the conduction band or the valance band to an unoccupied state in the electrolyte (oxidant).

Electron transfer across the semiconductor-electrolyte interface requires the density of energy states of occupied and unoccupied states in the electrolyte to overlap with conduction or valance band in the semiconductor (see Figure 2.6). Due to the narrowness of the redox density of energy states one

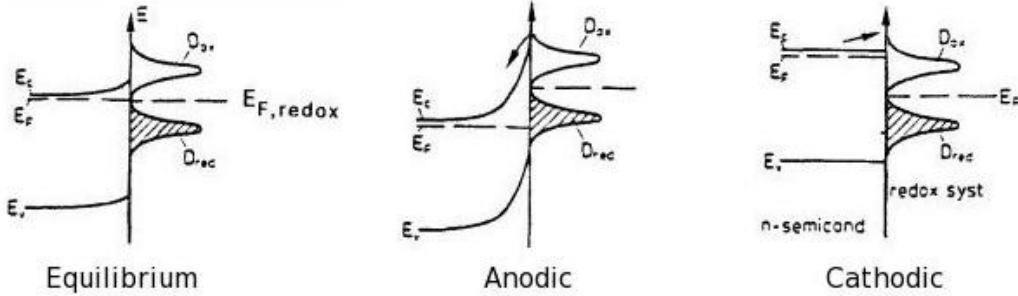


Figure 2.6: Energy levels of the semiconductor and electrolyte under an applied biases. Source: [111]

can approximate that electron transfer occur within $k_B T$ of the conduction or valance band [111]. Using this approximation the cathodic transfer of electrons from the conduction band to the unoccupied in the electrolyte state is of the form [111],

$$\mathbf{n}_{\Sigma^S} \cdot \mathbf{J}_c^- = -q k_0 \rho_n W_0 D_o(E) = -q k_0 e^{-(E_C - E_{\text{Ox.}}^0)^2/W_0^2} \rho_n \rho_o, \quad (2.3.18)$$

while the anodic transfer of electrons from the occupied electrolyte state to conduction band is of the form [111],

$$\mathbf{n}_{\Sigma^S} \cdot \mathbf{J}_c^+ = q k_0 N_C W_0 D_r(E) = q k_0 e^{-(E_C - E_{\text{Red.}}^0)^2/W_0^2} N_C \rho_r. \quad (2.3.19)$$

We define the total current for electron transfer involving the conduction band to be,

$$\begin{aligned} \mathbf{n}_{\Sigma^S} \cdot \mathbf{J}_n &= \mathbf{n}_{\Sigma^S} \cdot \mathbf{J}_c^- + \mathbf{n}_{\Sigma^S} \cdot \mathbf{J}_c^+, \\ &= -q k_0 \left(e^{-(E_C - E_{\text{Ox.}}^0)^2/W_0^2} \rho_n \rho_o - e^{-(E_C - E_{\text{Red.}}^0)^2/W_0^2} N_C \rho_r \right). \end{aligned} \quad (2.3.20)$$

Similarly, we can define the anodic transfer of electron from an occupied state in the electrolyte to the valance band as [111],

$$\mathbf{n}_{\Sigma^S} \cdot \mathbf{J}_v^+ = q k_0 W_0 \rho_p D_r(E) = q k_0 e^{-(E_V - E_{\text{Red.}}^0)^2/W_0^2} \rho_p \rho_r, \quad (2.3.21)$$

while the cathodic transfer of electrons from the valance band to an unoccupied state in the electrolyte is [111],

$$\mathbf{n}_{\Sigma^S} \cdot \mathbf{J}_v^- = -q k_0 N_V W_0 D_o(E) = -q k_0 e^{-(E_V - E_{\text{Ox.}}^0)^2/W_0^2} N_V \rho_o. \quad (2.3.22)$$

We define the total current for valance band electron transfer to be,

$$\begin{aligned} \mathbf{n}_{\Sigma^S} \cdot \mathbf{J}_p &= \mathbf{n}_{\Sigma^S} \cdot \mathbf{J}_v^+ + \mathbf{n}_{\Sigma^S} \cdot \mathbf{J}_v^- \\ &= q k_0 \left(e^{-(E_V - E_{\text{Red.}}^0)^2/W_0^2} \rho_p \rho_r - e^{-(E_V - E_{\text{Ox.}}^0)^2/W_0^2} N_V \rho_o \right). \end{aligned} \quad (2.3.23)$$

We rewrite (2.3.20) and (2.3.23) in a more useful form by noting that in equilibrium there is no net current through the interface, i.e. $\mathbf{J}_n \cdot \mathbf{n}_{\Sigma^S} = \mathbf{J}_p \cdot \mathbf{n}_{\Sigma^S} = 0$. Therefore equilibrium conditions for the conduction band imply,

$$\mathbf{n}_{\Sigma^S} \cdot \mathbf{J}_c^+ = \mathbf{n}_{\Sigma^S} \cdot \mathbf{J}_c^-. \quad (2.3.24)$$

Substituting in (2.3.18) and (2.3.19) yields,

$$e^{-(E_V - E_{\text{Red.}}^0)^2/W_0^2} N_C \rho_r = e^{-(E_C - E_{\text{Ox.}}^0)^2/W_0^2} \rho_n^e \rho_o. \quad (2.3.25)$$

Substituting this expression into (2.3.20) we find,

$$\mathbf{n}_{\Sigma^S} \cdot \mathbf{J}_n = -q k_{et} (\rho_n - \rho_n^e) \rho_o, \quad (2.3.26)$$

where the electron transfer rate, k_{et} , is defined to be,

$$k_{et} := k_0 e^{-(E_C - E_{\text{Ox.}}^0)^2/W_0^2}. \quad (2.3.27)$$

Repeating the same arguments for \mathbf{J}_p we find,

$$\mathbf{n}_{\Sigma^S} \cdot \mathbf{J}_p = q k_{ht} (\rho_p - \rho_p^e) \rho_r, \quad (2.3.28)$$

where the hole transfer rate, k_{ht} , is defined to be,

$$k_{ht} := k_0 W_0 e^{-(E_V - E_{\text{Red.}}^0)^2/W_0^2}. \quad (2.3.29)$$

The total flux of reductants out of the electrolyte then must be the the valance band current minus the conduction band current,

$$\begin{aligned} \mathbf{n}_{\Sigma^E} \cdot \mathbf{J}_r &= \mathbf{n}_{\Sigma^S} \cdot \mathbf{J}_p - \mathbf{n}_{\Sigma^S} \cdot \mathbf{J}_n, \\ &= q k_{ht} (\rho_p - \rho_p^e) \rho_r - q k_{et} (\rho_n - \rho_n^e) \rho_o. \end{aligned} \quad (2.3.30)$$

Similarly, the total flux of oxidants out of the electrolyte must then be the conduction band current minus the valance band current,

$$\begin{aligned} \mathbf{n}_{\Sigma^E} \cdot \mathbf{J}_o &= \mathbf{n}_{\Sigma^S} \cdot \mathbf{J}_n - \mathbf{n}_{\Sigma^S} \cdot \mathbf{J}_p, \\ &= q k_{et} (\rho_n - \rho_n^e) \rho_o - q k_{ht} (\rho_p - \rho_p^e) \rho_r. \end{aligned} \quad (2.3.31)$$

We define the total current throughout the device as,

$$\mathbf{J} := \begin{cases} \mathbf{J}_n - \mathbf{J}_p & \text{in } \Omega_S \\ -\alpha_r \mathbf{J}_r - \alpha_o \mathbf{J}_o & \text{in } \Omega_E \end{cases} \quad (2.3.32)$$

The conservation of charge requires that $\alpha_o - \alpha_r = 1$. Using this property as well as the boundary conditions (2.3.26), (2.3.28), (2.3.30) and (2.3.31) we see that the current (2.3.32) through the interface is continuous.

Remark 2.3.4. Due to the presence of doping profiles and the SCR potential, the current in semiconductors will usually be due to primarily either the transport of minority or the transport of majority carriers. In contrast, currents in the electrolyte are due to transport of both reductants and oxidants [111].

2.3.3 Relationship Of Interface Conditions To Other Models In Electrochemistry

2.3.3.1 Butler-Volmer Model

In electrochemistry, currents are caused by a transfer of electrons across the solid-liquid interface. *In a semiconductor-electrode-electrolyte interface the transfer of electrons can occur across different bands. Which band the electron transfer occurs across depends on the availability of free carriers in that band as well as its overlap with the density of states of the redox species. The transfer rates of the electrons across the semiconductor interface (k_{et} and k_{ht}) remain fixed under all applied biases due to band edge pinning [111]. However, the density of electrons (holes) at the interface will increase (decrease) with an applied bias or vice versa due to band bending.*

In contrast, currents across metal electrode-electrolyte interfaces are driven by transfer of electrons from occupied states in the metal to unoccupied states in the electrolyte or from occupied states in the electrolyte to unoccupied states in the metal. The transfer of an electron from the metal to the electrolyte occurs when the Fermi-level of the metal overlaps with the oxidant density of states. The transfer of an electron from the electrolyte to the metal occurs when the Fermi-level of the metal overlaps with the reductant density of states.

In contrast to a semiconductor, there is no SCR in a metal and any applied bias will correspond to a drop in potential across the Helmholtz layer. Therefore the Fermi-level of the electrolyte will move up and down under applied biases, while the Fermi-level of the metal will remain fixed. Since the position of the Fermi-level dictates the position the redox density of states this implies that the transfer rate of electron from the metal to the semiconductor are controlled by the applied bias. The traditional model used for metal-electrodes in electrochemistry is the Butler-Volmer equation [94, 111],

$$\mathbf{J} \cdot \mathbf{n}_{\Sigma^S} = J_0 (e^{(1-\alpha)\nu/U_T} - e^{-\alpha\nu/U_T}) \quad (2.3.33)$$

The term J_0 [A cm^{-2}] is the exchange current, α is the transfer factor and ν [V] is the over-potential and is a linear function of applied bias. This model assumes that anodic and cathodic currents increase or decrease exponentially with respect to the applied bias. *This reflects the fact that the electron transfer rate in a metal-electrolyte system depends exponentially on the applied bias. In contrast to a semiconductor electrode, in a metal electrode the density of electrons does not appreciably changed under applied biases since its Fermi-level remains unchanged [111].*

The model of the reactive interface conditions from Section 2.3.2 for semiconductor-electrolytes can be related to the Butler-Volmer model (2.3.33) under certain conditions. However, we stress that the physics of charge transfer across the two interface is very different and the Butler-Volmer model alone is not sufficient to describe the dynamics of the interface, even when the semi-

conductor is covered by a catalyst [94, 113]. If we assume the semiconductor is in quasi-equilibrium, then the electron and hole pairs can be modeled using Boltzmann statistics,

$$\rho_n = \rho_n^e e^{(\Phi_{\text{app.}} - \Phi_{\text{SCR}})/U_T} \quad \text{on } \Sigma, \quad (2.3.34)$$

$$\rho_p = \rho_p^e e^{-(\Phi_{\text{app.}} - \Phi_{\text{SCR}})/U_T} \quad \text{on } \Sigma. \quad (2.3.35)$$

Under an excitation event there will be an increase of free carrier at the interface. This will lead to an increase in the transfer of electrons to or from the semiconductor. Using (2.3.34), (2.3.35), (2.3.26), (2.3.28) and (2.3.32) it can be seen that the current through the interface is then controlled by the applied biases with the equation,

$$\mathbf{J} \cdot \mathbf{n}_{\Sigma^S} = -qk_{et} \rho_n^e \rho_o (e^{\nu/U_T} - 1) + qk_{ht} \rho_p^e \rho_r (e^{-\nu/U_T} - 1), \quad (2.3.36)$$

where we refer to $\nu = \Phi_{\text{app.}} - \Phi_{\text{SCR}}$ as the over-potential. We can now see that increasing or decreasing the applied bias will effect the current exponentially. A more thorough discussion on the Butler-Volmer model in electrochemistry can be found in [24, 94, 111].

2.3.3.2 Schottky Model

In most previous simulation based studies of PECs, such as [61, 67, 93, 127, 147], researchers linearized the reactive interface conditions by using the so-called “Schottky approximation.” This approximation involves the assumption that the concentrations of the redox species are high compared to

electron and hole densities. Additionally, it is assumed that the redox concentrations will not change appreciably over time or over all applied biases. These assumptions allows one to neglect simulations of the electrolyte and its interaction with the semiconductor altogether. We therefore replace the interface conditions on the semiconductor with the “Schottky conditions” [107],

$$\mathbf{J}_n \cdot \mathbf{n}_{\Sigma^S} = -qv_n(\rho_n - \rho_n^e), \quad (2.3.37)$$

$$\mathbf{J}_p \cdot \mathbf{n}_{\Sigma^S} = qv_p(\rho_p - \rho_p^e), \quad (2.3.38)$$

where v_n [cm²s⁻¹] and v_p [cm²s⁻¹] are respectively the electron and hole recombination velocities. It was shown by the authors of [84] that the Schottky approximation produces results which are close to the results from simulations of the full semiconductor-electrolyte system when redox concentrations are high. However, when redox concentrations are comparable to the densities of electrons and holes the results of simulations using the Schottky approximation produce appreciable deviations from results which use the full system. We will discuss this further in Chapter 5.

Remark 2.3.5. The Schottky condition was originally proposed as a model for parasitic resistance at a semiconductor-metal junction [107, 114]. In such scenarios, there will be an associated potential with the contact called the “barrier height.” The barrier height when using the Schottky condition will be assumed to be coincide with the value of the space charge region potential in the full system of equations.

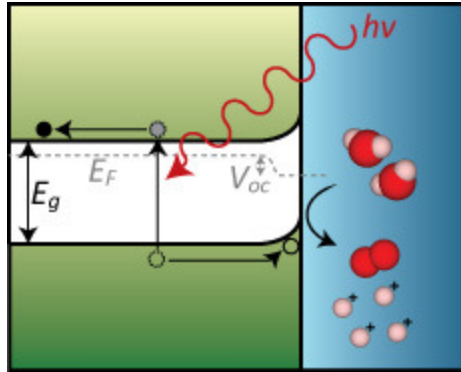


Figure 2.7: Dynamics of a n-type semiconductor PEC solar cell under illumination. [4]

2.3.4 Photoelectrochemical Solar Cells

At a semiconductor-electrolyte interface the potential from the space charge region, Φ_{SCR} , depletes the interface of majority carriers. A few majority carriers may be able to overcome the potential through thermionic emission and reach the interface to cause chemical reactions. Therefore in the dark there is a small current called the “dark current” that is due to the chemical reactions with the majority carriers. When the device is illuminated, photo-generated majority and minority carriers will be created. Minority carriers within or that diffuse into the SCR will be forced toward the interface by the SCR’s electric field. The corresponding photo-generated majority carriers will be transferred away from the interface by the same electric field. Minority carriers that reach the interface will cause redox reactions that lead to so-called “illuminated currents.” The dynamics of the PEC using an n-type semiconductor under illumination are displayed in Figure 2.7

One obtains power from a solar cell by applying loads (motors, appliances, or any device that requires electrical power) in the form of applied voltage biases. There is always a fundamental compromise between the produced current and the applied voltage obtained from the cell. In the dark under no applied bias the current will be effectively zero. Applying positive or forward biases to the cell will result in a positive current called the “dark current.” The dark current increases exponentially with the applied bias as displayed in Figure 2.8. When a solar cell is illuminated there will be a negative current called the “illuminated current.” Under zero applied bias the absolute value of illuminated current will be maximized. This current is called the “short circuit current” and will be labeled J_{SC} [A cm^{-2}]. Applying a forward bias will weaken the electric field in the space charge region. The decreases in the electric field leads to a decrease in the illuminated current and an increase in the dark current. Increasing the applied bias will diminish the magnitude of total current until it reaches zero. The applied voltage at which this occurs is called the “open circuit voltage” and denoted Φ_{OC} [V]. Under these conditions the dark current exactly cancels the illuminated current. Applying biases larger than the open circuit voltage will result in positive currents which increase exponentially. The exponential dependence of the current on the applied voltage is called the diode effect and is displayed in current-voltage plot in Figure 2.8

Solar cells generate power when applied voltages have values in the range $(0, \Phi_{OC})$. The efficiency of a solar cell is defined as the ratio of the

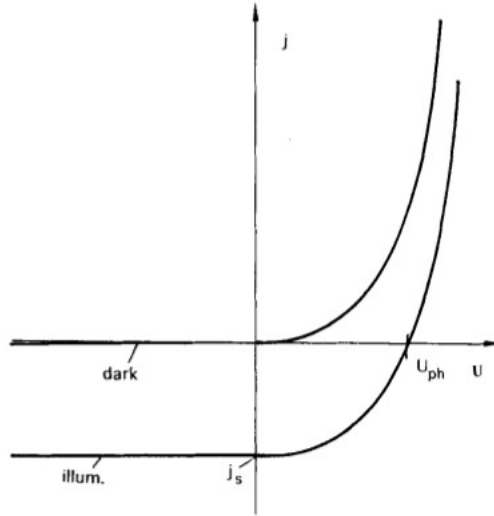


Figure 2.8: Solar cell current-voltage curve. Here I , U are the current and applied voltage respectively; I_s , U_{ph} are the short circuit current and open circuit respectively. [111]

maximum power,

$$\eta_{\text{eff}} = \frac{P_m}{P_{\text{in}}} = \frac{J_m \Phi_m}{P_{\text{in}}}. \quad (2.3.39)$$

The values J_m [A cm^{-2}] and V_m [V] are the current density and voltage values whose product produces the maximum power output produced by the cell and P_{in} [mW cm^{-2}] is the power supplied by the sun. The fill factor of a solar cell is,

$$ff = \frac{J_m \Phi_m}{J_{SC} \Phi_{OC}}, \quad (2.3.40)$$

and is used to measure the parasitic resistance in a solar cell. A lower fill factor corresponds to higher resistance within the cell.

2.4 Summary Of Mathematical Model

Before summarizing the mathematical model for electron transfer across semiconductor-electrolyte interfaces we review the underlying assumptions we have made. The necessary assumptions for validity of the model in the semiconductors are:

1. We use a non-degenerate and compositionally invariant semiconductor.
2. The device length is larger than the mean free path.
3. The temperature of electrons and holes is the same as the crystal lattice.
4. The mobility of electrons and holes may depend upon the electric field, temperature and doping level.
5. The Einstein relation (2.2.13) is valid.
6. Generation of electron-hole pairs only occurs through photon absorption or by thermal excitation through SRH recombination.
7. The only recombination mechanism of electrons and hole pairs occurs through a single trap that has a energy level in the middle of the band gap.
8. Besides the interface with the electrolyte, the semiconductor has only Ohmic metal contacts, an insulating oxide or glass layer.

To model the reactive interface in a PEC we assume:

1. There is no supporting electrolyte and besides the the charges of the redox species, the electrolyte is charge neutral.
 2. Redox species are only created/eliminated through the heterogeneous reaction,
- $$\text{Red.} \rightleftharpoons \text{Ox.} + \text{Semi.}(e^-). \quad (2.4.1)$$
3. We assume that the Geirscher model is valid and that electron transfer between the semiconductor and electrolyte occurs within $k_B T$ of either the conduction or valance band.
 4. The density of redox species is high enough to ignore the Gouy layer.
 5. Applied potentials occur over the SCR region and the Helmholtz potential remains constant on the boundary of the electrolyte.
 6. Other than the semiconductor, the electrolyte is isolated and redox species take on their bulk values on the boundary of the electrolyte.
 7. The potential and displacement electric field are continuous across the solid-liquid interface.
 8. Initial conditions are taken to match the equilibrium and bulk densities in the semiconductor and electrolyte respectively.

We now summarize the model for the semiconductor-electrolyte interface problem. We note that we have introduced charge numbers $\alpha_n = -1$ and $\alpha_p = +1$ for electrons and holes respectively. We eliminated the charge of

the electron q in all equations except for the Poisson equations. Additionally, we replace the electric field \mathbf{E} by $-\nabla\Phi$. This changes our definition of the individual carriers current to be,

$$\begin{aligned}\mathbf{J}_n &= -\alpha_n \mu_n \nabla \Phi \rho_n - D_n \nabla \rho_n && \text{in } \Omega_S \times (0, T), \\ \mathbf{J}_p &= -\alpha_p \mu_p \nabla \Phi \rho_p - D_p \nabla \rho_p && \text{in } \Omega_S \times (0, T), \\ \mathbf{J}_r &= -\alpha_r \mu_r \nabla \Phi \rho_r - D_r \nabla \rho_r && \text{in } \Omega_E \times (0, T), \\ \mathbf{J}_o &= -\alpha_o \mu_o \nabla \Phi \rho_o - D_o \nabla \rho_o && \text{in } \Omega_E \times (0, T).\end{aligned}\tag{2.4.2}$$

In the semiconductor we have the system of equations,

$$\begin{aligned}\frac{\partial \rho_n}{\partial t} + \nabla \cdot (-\alpha_n \mu_n \nabla \Phi \rho_n - D_n \nabla \rho_n) &= G(\mathbf{x}) - R(\rho_n, \rho_p) && \text{in } \Omega_S \times (0, T), \\ \frac{\partial \rho_p}{\partial t} + \nabla \cdot (-\alpha_p \mu_p \nabla \Phi \rho_p - D_p \nabla \rho_p) &= G(\mathbf{x}) - R(\rho_n, \rho_p) && \text{in } \Omega_S \times (0, T), \\ -\nabla \cdot (\epsilon_S \nabla \Phi) &= \frac{q}{\epsilon_0} (C(\mathbf{x}) + \alpha_n \rho_n + \alpha_p \rho_p) && \text{in } \Omega_S \times (0, T).\end{aligned}\tag{2.4.3}$$

Subject to the boundary conditions,

$$\begin{aligned}\rho_n &= \rho_n^e, \quad \rho_p = \rho_p^e, \quad \Phi = \Phi_{\text{SCR}} + \Phi_{\text{app.}} \quad \text{on } \Gamma_{S,D} \times (0, T), \\ \mathbf{n} \cdot \mathbf{J}_n &= 0, \quad \mathbf{n} \cdot \mathbf{J}_p = 0, \quad \mathbf{n} \cdot (-\nabla \Phi) = 0 \quad \text{on } \Gamma_{S,N} \times (0, T).\end{aligned}\tag{2.4.4}$$

In the electrolyte we have the system of equations,

$$\begin{aligned}\frac{\partial \rho_r}{\partial t} + \nabla \cdot (-\alpha_r \mu_r \nabla \Phi \rho_r - D_r \nabla \rho_r) &= 0 && \text{in } \Omega_E \times (0, T), \\ \frac{\partial \rho_o}{\partial t} + \nabla \cdot (-\alpha_o \mu_o \nabla \Phi \rho_o - D_o \nabla \rho_o) &= 0 && \text{in } \Omega_E \times (0, T), \\ -\nabla \cdot (\epsilon_E \nabla \Phi) &= \frac{q}{\epsilon_0} (\alpha_r \rho_r + \alpha_o \rho_o) && \text{in } \Omega_E \times (0, T).\end{aligned}\tag{2.4.5}$$

Subject to the boundary conditions,

$$\begin{aligned}\rho_r &= \rho_r^\infty, \quad \rho_o = \rho_o^\infty, \quad \Phi = \Phi^\infty \quad \text{on } \Gamma_{E,D} \times (0, T), \\ \mathbf{n} \cdot \mathbf{J}_r &= 0, \quad \mathbf{n} \cdot \mathbf{J}_o = 0, \quad \mathbf{n} \cdot (-\nabla \Phi) = 0 \quad \text{on } \Gamma_{E,N} \times (0, T).\end{aligned}\tag{2.4.6}$$

The interface conditions (2.3.26), (2.3.28), (2.3.30), and (2.3.31) on $\Sigma \times (0, T)$ are reweriten as,

$$\mathbf{n}_{\Sigma^S} \cdot \mathbf{J}_n = I_{et}(\rho_n - \rho_n^e, \rho_o), \quad (2.4.7)$$

$$\mathbf{n}_{\Sigma^S} \cdot \mathbf{J}_p = I_{ht}(\rho_p - \rho_p^e, \rho_r), \quad (2.4.8)$$

$$\mathbf{n}_{\Sigma^E} \cdot \mathbf{J}_r = I_{ht}(\rho_p - \rho_p^e, \rho_r) - I_{et}(\rho_n - \rho_n^e, \rho_o), \quad (2.4.9)$$

$$\mathbf{n}_{\Sigma^E} \cdot \mathbf{J}_o = -I_{ht}(\rho_p - \rho_p^e, \rho_r) + I_{et}(\rho_n - \rho_n^e, \rho_o), \quad (2.4.10)$$

where the functions $I_{et}(x, y) = k_{et}xy$, $I_{ht}(x, y) = k_{ht}xy$. We remark that in this form we have divided out the charge of electron q . In addition, the interface conditions for the Poisson equations are,

$$\Phi|_{\Sigma^S} = \Phi|_{\Sigma^E} \quad \text{and} \quad \mathbf{n}_{\Sigma^S} \cdot \epsilon_S \nabla \Phi + \mathbf{n}_{\Sigma^E} \cdot \epsilon_E \nabla \Phi = 0. \quad (2.4.11)$$

Finally we have the initial conditions for the charge densities,

$$\begin{aligned} \rho_n &= \rho_n^e, & \rho_p &= \rho_p^e & \text{on } \Omega_S \times \{t = 0\}, \\ \rho_r &= \rho_r^\infty, & \rho_o &= \rho_o^\infty & \text{on } \Omega_E \times \{t = 0\}. \end{aligned} \quad (2.4.12)$$

The total electrical current density throughout out the device is,

$$\mathbf{J} = \begin{cases} -\alpha_n q \mathbf{J}_n - \alpha_p q \mathbf{J}_p & \text{in } \Omega_S \times (0, T), \\ -\alpha_r q \mathbf{J}_r - \alpha_o q \mathbf{J}_o & \text{in } \Omega_E \times (0, T). \end{cases} \quad (2.4.13)$$

Chapter 3

Numerical Approximations To Model Problem

In this chapter we discuss the numerical approximations used to simulate the reactive-flow-transport systems that model photoelectrochemical solar cells. We first discuss the choice of scaling and notation for the model problem and present our equations in non-dimensional form. We then introduce a mixed finite element method for to approximate solutions to the Poisson equation and a local discontinuous Galerkin (LDG) for the spatial discretization of the drift-diffusion equation. Next we propose different time stepping algorithms which were specifically developed to overcome the stiffness inherent in the drift-diffusion-Poisson systems. Finally, we summarize the numerical software which was developed to simulate photoelectrochemical solar cells in one and two dimensions.

3.1 Preliminaries

3.1.1 Non-Dimensional Formulation

Many variables in semiconductor-electrochemistry have values that differ by large orders of magnitude, for example, the densities values of charge carriers can routinely obtain values of $10^8 - 10^{19}$ [cm⁻³]. In order to avoid

issues with numerical overflow and underflow we utilize a first-order perturbation scaling routine [107, 130] to obtain systems which are in non-dimensional form. In choosing the first order perturbation scaling we denote the characteristic length scale (l^*), time scale (t^*), voltage scale (Φ^*), and density scale (C^*). The values for these characteristics scales are chosen to be (see [84]):

$$l^* = 10^{-4} \text{ [cm}^{-1}\text{]}, \quad t^* = 10^{-12} \text{ [s]}, \\ \Phi^* = U_T \simeq 25.85 \text{ [mV]}, \quad C^* = 10^{16} \text{ [cm}^{-3}\text{]}.$$

We introduce the the Debeye length $\lambda_r^2 = \frac{1}{l^*} \sqrt{\frac{\Phi^* \epsilon_r \epsilon_0}{q C^*}}$ for the semiconductor ($r = S$) and electrolyte ($r = E$). The other rescaled quantities are,

$$t' = \frac{t}{t^*}, \quad \mathbf{x}' = \frac{\mathbf{x}}{l^*}, \quad \Phi' = \frac{\Phi}{\Phi^*}, \quad \rho'_c = \frac{\rho_c}{C^*}, \quad \text{for } c = n, p, r, o, \\ R'(\rho'_n, \rho'_p) = \frac{t^*}{C^*} R(C^* \rho'_n, C^* \rho'_p), \quad G' = \frac{t^*}{C^*} G, \quad \Phi'_{\text{app}} = \frac{\Phi_{\text{app}}}{\Phi^*}, \\ \rho_c^{e'} = \frac{\rho_c^e}{C^*}, \quad \text{for } c = n, p, \quad \rho_c^{\infty'} = \frac{\rho_c^{\infty}}{C^*} \quad \text{for } c = r, o, \quad \Phi'_{\text{SCR}} = \frac{\Phi_{\text{SCR}}}{\Phi^*}, \\ C = \frac{C}{C^*}, \quad k'_{et} = \frac{k_{et} t^* C^*}{l^*}, \quad k'_{ht} = \frac{k_{ht} t^* C^*}{l^*}, \quad v'_n = \frac{v_n t^*}{l^*}, \quad v'_p = \frac{v_p t^*}{l^*}, \\ \mu'_c = \frac{\Phi^* \mu_c t^*}{(l^*)^2} \quad \text{for } c = n, p, r, o, \quad \rho'_i = \frac{\rho_i}{C^*}, \quad \Phi'_{\text{app}} = \frac{\Phi_{\text{app}}}{\Phi^*}. \quad (3.1.1)$$

Additionally, we use the Einstein relation (2.2.13) to obtain the non-dimensional formulation for (2.4.3) and (2.4.5) (we have dropped the ' for ease of notation):

$$\frac{\partial \rho_n}{\partial t} + \nabla \cdot \mu_n (-\alpha_n \nabla \Phi \rho_n - \nabla \rho_n) = G(\mathbf{x}) - R(\rho_n, \rho_p) \quad \text{in } \Omega_S \times (0, T), \\ \frac{\partial \rho_p}{\partial t} + \nabla \cdot \mu_p (-\alpha_p \nabla \Phi \rho_p - \nabla \rho_p) = G(\mathbf{x}) - R(\rho_n, \rho_p) \quad \text{in } \Omega_S \times (0, T), \\ -\nabla \cdot (\lambda_S^2 \nabla \Phi) = (C(\mathbf{x}) + \alpha_n \rho_n + \alpha_p \rho_p) \quad \text{in } \Omega_S \times (0, T). \quad (3.1.2)$$

And,

$$\begin{aligned} \frac{\partial \rho_r}{\partial t} + \nabla \cdot \mu_r (-\alpha_r \nabla \Phi \rho_r - \nabla \rho_r) &= 0 \quad \text{in } \Omega_E \times (0, T), \\ \frac{\partial \rho_o}{\partial t} + \nabla \cdot \mu_o (-\alpha_o \nabla \Phi \rho_o - \nabla \rho_o) &= 0 \quad \text{in } \Omega_E \times (0, T), \\ -\nabla \cdot (\lambda_E^2 \nabla \Phi) &= (\alpha_r \rho_r + \alpha_o \rho_o) \quad \text{in } \Omega_E \times (0, T). \end{aligned} \quad (3.1.3)$$

The non-dimensional formulation of the boundary (2.4.4), (2.4.6), interface (2.4.7)-(2.4.11) and initial conditions (2.4.12) are of the same form as previously displayed, but with rescaled values.

3.1.2 Preliminary Notation

Let $\mathcal{T}_h(\Omega) = \{\Omega_e\}_{e=1}^N$ be the general triangulation of a domain $\Omega \subset \mathbb{R}^d$, $d = 1, 2$, into N non-overlapping elements Ω_e of diameter h_e . The maximum size of the diameters of all the elements is $h = \max(h_e)$. We define \mathcal{E}_h to be the set of all element faces and \mathcal{E}_h^i to be the set of all interior faces of elements which do not intersect the total boundary $(\partial\Omega)$. Let $\partial\Omega_e \in \mathcal{E}_h^i$ be a interior boundary face element, we define the unit normal vector to be,

$$\mathbf{n} = \text{unit normal vector to } \partial\Omega_e \text{ pointing from } \Omega_e^- \rightarrow \Omega_e^+. \quad (3.1.4)$$

We take the following definition on limits of functions on element faces,

$$w^-(\mathbf{x})|_{\partial\Omega_e} = \lim_{s \rightarrow 0^-} w(\mathbf{x} + s\mathbf{n}), \quad w^+(\mathbf{x})|_{\partial\Omega_e} = \lim_{s \rightarrow 0^+} w(\mathbf{x} + s\mathbf{n}). \quad (3.1.5)$$

We define the average and jump of a function across an element face as,

$$\{f\} = \frac{1}{2}(f^- + f^+), \quad \text{and} \quad [f] = f^+ \mathbf{n}^+ + f^- \mathbf{n}^-, \quad (3.1.6)$$

and,

$$\{\mathbf{f}\} = \frac{1}{2}(\mathbf{f}^- + \mathbf{f}^+), \quad \text{and} \quad \llbracket \mathbf{f} \rrbracket = \mathbf{f}^+ \cdot \mathbf{n}^+ + \mathbf{f}^- \cdot \mathbf{n}^-, \quad (3.1.7)$$

where f is a scalar function and \mathbf{f} is vector-valued function. We note that for a faces that are on the boundary of the domain we have,

$$\llbracket f \rrbracket = f \mathbf{n} \quad \text{and} \quad \llbracket \mathbf{f} \rrbracket = \mathbf{f} \cdot \mathbf{n}. \quad (3.1.8)$$

We denote the volume integrals and surface integrals using the $L^2(\Omega)$ inner products by $(\cdot, \cdot)_\Omega$ and $\langle \cdot, \cdot \rangle_{\partial\Omega}$ respectively. We introduce the following Sobolev spaces for a domain Ω and integer $s \geq 0$,

$$H^s(\Omega) = \{u \in L^2(\Omega) : \forall 0 \leq |\alpha| \leq s, D^\alpha u \in L^2(\Omega)\}, \quad (3.1.9)$$

$$H_{\text{div}}(\Omega) = \left\{ \mathbf{u} \in (L^2(\Omega))^d : \nabla \cdot \mathbf{u} \in L^2(\Omega) \right\}, \quad (3.1.10)$$

where D is the distributional derivative. The broken Sobolev space for a general triangulation $\mathcal{T}_h(\Omega)$ and integer $s \geq 0$ is,

$$H^s(\mathcal{T}_h) = \{w \in L^2(\Omega) : w|_{\Omega_e} \in H^s(\Omega_e), \forall \Omega_e \in \mathcal{T}_h(\Omega)\}. \quad (3.1.11)$$

We label the domain for Poisson's equation Ω_P . The Poisson domain is the union of the semiconductor and electrolyte domains,

$$\Omega_P = \Omega_S \cup \Omega_E. \quad (3.1.12)$$

Our model problem now has three domains Ω_S, Ω_E and Ω_P . Therefore our numerical methods will use three triangulations: the triangulation for Poisson's equation,

$$\mathcal{T}_h^P = \mathcal{T}_h(\Omega_P),$$

which has N_P elements. The triangulation for the semiconductor,

$$\mathcal{T}_h^S = \mathcal{T}_h(\Omega_S),$$

which has N_S elements and the triangulation for the electrolyte,

$$\mathcal{T}_h^E = \mathcal{T}_h(\Omega_E),$$

which has N_E elements. The set of all internal element faces for the semiconductor and electrolyte are labeled $\mathcal{E}_h^{i,S}$ and $\mathcal{E}_h^{i,E}$ respectively. The set of all element faces which lie on the Dirichlet, Neumann and interface boundaries of the semiconductor are respectively labeled \mathcal{E}_D^S , \mathcal{E}_N^S and \mathcal{E}_Σ^S . The set of all element faces which lie on the Dirichlet, Neumann and interface boundaries of the electrolyte are respectively labeled \mathcal{E}_D^E , \mathcal{E}_N^E and \mathcal{E}_Σ^E .

Remark 3.1.1. We require all triangulations to be regular meshes. In addition, the Poisson triangulation is required to be the union of the semiconductor and electrolyte triangulations,

$$\mathcal{T}_h^P = \mathcal{T}_h^S \cup \mathcal{T}_h^E. \quad (3.1.13)$$

Therefore $N_P = N_S + N_E$. Requiring (3.1.13) guarantees the existence and uniqueness of one-to-one mappings from the elements in \mathcal{T}_h^P to elements of \mathcal{T}_h^S and \mathcal{T}_h^E . We remind the reader that $\overline{\Omega}_S \cap \overline{\Omega}_E = \Sigma$. We additionally restrict our triangulations of the semiconductor and electrolyte domains such that element faces on opposite sides of the interface match. That is elements that lie adjacent to one another on the interface, but are in different meshes have a common face. This requirement specifically implies,

$$E_\Sigma^S = \mathcal{E}_\Sigma^E = \mathcal{E}_\Sigma. \quad (3.1.14)$$

Requiring (3.1.14) is not severe; indeed, it prohibits the presence of hanging nodes on the interface, but does not prohibit them on interior faces $\mathcal{E}_h^{i,S}$ and $\mathcal{E}_h^{i,E}$.

In our numerical methods we will use approximations to scalar valued functions that reside in the finite-dimensional broken Sobolev spaces,

$$W_{h,k}^m(\mathcal{T}_h^m) = \{w \in L^2(\Omega_m) : w|_{\Omega_e} \in \mathcal{Q}_{k,k}(\Omega_e), \quad \forall \Omega_e \in \mathcal{T}_h^m\}, \quad (3.1.15)$$

for $m = S, E, P$. $\mathcal{Q}_{k,k}(\Omega_e)$ denotes the tensor product of polynomials of order k on the element Ω_e . For the drift-diffusion equation use approximations of vector valued functions (i.e. current fluxes) that are in,

$$\mathbf{W}_{h,k}^m(\mathcal{T}_h^m) = \left\{ \mathbf{w} \in (L^2(\Omega_m))^d : \mathbf{w}|_{\Omega_e} \in (\mathcal{Q}_{k,k}(\Omega_e))^d, \quad \forall \Omega_e \in \mathcal{T}_h^m \right\} \quad (3.1.16)$$

for $m = S, E$.

To approximate the displacement electric field $(-\lambda_m^2 \nabla \Phi)$ in Poisson's equations we use the Raviart-Thomas finite element space [123]. The Raviart-Thomas finite element space ($\mathbf{RT}_{h,k}^P = \mathbf{RT}_{h,k}(\mathcal{T}_h^P)$) in two dimensions is,

$$\mathbf{RT}_{h,k}^P = \{ \mathbf{v} \in H_{\text{div}}(\Omega_P) : \mathbf{v}|_{\Omega_e} \in \mathcal{Q}_{k+1,k}(\Omega_e) \times \mathcal{Q}_{k,k+1}(\Omega_e), \quad \forall \Omega_e \in \mathcal{T}_h^P \}. \quad (3.1.17)$$

The subspace $\mathbf{V}_{h,k}^P \subset \mathbf{RT}_{h,k}^P$ is defined as,

$$\mathbf{V}_{h,k}^P = \{ \mathbf{v} \in \mathbf{RT}_{h,k}^P(\mathcal{T}_h^P) : \mathbf{v} \cdot \mathbf{n}|_{\Gamma_{S,N} \cup \Gamma_{E,N}} = 0 \}. \quad (3.1.18)$$

In one dimension, $\mathbf{RT}_{h,k}^P = W_{h,k+1}^P$. We remark that with this definition we have,

$$\nabla \cdot \mathbf{RT}_{h,k}^P = W_{h,k}^P \quad (3.1.19)$$

in both one and two dimensions. Furthermore, we have the property that [123],

$$\forall \mathbf{v} \in \mathbf{RT}_{h,k}^P, \quad \llbracket \mathbf{v} \rrbracket = 0 \quad \text{on } \in \mathcal{E}_h^{i,S} \cup \mathcal{E}_h^{i,E} \cup \mathcal{E}_\Sigma. \quad (3.1.20)$$

Let $m = S$ or E , then the L^2 norm is,

$$\|w\|_{L^2(\mathcal{T}_h^m)} = \left(\sum_{\Omega_e \in \mathcal{T}_h^m} \|w\|_{L^2(\Omega_e)}^2 \right)^{1/2}, \quad (3.1.21)$$

and the H^s norm with s any positive integer,

$$\|w\|_{H^s(\mathcal{T}_h^m)} = \left(\sum_{0 \leq |s| \leq \alpha} \|D^s w\|_{L^2(\mathcal{T}_h^m)}^2 \right)^{1/2}. \quad (3.1.22)$$

The H^s semi-norm is then,

$$|w|_{H^s(\mathcal{T}_h^m)} = \left(\sum_{|s|=\alpha} \|D^s w\|_{L^2(\mathcal{T}_h^m)}^2 \right)^{1/2}. \quad (3.1.23)$$

The DG norm is defined as,

$$\|w\|_{\text{DG,m}} = \left(\|\nabla w\|_{L^2(\mathcal{T}_h^m)}^2 + \|h^{-1/2} \llbracket w \rrbracket\|_{L^2(\mathcal{E}_h^{i,m})}^2 + \|h^{-1/2} w\|_{L^2(\mathcal{E}_D^m)}^2 \right)^{1/2}, \quad (3.1.24)$$

where $\mathcal{E}_h^{i,m}$, \mathcal{E}_D^m are respectively the element faces on the interior and Dirichlet boundary for $m = S, E$. Additionally, let us define the time dependent Sobolev space for a general Banach space V and $r \geq 1$,

$$L^r(V; (0, T)) = \left\{ w : (0, T) \rightarrow V, \text{ meas. : } \int_0^T \|w(t)\|_V^r dt < \infty \right\}, \quad (3.1.25)$$

with norm,

$$\|w\|_{L^r(V;(0,T))} = \left(\int_0^T \|w(t)\|_V^r dt \right)^{1/r}. \quad (3.1.26)$$

Finally the space, $H^1(H^s(\mathcal{T}_h); (0, T))$ is the space of all $w \in L^2(H^s(\mathcal{T}_h); (0, T))$ such that $\frac{\partial w}{\partial t}$ exists in the weak sense and $\frac{\partial w}{\partial t} \in L^2(H^s(\mathcal{T}_h); (0, T))$.

In the following sections we use the above notation to present our numerical approximations to the model problem. We begin with the discretization of Poisson's equation for the potential and electric field.

3.2 Mixed Finite Element Method (MFEM)

To approximate solutions to Poisson's equation we implement a mixed finite element method (MFEM). We introduce the so-called displacement electric field, \mathbf{D} , and rewrite Poisson's equation in mixed form,

$$\nabla \cdot \mathbf{D}(\mathbf{x}, t) = f(\mathbf{x}, t), \quad (3.2.1)$$

$$\mathbf{D}(\mathbf{x}, t) + \lambda^2(\mathbf{x}) \nabla \Phi(\mathbf{x}, t) = 0, \quad (3.2.2)$$

We require the Debeye length function $\lambda^2(\mathbf{x}) \in L^\infty(\Omega_P)$ and the right hand side function $f(\mathbf{x}, t) \in (L^2(\Omega_P) \times (0, T))$. These are defined as follows,

$$\lambda(\mathbf{x}) = \begin{cases} \lambda_S^2 & \text{in } \Omega_S, \\ \lambda_E^2 & \text{in } \Omega_E, \end{cases} \quad (3.2.3)$$

$$f(\mathbf{x}, t) = \begin{cases} C(\mathbf{x}) + \alpha_n \rho_n(\mathbf{x}, t) + \alpha_p \rho_p(\mathbf{x}, t) & \text{in } \Omega_S \times (0, T), \\ \alpha_r \rho_r(\mathbf{x}, t) + \alpha_o \rho_o(\mathbf{x}, t) & \text{in } \Omega_E \times (0, T). \end{cases} \quad (3.2.4)$$

The electric field can then be obtained from \mathbf{D} by the equation,

$$\mathbf{E}(\mathbf{x}, t) = (\lambda^2)^{-1} \mathbf{D}(\mathbf{x}, t). \quad (3.2.5)$$

We note that λ^2 is invertible because all Debye lengths are positive definite. The boundary conditions for this problem are either Dirichlet or Neumann conditions. For the Dirichlet conditions, we require that $\Phi_{\text{app.}}(\mathbf{x}) \in L^2(\Gamma_{S,D})$, $\Phi_{\text{SCR}}(\mathbf{x}) \in L^2(\Gamma_{S,D})$ and $\Phi^\infty(\mathbf{x}) \in L^2(\Gamma_{E,D})$. Neumann conditions will be imposed in the numerical approximations as constraints on the space $\mathbf{V}_{h,k}^P$.

We approximate solutions to Φ and \mathbf{D} using the finite element approximations $\Phi(\cdot, t) \approx \Phi_h(\cdot, t) \in W_{h,k}^P \subset H^s(\mathcal{T}_h^P)$ and $\mathbf{D}(\cdot, t) \approx \mathbf{D}_h(\cdot, t) \in \mathbf{V}_{h,k}^P \subset \mathbf{RT}_{h,k}^P$. The mixed finite element approximation to Poisson's equation is obtained by multiplying (3.2.1) by $v \in W_{h,k}^P$ and integrating over Ω_P as well as multiplying (3.2.2) by $\mathbf{v} \in \mathbf{V}_{h,k}^P$ and integrating by parts over Ω_P . The MFEM is then,

$$\begin{aligned} \text{Find } (\Phi_h, \mathbf{D}_h) \in (W_{h,k}^P \times (0, T)) \times (\mathbf{V}_{h,k}^P \times (0, T)) \text{ such that,} \\ (\mathbf{v}, (\lambda_r^2)^{-1} \mathbf{D}_h)_{\Omega_P} - (\nabla \cdot \mathbf{v}, \Phi_h)_{\Omega_P} = -\langle \mathbf{v}, \Phi_{\text{SCR}} + \Phi_{\text{app.}} \rangle_{\mathcal{E}_D^S} - \langle \mathbf{v}, \Phi^\infty \rangle_{\mathcal{E}_D^E}, \\ (v, \nabla \cdot \mathbf{D}_h)_{\Omega_P} = (v, f)_{\Omega_P}, \end{aligned} \quad (3.2.6)$$

for all $(v, \mathbf{v}) \in W_{h,k}^P \times \mathbf{V}_{h,k}^P$.

The approximation of the potential Φ_h is a linear combination of basis functions $\psi_{n,p}^P$ of $W_{h,k}^P$,

$$\Phi_h(\mathbf{x}, t) = \sum_{i=1}^{N_P} \sum_{j=0}^k \phi_{i,j}(t) \psi_{i,j}^P(\mathbf{x}). \quad (3.2.7)$$

The basis functions $\psi_{i,j}^P$ of $W_{h,k}^P$ are local polynomials of order j on element i .

The local coefficient corresponding to this local basis function is $\phi_{i,j}$. We can repeat the same procedure for the displacement electric field and write \mathbf{D}_h as the linear combination of local basis functions $\mathbf{\Upsilon}_{i,j}^P$ of $\mathbf{V}_{h,k}^P$ and corresponding coefficients $d_{i,j}$,

$$\mathbf{D}_h(\mathbf{x}, t) = \sum_{i=1}^{N_P} \sum_{j=0}^k d_{i,j}(t) \mathbf{\Upsilon}_{i,j}^P(\mathbf{x}). \quad (3.2.8)$$

Substituting (3.2.7) for Φ_h and (3.2.8) for \mathbf{D}_h in (3.2.6) results in the following linear system for the degree of freedom vectors (which we denote by the same symbols),

$$\begin{bmatrix} A & B^T \\ B & 0 \end{bmatrix} \begin{bmatrix} \mathbf{D}_h(\cdot, t) \\ \Phi_h(\cdot, t) \end{bmatrix} = \begin{bmatrix} \mathbf{L}_1(t) \\ \mathbf{L}_2(t) \end{bmatrix} \quad \forall t \in (0, T). \quad (3.2.9)$$

The matrices A, B and B^T correspond to,

$$A \Leftarrow (\mathbf{v}, (\lambda_r^2)^{-1} \mathbf{D}_h)_{\Omega_P} \quad (3.2.10)$$

$$B^T \Leftarrow -(\nabla \cdot \mathbf{v}, \Phi_h)_{\Omega_P} \quad (3.2.11)$$

$$B \Leftarrow (v, \nabla \cdot \mathbf{D}_h)_{\Omega_P} \quad (3.2.12)$$

The right hand side $\mathbf{L}_1(t)$ and $\mathbf{L}_2(t)$ are vectors that incorporate the boundary conditions and right hand side of Poisson's equation respectively,

$$\mathbf{L}_1(t) \Leftarrow -\langle \mathbf{v}, \Phi_{\text{SCR}} + \Phi_{\text{app.}} \rangle_{\mathcal{E}_D^S} - \langle \mathbf{v}, \Phi^\infty \rangle_{\mathcal{E}_D^E} \quad (3.2.13)$$

$$\mathbf{L}_2(t) \Leftarrow (v, f(\mathbf{x}, t))_{\Omega_P}. \quad (3.2.14)$$

The right hand side vectors must be updated at every time step to incorporate updates in charge densities. However, the matrices A , B^T , and B only need to be assembled once since they are independent of time. The matrix resulting from the mixed method applied to Poisson's equation is symmetric indefinite and this poses challenges for linear solvers as will be discussed in Section 3.5.

Remark 3.2.1. We stress that the choice of Raviart-Thomas elements to approximation \mathbf{D} is essential. First, this choice of elements in conjunction with discontinuous elements to approximate Φ yields a formulation for elliptic problems that satisfies the discrete version of the *inf-sup* or “Babuska-Brezzi” conditions [20, 34]. The *inf-sup* conditions guarantee that the matrix in (3.2.9) is nonsingular. Second, the property, (3.1.20), of the Raviart-Thomas elements ensures that the normal component of \mathbf{D}_h will be continuous through the semiconductor-electrolyte interface as needed by (2.4.11). Continuity of Φ_h through the interface is implicitly enforced through the weak formulation.

3.3 Local Discontinuous Galerkin (LDG) Method

In this subsection we discuss the local discontinuous Galerkin (LDG) method to approximate solutions of the drift-diffusion equation. Each charge carrier will have their own LDG discretization. The coupling between the drift-diffusion equations as well as with Poisson's equation will be addressed in Section 3.4. In this section we shall only discuss the spatial discretizations of the drift-diffusion equation. To simplify the presentation of the discretization,

we only consider the drift-diffusion equation for the electrons in the system:

$$\begin{aligned}
\partial_t \rho_n + \nabla \cdot \mu_n (\alpha_n \mathbf{E} \rho_n - \nabla \rho_n) &= -R(\rho_n, \rho_p) + \gamma G(\mathbf{x}) \quad \text{in } \Omega_S \times (0, T), \\
\mathbf{n}_{\Sigma^S} \cdot \mu_n (\alpha_n \mathbf{E} \rho_n - \nabla \rho_n) &= I_{et}(\rho_n - \rho_n^e, \rho_o) \quad \text{on } \Sigma \times (0, T), \\
\mathbf{n} \cdot \mu_n (-\alpha_n \mathbf{E} \rho_n - \nabla \rho_n) &= 0 \quad \text{on } \Gamma_{S,N} \times (0, T), \\
\rho_n &= \rho_n^e \quad \text{on } \Gamma_{S,D} \times (0, T),
\end{aligned} \tag{3.3.1}$$

The equations for other charge carriers are discretized in a similar way.

As with the mixed finite element method, the LDG discretization requires the drift-diffusion equations be written as a first-order system. We do this by introducing an auxiliary variable which we call the current flux variable \mathbf{q}_n :

$$\partial_t \rho_n + \nabla \cdot \mathbf{q}_n = -R(\rho_n, \rho_p) + \gamma G(\mathbf{x}) \quad \text{in } \Omega_S \times (0, T), \tag{3.3.2}$$

$$\mu^{-1} \mathbf{q}_n = \alpha_n \mathbf{E} \rho_n - \nabla \rho_n \quad \text{in } \Omega_S \times (0, T), \tag{3.3.3}$$

$$\mathbf{n}_{\Sigma^S} \cdot \mu^{-1} \mathbf{q}_n = I_{et}(\rho_n - \rho_n^e, \rho_o) \quad \text{on } \Sigma \times (0, T), \tag{3.3.4}$$

$$\mathbf{n} \cdot \mu^{-1} \mathbf{q}_n = 0 \quad \text{on } \Gamma_N \times (0, T), \tag{3.3.5}$$

$$\rho_n = \rho_n^e \quad \text{on } \Gamma_{S,N} \times (0, T). \tag{3.3.6}$$

We seek approximations for densities $\rho_{n,h}(\cdot, t) \in W_{h,k}^S$ and currents $\mathbf{q}_{n,h}(\cdot, t) \in \mathbf{W}_{h,k}^S$ for all $t \in (0, T)$. Multiplying (3.3.2) by $w \in W_{h,k}^S$ and (3.3.3) by $\mathbf{w} \in \mathbf{W}_{h,k}^S$ and integrating the divergence terms by parts over an element

$\Omega_e \in \mathcal{T}_h^S$ we obtain,

$$\begin{aligned} (w, \partial_t \rho_{n,h})_{\Omega_e} - (\nabla w, \mathbf{q}_{n,h})_{\Omega_e} + \langle w, \mathbf{q}_{n,h} \rangle_{\partial \Omega_e} &= \left(w, \tilde{R}(\rho_{n,h}, \rho_{p,h}) \right)_{\Omega_e}, \\ (\mathbf{w}, \mathbf{q}_{n,h})_{\Omega_e} - (\nabla \cdot \mathbf{w}, \rho_{n,h})_{\Omega_e} - (\alpha_n \mathbf{w} \cdot \mathbf{E}, \rho_{n,h})_{\Omega_e} + \langle \mathbf{w}, \rho_{n,h} \rangle_{\partial \Omega_e} &= 0, \end{aligned}$$

where $\tilde{R}(\rho_{n,h}, \rho_{p,h}) = -R(\rho_{n,h}, \rho_{p,h}) + \gamma G(\mathbf{x})$. Summing over all the elements leads to the semi-discrete LDG formulation for the drift-diffusion equation,

Find $\rho_{n,h}(\cdot, t) \in W_{h,k}^S$ and $\mathbf{q}_{n,h}(\cdot, t) \in \mathbf{W}_{h,k}^S$ such that,

$$\begin{aligned} (w, \partial_t \rho_{n,h})_{\Omega_S} - (\nabla w, \mathbf{q}_{n,h})_{\Omega_S} + \langle \llbracket w \rrbracket, \hat{\mathbf{q}}_{n,h} \rangle_{\mathcal{E}_h^{i,S}} + \langle \llbracket w \rrbracket, \hat{\mathbf{q}}_{n,h} \rangle_{\mathcal{E}_D^S \cup \mathcal{E}_N^S \cup \mathcal{E}_\Sigma^S} &= \left(w, \tilde{R}(\rho_{n,h}, \rho_{p,h}) \right)_{\Omega_S} \\ (3.3.7) \end{aligned}$$

$$\begin{aligned} (\mathbf{w}, \mathbf{q}_{n,h})_{\Omega_S} - (\nabla \cdot \mathbf{w}, \rho_{n,h})_{\Omega_S} - (\alpha_n \mathbf{w} \cdot \mathbf{E}, \rho_{n,h})_{\Omega_S} + \langle \llbracket \mathbf{w} \rrbracket, \hat{\rho}_{n,h} \rangle_{\mathcal{E}_h^{i,S}} \\ + \langle \llbracket \mathbf{w} \rrbracket, \hat{\rho}_{n,h} \rangle_{\mathcal{E}_D^S \cup \mathcal{E}_N^S \cup \mathcal{E}_\Sigma^S} &= 0 \end{aligned} \quad (3.3.8)$$

for all $(w, \mathbf{w}) \in W_{h,k}^S \times \mathbf{W}_{h,k}^S$ and all $t \in (0, T)$.

The terms $\hat{\mathbf{q}}_{n,h}$ and $\hat{\rho}_{n,h}$ are the numerical fluxes. The numerical fluxes are introduced to ensure consistency, stability, and enforce the boundary conditions weakly [85]. The flux $\hat{\rho}_{n,h}$ is,

$$\hat{\rho}_{n,h} = \begin{cases} \{\rho_{n,h}\} + \boldsymbol{\beta} \cdot \llbracket \rho_{n,h} \rrbracket & \text{in } \mathcal{E}_h^{i,S} \\ \rho_{n,h} & \text{in } \mathcal{E}_\Sigma^S \\ \rho_{n,h} & \text{in } \mathcal{E}_N^S \\ \rho_n^e & \text{in } \mathcal{E}_D^S \end{cases} \quad (3.3.9)$$

The flux $\hat{\mathbf{q}}_{n,h}$ is,

$$\hat{\mathbf{q}}_{n,h} = \begin{cases} \{\mathbf{q}_{n,h}\} - \llbracket \mathbf{q}_{n,h} \rrbracket \boldsymbol{\beta} + \sigma_n \llbracket \rho_{n,h} \rrbracket & \text{in } \mathcal{E}_h^{i,S} \\ I_{et}(\rho_{n,h} - \rho_n^e, \rho_{o,h}) \mathbf{n}_\Sigma^S & \text{in } \mathcal{E}_\Sigma^S \\ \mathbf{0} & \text{in } \mathcal{E}_N^S \\ \mathbf{q}_{n,h} + \sigma_n (\rho_{n,h} - \rho_n^e) \mathbf{n} & \text{in } \mathcal{E}_D^S \end{cases} \quad (3.3.10)$$

The term β is a constant vector which does not lie parallel to any element face in $\mathcal{E}_h^{i,S}$. For $\beta = 0$, $\hat{\mathbf{q}}_{n,h}$ and $\hat{\rho}_h$ are called the central or Brezzi et. al. fluxes [12]. For $\beta \neq 0$, $\hat{\mathbf{q}}_{n,h}$ and $\hat{\rho}_{n,h}$ are called the LDG/alternating fluxes [12].

The term σ_n is the penalty parameter that is defined as,

$$\sigma_n = \begin{cases} \tilde{\sigma}_n \min(h_{e_1}^{-1}, h_{e_2}^{-1}) & \mathbf{x} \in \langle \Omega_{e_1}, \Omega_{e_2} \rangle \\ \tilde{\sigma}_n h_e^{-1} & \mathbf{x} \in \partial\Omega_e \cap \mathcal{E}_D^S \end{cases} \quad (3.3.11)$$

with $\tilde{\sigma}_n$ being a positive constant.

We can now substitute (3.3.9) and (3.3.10) into (3.3.7) and (3.3.8) to obtain the solution pair $(\rho_{n,h}, \mathbf{q}_{n,h})$ to the semi-discrete LDG approximation to the drift-diffusion equation given by:

Find $\rho_{n,h}(\cdot, t) \in W_{h,k}^S$ and $\mathbf{q}_{n,h}(\cdot, t) \in \mathbf{W}_{h,k}^S$ such that,

$$\begin{aligned} (w, \partial_t \rho_{n,h}) + \mathcal{L}_{n,S}(w, \mathbf{w}; \rho_{n,h}, \mathbf{q}_{n,h}) + \langle w, I_{et}(\rho_{n,h} - \rho_n^e, \rho_{o,h}) \rangle_{\mathcal{E}_\Sigma^S} \\ = \left(w, \tilde{R}(\rho_{n,h}, \rho_{p,h}) \right)_{\Omega_S} + \langle w, \sigma_n \rho_n^e \rangle_{\mathcal{E}_D^S} \end{aligned} \quad (3.3.12)$$

$$\mathcal{A}_{n,S}(w, \mathbf{w}; \rho_{n,h}, \mathbf{q}_{n,h}) - (w, \alpha_n \mathbf{E} \rho_{n,h})_{\Omega_S} = -\langle \mathbf{n} \cdot \mathbf{w}, \rho_n^e \rangle_{\mathcal{E}_D^S} \quad (3.3.13)$$

for all $(w, \mathbf{w}) \in W_{h,k}^S \times \mathbf{W}_{h,k}^S$ and all $t \in (0, T)$. The quadlinear forms $\mathcal{L}_{n,S}$ and $\mathcal{A}_{n,S}$ are defined as,

$$\begin{aligned} \mathcal{L}_{n,S} = -(\nabla w, \mathbf{q}_{n,h})_{\Omega_S} + \langle \llbracket w \rrbracket, \sigma_n \llbracket \rho_{n,h} \rrbracket \rangle_{\mathcal{E}_h^{i,S}} + \langle \llbracket w \rrbracket, \{ \mathbf{q}_{n,h} \} - \llbracket \mathbf{q}_{n,h} \rrbracket \beta \rangle_{\mathcal{E}_h^{i,S}} \\ + \langle w, \mathbf{n} \cdot \mathbf{q}_{n,h} \rangle_{\mathcal{E}_D^S} + \langle w, \sigma_n \rho_{n,h} \rangle_{\mathcal{E}_D^S}, \end{aligned} \quad (3.3.14)$$

$$\begin{aligned} \mathcal{A}_{n,S} = (\mathbf{w}, \mu_n^{-1} \mathbf{q}_{n,h})_{\Omega_S} - (\nabla \cdot \mathbf{w}, \rho_{n,h})_{\Omega_S} + \langle \llbracket \mathbf{w} \rrbracket, \{ \rho_{n,h} \} + \beta \cdot \llbracket \rho_{n,h} \rrbracket \rangle_{\mathcal{E}_h^{i,S}} \\ + \langle w, \rho_{n,h} \rangle_{\mathcal{E}_N^S \cup \mathcal{E}_\Sigma^S}. \end{aligned} \quad (3.3.15)$$

As with the mixed finite element method, we write our variables $\rho_{n,h}$ and $\mathbf{q}_{n,h}$ as a linear combination of basis functions in $W_{h,k}^S$ and $\mathbf{W}_{h,k}^S$ respectively. The expansion of $\rho_{n,h}$ in terms of coefficients $u_{i,j}^n(t)$ over the local basis functions $\psi_{i,j}^S \in W_{h,k}^S$ has the form,

$$\rho_{n,h}(\mathbf{x}, t) = \sum_{i=1}^{N_S} \sum_{j=0}^k u_{i,j}^n(t) \psi_{i,j}^S(\mathbf{x}). \quad (3.3.16)$$

The expansion of $\mathbf{q}_{n,h}$ in terms of coefficients $q_{i,j}^n(t)$ over the local vector valued basis functions $\psi_{i,j}^S \in \mathbf{W}_{h,k}^S$ has the form,

$$\mathbf{q}_{n,h}(\mathbf{x}, t) = \sum_{i=1}^{N_S} \sum_{j=0}^k q_{i,j}^n(t) \psi_{i,j}^S(\mathbf{x}). \quad (3.3.17)$$

The form of the resulting system upon substituting (3.3.16) and (3.3.17) into (3.3.12) and (3.3.13) depends on the time stepping routine employed as will be addressed in the next section.

Remark 3.3.1. We remark that in this LDG formulation the auxiliary variable $\mathbf{q}_{n,h}$ is defined as the total flux as was similarly done in [15].

Remark 3.3.2. Since they reside in the same domain, electrons and holes have the same basis functions. Similarly, reductants and oxidants have the same basis functions. However, electrons/holes do not have the same basis functions as redox couples since they reside in separate domains.

3.4 Implicit/Explicit (IMEX) Time Stepping Algorithms

We can combine the mixed finite element discretization of the Poisson equation (3.2.6) with the semi-discrete LDG discretization of the drift-diffusion

equation (3.3.12)-(3.3.13) to obtain a discretization scheme for the whole system of coupled drift-diffusion-Poisson equations. The resulting system will be nonlinear due to the various nonlinearities in the PDE system, including for instance, the nonlinear recombination-generation effects, the coupling between the drift-diffusion components of the densities through drift terms such as $\alpha_n \mathbf{E} \rho_n$, as well as the nonlinear interface transfer conditions.

To deal with the nonlinearities in the system, we combine different time-stepping schemes with domain decomposition techniques. More precisely, we use explicit time-stepping to treat the recombination-generation nonlinearity, use a “time lagging” technique [45–47, 126, 130] to treat the coupling between the densities and the electric potential, and use a Schwarz domain decomposition technique [102–104, 109, 121, 140] coupled with explicit stepping, to treat the coupling between the semiconductor and electrolyte domains. To overcome the limitation on the size of the time steps imposed by the Courant-Friedrichs-Lowy (CFL) condition when an explicit time stepping scheme is used, we use implicit scheme on the diffusion terms whenever it is possible. Therefore, our marching in time is done by an overall implicit-explicit (IMEX) time stepping scheme.

We present two classes of time stepping algorithms that are based on IMEX time stepping and domain decomposition methods. The first class, in Sections 3.4.1 and 3.4.2, uses the alternating Schwarz method. The second class, in Sections 3.4.3 and 3.4.4, uses the parallel Schwarz strategy. The main difference between the two classes of methods lies in how they treat the carrier

densities on the semiconductor-electrolyte interface.

Remark 3.4.1. For notational convenience we drop the subscript h from our approximations.

3.4.1 The Implicit-Implicit-Explicit Alternating Schwarz Scheme

In the implicit-implicit-explicit alternating Schwarz (AS-IMIMEX) scheme, we first use a “time lagging” technique to decouple the Poisson equations from the drift-diffusion equations. We then apply an implicit scheme on the diffusion terms, an implicit scheme on the drift terms, and an explicit scheme on the recombination-generation terms. To decouple the equations in the semiconductor domain from those in the electrolyte domain, we use a strategy based on the alternating Schwarz domain decomposition method.

The algorithm works as follows. At time step k , we first solve the Poisson equation for the electric potential (and therefore the electric field) using charge densities at the previous time step $k - 1$. That is, we solve for $(\Phi^{k-1}, \mathbf{D}^{k-1})$ from the Poisson equation:

$$\begin{aligned} (\mathbf{v}, \lambda^{-2} \mathbf{D}^{k-1})_{\Omega_P} - (\nabla \cdot \mathbf{v}, \Phi^{k-1})_{\Omega_P} &= -\langle \mathbf{n} \cdot \mathbf{v}, \Phi_{\text{app}} + \Phi_{\text{bi}} \rangle_{\mathcal{E}_D^S} - \langle \mathbf{n} \cdot \mathbf{v}, \Phi^\infty \rangle_{\mathcal{E}_D^E}, \\ (v, \nabla \cdot \mathbf{D}^{k-1})_{\Omega_P} &= (v, f^{k-1})_{\Omega}, \end{aligned} \quad (3.4.1)$$

where f^{k-1} is evaluated with the densities $(\rho_n^{k-1}, \rho_p^{k-1}, \rho_r^{k-1}, \rho_o^{k-1})$. We then use \mathbf{E}^{k-1} (obtaining it from \mathbf{D}^{k-1} by (3.2.5)) in the drift-diffusion equations for the charge densities to find updates of these densities. This time lagging technique is called the IMPES (implicit pressure, explicit saturation) method

in the subsurface flow simulation literature [10, 46, 47, 130, 131, 136], and is conceptually the same as the Gummel iteration method [83, 128] which is often used semiconductor device simulations to decouple the Poisson component and the drift-diffusion component of the system in the steady state equations.

To update the charge densities using the drift-diffusion equations, we use a alternating Schwarz domain decomposition idea to decouple the equations in the semiconductor domain with those in the electrolyte domain. To be precise, we first update the electron and hole densities. This would require the densities of the reductant and the oxidant at the semiconductor-electrolyte interface Σ , in the interface conditions (2.4.7) and (2.4.8). We use the $k-1$ step values of these densities, ρ_r^{k-1} and ρ_o^{k-1} . Therefore, we solve for (ρ_n^k, ρ_p^k) from:

$$\begin{aligned} (w_n, \rho_n^k)_{\Omega_S} + \Delta t_k \mathcal{L}_{n,S} (w_n, \mathbf{w}_n; \rho_n^k, \mathbf{q}_n^k) + \Delta t_k \langle w_n, I_{et}(\rho_n^k, \rho_o^{k-1}) \rangle_{\mathcal{E}_\Sigma^S} \\ = (w_n, \rho_n^{k-1})_{\Omega_S} + \Delta t_k \langle w_n, I_{et}(\rho_n^e, \rho_o^{k-1}) \rangle_{\mathcal{E}_\Sigma^S} \\ - \Delta t_k (w_n, \tilde{R}(\rho_n^{k-1}, \rho_p^{k-1}))_{\Omega_S} + \Delta t_k \langle w_n, \sigma_n \rho_n^e \rangle_{\mathcal{E}_D^S}, \end{aligned} \quad (3.4.2)$$

$$\mathcal{A}_{n,S} (w_n, \mathbf{w}_n; \rho_n^k, \mathbf{q}_n^k) - (\mathbf{w}_n, \alpha_n \mathbf{E}^{k-1} \rho_n^k)_{\Omega_S} = - \langle \mathbf{n} \cdot \mathbf{w}_n, \rho_n^e \rangle_{\mathcal{E}_D^S}, \quad (3.4.3)$$

$$\begin{aligned} (w_p, \rho_p^k)_{\Omega_S} + \Delta t_k \mathcal{L}_{p,S} (w_p, \mathbf{w}_p; \rho_p^k, \mathbf{q}_p^k) + \Delta t_k \langle w_p, I_{ht}(\rho_p^k, \rho_r^{k-1}) \rangle_{\mathcal{E}_\Sigma^S} \\ = (w_p, \rho_p^{k-1})_{\Omega_S} + \Delta t_k \langle w_p, I_{ht}(\rho_p^e, \rho_r^{k-1}) \rangle_{\mathcal{E}_\Sigma^S} \\ - \Delta t_k (w_p, \tilde{R}(\rho_n^{k-1}, \rho_p^{k-1}))_{\Omega_S} + \Delta t_k \langle w_p, \sigma_p \rho_p^e \rangle_{\mathcal{E}_D^S}, \end{aligned} \quad (3.4.4)$$

$$\mathcal{A}_{p,S} (w_p, \mathbf{w}_p; \rho_p^k, \mathbf{q}_p^k) - (\mathbf{w}_p, \alpha_p \mathbf{E}^{k-1} \rho_p^k)_{\Omega_S} = - \langle \mathbf{n} \cdot \mathbf{w}_p, \rho_p^e \rangle_{\mathcal{E}_D^S}. \quad (3.4.5)$$

Here the diffusion terms are treated implicitly, the drift terms are treated implicitly, while the recombination-generation terms (which is now incorporated into the function \tilde{R}) are treated explicitly.

Now that we have obtained the electron and hole densities at step k , (ρ_n^k, ρ_p^k) , we can use these values in the interface conditions (2.4.9) to update the reductant density:

$$\begin{aligned} & (w_r, \rho_r^k)_{\Omega_E} + \Delta t_k \mathcal{L}_{r,E} (w_r, \mathbf{w}_r; \rho_r^k, \mathbf{q}_r^k) + \Delta t_k \langle w_r, I_{ht}(\rho_p^k - \rho_p^e, \rho_r^k) \rangle_{\mathcal{E}_\Sigma^E} \\ &= (w_r, \rho_r^{k-1})_{\Omega_E} + \Delta t_k \langle w_r, I_{et}(\rho_n^k - \rho_n^e, \rho_o^k) \rangle_{\mathcal{E}_\Sigma^E} + \Delta t_k \langle w_r, \sigma_r \rho_r^\infty \rangle_{\mathcal{E}_D^E}, \end{aligned} \quad (3.4.6)$$

$$\mathcal{A}_{r,E} (w_r, \mathbf{w}_r; \rho_r^k, \mathbf{q}_r^k) - (\mathbf{w}_r, \alpha_r \mathbf{E}^{k-1} \rho_r^k)_{\Omega_E} = -\langle \mathbf{n} \cdot \mathbf{w}_r, \rho_r^\infty \rangle_{\mathcal{E}_D^E}. \quad (3.4.7)$$

With the updated values $(\rho_n^k, \rho_p^k, \rho_r^k)$, we can now update the oxidant density following the equations:

$$\begin{aligned} & (w_o, \rho_o^k)_{\Omega_E} + \Delta t_k \mathcal{L}_{o,E} (w_o, \mathbf{w}_o; \rho_o^k, \mathbf{q}_o^k) + \Delta t_k \langle w_o, I_{et}(\rho_p^k - \rho_p^e, \rho_o^k) \rangle_{\mathcal{E}_\Sigma^E} \\ &= (w_o, \rho_o^{k-1})_{\Omega_E} + \Delta t_k \langle w_o, I_{ht}(\rho_p^k - \rho_p^e, \rho_r^k) \rangle_{\mathcal{E}_\Sigma^E} + \Delta t_k \langle w_o, \sigma_o \rho_o^\infty \rangle_{\mathcal{E}_D^E}, \end{aligned} \quad (3.4.8)$$

$$\mathcal{A}_{o,E} (w_o, \mathbf{w}_o; \rho_o^k, \mathbf{q}_o^k) - (\mathbf{w}_o, \alpha_o \mathbf{E}^{k-1} \rho_o^k)_{\Omega_E} = -\langle \mathbf{n} \cdot \mathbf{w}_o, \rho_o^\infty \rangle_{\mathcal{E}_D^E}. \quad (3.4.9)$$

The flow of the AS-IMIMEX algorithm is summarized in Algorithm 1. The corresponding linear systems for the degrees of freedom for each of the carriers will have the same form. In order to simplify the presentation we will only display the linear system corresponding to the drift diffusion equations for electrons. Substituting in (3.3.16) and (3.3.17) into (3.4.2) and (3.4.3) results

in the linear system for the degrees of freedom vectors (which we denote by the same symbols),

$$\begin{bmatrix} M + \Delta t_k P + \Delta t_k K & \Delta t_k C^T \\ C + F & J \end{bmatrix} \begin{bmatrix} \rho_n(\cdot, t^k) \\ \mathbf{q}_n(\cdot, t^k) \end{bmatrix} = \begin{bmatrix} \mathbf{G}_1(t^{k-1}) \\ \mathbf{G}_2(t^{k-1}) \end{bmatrix}. \quad (3.4.10)$$

The matrices M, P, C, C^T and J are constant in time and correspond to,

$$M \Leftarrow (w_n, \rho_n^k)_{\Omega_S} \quad (3.4.11)$$

$$P \Leftarrow \langle [\![w_n]\!], \sigma_n [\![\rho_n^k]\!] \rangle_{\mathcal{E}_h^{i,S}} + \langle w_n, \sigma_n \rho_n^k \rangle_{\mathcal{E}_D^S} \quad (3.4.12)$$

$$J \Leftarrow (\mathbf{w}_n, \mu_n^{-1} \mathbf{q}_n^k)_{\Omega_S} \quad (3.4.13)$$

$$C^T \Leftarrow -(\nabla w_n, \mathbf{q}_n^k)_{\Omega_S} + \langle [\![w_n]\!], \{ \mathbf{q}_n^k \} - [\![\mathbf{q}_n^k]\!] \boldsymbol{\beta} \rangle_{\mathcal{E}_h^{i,S}} + \langle w_n, \mathbf{n} \cdot \mathbf{q}_n^k \rangle_{\mathcal{E}_D^S} \quad (3.4.14)$$

$$C \Leftarrow -(\nabla \cdot \mathbf{w}_n, \rho_n^k)_{\Omega_S} + \langle [\![\mathbf{w}_n]\!], \{ \rho_n^k \} + \boldsymbol{\beta} \cdot [\![\rho_n^k]\!] \rangle_{\mathcal{E}_h^{i,S}} + \langle w_n, \rho_n^k \rangle_{\mathcal{E}_N^S \cup \mathcal{E}_\Sigma^S} \quad (3.4.15)$$

The matrices F and K and correspond to,

$$F \Leftarrow - (w_n, \alpha_n \mathbf{E}^{k-1} \rho_n^k)_{\Omega_S} \quad (3.4.16)$$

$$K \Leftarrow \langle w_n, I_{et}(\rho_n^k, \rho_o^{k-1}) \rangle_{\mathcal{E}_\Sigma^S} \quad (3.4.17)$$

These two matrices must be assembled at every time step to incorporate changes in \mathbf{E} as well as in ρ_o . The right hand sides $\mathbf{G}_1(t)$ and $\mathbf{G}_2(t)$ are vectors that incorporate the boundary and interface conditions as well as the right-hand side of drift diffusion equations,

$$\begin{aligned} \mathbf{G}_1 \Leftarrow & (w_n, \rho_n^{k-1})_{\Omega_S} + \Delta t_k \langle w_n, I_{kt}(\rho_n^e, \rho_o^{k-1}) \rangle_{\mathcal{E}_\Sigma^S} - \Delta t_k (w_n, \tilde{R}(\rho_n^{k-1}, \rho_p^{k-1}))_{\Omega_S} \\ & + \Delta t_k \langle w_n, \sigma_n \rho_n^e \rangle_{\mathcal{E}_D^S} \end{aligned} \quad (3.4.18)$$

$$\mathbf{G}_2 \Leftarrow - \langle \mathbf{n} \cdot \mathbf{w}_n, \rho_n^e \rangle_{\mathcal{E}_D^S}, \quad (3.4.19)$$

These vectors must be assembled at every time step.

Our experience in the numerical experiments is that the use of implicit time stepping for the diffusion terms allows us to use time steps that are a few order of magnitude greater than what an explicit scheme, for instance the adaptive forward Euler scheme, on the diffusion terms would allow. However, treating the drift term implicitly is very expensive. This is because the electric field changes at every time step. Therefore, we have to update (3.4.16) in each of the LDG matrices at each time step of the calculation. As will be discussed further in Section 5.2.1, assembling and factorizing the LDG matrices take up a significant portion of the run-time.

Algorithm 1 The AS-IMIMEX [resp. AS-IMEXEX] Algorithm

- 1: Initialize the density data $(\rho_n^0, \rho_p^0, \rho_r^0, \rho_o^0)$; set $t_0 = 0$; set $k = 1$;
 - 2: **while** not reaching steady state **do**
 - 3: Solve the Poisson problem (3.4.1) for $(\Phi^{k-1}, \mathbf{E}^{k-1})$ using $(\rho_n^{k-1}, \rho_p^{k-1}, \rho_r^{k-1}, \rho_o^{k-1})$ as data.
 - 4: Determine Δt_k from the CFL condition with \mathbf{E}^{k-1} and $(\rho_n^{k-1}, \rho_p^{k-1}, \rho_r^{k-1}, \rho_o^{k-1})$.
 - 5: Update electron and hole densities from (3.4.2)-(3.4.5) [resp. (3.4.20)-(3.4.23)].
 - 6: Update reductant density from (3.4.6)-(3.4.7) [resp. (3.4.24)-(3.4.25)] using (ρ_n^k, ρ_p^k) .
 - 7: Update oxidant density from (3.4.8)-(3.4.9) [resp. (3.4.26)-(3.4.27)] using $(\rho_n^k, \rho_p^k, \rho_r^k)$.
 - 8: $t_k = t_{k-1} + \Delta t_k$, $k = k + 1$
 - 9: **end while**
-

3.4.2 The Implicit-Explicit-Explicit Alternating Schwarz Scheme

The implicit-explicit-explicit alternating Schwarz (AS-IMEXEX)

scheme is similar to the AS-IMIMEX scheme in the previous section. The only difference is that here we treat the drift terms in the drift-diffusion equations explicitly in time. That is, the charge densities in the drift terms are taken as there values at the previous step $k - 1$, not the current k .

The algorithm works as follows. At time step k , we first solve the Poisson equation (3.4.1) for $(\Phi^{k-1}, \mathbf{E}^{k-1})$. We then update the electron and hole densities as in the AS-IMIMEX scheme, but treat the drift terms explicitly to get (ρ_n^k, ρ_p^k) :

$$\begin{aligned} (w_n, \rho_n^k)_{\Omega_S} + \Delta t_k \mathcal{L}_{n,S} (w_n, \mathbf{w}_n; \rho_n^k, \mathbf{q}_n^k) + \Delta t_k \langle w_n, I_{et}(\rho_n^k, \rho_o^{k-1}) \rangle_{\mathcal{E}_\Sigma^S} \\ = (w_n, \rho_n^{k-1})_{\Omega_S} + \Delta t_k \langle w_n, I_{et}(\rho_n^e, \rho_o^{k-1}) \rangle_{\mathcal{E}_\Sigma^S} \\ - \Delta t_k (w_n, \tilde{R}(\rho_n^{k-1}, \rho_p^{k-1}))_{\Omega_S} + \Delta t_k \langle w_n, \sigma_n \rho_n^e \rangle_{\mathcal{E}_D^S}, \end{aligned} \quad (3.4.20)$$

$$\mathcal{A}_{n,S} (w_n, \mathbf{w}_n; \rho_n^k, \mathbf{q}_n^k) = (\mathbf{w}_n, \alpha_n \mathbf{E}^{k-1} \rho_n^{k-1})_{\Omega_S} - \langle \mathbf{n} \cdot \mathbf{w}_n, \rho_n^e \rangle_{\mathcal{E}_D^S}, \quad (3.4.21)$$

$$\begin{aligned} (w_p, \rho_p^k)_{\Omega_S} + \Delta t_k \mathcal{L}_{p,S} (w_p, \mathbf{w}_p; \rho_p^k, \mathbf{q}_p^k) + \Delta t_k \langle w_p, I_{ht}(\rho_p^k, \rho_r^{k-1}) \rangle_{\mathcal{E}_\Sigma^S} \\ = (w_p, \rho_p^{k-1})_{\Omega_S} + \Delta t_k \langle w_p, I_{ht}(\rho_p^e, \rho_r^{k-1}) \rangle_{\mathcal{E}_\Sigma^S} \\ - \Delta t_k (w_p, \tilde{R}(\rho_n^{k-1}, \rho_p^{k-1}))_{\Omega_S} + \Delta t_k \langle w_p, \sigma_p \rho_p^e \rangle_{\mathcal{E}_D^S}, \end{aligned} \quad (3.4.22)$$

$$\mathcal{A}_{p,S} (w_p, \mathbf{w}_p; \rho_p^k, \mathbf{q}_p^k) = (w_p, \alpha_p \mathbf{E}^{k-1} \rho_p^{k-1})_{\Omega_S} - \langle \mathbf{n} \cdot \mathbf{w}_p, \rho_p^e \rangle_{\mathcal{E}_D^S}. \quad (3.4.23)$$

Now that we have obtained the electron and hole densities at step k , (ρ_n^k, ρ_p^k) ,

we can use these values to update the reductant density:

$$\begin{aligned} & (w_r, \rho_r^k)_{\Omega_E} + \Delta t_k \mathcal{L}_{r,E} (w_r, \mathbf{w}_r; \rho_r^k, \mathbf{q}_r^k) + \Delta t_k \langle w_r, I_{ht}(\rho_p^k - \rho_p^e, \rho_r^k) \rangle_{\mathcal{E}_\Sigma^E} \\ &= (w_r, \rho_r^{k-1})_{\Omega_E} + \Delta t_k \langle w_r, I_{et}(\rho_n^k - \rho_n^e, \rho_o^k) \rangle_{\mathcal{E}_\Sigma^E} + \Delta t_k \langle w_r, \sigma_r \rho_r^\infty \rangle_{\mathcal{E}_D^E}, \end{aligned} \quad (3.4.24)$$

$$\mathcal{A}_{r,E} (w_r, \mathbf{w}_r; \rho_r^k, \mathbf{q}_r^k) = (\mathbf{w}_r, \alpha_r \mathbf{E}^{k-1} \rho_r^{k-1})_{\Omega_E} - \langle \mathbf{n} \cdot \mathbf{w}_r, \rho_r^\infty \rangle_{\mathcal{E}_D^E}. \quad (3.4.25)$$

Note again that the drift term is treated explicitly here. With the updated values $(\rho_n^k, \rho_p^k, \rho_r^k)$, we can now update the oxidant density following the equations:

$$\begin{aligned} & (w_o, \rho_o^k)_{\Omega_E} + \Delta t_k \mathcal{L}_{o,E} (w_o, \mathbf{w}_o; \rho_o^k, \mathbf{q}_o^k) + \Delta t_k \langle w_o, I_{et}(\rho_n^k - \rho_n^e, \rho_o^k) \rangle_{\mathcal{E}_\Sigma^E} \\ &= (w_o, \rho_o^{k-1})_{\Omega_E} + \Delta t_k \langle w_o, I_{ht}(\rho_p^k - \rho_p^e, \rho_r^k) \rangle_{\mathcal{E}_\Sigma^E} + \Delta t_k \langle w_o, \sigma_o \rho_o^\infty \rangle_{\mathcal{E}_D^E}, \end{aligned} \quad (3.4.26)$$

$$\mathcal{A}_{o,E} (w_o, \mathbf{w}_o; \rho_o^k, \mathbf{q}_o^k) = (\mathbf{w}_o, \alpha_o \mathbf{E}^{k-1} \rho_o^{k-1})_{\Omega_E} - \langle \mathbf{n} \cdot \mathbf{w}_o, \rho_o^\infty \rangle_{\mathcal{E}_D^E}. \quad (3.4.27)$$

The overall flow of the AS-IMEXEX algorithm is identical to that of the AS-IMIMEX algorithm, and is summarized in Algorithm 1, in the brackets. Upon substituting in (3.3.16) and (3.3.17) into (3.4.20) and (3.4.21) results in the linear system for the degrees of freedom vectors (which we denote by the same symbols),

$$\begin{bmatrix} M + \Delta t_k P + \Delta t_k K & \Delta t_k C^T \\ C & J \end{bmatrix} \begin{bmatrix} \rho_n(\cdot, t^k) \\ \mathbf{q}_n(\cdot, t^k) \end{bmatrix} = \begin{bmatrix} \mathbf{G}_1(t^{k-1}) \\ \mathbf{G}_2(t^{k-1}) \end{bmatrix}. \quad (3.4.28)$$

The matrices M, P, C, C^T, J, K and vector \mathbf{G}_1 are the same as in the AS-IMIMEX method. However, the right hand side vector \mathbf{G}_2 is now,

$$\mathbf{G}_2 \leftarrow (w_n, \alpha_n \mathbf{E}^{k-1} \rho_n^{k-1})_{\Omega_S} - \langle \mathbf{n} \cdot \mathbf{w}_n, \rho_n^e \rangle_{\mathcal{E}_D^S}. \quad (3.4.29)$$

As discussed in Section 5.2.1, numerical experiments showed that treating the drift term explicitly, as in (3.4.29), saves significant computational cost overall.

3.4.3 The Implicit-Explicit-Explicit Parallel Schwarz Scheme

In the implicit-explicit-explicit parallel Schwarz (PS-IMEXEX) scheme, we treat the diffusion terms implicitly, the drift terms explicitly, and the recombination-generation term explicitly. This is the same as was done in the AS-IMEXEX scheme. The difference here is that we now treat the reactive interface conditions explicitly in all the drift-diffusion equations. This way, all four drift-diffusion equations are decoupled from each other and can be solved simultaneously in parallel. To be precise, we use the values of all the densities at time step $k - 1$ in the functions I_{et} and I_{ht} in interface conditions (2.4.7)-(2.4.10) to update the values of the densities simultaneously to the current time step:

$$\begin{aligned} (w_n, \rho_n^k)_{\Omega_S} + \Delta t \mathcal{L}_{n,S} (w_n, \mathbf{w}_n; \rho_n^k, \mathbf{q}_n^k) \\ = (w_n, \rho_n^{k-1})_{\Omega_S} - \Delta t \langle w_n, I_{et}(\rho_n^{k-1} - \rho_n^e, \rho_o^{k-1}) \rangle_{\mathcal{E}_\Sigma^S} \\ - \Delta t (w_n, \tilde{R}(\rho_n^{k-1}, \rho_p^{k-1}))_{\Omega_S} + \Delta t_k \langle w_n, \sigma_n \rho_n^e \rangle_{\mathcal{E}_D^S}, \end{aligned} \quad (3.4.30)$$

$$\mathcal{A}_{n,S} (w_n, \mathbf{w}_n; \rho_n^k, \mathbf{q}_n^k) = (\mathbf{w}_n, \alpha_n \mathbf{E}^{k-1} \rho_n^{k-1})_{\Omega_S} - \langle \mathbf{n} \cdot \mathbf{w}_n, \rho_n^e \rangle_{\mathcal{E}_D^S}, \quad (3.4.31)$$

$$\begin{aligned} (w_p, \rho_p^k)_{\Omega_S} + \Delta t \mathcal{L}_{p,S} (w_p, \mathbf{w}_p; \rho_p^k, \mathbf{q}_p^k) \\ = (w_p, \rho_p^{k-1})_{\Omega_S} - \Delta t \langle w_p, I_{ht}(\rho_p^{k-1} - \rho_p^e, \rho_r^{k-1}) \rangle_{\mathcal{E}_\Sigma^S} \\ - \Delta t (w_p, \tilde{R}(\rho_n^{k-1}, \rho_p^{k-1}))_{\Omega_S} + \Delta t_k \langle w_p, \sigma_p \rho_p^e \rangle_{\mathcal{E}_D^S}, \end{aligned} \quad (3.4.32)$$

$$\mathcal{A}_{p,S} (w_p, \mathbf{w}_p; \rho_p^k, \mathbf{q}_p^k) = (\mathbf{w}_p \alpha_p \mathbf{E}^{k-1} \rho_p^{k-1})_{\Omega_S} - \langle \mathbf{n} \cdot \mathbf{w}_p, \rho_p^e \rangle_{\mathcal{E}_D^S}, \quad (3.4.33)$$

$$\begin{aligned} (w_r, \rho_r^k)_{\Omega_E} + \Delta t \mathcal{L}_{r,E} (w_r, \mathbf{w}_r; \rho_r^k, \mathbf{q}_r^k) \\ = (w_r, \rho_r^{k-1})_{\Omega_E} + \Delta t_k \langle w_r, \sigma_r \rho_r^\infty \rangle_{\mathcal{E}_D^E} \\ - \Delta t \langle w_r, I_{ht}(\rho_p^{k-1} - \rho_p^e, \rho_r^{k-1}) - I_{et}(\rho_n^{k-1} - \rho_n^e, \rho_o^{k-1}) \rangle_{\mathcal{E}_\Sigma^E}, \end{aligned} \quad (3.4.34)$$

$$\mathcal{A}_{r,E} (w_r, \mathbf{w}_r; \rho_r^k, \mathbf{q}_r^k) = (\mathbf{w}_r \alpha_r \mathbf{E}^{k-1} \rho_r^{k-1})_{\Omega_E} - \langle \mathbf{n} \cdot \mathbf{w}_r, \rho_r^\infty \rangle_{\mathcal{E}_D^E}, \quad (3.4.35)$$

$$\begin{aligned} (w_o, \rho_o^k)_{\Omega_E} + \Delta t \mathcal{L}_{o,E} (w_o, \mathbf{w}_o; \rho_o^k, \mathbf{q}_o^k) \\ = (w_o, \rho_o^{k-1})_{\Omega_E} + \Delta t_k \langle w_o, \sigma_o \rho_o^\infty \rangle_{\mathcal{E}_D^E} \\ - \Delta t \langle w_o, I_{et}(\rho_n^{k-1} - \rho_n^e, \rho_o^{k-1}) - I_{ht}(\rho_p^{k-1} - \rho_p^e, \rho_r^{k-1}) \rangle_{\mathcal{E}_\Sigma^E}, \end{aligned} \quad (3.4.36)$$

$$\mathcal{A}_{o,E} (w_o, \mathbf{w}_o; \rho_o^k, \mathbf{q}_o^k) = (\mathbf{w}_o \alpha_o \mathbf{E}^{k-1} \rho_o^{k-1})_{\Omega_E} - \langle \mathbf{n} \cdot \mathbf{w}_o, \rho_o^\infty \rangle_{\mathcal{E}_D^E}. \quad (3.4.37)$$

The PS-IMEXEX algorithm is summarized in Algorithm 2. Upon substituting in (3.3.16) and (3.3.17) into (3.4.30) and (3.4.31) results in the linear system for the degrees of freedom vectors (which we denote by the same symbols),

$$\begin{bmatrix} M + \Delta t_k P & \Delta t_k C^T \\ C & J \end{bmatrix} \begin{bmatrix} \rho_n(\cdot, t^k) \\ \mathbf{q}_n(\cdot, t^k) \end{bmatrix} = \begin{bmatrix} \mathbf{G}_1(t^{k-1}) \\ \mathbf{G}_2(t^{k-1}) \end{bmatrix}. \quad (3.4.38)$$

The matrices M, P, C, C^T and J are the same as in the AS-IMIMEX method. The right hand side vector \mathbf{G}_2 is the same as in the AS-IMEXEX method (3.4.29). However, the right hand side vector \mathbf{G}_1 is now,

$$\begin{aligned} \mathbf{G}_1 \Leftarrow (w_n, \rho_n^{k-1})_{\Omega_S} - \Delta t_k (w_n, \widetilde{R}(\rho_n^{k-1}, \rho_p^{k-1}))_{\Omega_S} + \Delta t_k \langle w_n, \sigma_n \rho_n^e \rangle_{\mathcal{E}_D^S} \\ - \Delta t_k \langle w_n, I_{et}(\rho_n^{k-1} - \rho_n^e, \rho_o^{k-1}) \rangle_{\mathcal{E}_\Sigma^S} \end{aligned} \quad (3.4.39)$$

Note that due to the fact that all the nonlinear terms are treated explicitly if we choose a constant time step $\Delta t_k = \Delta t$, then we only need to factorize the system matrix once at the beginning of this algorithm.

Algorithm 2 The PS-IMEXEX Algorithm

- 1: Initialize the density data $(\rho_n^0, \rho_p^0, \rho_r^0, \rho_o^0)$; set $t_0 = 0$; set $k = 1$;
 - 2: Determine Δt from the CFL condition;
 - 3: **while** not reaching steady state **do**
 - 4: Solve the Poisson problem (3.4.1) for $(\Phi^{k-1}, \mathbf{E}^{k-1})$ using $(\rho_n^{k-1}, \rho_p^{k-1}, \rho_r^{k-1}, \rho_o^{k-1})$ as data;
 - 5: Update the densities from (3.4.30)-(3.4.37) using \mathbf{E}^{k-1} and $(\rho_n^{k-1}, \rho_p^{k-1}, \rho_r^{k-1}, \rho_o^{k-1})$ as data;
 - 6: $t_k = t_{k-1} + \Delta t$, $k = k + 1$;
 - 7: **end while**
-

3.4.4 The Two-Scale Implicit-Explicit-Explicit Parallel Schwarz Scheme

In the PS-IMEXEX algorithm, we choose a fixed time step Δt even though it can be calculated in an adaptive manner. In our numerical experiments, we observe that we can take a Δt that is much larger than the one that we calculated using the CFL condition for the drift-diffusion equations in the semiconductor system (mainly based on the operator pairs $(\mathcal{L}_n, \mathcal{A}_n)$ and $(\mathcal{L}_p, \mathcal{A}_p)$). Intuitively, this is due to the fact that the characteristic time scale for the semiconductor drift-diffusion system and that for the electrolyte drift-diffusion system are quite different. In general, the electrolyte system evolves at a much slower pace than the semiconductor system. To take advantage of this scale separation, we implemented the two-scale PS-IMEXEX (TsPS-IMEXEX) algorithm. The main idea here is to update quantities in the

semiconductor domain more frequently than the quantities in the electrolyte domain.

Let Δt_s and Δt_e be the time steps given by the CFL conditions in the semiconductor and electrolyte domains respectively. Let K be the positive integer such that $\Delta t_e = K\Delta t_s$. At time step k , we first solve the Poisson equation (3.4.1) to get $(\Phi^{k-1}, \mathbf{E}^{k-1})$. We then perform K time steps for the semiconductor system, starting with the initial condition $(\tilde{\rho}_n^0, \tilde{\rho}_p^0) = (\rho_n^{k-1}, \rho_p^{k-1})$:

$$\begin{aligned} & (w_n, \tilde{\rho}_n^j)_{\Omega_S} + \Delta t_s \mathcal{L}_{n,S} (w_n, \mathbf{w}_n; \tilde{\rho}_n^j, \tilde{\mathbf{q}}_n^j) \\ &= (w_n, \rho_n^{j-1})_{\Omega_S} - \Delta t_s \langle w_n, I_{et}(\tilde{\rho}_n^{j-1} - \rho_n^e, \rho_o^{k-1}) \rangle_{\mathcal{E}_\Sigma^S} \\ & \quad - \Delta t_s (w_n, \tilde{R}(\tilde{\rho}_n^{j-1}, \tilde{\rho}_p^{j-1}))_{\Omega_S} + \Delta t_s \langle w_n, \sigma_n \rho_n^e \rangle_{\mathcal{E}_D^S}, \end{aligned} \quad (3.4.40)$$

$$\mathcal{A}_{n,S} (w_n, \mathbf{w}_n; \tilde{\rho}_n^j, \tilde{\mathbf{q}}_n^j) = (\mathbf{w}_n, \alpha_n \mathbf{E}^{k-1} \tilde{\rho}_n^{j-1})_{\Omega_S} - \langle \mathbf{n} \cdot \mathbf{w}_n, \rho_n^e \rangle_{\mathcal{E}_D^S}, \quad (3.4.41)$$

$$\begin{aligned} & (w_p, \tilde{\rho}_p^j)_{\Omega_S} + \Delta t_s \mathcal{L}_{p,S} (w_p, \mathbf{w}_p; \tilde{\rho}_p^j, \tilde{\mathbf{q}}_p^j) \\ &= (w_p, \tilde{\rho}_p^{j-1})_{\Omega_S} - \Delta t_s \langle w_p, I_{ht}(\tilde{\rho}_p^{j-1} - \rho_p^e, \rho_r^{k-1}) \rangle_{\mathcal{E}_\Sigma^S} \\ & \quad - \Delta t_s (w_p, \tilde{R}(\tilde{\rho}_n^{j-1}, \tilde{\rho}_p^{j-1}))_{\Omega_S} + \Delta t_s \langle w_p, \sigma_p \rho_p^e \rangle_{\mathcal{E}_D^S}, \end{aligned} \quad (3.4.42)$$

$$\mathcal{A}_{p,S} (w_p, \mathbf{w}_p; \tilde{\rho}_p^j, \tilde{\mathbf{q}}_p^j) = (\mathbf{w}_p, \alpha_p \mathbf{E}^{k-1} \tilde{\rho}_p^{j-1})_{\Omega_S} - \langle \mathbf{n} \cdot \mathbf{w}_p, \rho_p^e \rangle_{\mathcal{E}_D^S}, \quad (3.4.43)$$

Note that the values for the densities of the reductants and the oxidants are kept unchanged during this iteration.

We then set $(\rho_n^{k-1}, \rho_p^{k-1}) = (\tilde{\rho}_n^K, \tilde{\rho}_p^K)$, and update the density values of the reductants and the oxidants using time step Δt_e following (3.4.24)-(3.4.27),

that is:

$$\begin{aligned}
(w_r, \rho_r^k)_{\Omega_E} + \Delta t_e \mathcal{L}_{r,E} (w_r, \mathbf{w}_r; \rho_r^k, \mathbf{q}_r^k) \\
= (w_r, \rho_r^{k-1})_{\Omega_E} + \Delta t_e \langle w_r, \sigma_r \rho_r^\infty \rangle_{\mathcal{E}_D^E} \\
- \Delta t_e \langle w_r, I_{ht}(\rho_p^{k-1} - \rho_p^e, \rho_r^{k-1}) - I_{et}(\rho_n^{k-1} - \rho_n^e, \rho_o^{k-1}) \rangle_{\mathcal{E}_\Sigma^E}, \quad (3.4.44)
\end{aligned}$$

$$\mathcal{A}_{r,E} (w_r, \mathbf{w}_r; \rho_r^k, \mathbf{q}_r^k) = (\mathbf{w}_r, \alpha_r \mathbf{E}^{k-1} \rho_r^{k-1})_{\Omega_E} - \langle \mathbf{n} \cdot \mathbf{w}_r, \rho_r^\infty \rangle_{\mathcal{E}_D^E}, \quad (3.4.45)$$

$$\begin{aligned}
(w_o, \rho_o^k)_{\Omega_E} + \Delta t_e \mathcal{L}_{o,E} (w_o, \mathbf{w}_o; \rho_o^k, \mathbf{q}_o^k) \\
= (w_o, \rho_o^{k-1})_{\Omega_E} + \Delta t_e \langle w_o, \sigma_o \rho_o^\infty \rangle_{\mathcal{E}_D^E} \\
- \Delta t_e \langle w_o, I_{et}(\rho_n^{k-1} - \rho_n^e, \rho_o^{k-1}) - I_{ht}(\rho_p^{k-1} - \rho_p^e, \rho_r^{k-1}) \rangle_{\mathcal{E}_\Sigma^E}, \quad (3.4.46)
\end{aligned}$$

$$\mathcal{A}_{o,E} (w_o, \mathbf{w}_o; \rho_o^k, \mathbf{q}_o^k) = (\mathbf{w}_o, \alpha_o \mathbf{E}^{k-1} \rho_o^{k-1})_{\Omega_E} - \langle \mathbf{n} \cdot \mathbf{w}_o, \rho_o^\infty \rangle_{\mathcal{E}_D^E}. \quad (3.4.47)$$

The algorithm is summarized in Algorithm 3 and the resulting linear systems are the same as in PS-IMEXEX. In the numerical simulations, we are relatively conservative on the selection of K . We take a K that is smaller than the one determined by Δt_s and Δt_e . We are able to significantly achieve faster simulations with K between 5 and 10, without sacrificing the accuracy and stability of the algorithm.

3.5 Overview of Numerical Software

We briefly review the development of the code base for numerical simulations of semiconductor-electrolyte interfaces. The codes can be broken up into two case: the code for one dimensional simulations and the code for two

Algorithm 3 The TsPS-IMEXEX Algorithm

- 1: Initialize the density data $(\rho_n^0, \rho_p^0, \rho_r^0, \rho_o^0)$; set $t_0 = 0$; set $k = 1$;
 - 2: Determine Δt_s from $(\mathcal{L}_{n,S}, \mathcal{A}_{n,S})$ and $(\mathcal{L}_{p,S}, \mathcal{A}_{p,S})$; determine Δt_e from $(\mathcal{L}_{r,E}, \mathcal{A}_{r,E})$ and $(\mathcal{L}_{o,E}, \mathcal{A}_{o,E})$; set $K = \Delta t_e / \Delta t_s$;
 - 3: **while** not reaching steady state **do**
 - 4: Solve the Poisson problem (3.4.1) for $(\Phi^{k-1}, \mathbf{E}^{k-1})$ using $(\rho_n^{k-1}, \rho_p^{k-1}, \rho_r^{k-1}, \rho_o^{k-1})$ as data;
 - 5: Set $(\tilde{\rho}_n^0, \tilde{\rho}_p^0) = (\rho_n^{k-1}, \rho_p^{k-1})$;
 - 6: **for** $j=0, \dots, K$ **do**
 - 7: Update the densities $(\tilde{\rho}_n, \tilde{\rho}_p)$ according to (3.4.40)-(3.4.43);
 - 8: **end for**
 - 9: Set $(\rho_n^{k-1}, \rho_p^{k-1}) = (\tilde{\rho}_n^K, \tilde{\rho}_p^K)$;
 - 10: Update the reductant and oxidant densities according to (3.4.44)-(3.4.47);
 - 11: $t_k = t_{k-1} + \Delta t_e$, $k = k + 1$;
 - 12: **end while**
-

dimensional simulations. Both codes, which are written in C++, use the same numerical methods and object oriented approach. Both codes are well tested and have user manual provided through the Doxygen [?] documentation generator. However, the codes do differ in their use of numerical libraries and data structures.

One key challenge for the development of these codes was mesh generation for the domain decomposition. We must ensure that the mesh does not have cells which intersect the semiconductor-electrolyte interface. Furthermore, the assembly of nonlinear coupling terms is greatly complicated by the domain decomposition and the introduction of multiple meshes. Specifically, the assembly of coupling terms between Poisson's equation and the charge carriers can be complicated if the quadrature points in the different meshes do

not coincide with one another. In such instances one must perform a search for overlapping cell between the two meshes and interpolate the desired variables. We avoided having to perform such operations by first creating meshes for the semiconductor and electrolyte subdomains separately and then merging the two together to form the mesh for Poisson’s equation. This is the reasoning for the constraint (3.1.13). This procedure guarantees that the cells between the semiconductor/electrolyte subdomains are the same as those for Poisson’s equation and assures they have the same quadrature points. Thus enforcing the constraint (3.1.13) in our code we avoid any search and interpolation of variables when constructing coupling terms between the drift-diffusion and Poisson equation. Similarly, if the constraint (3.1.14) is not satisfied then a search of the mesh faces and interpolation of the appropriate variables must be performed whenever one of the interface conditions (2.4.7)- (2.4.10) on an element face is assembled.

3.5.1 One Dimensional Code

The one dimensional code was developed from scratch and uses the minimal amount of dependencies. It uses Eigen [3] which is a linear algebra library written in C++. Eigen has a built in sparse direct solver, SparseLU [62, 100, 101], that is used to solve the linear systems for the mixed and LDG method. The GNU Scientific Library [5] is used for access to the Legendre polynomials which allow for calculations with basis functions of arbitrary order. Computationally intensive subroutines are parallelized using OpenMP [7]

if the library is present. All material and computational parameters (except for doping profiles) are read in through an input file by the Boost library [1]. This is useful for users to experiment with different parameter values without the need to recompile the code. CMake [2] is used as a build system allowing for the software to be platform independent and easy to install.

3.5.2 Two Dimensional Code

The two dimensional code is built using the deal.II finite element library [21, 22]. It has the additional dependency of CMake, and a visualization program which can read .vtu [8] format data files. The code uses deal.II's built in sparse linear algebra library and the sparse direct solver UMFPACK [54–57]. Assembly of matrices and vectors are computed in parallel using Intel Thread Building Blocks [6] for shared memory parallelization. All material and computational parameters (except for doping profiles) are again read in through an input file. CMake [2] is used as the build system of this code allowing for easy and platform independent installation. The main bottleneck in scalability of this code is the caused the sequential nature and large memory needs of the direct solver.

Chapter 4

Analysis Of Local Discontinuous Galerkin Methods

In this chapter we analyze the approximations to solutions of the mathematical model of semiconductor-electrolyte solar cells in two dimensions. We focus only on the transport of charges as well as their interaction at reactive interface. We do not consider the self-consistent interaction with the electric field. We first introduce the simplified model and then discuss notation, identities and theorems that will be used throughout this chapter. We introduce the primal form of the semidiscrete local discontinuous Galerkin method discussed in Chapter 3 and prove some necessary properties of it. Finally, we use the properties of the primal form to prove *a-priori* L^2 error estimates for semidiscrete local discontinuous Galerkin method developed for the semiconductor-electrolyte interface model.

4.1 Preliminaries

4.1.1 Model Properties

Remark 4.1.1. In Chapter 3 we developed approximations to the non-dimensional versions of the drift-diffusion equations. We now use a more general form of the equations. The reason being is that we require the carrier diffusion coeffi-

cient to bound the carrier velocity saturation constant. While this a stringent requirement, it is valid under low biases. Our results do not require that the electric field be divergence free. Requiring the electric field to be divergence free or other such constraints have been a requirement in other studies of LDG methods on reaction-convection-diffusion problems [15, 50, 126], but are not valid for the drift-diffusion-Poisson system.

Remark 4.1.2. We require that the electric field $\mathbf{E} \in H_{\text{div}}(\Omega_S) \cup H_{\text{div}}(\Omega_E)$. This enforces the fact that normal component of electric field is continuous across any interior element face,

$$[\![\mathbf{E}]\!] = 0 \quad \text{on } \mathcal{E}_h^{i,S} \cup \mathcal{E}_h^{i,E}. \quad (4.1.1)$$

However, we do not require the normal component of the electric field to be continuous across the semiconductor-electrolyte interface.

We define the cut-off operator \mathcal{M} as in [137, 138],

$$\mathcal{M}(w)(\mathbf{x}, \cdot) = \min(w(\mathbf{x}, \cdot), M), \quad (4.1.2)$$

where M is a large positive constant. Both interface conditions $I_{et}(\cdot, \cdot)$ and $I_{ht}(\cdot, \cdot)$ are bilinear functions and therefore locally Lipschitz in a bounded domain. We will use the cut-off operator, \mathcal{M} , to make the reactive interface conditions $I_{et}(\mathcal{M}(\cdot), \mathcal{M}(\cdot))$ and $I_{ht}(\mathcal{M}(\cdot), \mathcal{M}(\cdot))$ globally Lipschitz with Lipschitz constants $k_{et}M$ and $k_{ht}M$ respectively. We expect that the analytical problem admits a comparison principle. In such a case, the constant M can be taken, for example, to be a multiple of $\max(\rho_n^e, \rho_p^e, \rho_r^\infty, \rho_o^\infty)$.

We now introduce the simplified model of the transport of charges and their interaction at reactive interface. The reaction-transport systems for the electrons and holes in the semiconductor are,

$$\partial_t \rho_n + \nabla \cdot (\alpha_n \mu_n \mathbf{E} \rho_n - D_n \nabla \rho_n) = \tilde{R}(\rho_n, \rho_p) \quad \text{in } \Omega_S \times (0, T), \quad (4.1.3)$$

$$\mathbf{n}_{\Sigma^S} \cdot (\alpha_n \mu_n \mathbf{E} \rho_n - D_n \nabla \rho_n) = I_{et}(\mathcal{M}(\rho_n - \rho_n^e), \mathcal{M}(\rho_o)) \quad \text{on } \Sigma \times (0, T), \quad (4.1.4)$$

$$\mathbf{n} \cdot (\alpha_n \mu_n \mathbf{E} \rho_n - D_n \nabla \rho_n) = 0 \quad \text{on } \Gamma_{S,N} \times (0, T), \quad (4.1.5)$$

$$\rho_n = \rho_n^e \quad \text{on } \Gamma_{S,D} \times (0, T), \quad (4.1.6)$$

and,

$$\begin{aligned} \partial_t \rho_p + \nabla \cdot (\alpha_p \mu_p \mathbf{E} \rho_p - D_p \nabla \rho_p) &= \tilde{R}(\rho_n, \rho_p) \quad \text{in } \Omega_S \times (0, T), \\ \mathbf{n}_{\Sigma^S} \cdot (\alpha_p \mu_p \mathbf{E} \rho_p - D_p \nabla \rho_p) &= I_{ht}(\mathcal{M}(\rho_p - \rho_p^e), \mathcal{M}(\rho_r)), \quad \text{on } \Sigma \times (0, T), \\ \mathbf{n} \cdot (\alpha_p \mu_p \mathbf{E} \rho_p - D_p \nabla \rho_p) &= 0 \quad \text{on } \Gamma_{S,N} \times (0, T), \\ \rho_p &= \rho_p^e \quad \text{on } \Gamma_{S,D} \times (0, T). \end{aligned} \quad (4.1.7)$$

The reaction-transport equations for reductants and oxidants are,

$$\partial_t \rho_r + \nabla \cdot (\alpha_r \mu_r \mathbf{E} \rho_r - D_r \nabla \rho_r) = 0 \quad \text{in } \Omega_E \times (0, T),$$

$$\begin{aligned} \mathbf{n}_{\Sigma^E} \cdot (\alpha_r \mu_r \mathbf{E} \rho_r - D_r \nabla \rho_r) &= I_{ht}(\mathcal{M}(\rho_p - \rho_p^e), \mathcal{M}(\rho_r)) \\ &\quad - I_{et}(\mathcal{M}(\rho_n - \rho_n^e), \mathcal{M}(\rho_o)) \quad \text{on } \Sigma \times (0, T), \end{aligned}$$

$$\mathbf{n} \cdot (\alpha_r \mu_r \mathbf{E} \rho_r - D_r \nabla \rho_r) = 0 \quad \text{on } \Gamma_{E,N} \times (0, T),$$

$$\rho_r = \rho_r^\infty \quad \text{on } \Gamma_{E,D} \times (0, T),$$

and,

$$\begin{aligned}
\partial_t \rho_o + \nabla \cdot (\alpha_o \mu_o \mathbf{E} \rho_o - D_o \nabla \rho_o) &= 0 & \text{in } \Omega_E \times (0, T), \\
\mathbf{n}_{\Sigma^E} \cdot (\alpha_o \mu_o \mathbf{E} \rho_o - D_o \nabla \rho_o) &= \\
&\quad -I_{ht}(\mathcal{M}(\rho_p - \rho_p^e), \mathcal{M}(\rho_r)) \\
&\quad + I_{et}(\mathcal{M}(\rho_n - \rho_n^e), \mathcal{M}(\rho_o)) \quad \text{on } \Sigma \times (0, T), \\
\mathbf{n} \cdot (\alpha_o \mu_o \mathbf{E} \rho_o - D_o \nabla \rho_n) &= 0 & \text{on } \Gamma_{E,N} \times (0, T), \\
\rho_o &= \rho_o^\infty & \text{on } \Gamma_{E,D} \times (0, T). \\
\end{aligned} \tag{4.1.8}$$

The initial conditions are taken to be,

$$\begin{aligned}
\rho_n &= \rho_n^e, & \rho_p &= \rho_p^e & \text{in } \Omega_S \times \{t = 0\}, \\
\rho_r &= \rho_r^\infty, & \rho_o &= \rho_o^\infty & \text{in } \Omega_E \times \{t = 0\}.
\end{aligned} \tag{4.1.9}$$

Remark 4.1.3. In the semiconductor domain we assume that our model includes velocity saturation effects through the definition of $\mu(\mathbf{E})$. This insures that our drift-component of transport is bounded,

$$\lim_{\|\mathbf{E}\|_{L^\infty} \rightarrow \infty} \|\mu_n(\mathbf{E}) \mathbf{E}\|_{L^\infty(\Omega_S)} = v_n^{\text{sat}}, \tag{4.1.10}$$

$$\lim_{\|\mathbf{E}\|_{L^\infty} \rightarrow \infty} \|\mu_p(\mathbf{E}) \mathbf{E}\|_{L^\infty(\Omega_S)} = v_p^{\text{sat}}. \tag{4.1.11}$$

While in the electrolyte the mobility does not have the property of being bounded in the mathematical form, the permittivity of electrolytes is extremely high and mobilities of the ions is very low so that the current is generally diffusion dominated [111].

We assume that the mobility function μ_c is a spatially continuous function for $c = \{n, p, r, o\}$. From Remark 4.1.3 we have that,

$$\|\alpha_c \mu_c \mathbf{E}\|_{L^\infty} \leq v_c^* < \infty \quad \text{for } c = n, p, r, o. \quad (4.1.12)$$

We require the diffusion tensors to be in continuous, invertible, and bounded. That is for $c = \{n, p\}$,

$$0 < D_{c,*} \leq D_c(\mathbf{x}) \leq D_c^* < \infty \quad \forall \mathbf{x} \in \Omega_S, \quad (4.1.13)$$

and for $c = \{r, o\}$,

$$0 < D_{c,*} \leq D_c(\mathbf{x}) \leq D_c^* < \infty \quad \forall \mathbf{x} \in \Omega_E, \quad (4.1.14)$$

The function $\tilde{R}(\rho_{n,h}, \rho_{p,h}) = -R(\rho_{n,h}, \rho_{p,h}) + \gamma G(\mathbf{x})$ is the same as was introduced in Chapter 3. We note that the form of Shockley-Reed-Hall recombination is a globally Lipschitz function. The proof of the following theorem can be found in Section A.1.1 of the Appendix.

Theorem 4.1.1 (Lipschitz Property of Recombination). *The function for Shockley-Reed-Hall recombination given in (2.2.21) is globally Lipschitz with respect to the norm $\|\cdot\|_{L^2(\Omega_S)}$ whenever $\rho_n(\cdot, t), \rho_p(\cdot, t) \in H^s(\Omega_S)$. In particular we have for almost every $t \in (0, T)$,*

$$\|R(\rho_n^1, \rho_p) - R(\rho_n^2, \rho_p)\|_{L^2(\Omega_S)}^2 \leq \frac{1}{\tau_n^2} \|(\rho_n^1, \rho_p) - (\rho_n^2, \rho_p)\|_{L^2(\Omega_S)}^2, \quad (4.1.15)$$

$$\|R(\rho_n, \rho_p^1) - R(\rho_n, \rho_p^2)\|_{L^2(\Omega_S)}^2 \leq \frac{1}{\tau_p^2} \|(\rho_n, \rho_p^1) - (\rho_n, \rho_p^2)\|_{L^2(\Omega_S)}^2, \quad (4.1.16)$$

and,

$$\|R(\rho_n^1, \rho_p^1) - R(\rho_n^2, \rho_p^2)\|_{L^2(\Omega_S)}^2 \leq C_R^2 \|(\rho_n^1, \rho_p^1) - (\rho_n^2, \rho_p^2)\|_{L^2(\Omega_S)}^2, \quad (4.1.17)$$

where $C_R^2 = \max\left(\frac{1}{\tau_n^2}, \frac{1}{\tau_p^2}\right)$.

Using Theorem 4.1.1 and fact that $G(\mathbf{x})$ given by (2.2.20) is independent of ρ_n and ρ_p , then function $\tilde{R}(\rho_{n,h}, \rho_{p,h})$ is a globally Lipschitz function on $\Omega_S \times (0, T)$.

4.1.2 Identities and Theorems

We continue to use the notation introduced in Section 3.1.2. Specifically, we use two triangulations, one for the semiconductor \mathcal{T}_h^S and one for the electrolyte \mathcal{T}_h^E . We now discuss some identities and theorems which we will use repeatedly throughout this chapter. The first few are standard inequalities [33, 85, 126],

Lemma 4.1.2 (Young's Inequality). *Let $a > 0$ and $b > 0$ then for any $\delta \geq 0$,*

$$ab \leq \frac{\delta}{2}a^2 + \frac{1}{2\delta}b^2. \quad (4.1.18)$$

Theorem 4.1.3 (Trace Theorem). *For a bounded domain Ω in \mathbb{R}^d with Lipschitz boundary $\partial\Omega$, there exist a bounded linear operator $T : H^1(\Omega) \rightarrow L^2(\partial\Omega)$ such that,*

$$\|Tw\|_{L^2(\partial\Omega)} \leq C_{tr} \|w\|_{H^1(\Omega)}, \quad (4.1.19)$$

where $C_{tr} = C_{tr}(\Omega) \in \mathbb{R}$.

Theorem 4.1.4 (Inverse Inequality). *Let Ω_e be a bounded domain in \mathbb{R}^d with diameter h_e . Then there exists a constant C_{inv} independent of h_e such that for any $w \in \mathcal{Q}_{k,k}(\Omega_e)$,*

$$\|\nabla^j w\|_{L^2(\Omega_e)} \leq C_{inv} h_e^{-j} \|w\|_{L^2(\Omega_e)} \quad \forall 0 \leq j \leq k. \quad (4.1.20)$$

Theorem 4.1.5 (Gronwall's Inequality). *Let f, g and h be piecewise continuous functions defined on interval $(0, T)$. Assume that g is a non-decreasing function and that there exists a positive constant C (independent of t) such that,*

$$f(t) + h(t) \leq g(t) + C \int_0^T f(s) ds \quad \forall t \in (0, T). \quad (4.1.21)$$

Then,

$$f(t) + h(t) \leq e^{CT} g(t) \quad \forall t \in (0, T). \quad (4.1.22)$$

Theorem 4.1.6 (Approximation Property). *Let Ω_e be a parallelogram. Let $w \in H^s(\Omega_e)$ for $s > 1$ and an integer $k \geq 0$. There exists a constant independent of w and h_e and a function $\tilde{w} \in \mathcal{Q}_{k,k}(\Omega_e)$ such that,*

$$\|w - \tilde{w}\|_{H^q(\Omega_e)} \leq C h_e^{\min(k+1, s)-q} |w|_{H^s(\Omega_e)}, \quad \forall 0 \leq q \leq s. \quad (4.1.23)$$

We will make frequent use of the following identity for functions in broken Sobolev spaces [12],

Lemma 4.1.7. For $w_h \in W_{h,k}^m$ and $\mathbf{w}_h \in \mathbf{W}_{h,k}^m$ ($m = S, E$),

$$\begin{aligned} \int_{\Omega_m} \nabla_h \cdot \mathbf{w} w dx &= - \int_{\Omega_m} \mathbf{w} \cdot \nabla_h w dx + \int_{\mathcal{E}_h^{i,m}} \llbracket \mathbf{w} \rrbracket \{w\} ds + \int_{\mathcal{E}_h^{i,m}} \{\mathbf{w}\} \cdot \llbracket w \rrbracket ds \\ &+ \int_{\mathcal{E}_D^m \cup \mathcal{E}_N^m \cup \mathcal{E}_\Sigma^m} \mathbf{n} \cdot \mathbf{w} w ds. \end{aligned} \quad (4.1.24)$$

Additionally, we will use the following inequalities for functions in broken Sobolev spaces [126],

Theorem 4.1.8 (Cauchy-Schwarz Inequality). Let $w_1, w_2 \in W_{h,k}^m$ ($m = S, E$) then,

$$\int_{\Omega_m} w_1 w_2 dx \leq \|w_1\|_{L^2(\mathcal{T}_h^m)} \|w_2\|_{L^2(\mathcal{T}_h^m)} \quad (4.1.25)$$

Theorem 4.1.9 (Poincare Inequality). For all $w \in W_{h,k}^m$ there exists a constant $C_P^m = C_P(\Omega_m) \in \mathbb{R}$ ($m = S, E$) such that,

$$\|w\|_{L^2(\mathcal{T}_h^m)} \leq C_P^m \|w\|_{DG,m}. \quad (4.1.26)$$

We define the lift operators [12, 85, 119], $\mathbf{r}^m : L^2(\mathcal{E}_h^{i,m}) \rightarrow \mathbf{W}_{h,k}^m$, $\mathbf{l}^m : L^2(\mathcal{E}_h^{i,m}) \rightarrow \mathbf{W}_{h,k}^m$ and $\mathbf{r}_D^m : L^2(\mathcal{E}_D^m) \rightarrow \mathbf{W}_{h,k}^m$ as,

$$\int_{\Omega_m} \mathbf{w} \cdot \mathbf{r}^m(w) dx = \int_{\mathcal{E}_h^{i,m}} \mathbf{n} \cdot \{\mathbf{w}\} w ds \quad \forall \mathbf{w} \in \mathbf{W}_{h,k}^m, \quad (4.1.27)$$

$$\int_{\Omega_m} \mathbf{w} \cdot \mathbf{l}^m(w) dx = - \int_{\mathcal{E}_h^{i,m}} \llbracket \mathbf{w} \rrbracket w ds \quad \forall \mathbf{w} \in \mathbf{W}_{h,k}^m, \quad (4.1.28)$$

$$\int_{\Omega_m} \mathbf{w} \cdot \mathbf{r}_D^m(w) dx = \int_{\mathcal{E}_D^m} \mathbf{n} \cdot \mathbf{w} w ds \quad \forall \mathbf{w} \in \mathbf{W}_{h,k}^m. \quad (4.1.29)$$

We will frequently use the following lemma whose proof can be found can be found in [12, 126]:

Lemma 4.1.10. *If $w \in W_{h,k}^m$ and $\beta \in \mathbb{R}^d$ be a vector that is not parallel to any element face in \mathcal{T}_h^m then,*

$$\begin{aligned} \|\mathbf{r}^m(\llbracket w \rrbracket) + \mathbf{l}^m(\beta \cdot \llbracket w \rrbracket) + \mathbf{r}_D(w)\|_{L^2(\mathcal{T}_h^m)} &\leq \\ C_{inv}^m C_{tr}^m \left(\|h^{-1/2}w\|_{L^2(\mathcal{E}_h^{i,m})} + \|h^{-1/2}w\|_{L^2(\mathcal{E}_D^m)} \right), \end{aligned} \quad (4.1.30)$$

Where C_{tr}^m and C_{inv}^m are the trace and inverse inequality constants respectively for $m = S, E$.

We prove the following inequality that will be needed for our error estimates:

Theorem 4.1.11 (Trace Theorem For Broken Sobolev Spaces). *Let $m = S, E$ and $s > 3/2$. For the bounded domain Ω_m with Lipschitz boundary $\partial\Omega_m$. Let \mathcal{T}_h^m be the triangulation of the domain Ω_m such that,*

$$\partial\Omega_m = \mathcal{E}_D^m \cup \mathcal{E}_N^m \cup \mathcal{E}_\Sigma. \quad (4.1.31)$$

Then there exists $C_{tr}^m \in \mathbb{R}^+$ such that,

$$\|w\|_{L^2(\mathcal{E}_\Sigma)} \leq C_{tr}^m (1 + C_P^m) \|w\|_{DG,m}, \quad \forall w \in H^s(\mathcal{T}_h^m) \quad (4.1.32)$$

Proof: Let $w \in H^s(\mathcal{T}_h^m)$ for $s > 3/2$ then by Theorem 4.1.3 and Theorem 4.1.9

we have,

$$\begin{aligned}
\|w\|_{L^2(\mathcal{E}_\Sigma)} &\leq \sum_{\substack{\Omega_e \in \mathcal{T}_h^m \\ \partial\Omega_e \in \mathcal{E}_\Sigma}} C_{\text{tr}} \|w\|_{H^1(\Omega_e)} \\
&\leq \sum_{\Omega_e \in \mathcal{T}_h^m} C_{\text{tr}}^m \|w\|_{H^1(\Omega_e)} \\
&= \sum_{\Omega_e \in \mathcal{T}_h^m} C_{\text{tr}}^m (\|w\|_{L^2(\Omega_e)} + \|\nabla w\|_{L^2(\Omega_e)}) \\
&\leq C_{\text{tr}}^m C_P^m \|w\|_{DG,m} + \sum_{\Omega_e \in \mathcal{T}_h^m} C_{\text{tr}}^m \|\nabla w\|_{L^2(\Omega_e)} \\
&\leq C_{\text{tr}}^m (1 + C_P^m) \|w\|_{DG,m}
\end{aligned} \tag{4.1.33}$$

□

4.2 Primal Form

The primal forms of the semidiscrete local discontinuous Galerkin methods for the problems in (4.1.3)- (4.1.8) are,

Find $\rho_{n,h}(\cdot, t), \rho_{p,h}(\cdot, t) \in W_{h,k}^S$ and $\rho_{r,h}(\cdot, t), \rho_{o,h}(\cdot, t) \in W_{h,k}^E$ such that,

$$\begin{aligned}
&(w_n, \partial_t \rho_{n,h})_{\Omega_S} + B_{n,S}(w_n, \rho_{n,h}) + \langle w, I_{et}(\mathcal{M}(\rho_{n,h} - \rho_n^e), \mathcal{M}(\rho_{o,h})) \rangle_{\mathcal{E}_\Sigma} \\
&= \left(w_n, \tilde{R}(\rho_{n,h}, \rho_{p,h}) \right)_{\Omega_S} + \langle w_n, \sigma_n \rho_n^e \rangle_{\mathcal{E}_D^S} \\
&\quad - D_n(-\nabla_h w_n + \mathbf{r}^S(\llbracket w_n \rrbracket) + \mathbf{l}^S(\boldsymbol{\beta} \cdot \llbracket w_n \rrbracket) + \mathbf{r}_D^S(w_n)), \mathbf{r}_D^S(\rho_n^e))_{\Omega_S},
\end{aligned} \tag{4.2.1}$$

$$(w_p, \partial_t \rho_{p,h})_{\Omega_S} + B_{p,S}(w_p, \rho_{p,h}) + \langle w_p, I_{ht}(\mathcal{M}(\rho_{p,h} - \rho_p^e), \mathcal{M}(\rho_{r,h})) \rangle_{\mathcal{E}_\Sigma}$$

$$\begin{aligned}
&= \left(w_p, \tilde{R}(\rho_{n,h}, \rho_{p,h}) \right)_{\Omega_S} + \langle w_p, \sigma_p \rho_p^e \rangle_{\mathcal{E}_D^S} \\
&\quad - (D_p(-\nabla_h w_p + \mathbf{r}^S(\llbracket w_p \rrbracket) + \mathbf{l}^S(\boldsymbol{\beta} \cdot \llbracket w_p \rrbracket) + \mathbf{r}_D^S(w_p)), \mathbf{r}_D^S(\rho_p^e))_{\Omega_S},
\end{aligned} \tag{4.2.2}$$

$$\begin{aligned}
& (w_r, \partial_t \rho_{r,h})_{\Omega_E} + B_{r,E}(w_r, \rho_{r,h}) + \langle w_r, I_{ht}(\mathcal{M}(\rho_{p,h} - \rho_p^e), \mathcal{M}(\rho_{r,h})) \rangle_{\mathcal{E}_\Sigma} \\
& - \langle w_r, I_{et}(\mathcal{M}(\rho_{n,h} - \rho_n^e), \mathcal{M}(\rho_{o,h})) \rangle_{\mathcal{E}_\Sigma} = \langle w_r, \sigma_r \rho_r^\infty \rangle_{\mathcal{E}_D^E} \\
& - (D_r(-\nabla_h w_r + \mathbf{r}^E(\llbracket w_r \rrbracket) + \mathbf{l}^E(\boldsymbol{\beta} \cdot \llbracket w_r \rrbracket) + \mathbf{r}_D^E(w_r)), \mathbf{r}_D^S(\rho_r^\infty))_{\Omega_E}, \tag{4.2.3}
\end{aligned}$$

$$\begin{aligned}
& (w_o, \partial_t \rho_{o,h})_{\Omega_E} + B_{o,E}(w_o, \rho_{o,h}) - \langle w_o, I_{ht}(\mathcal{M}(\rho_{p,h} - \rho_p^e), \mathcal{M}(\rho_{r,h})) \rangle_{\mathcal{E}_\Sigma} \\
& + \langle w_o, I_{et}(\mathcal{M}(\rho_{n,h} - \rho_n^e), \mathcal{M}(\rho_{o,h})) \rangle_{\mathcal{E}_\Sigma} = \langle w_o, \sigma_o \rho_o^\infty \rangle_{\mathcal{E}_D^E} \\
& - (D_o(-\nabla_h w_o + \mathbf{r}^E(\llbracket w_o \rrbracket) + \mathbf{l}^E(\boldsymbol{\beta} \cdot \llbracket w_o \rrbracket) + \mathbf{r}_D^E(w_o)), \mathbf{r}_D^S(\rho_o^\infty))_{\Omega_E}, \tag{4.2.4}
\end{aligned}$$

for all $w_n, w_p \in W_{h,k}^S$, $w_r, w_o \in W_{h,k}^E$ and all $t \in (0, T)$. The derivation of the primal form can be found in the Appendix (Section A.1.2). The bilinear forms for the semiconductor $B_{c,S} : W_{h,k}^S \times W_{h,k}^S \rightarrow \mathbb{R}$ are defined (for $c = \{n, p\}$) for all $t \in (0, T)$ as,

$$\begin{aligned}
B_{c,S}(w_c, \rho_{c,h}) & := \\
& (-\nabla_h w_c + \mathbf{r}^S(\llbracket w_c \rrbracket) + \mathbf{l}^S(\boldsymbol{\beta} \cdot \llbracket w_c \rrbracket) + \mathbf{r}_D^S(w_c), \\
& D_c(-\nabla_h \rho_{c,h} + \mathbf{r}^S(\llbracket \rho_{c,h} \rrbracket) + \mathbf{l}^S(\boldsymbol{\beta} \cdot \llbracket \rho_{c,h} \rrbracket) + \mathbf{r}_D^S(\rho_{c,h})))_{\Omega_S} \tag{4.2.5} \\
& - (\nabla_h w_c - \mathbf{r}^S(\llbracket w_c \rrbracket) - \mathbf{l}^S(\boldsymbol{\beta} \cdot \llbracket w_c \rrbracket) - \mathbf{r}_D^S(w_c), \alpha_c \mu_c \mathbf{E} \rho_{c,h})_{\Omega_S} \\
& + \langle \llbracket w_c \rrbracket, \sigma_c \llbracket \rho_{c,h} \rrbracket \rangle_{\mathcal{E}_h^{i,S}} + \langle w_c, \sigma_c \rho_{c,h} \rangle_{\mathcal{E}_D^S}.
\end{aligned}$$

The bilinear forms for the electrolyte $B_{c,E} : W_{h,k}^E \times W_{h,k}^E \rightarrow \mathbb{R}$ are defined (for

$c = \{r, o\}$) for all $t \in (0, T)$ as ,

$$B_{c,E}(w_c, \rho_{c,h}) :=$$

$$\begin{aligned} & (-\nabla_h w_c + \mathbf{r}^E(\llbracket w_c \rrbracket) + \mathbf{l}^E(\boldsymbol{\beta} \cdot \llbracket w_c \rrbracket) + \mathbf{r}_D^E(w_c), \\ & D_c(-\nabla_h \rho_{c,h} + \mathbf{r}^E(\llbracket \rho_{c,h} \rrbracket) + \mathbf{l}^E(\boldsymbol{\beta} \cdot \llbracket \rho_{c,h} \rrbracket) + \mathbf{r}_D^E(\rho_{c,h})))_{\Omega_E} \quad (4.2.6) \\ & - (\nabla_h w_c - \mathbf{r}^E(\llbracket w_c \rrbracket) - \mathbf{l}^E(\boldsymbol{\beta} \cdot \llbracket w_c \rrbracket) - \mathbf{r}_D^E(w_c), \alpha_c \mu_c \mathbf{E} \rho_{c,h})_{\Omega_E} \\ & + \langle \llbracket w_c \rrbracket, \sigma_c \llbracket \rho_{c,h} \rrbracket \rangle_{\mathcal{E}_h^{i,E}} + \langle w_c, \sigma_c \rho_{c,h} \rangle_{\mathcal{E}_D^E}. \end{aligned}$$

Remark 4.2.1. In our definitions of the primal forms we made use of Remark 3.1.1. Specifically that,

$$\mathcal{E}_\Sigma^S = \mathcal{E}_\Sigma^E = \mathcal{E}_\Sigma$$

We can rewrite (4.2.1), (4.2.2), (4.2.3) and (4.2.4) as a single system:

Find $\rho_{n,h}(\cdot, t), \rho_{p,h}(\cdot, t) \in W_{h,k}^S$ and $\rho_{r,h}(\cdot, t), \rho_{o,h}(\cdot, t) \in W_{h,k}^E$ such that,

$$\begin{aligned} & (w_n, \partial_t \rho_{n,h})_{\Omega_S} + (w_p, \partial_t \rho_{p,h})_{\Omega_S} + (w_r, \partial_t \rho_{r,h})_{\Omega_E} + (w_o, \partial_t \rho_{o,h})_{\Omega_E} \\ & + \mathcal{B}(w_n, w_p, w_r, w_o; \rho_{n,h}, \rho_{p,h}, \rho_{r,h}, \rho_{o,h}) \\ & + \mathcal{I}(w_n, w_p, w_r, w_o; \rho_{n,h}, \rho_{p,h}, \rho_{r,h}, \rho_{o,h}) \\ & = \mathcal{F}(w_n, w_p, w_r, w_o; \rho_{n,h}, \rho_{p,h}, \rho_{r,h}, \rho_{o,h}), \quad (4.2.7) \end{aligned}$$

for all $w_n, w_p \in W_{h,k}^S$, $w_r, w_o \in W_{h,k}^E$ and all $t \in (0, T)$. The multilinear forms are,

$$\begin{aligned} & \mathcal{B}(w_n, w_p, w_r, w_o; \rho_{n,h}, \rho_{p,h}, \rho_{r,h}, \rho_{o,h}) := \\ & B_{n,S}(w_n, \rho_{n,h}) + B_{p,S}(w_p, \rho_{p,h}) + B_{r,E}(w_r, \rho_{r,h}) + B_{o,E}(w_o, \rho_{o,h}), \quad (4.2.8) \end{aligned}$$

$$\begin{aligned}
\mathcal{I}(w_n, w_p, w_r, w_o; \rho_{n,h}, \rho_{p,h}, \rho_{r,h}, \rho_{o,h}) &:= \\
\langle w_n, I_{et}(\mathcal{M}(\rho_{n,h} - \rho_n^e), \mathcal{M}(\rho_{o,h})) \rangle_{\mathcal{E}_\Sigma} \\
+ \langle w_p, I_{ht}(\mathcal{M}(\rho_{p,h} - \rho_p^e), \mathcal{M}(\rho_{r,h})) \rangle_{\mathcal{E}_\Sigma} \\
+ \langle w_r, I_{ht}(\mathcal{M}(\rho_{p,h} - \rho_p^e), \mathcal{M}(\rho_{r,h})) - I_{et}(\mathcal{M}(\rho_{n,h} - \rho_n^e), \mathcal{M}(\rho_{o,h})) \rangle_{\mathcal{E}_\Sigma} \\
+ \langle w_o, -I_{ht}(\mathcal{M}(\rho_{p,h} - \rho_p^e), \mathcal{M}(\rho_{r,h})) + I_{et}(\mathcal{M}(\rho_{n,h} - \rho_n^e), \mathcal{M}(\rho_{o,h})) \rangle_{\mathcal{E}_\Sigma}, \tag{4.2.9}
\end{aligned}$$

and,

$$\begin{aligned}
\mathcal{F}(w_n, w_p, w_r, w_o; \rho_{n,h}, \rho_{p,h}, \rho_{r,h}, \rho_{o,h}) &:= \\
\left(w_n, \tilde{R}(\rho_{n,h}, \rho_{p,h}) \right)_{\Omega_S} + \left(w_p, \tilde{R}(\rho_{n,h}, \rho_{p,h}) \right)_{\Omega_S} \\
+ \langle w_n, \sigma_n \rho_n^e \rangle_{\mathcal{E}_D^S} + \langle w_p, \sigma_p \rho_p^e \rangle_{\mathcal{E}_D^S} + \langle w_r, \sigma_r \rho_r^\infty \rangle_{\mathcal{E}_D^E} + \langle w_o, \sigma_o \rho_o^\infty \rangle_{\mathcal{E}_D^E} \\
- (D_n(-\nabla_h w_n + \mathbf{r}^S(\llbracket w_n \rrbracket) + \mathbf{l}^S(\boldsymbol{\beta} \cdot \llbracket w_n \rrbracket) + \mathbf{r}_D^S(w_n)), \rho_n^e)_{\Omega_S} \tag{4.2.10} \\
- (D_p(-\nabla_h w_p + \mathbf{r}^S(\llbracket w_p \rrbracket) + \mathbf{l}^S(\boldsymbol{\beta} \cdot \llbracket w_p \rrbracket) + \mathbf{r}_D^S(w_p)), \rho_p^e)_{\Omega_S} \\
- (D_r(-\nabla_h w_r + \mathbf{r}^E(\llbracket w_r \rrbracket) + \mathbf{l}^E(\boldsymbol{\beta} \cdot \llbracket w_r \rrbracket) + \mathbf{r}_D^E(w_r)), \rho_r^\infty)_{\Omega_E} \\
- (D_o(-\nabla_h w_o + \mathbf{r}^E(\llbracket w_o \rrbracket) + \mathbf{l}^E(\boldsymbol{\beta} \cdot \llbracket w_o \rrbracket) + \mathbf{r}_D^E(w_o)), \rho_o^\infty)_{\Omega_E}.
\end{aligned}$$

4.3 Consistency Of Primal Form

Theorem 4.3.1. (*Consistency*) Let $s > 3/2$. Let $\rho_n, \rho_p \in H^1(H^s(\mathcal{T}_h^S); (0, T))$ and $\rho_r, \rho_o \in H^1(H^s(\mathcal{T}_h^E); (0, T))$ be solutions to (4.1.3)- (4.1.8), then $\rho_n, \rho_p, \rho_r, \rho_o$ also satisfy (4.2.1)- (4.2.4).

Proof:

Let $s > 3/2$ and $\rho_n, \rho_p \in H^1(H^s(\mathcal{T}_h^S); (0, T))$ and $\rho_r, \rho_o \in H^1(H^s(\mathcal{T}_h^E); (0, T))$ be solutions to (4.1.3)- (4.1.8). We prove that ρ_n satisfies (4.2.1). The proof for the other carriers is the same. Multiplying (4.1.3) by $w \in W_{h,k}^S$ and integrate over Ω_S to obtain,

$$(w, \partial_t \rho_n)_{\Omega_S} + (w, \nabla(\alpha_n \mu_n \mathbf{E} \rho_n - D_n \nabla_h \rho_n))_{\Omega_S} = \left(w, \tilde{R}(\rho_n, \rho_p) \right)_{\Omega_S}. \quad (4.3.1)$$

An application of Lemma 4.1.7 yields,

$$\begin{aligned} (w, \partial_t \rho_n)_{\Omega_S} - (\nabla_h w, \alpha_n \mu_n \mathbf{E} \rho_n - D_n \nabla_h \rho_n)_{\Omega_S} \\ + \langle \llbracket w \rrbracket, \{\alpha_n \mu_n \mathbf{E} \rho_n - D_n \nabla_h \rho_n\} \rangle_{\mathcal{E}_h^{i,S}} \\ + \langle \{w\}, \llbracket \alpha_n \mu_n \mathbf{E} \rho_n - D_n \nabla_h \rho_n \rrbracket \rangle_{\mathcal{E}_h^{i,S}} \\ + \langle w, \mathbf{n}_{\Sigma^S} \cdot (\alpha_n \mu_n \mathbf{E} \rho_n - D_n \nabla_h \rho_n) \rangle_{\mathcal{E}_{\Sigma}^S} \\ + \langle w, \mathbf{n} \cdot (\alpha_n \mu_n \mathbf{E} \rho_n - D_n \nabla_h \rho_n) \rangle_{\mathcal{E}_D^S} \\ + \langle w, \mathbf{n} \cdot (\alpha_n \mu_n \mathbf{E} \rho_n - D_n \nabla_h \rho_n) \rangle_{\mathcal{E}_N^S} \\ = \left(w, \tilde{R}(\rho_n, \rho_p) \right)_{\Omega_S}. \end{aligned} \quad (4.3.2)$$

Substituting in the interface (4.1.4) and Neumann boundary (4.1.5) conditions into the above we have,

$$\begin{aligned} (w, \partial_t \rho_n)_{\Omega_S} - (\nabla_h w, \alpha_n \mu_n \mathbf{E} \rho_n - D_n \nabla_h \rho_n)_{\Omega_S} \\ + \langle \llbracket w \rrbracket, \{\alpha_n \mu_n \mathbf{E} \rho_n - D_n \nabla_h \rho_n\} \rangle_{\mathcal{E}_h^{i,S}} \\ + \langle \{w\}, \llbracket \alpha_n \mu_n \mathbf{E} \rho_n - D_n \nabla_h \rho_n \rrbracket \rangle_{\mathcal{E}_h^{i,S}} \\ + \langle w, I_{et}(\mathcal{M}(\rho_n - \rho_n^e), \mathcal{M}(\rho_o)) \rangle_{\mathcal{E}_{\Sigma}^S} \\ + \langle w, \mathbf{n} \cdot (\alpha_n \mu_n \mathbf{E} \rho_n - D_n \nabla_h \rho_n) \rangle_{\mathcal{E}_D^S} \\ = \left(w, \tilde{R}(\rho_n, \rho_p) \right)_{\Omega_S}. \end{aligned} \quad (4.3.3)$$

We now rearrange terms to obtain,

$$(w, \partial_t \rho_n)_{\Omega_S} + T_1 + T_2 + \langle w, I_{et}(\mathcal{M}(\rho_n - \rho_n^e), \mathcal{M}(\rho_o)) \rangle_{\mathcal{E}_\Sigma^S} = \left(w, \tilde{R}(\rho_n, \rho_p) \right)_{\Omega_S}. \quad (4.3.4)$$

where,

$$\begin{aligned} T_1 &= (-\nabla_h w, -D_n \nabla_h \rho_n)_{\Omega_S} - \langle [\![w]\!], \{D_n \nabla_h \rho_n\} \rangle_{\mathcal{E}_h^{i,S}} \\ &\quad - \langle \{w\}, [\![D_n \nabla_h \rho_n]\!] \rangle_{\mathcal{E}_h^{i,S}} - \langle w, \mathbf{n} \cdot D_n \nabla_h \rho_n \rangle_{\mathcal{E}_D^S} \end{aligned} \quad (4.3.5)$$

and,

$$\begin{aligned} T_2 &= (-\nabla_h w, \alpha_n \mu_n \mathbf{E} \rho_n)_{\Omega_S} + \langle [\![w]\!], \{\alpha_n \mu_n \mathbf{E} \rho_n\} \rangle_{\mathcal{E}_h^{i,S}} \\ &\quad + \langle \{w\}, [\![\alpha_n \mu_n \mathbf{E} \rho_n]\!] \rangle_{\mathcal{E}_h^{i,S}} + \langle w, \alpha_n \mu_n \mathbf{n} \cdot \mathbf{E} \rho_n \rangle_{\mathcal{E}_D^S} \end{aligned} \quad (4.3.6)$$

We first work on T_1 . Using the lift operators (4.1.27) and (4.1.29) then (4.3.5) becomes,

$$\begin{aligned} T_1 &= (-\nabla_h w, -D_n \nabla_h \rho_n)_{\Omega_S} - (\mathbf{r}^S([\![w]\!]), D_n \nabla_h \rho_n)_{\Omega_S} \\ &\quad - \langle \{w\}, [\![D_n \nabla_h \rho_n]\!] \rangle_{\mathcal{E}_h^{i,S}} - (\mathbf{r}_D^S(w), D_n \nabla_h \rho_n)_{\Omega_S} \\ &= (-\nabla_h w + \mathbf{r}^S([\![w]\!]) + \mathbf{r}_D^S(w), -D_n \nabla_h \rho_n)_{\Omega_S} - \langle \{w\}, [\![D_n \nabla_h \rho_n]\!] \rangle_{\mathcal{E}_h^{i,S}} \end{aligned} \quad (4.3.7)$$

We note that since D_n is continuous and because of the regularity of $\rho_n(\cdot, t) \in H^s(\mathcal{T}_h^S)$ we have that,

$$[\![D_n \nabla \rho_n]\!] = 0 \quad \text{on } \mathcal{E}_h^{i,S} \quad (4.3.8)$$

We can then turn (4.3.7) into,

$$\begin{aligned}
T_1 &= (-\nabla_h w + \mathbf{r}^S(\llbracket w \rrbracket) + \mathbf{r}_D^S(w), -D_n \nabla_h \rho_n)_{\Omega_S} - \langle \{w\}, \llbracket D_n \nabla_h \rho_n \rrbracket \rangle_{\mathcal{E}_h^{i,S}}, \\
&= (-\nabla_h w + \mathbf{r}^S(\llbracket w \rrbracket) + \mathbf{r}_D^S(w), -D_n \nabla_h \rho_n)_{\Omega_S}, \\
&= (-\nabla_h w + \mathbf{r}^S(\llbracket w \rrbracket) + \mathbf{r}_D^S(w), -D_n \nabla_h \rho_n)_{\Omega_S} + \langle \boldsymbol{\beta} \cdot \llbracket w \rrbracket, \llbracket D_n \nabla_h \rho_n \rrbracket \rangle_{\mathcal{E}_{i,h}^S}, \\
&= (-\nabla_h w + \mathbf{r}^S(\llbracket w \rrbracket) + \mathbf{r}_D^S(w), -D_n \nabla_h \rho_n)_{\Omega_S} - (\mathbf{l}^S(\boldsymbol{\beta} \cdot \llbracket w \rrbracket), D_n \nabla_h \rho_n)_{\Omega_S}, \\
&= (-\nabla_h w + \mathbf{r}^S(\llbracket w \rrbracket) + \mathbf{l}^S(\boldsymbol{\beta} \cdot \llbracket w \rrbracket) + \mathbf{r}_D^S(w), -D_n \nabla_h \rho_n)_{\Omega_S}, \tag{4.3.9}
\end{aligned}$$

for any $\boldsymbol{\beta} \in \mathbb{R}^d$. Again, noting the regularity of $\rho_n(\cdot, t) \in H^s(\mathcal{T}_h^S)$ we then have that,

$$\llbracket \rho_n \rrbracket = \mathbf{0} \quad \text{on } \mathcal{E}_h^{i,S} \tag{4.3.10}$$

This implies,

$$(-\nabla_h w + \mathbf{r}^S(\llbracket w \rrbracket) + \mathbf{l}^S(\boldsymbol{\beta} \cdot \llbracket w \rrbracket) + \mathbf{r}_D^S(w), D_n \mathbf{r}^S(\llbracket \rho_n \rrbracket))_{\Omega_S} = 0, \tag{4.3.11}$$

$$(-\nabla_h w + \mathbf{r}^S(\llbracket w \rrbracket) + \mathbf{l}^S(\boldsymbol{\beta} \cdot \llbracket w \rrbracket) + \mathbf{r}_D^S(w), D_n \mathbf{l}^S(\boldsymbol{\beta} \cdot \llbracket \rho_n \rrbracket))_{\Omega_S} = 0, \tag{4.3.12}$$

and,

$$\langle \llbracket w \rrbracket, \sigma_n \llbracket \rho_n \rrbracket \rangle_{\mathcal{E}_h^{i,S}} = 0. \tag{4.3.13}$$

Using (4.3.11), (4.3.12) and (4.3.13), then (4.3.9) becomes,

$$\begin{aligned}
T_1 &= (-\nabla_h w + \mathbf{r}^S(\llbracket w \rrbracket) + \mathbf{l}^S(\boldsymbol{\beta} \cdot \llbracket w \rrbracket) + \mathbf{r}_D^S(w), \\
&\quad -D_n(\nabla_h \rho_n + \mathbf{r}^S(\llbracket \rho_n \rrbracket) + \mathbf{l}^S(\boldsymbol{\beta} \cdot \llbracket \rho_n \rrbracket)))_{\Omega_S} + \langle \llbracket w \rrbracket, \sigma_n \llbracket \rho_n \rrbracket \rangle_{\mathcal{E}_h^{i,S}} \tag{4.3.14}
\end{aligned}$$

From the Dirichlet boundary condition (4.1.6) we know that,

$$\rho_n - \rho_n^e = 0 \quad \text{on } \mathcal{E}_D^S. \quad (4.3.15)$$

This implies,

$$(-\nabla_h w + \mathbf{r}^S(\llbracket w \rrbracket) + \mathbf{l}^S(\boldsymbol{\beta} \cdot \llbracket w \rrbracket) + \mathbf{r}_D^S(w), D_n \mathbf{r}_D^S(\rho_n - \rho_n^e))_{\Omega_S} = 0, \quad (4.3.16)$$

and,

$$\langle w, \sigma_n(\rho_n - \rho_n^e) \rangle_{\mathcal{E}_D^S} = 0. \quad (4.3.17)$$

Using (4.3.16) and (4.3.17) then T_1 is,

$$\begin{aligned} T_1 = & (-\nabla_h w + \mathbf{r}^S(\llbracket w \rrbracket) + \mathbf{l}^S(\boldsymbol{\beta} \cdot \llbracket w \rrbracket) + \mathbf{r}_D^S(w), \\ & -D_n(\nabla_h \rho_n + \mathbf{r}^S(\llbracket \rho_n \rrbracket) + \mathbf{l}^S(\boldsymbol{\beta} \cdot \llbracket \rho_n \rrbracket) + \mathbf{r}_D^S(\rho_n)))_{\Omega_S} \\ & + (D_n(-\nabla_h w + \mathbf{r}^S(\llbracket w \rrbracket) + \mathbf{l}^S(\boldsymbol{\beta} \cdot \llbracket w \rrbracket) + \mathbf{r}_D^S(w)), \mathbf{r}_D^S(\rho_n^e))_{\Omega_S} \\ & + \langle \llbracket w \rrbracket, \sigma_n \llbracket \rho_n \rrbracket \rangle_{\mathcal{E}_h^{i,S}} + \langle w, \sigma_n(\rho_n - \rho_n^e) \rangle_{\mathcal{E}_D^S} \end{aligned} \quad (4.3.18)$$

Working on T_2 we use the definition of lift operators (4.1.27) and (4.1.29) to turn (4.3.6) into,

$$T_2 = ((-\nabla_h w + \mathbf{r}^S(\llbracket w \rrbracket) + \mathbf{r}_D^S(w)), \alpha_n \mu_n \mathbf{E} \rho_n)_{\Omega_S} + \langle \{w\}, \llbracket \alpha_n \mu_n \mathbf{E} \rho_n \rrbracket \rangle_{\mathcal{E}_h^{i,S}}. \quad (4.3.19)$$

Since μ_n is continuous and \mathbf{E} has a continuous normal component (Remark 4.1.2), then using the regularity of $\rho_n(\cdot, t) \in H^s(\mathcal{T}_h^S)$ we have,

$$\llbracket \alpha_n \mu_n \mathbf{E} \rho_n \rrbracket = 0 \quad \text{on } \mathcal{E}_h^{i,S} \quad (4.3.20)$$

This gives us that,

$$\begin{aligned}
T_2 &= \left((-\nabla_h w + \mathbf{r}^S(\llbracket w \rrbracket) + \mathbf{r}_D^S(w)), \alpha_n \mu_n \mathbf{E} \rho_n \right)_{\Omega_S} + \langle \{w\}, \llbracket \alpha_n \mu_n \mathbf{E} \rho_n \rrbracket \rangle_{\mathcal{E}_h^{i,S}}, \\
&= \left((-\nabla_h w + \mathbf{r}^S(\llbracket w \rrbracket) + \mathbf{r}_D^S(w)), \alpha_n \mu_n \mathbf{E} \rho_n \right)_{\Omega_S}, \\
&= \left((-\nabla_h w + \mathbf{r}^S(\llbracket w \rrbracket) + \mathbf{r}_D^S(w)), \alpha_n \mu_n \mathbf{E} \rho_n \right)_{\Omega_S} - \langle \boldsymbol{\beta} \cdot \llbracket w \rrbracket, \llbracket \alpha_n \mu_n \mathbf{E} \rho_n \rrbracket \rangle_{\mathcal{E}_h^{i,S}}, \\
&= \left((-\nabla_h w + \mathbf{r}^S(\llbracket w \rrbracket) + \mathbf{l}^S(\boldsymbol{\beta} \cdot \llbracket w \rrbracket) + \mathbf{r}_D^S(w)), \alpha_n \mu_n \mathbf{E} \rho_n \right)_{\Omega_S},
\end{aligned} \tag{4.3.21}$$

for any $\boldsymbol{\beta} \in \mathbb{R}^d$. Upon substituting (4.3.18) and (4.3.21) into (4.3.4) we arrive at the primal form of the semidiscrete LDG method (4.2.1) for $\rho_n \in H^1(H^s(\mathcal{T}_h^S); (0, T))$.

□

4.4 Continuity and Coercivity of Bilinear Forms

We first prove that the bilinear forms are continuous.

Lemma 4.4.1 (Continuity Of Bilinear Forms). *There exists positive constants K_n , K_p , K_r and K_o such that for all $t \in (0, T)$,*

$$|B_{n,S}(z, w)| \leq K_n \|z\|_{DG,S} \|w\|_{DG,S} \quad \forall z, w \in W_{h,k}^S, \tag{4.4.1}$$

$$|B_{p,S}(z, w)| \leq K_p \|z\|_{DG,S} \|w\|_{DG,S} \quad \forall z, w \in W_{h,k}^S, \tag{4.4.2}$$

$$|B_{r,E}(z, w)| \leq K_r \|z\|_{DG,E} \|w\|_{DG,E} \quad \forall z, w \in W_{h,k}^E, \tag{4.4.3}$$

$$|B_{o,E}(z, w)| \leq K_o \|z\|_{DG,E} \|w\|_{DG,E} \quad \forall z, w \in W_{h,k}^E. \tag{4.4.4}$$

Proof: We prove this lemma for the case of electrons only, the proofs for the other carriers are the same. We write the bilinear form $B_{n,S}$ from (4.2.5) as the sum of two bilinear forms,

$$B_{n,S}(z, w) = B_{n,S}^1(z, w) - B_{n,S}^2(z, w). \quad (4.4.5)$$

The first bilinear form is,

$$\begin{aligned} B_{n,S}^1(z, w) &:= (-\nabla_h z + \mathbf{r}^S(\llbracket z \rrbracket) + \mathbf{l}^S(\boldsymbol{\beta} \cdot \llbracket z \rrbracket) + \mathbf{r}_D^S(z), \\ &D_n(-\nabla_h w + \mathbf{r}^S(\llbracket w \rrbracket) + \mathbf{l}^S(\boldsymbol{\beta} \cdot \llbracket w \rrbracket) + \mathbf{r}_D^S(w)))_{\Omega_S} \quad (4.4.6) \\ &+ \langle \llbracket z \rrbracket, \sigma_n \llbracket w \rrbracket \rangle_{\mathcal{E}_h^{i,S}} + \langle z, \sigma_n w \rangle_{\mathcal{E}_D^S}. \end{aligned}$$

This bilinear form was shown to be continuous with constant C_{LDG} in [12].

The second bilinear form is,

$$B_{n,S}^2(z, w) := (\nabla_h z - \mathbf{r}^S(\llbracket z \rrbracket) - \mathbf{l}^S(\boldsymbol{\beta} \cdot \llbracket z \rrbracket) - \mathbf{r}_D^S(z), \alpha_n \mu_n \mathbf{E} w)_{\Omega_S}. \quad (4.4.7)$$

We use the Cauchy-Schwarz inequality (Theorem 4.1.8), the bound on the drift component (4.1.12) and the Poincare inequality (Theorem 4.1.9) to show,

$$\begin{aligned} |B_{n,S}^2(z, w)| &\leq \|\nabla_h z - \mathbf{r}^S(\llbracket z \rrbracket) - \mathbf{l}^S(\boldsymbol{\beta} \cdot \llbracket z \rrbracket) - \mathbf{r}_D^S(z)\|_{L^2(\mathcal{T}_h^S)} \|\alpha_n \mu_n \mathbf{E} w\|_{L^2(\mathcal{T}_h^S)}, \\ &= \| -\nabla_h z + \mathbf{r}^S(\llbracket z \rrbracket) + \mathbf{l}^S(\boldsymbol{\beta} \cdot \llbracket z \rrbracket) + \mathbf{r}_D^S(z) \|_{L^2(\mathcal{T}_h^S)} \|\alpha_n \mu_n \mathbf{E} w\|_{L^2(\mathcal{T}_h^S)}, \\ &\leq v_n^* \| -\nabla_h z + \mathbf{r}^S(\llbracket z \rrbracket) + \mathbf{l}^S(\boldsymbol{\beta} \cdot \llbracket z \rrbracket) + \mathbf{r}_D^S(z) \|_{L^2(\mathcal{T}_h^S)} \|w\|_{L^2(\mathcal{T}_h^S)}, \\ &\leq v_n^* C_P^S \| -\nabla_h z + \mathbf{r}^S(\llbracket z \rrbracket) + \mathbf{l}^S(\boldsymbol{\beta} \cdot \llbracket z \rrbracket) + \mathbf{r}_D^S(z) \|_{L^2(\mathcal{T}_h^S)} \|w\|_{\text{DG,S}}. \quad (4.4.8) \end{aligned}$$

Using the definition of the DG norm (3.1.24) and Lemma 4.1.10 then we have,

$$\|-\nabla_h z + \mathbf{r}^S(\llbracket z \rrbracket) + \mathbf{l}^S(\boldsymbol{\beta} \cdot \llbracket z \rrbracket) + \mathbf{r}_D^S(z)\|_{L^2(\mathcal{T}_h^S)} \leq \max(1, C_{\text{inv}}^S C_{\text{tr}}^S) \|z\|_{\text{DG,S}}. \quad (4.4.9)$$

Substituting (4.4.9) into (4.4.8) yields,

$$|B_{n,S}^2(z, w)| \leq v_n^* C_P^S \max(1, C_{\text{inv}}^S C_{\text{tr}}^S) \|z\|_{\text{DG,S}} \|w\|_{\text{DG,S}}. \quad (4.4.10)$$

Therefore we have,

$$\begin{aligned} |B_{n,S}(z, w)| &\leq |B_{n,S}^1(z, w)| + |B_{n,S}^2(z, w)| \\ &\leq K_n \|z\|_{\text{DG,S}} \|w\|_{\text{DG,S}} \quad \forall z, w \in W_{h,k}^S. \end{aligned} \quad (4.4.11)$$

We therefore choose the constant K_n is chosen to be,

$$K_n = C_{\text{LDG}} + v_n^* C_P^S \max(1, C_{\text{inv}}^S C_{\text{tr}}^S) \quad (4.4.12)$$

□

We will now use the continuity of the bilinear form to prove its coercivity.

Lemma 4.4.2 (Coercivity Of Bilinear Forms). *If the diffusion of the charge carriers satisfies,*

$$D_{c,*} > 2 v_c^* C_P^S \max(1, C_{\text{inv}}^S C_{\text{tr}}^S) \quad \text{for } c = n, p, \quad (4.4.13)$$

$$D_{c,*} > 2 v_c^* C_P^E \max(1, C_{\text{inv}}^E C_{\text{tr}}^E), \quad \text{for } c = r, o,$$

then there exists constants $\gamma_{n,S}^2$, $\gamma_{p,S}^2$, $\gamma_{r,E}^2$, and $\gamma_{o,E}^2$ such that,

$$B_{n,S}(w, w) \geq \frac{\gamma_{n,S}^2}{2} \|w\|_{DG,S}^2 \quad \forall w \in W_{h,k}^S, \quad (4.4.14)$$

$$B_{p,S}(w, w) \geq \frac{\gamma_{p,S}^2}{2} \|w\|_{DG,S}^2 \quad \forall w \in W_{h,k}^S, \quad (4.4.15)$$

$$B_{r,E}(w, w) \geq \frac{\gamma_{r,E}^2}{2} \|w\|_{DG,E}^2 \quad \forall w \in W_{h,k}^E, \quad (4.4.16)$$

$$B_{o,E}(w, w) \geq \frac{\gamma_{o,E}^2}{2} \|w\|_{DG,E}^2 \quad \forall w \in W_{h,k}^E. \quad (4.4.17)$$

Proof: We prove the above inequality for the case of electrons only, the proofs for the other carriers are similar. We first note that,

$$B_{n,S}(w, w) = B_{n,S}^1(w, w) - B_{n,S}^2(w, w). \quad (4.4.18)$$

We work on the first bilinear form. From the definition (4.4.6) we have,

$$\begin{aligned}
& B_{n,S}^1(w, w) \\
&= D_{n,*} \|(-\nabla_h w + \mathbf{r}^S(\llbracket w \rrbracket) + \mathbf{l}^S(\boldsymbol{\beta} \cdot \llbracket w \rrbracket) + \mathbf{r}_D^S(w))\|_{L^2(\mathfrak{T}_h^S)}^2 \\
&\quad + \|\sigma_n^{1/2} \llbracket w \rrbracket\|_{L^2(\mathcal{E}_h^{i,S})}^2 + \|\sigma_n^{1/2} w\|_{L^2(\mathcal{E}_D^S)}^2. \\
&\geq D_{n,*} \|\nabla_h w\|_{L^2(\mathfrak{T}_h^S)}^2 + D_{n,*} \|\mathbf{r}^S(\llbracket w \rrbracket) + \mathbf{l}^S(\boldsymbol{\beta} \cdot \llbracket w \rrbracket) + \mathbf{r}_D^S(w)\|_{L^2(\mathfrak{T}_h^S)}^2 \\
&\quad - 2D_{n,*} (\nabla_h w, \mathbf{r}^S(\llbracket w \rrbracket) + \mathbf{l}^S(\boldsymbol{\beta} \cdot \llbracket w \rrbracket) + \mathbf{r}_D^S(w))_{\Omega_S} \\
&\quad + \|\sigma_n^{1/2} \llbracket w \rrbracket\|_{L^2(\mathcal{E}_h^{i,S})}^2 + \|\sigma_n^{1/2} w\|_{L^2(\mathcal{E}_D^S)}^2.
\end{aligned} \quad (4.4.19)$$

Using Young's inequality (Theorem 4.1.2) yields,

$$\begin{aligned}
B_{n,S}^1(w, w) &\geq D_{n,*}(1 - \delta) \|\nabla_h w\|_{L^2(\mathcal{T}_h^S)}^2 \\
&\quad + D_{n,*}(1 - 1/\delta) \|\mathbf{r}^S(\llbracket w \rrbracket) + \mathbf{l}^S(\boldsymbol{\beta} \cdot \llbracket w \rrbracket) + \mathbf{r}_D^S(w)\|_{L^2(\mathcal{T}_h^S)}^2 \\
&\quad + \|\sigma_n^{1/2} \llbracket w \rrbracket\|_{L^2(\mathcal{E}_h^{i,S})}^2 + \|\sigma_n^{1/2} w\|_{L^2(\mathcal{E}_D^S)}^2 \\
&= D_{n,*}(1 - \delta) \|\nabla_h w\|_{L^2(\mathcal{T}_h^S)}^2 \\
&\quad + D_{n,*}(1 - 1/\delta) \|\mathbf{r}^S(\llbracket w \rrbracket) + \mathbf{l}^S(\boldsymbol{\beta} \cdot \llbracket w \rrbracket) + \mathbf{r}_D^S(w)\|_{L^2(\mathcal{T}_h^S)}^2 \\
&\quad + \tilde{\sigma}_n \left(\|h^{1/2} \llbracket w \rrbracket\|_{L^2(\mathcal{E}_h^{i,S})}^2 + \|h^{1/2} w\|_{L^2(\mathcal{E}_D^S)}^2 \right). \tag{4.4.20}
\end{aligned}$$

The equality comes from using the definition of the penalty term σ_n (3.3.11).

Choosing $\delta = D_{n,*}/2$ and using Lemma 4.1.10 on (4.4.20) yields,

$$\begin{aligned}
B_{n,S}^1(w, w) &\geq \frac{D_{n,*}}{2} \|\nabla_h w\|_{L^2(\mathcal{T}_h^S)}^2 \\
&\quad + (\tilde{\sigma}_n - C_{\text{tr}}^S C_{\text{inv}}^S D_{n,*}) \left(\|h^{1/2} \llbracket w \rrbracket\|_{L^2(\mathcal{E}_h^{i,S})}^2 + \|h^{1/2} w\|_{L^2(\mathcal{E}_D^S)}^2 \right), \\
&\geq \frac{D_{n,*}}{2} \|w\|_{\text{DG,S}}^2, \tag{4.4.21}
\end{aligned}$$

where we have chosen,

$$\tilde{\sigma}_n = \left(\frac{1}{2} + C_{\text{tr}}^S C_{\text{inv}}^S \right) D_{n,*}. \tag{4.4.22}$$

Returning to (4.4.18) and using (4.4.10) from Lemma 4.4.1 we have,

$$\begin{aligned}
B_{n,S}(w, w) &= B_{n,S}^1(w, w) - B_{n,S}^2(w, w), \\
&\geq \frac{D_{n,*}}{2} \|w\|_{\text{DG,S}}^2 - B_{n,S}^2(w, w), \\
&\geq \frac{D_{n,*}}{2} \|w\|_{\text{DG,S}}^2 - v_n^* C_P^S \max(1, C_{\text{inv}}^S C_{\text{tr}}^S) \|w\|_{\text{DG,S}}^2, \\
&\geq \frac{\gamma_n^2}{2} \|w\|_{\text{DG,S}}^2.
\end{aligned} \tag{4.4.23}$$

Where,

$$\gamma_n^2 = D_{n,*} - 2 v_n^* C_P^S \max(1, C_{\text{inv}}^S C_{\text{tr}}^S) > 0 \quad \text{by assumption.} \tag{4.4.24}$$

□

4.5 Error Estimates

Theorem 4.5.1. *Let $\rho_n, \rho_p \in H^1(H^s(\mathcal{T}_h^S); (0, T))$, $\rho_r, \rho_o \in H^1(H^s(\mathcal{T}_h^E); (0, T))$ be the solutions to (4.1.3)- (4.1.8) and $\rho_{n,h}(\cdot, t), \rho_{p,h}(\cdot, t) \in W_{h,k}^S$ and $\rho_{r,h}(\cdot, t), \rho_{o,h}(\cdot, t) \in W_{h,k}^E$ be solutions to the semidiscrete LDG method (4.2.1)-(4.2.4). If the coercivity constants satisfy,*

$$\gamma_n^2 \geq 24Mk_{et}(C_{tr}^S)^2 \tag{4.5.1}$$

$$\gamma_p^2 \geq 24Mk_{ht}(C_{tr}^S)^2 \tag{4.5.2}$$

$$\gamma_r^2 \geq 8M(3k_{ht} + k_{et})(C_{tr}^E)^2 \tag{4.5.3}$$

$$\gamma_o^2 \geq 8M(k_{ht} + 3k_{et})(C_{tr}^E)^2 \tag{4.5.4}$$

then there exists constants C_{L^2} and C_{DG} independent of h_S and h_E such that,

$$\begin{aligned}
& \sum_{c=n,p} \|\rho_c(T) - \rho_{c,h}(T)\|_{L^2(\mathcal{T}_h^S)}^2 + \sum_{c=r,o} \|\rho_c(T) - \rho_{c,h}(T)\|_{L^2(\mathcal{T}_h^E)}^2 \\
& + \sum_{c=n,p} \frac{\gamma_c^2}{2} \int_0^T \|\rho_c - \rho_{c,h}\|_{DG,S}^2 dt + \sum_{c=r,o} \frac{\gamma_c^2}{2} \int_0^T \|\rho_c - \rho_{c,h}\|_{DG,E}^2 dt \\
& \leq C_{L^2} \max \left(h_S^{2 \min(k+1,s)}, h_E^{2 \min(k+1,s)} \right) \\
& + C_{DG} \max \left(h_S^{2 \min(k+1,s)-2}, h_E^{2 \min(k+1,s)-2} \right). \quad (4.5.5)
\end{aligned}$$

Where,

$$\begin{aligned}
C_{L^2} &= C \left(T, \tau_n, \tau_p, \max_{c \in \{n,p\}} \left(|\rho_c|_{H^s(\mathcal{T}_h^S)} \right), \max_{c \in \{n,p\}} \left(\left| \frac{\partial \rho_c}{\partial t} \right|_{H^s(\mathcal{T}_h^S)} \right), \right. \\
&\quad \left. \max_{c \in \{r,o\}} \left(|\rho_c|_{H^s(\mathcal{T}_h^E)} \right), \max_{c \in \{r,o\}} \left(\left| \frac{\partial \rho_c}{\partial t} \right|_{H^s(\mathcal{T}_h^E)} \right) \right), \\
C_{DG} &= C \left(T, M, k_{et}, k_{ht}, C_{tr}^S, C_{tr}^E, \max_{c \in \{n,p\}} \left(|\rho_c|_{H^s(\mathcal{T}_h^S)} \right), \max_{c \in \{r,o\}} \left(|\rho_c|_{H^s(\mathcal{T}_h^E)} \right), \right. \\
&\quad \left. \max_{c \in \{n,p,r,o\}} (K_c) \right). \quad (4.5.6)
\end{aligned}$$

Proof: We use the consistency of the primal from Theorem 4.3.1 to write that the solutions $\rho_n, \rho_p \in H^1(H^s(\mathcal{T}_h^S); (0, T))$, $\rho_r, \rho_o \in H^1(H^s(\mathcal{T}_h^E); (0, T))$ to (4.1.3)-(4.1.8), then $\rho_n, \rho_p, \rho_r, \rho_o$ satisfy,

$$\begin{aligned}
& (w_n, \partial_t \rho_n)_{\Omega_S} + (w_p, \partial_t \rho_p)_{\Omega_S} + (w_r, \partial_t \rho_r)_{\Omega_E} + (w_o, \partial_t \rho_o)_{\Omega_E} \\
& + \mathcal{B}(w_n, w_p, w_r, w_o; \rho_n, \rho_p, \rho_r, \rho_o) \\
& + \mathcal{I}(w_n, w_p, w_r, w_o; \rho_n, \rho_p, \rho_r, \rho_o) \\
& = \mathcal{F}(w_n, w_p, w_r, w_o; \rho_n, \rho_p, \rho_r, \rho_o), \quad (4.5.7)
\end{aligned}$$

for all $w_n, w_p \in W_{h,k}^S$, $w_r, w_o \in W_{h,k}^E$ and all $t \in (0, T)$. Subtracting (4.2.8) from (4.5.7) we obtain,

$$\begin{aligned}
& (w_n, \partial_t(\rho_n - \rho_{n,h}))_{\Omega_S} + (w_p, \partial_t(\rho_p - \rho_{p,h}))_{\Omega_S} \\
& + (w_r, \partial_t(\rho_r - \rho_{r,h}))_{\Omega_E} + (w_o, \partial_t(\rho_o - \rho_{o,h}))_{\Omega_E} \\
& + \mathcal{B}(w_n, w_p, w_r, w_o; (\rho_n - \rho_{n,h}), (\rho_p - \rho_{p,h}), (\rho_r - \rho_{r,h}), (\rho_o - \rho_{o,h})) \\
& + \mathcal{I}(w_n, w_p, w_r, w_o; \rho_n, \rho_p, \rho_r, \rho_o) - \mathcal{I}(w_n, w_p, w_r, w_o; \rho_{n,h}, \rho_{p,h}, \rho_{r,h}, \rho_{o,h}) \\
& = \left(w_n, \tilde{R}(\rho_n, \rho_p) - \tilde{R}(\rho_{n,h}, \rho_{p,h}) \right)_{\Omega_S} + \left(w_p, \tilde{R}(\rho_n, \rho_p) - \tilde{R}(\rho_{n,h}, \rho_{p,h}) \right)_{\Omega_S}
\end{aligned} \tag{4.5.8}$$

for all $w_n, w_p \in W_{h,k}^S$, $w_r, w_o \in W_{h,k}^E$ and all $t \in (0, T)$.

Let $\Pi^S : H^s(\Omega_S) \rightarrow W_{h,k}^S$ and $\Pi^E : H^s(\Omega_E) \rightarrow W_{h,k}^E$ be L^2 projections.

From Theorem 4.1.6 we then have,

$$\|w - \Pi^S w\|_{L^2(\mathcal{T}_h^S)} \leq Ch_S^{\min(s, k+1)} |w|_{H^s(\mathcal{T}_h^S)}, \tag{4.5.9}$$

$$\|w - \Pi^E w\|_{L^2(\mathcal{T}_h^E)} \leq Ch_E^{\min(s, k+1)} |w|_{H^s(\mathcal{T}_h^E)}, \tag{4.5.10}$$

$$\|w - \Pi^S w\|_{\text{DG,S}} \leq Ch_S^{\min(s, k+1)-1} |w|_{H^s(\mathcal{T}_h^S)}, \tag{4.5.11}$$

$$\|w - \Pi^E w\|_{\text{DG,E}} \leq Ch_E^{\min(s, k+1)-1} |w|_{H^s(\mathcal{T}_h^E)}, \tag{4.5.12}$$

where h_S and h_E are the maximal element diameters in \mathcal{T}_h^S and \mathcal{T}_h^E respectively.

We label the approximation errors,

$$\xi_n^A(t) = \Pi^S \rho_n - \rho_{n,h} \in W_{h,k}^S, \quad (4.5.13)$$

$$\xi_p^A(t) = \Pi^S \rho_p - \rho_{p,h} \in W_{h,k}^S, \quad (4.5.14)$$

$$\xi_r^A(t) = \Pi^E \rho_r - \rho_{r,h} \in W_{h,k}^E, \quad (4.5.15)$$

$$\xi_o^A(t) = \Pi^E \rho_o - \rho_{o,h} \in W_{h,k}^E, \quad (4.5.16)$$

for all $t \in (0, T)$. And label the interpolation errors,

$$\xi_n^I(t) = \rho_n - \Pi^S \rho_n, \quad (4.5.17)$$

$$\xi_p^I(t) = \rho_p - \Pi^S \rho_p, \quad (4.5.18)$$

$$\xi_r^I(t) = \rho_r - \Pi^E \rho_r, \quad (4.5.19)$$

$$\xi_o^I(t) = \rho_o - \Pi^E \rho_o, \quad (4.5.20)$$

for all $t \in (0, T)$. Substituting these errors into (4.5.8) and taking $w_n = \xi_n^A(t)$,

$w_p = \xi_p^A(t)$, $w_r = \xi_r^A(t)$, and $w_o = \xi_o^A(t)$ we obtain,

$$\begin{aligned}
& \frac{1}{2} \frac{d}{dt} \left(\sum_{c=n,p} \|\xi_c^A\|_{L^2(\mathcal{T}_h^S)}^2 + \sum_{c=r,o} \|\xi_c^A\|_{L^2(\mathcal{T}_h^E)}^2 \right) \\
& + \left(\sum_{c=n,p} |B_{c,S}(\xi_c^A, \xi_c^A)| + \sum_{c=r,o} |B_{c,E}(\xi_c^A, \xi_c^A)| \right) \\
& \leq \left(\sum_{c=n,p} |(\xi_c^A, \partial_t \xi_c^I)_{\Omega_S}| + \sum_{c=r,o} |(\xi_c^A, \partial_t \xi_c^I)_{\Omega_S}| \right) \\
& + \left(\sum_{c=n,p} |B_{c,S}(\xi_c^A, \xi_c^I)| + \sum_{c=r,o} |B_{c,E}(\xi_c^A, \xi_c^I)| \right) \\
& + |\mathcal{J}(\xi_n^A, \xi_p^A, \xi_r^A, \xi_o^A; \rho_n, \rho_p, \rho_r, \rho_o) - \mathcal{J}(\xi_n^A, \xi_p^A, \xi_r^A, \xi_o^A; \rho_{n,h}, \rho_{p,h}, \rho_{r,h}, \rho_{o,h})| \\
& + |\left(\xi_n^A, \tilde{R}(\rho_n, \rho_p) - \tilde{R}(\rho_{n,h}, \rho_{p,h}) \right)_{\Omega_S}| + |\left(\xi_p^A, \tilde{R}(\rho_n, \rho_p) - \tilde{R}(\rho_{n,h}, \rho_{p,h}) \right)_{\Omega_S}|.
\end{aligned} \tag{4.5.21}$$

Multiplying both sides by 2 and using the coercivity of the bilinear forms

(Lemma 4.4.2) yields,

$$\begin{aligned}
& \frac{d}{dt} \left(\sum_{c=n,p} \|\xi_c^A\|_{L^2(\mathcal{T}_h^S)}^2 + \sum_{c=r,o} \|\xi_c^A\|_{L^2(\mathcal{T}_h^E)}^2 \right) \\
& \quad + \left(\sum_{c=n,p} \gamma_c^2 \|\xi_c^A\|_{\text{DG,S}}^2 + \sum_{c=r,o} \gamma_c^2 \|\xi_c^A\|_{\text{DG,E}}^2 \right) \\
& \leq \left(\sum_{c=n,p} 2|(\xi_c^A, \partial_t \xi_c^I)_{\Omega_S}| + \sum_{c=r,o} 2|(\xi_c^A, \partial_t \xi_c^I)_{\Omega_S}| \right) \\
& \quad + \left(\sum_{c=n,p} 2|B_{c,S}(\xi_c^A, \xi_c^I)| + \sum_{c=r,o} 2|B_{c,E}(\xi_c^A, \xi_c^I)| \right) \\
& \quad + 2|\mathcal{J}(\xi_n^A, \xi_p^A, \xi_r^A, \xi_o^A; \rho_n, \rho_p, \rho_r, \rho_o) - \mathcal{J}(\xi_n^A, \xi_p^A, \xi_r^A, \xi_o^A; \rho_{n,h}, \rho_{p,h}, \rho_{r,h}, \rho_{o,h})| \\
& \quad + 2|\left(\xi_n^A, \tilde{R}(\rho_n, \rho_p) - \tilde{R}(\rho_{n,h}, \rho_{p,h})\right)_{\Omega_S}| + 2|\left(\xi_p^A, \tilde{R}(\rho_n, \rho_p) - \tilde{R}(\rho_{n,h}, \rho_{p,h})\right)_{\Omega_S}|, \\
& = T_1 + T_2 + T_3 + T_4 + T_5.
\end{aligned} \tag{4.5.22}$$

For T_1 we use the Cauchy-Schwarz inequality (Theorem 4.1.8), Young's inequality (Lemma 4.1.2) and the projection properties (4.5.9) and (4.5.10) to obtain the bound,

$$\begin{aligned}
T_1 & \leq \sum_{c=n,p} \delta_{1,c} \|\xi_c^A\|_{L^2(\mathcal{T}_h^S)}^2 + \sum_{c=r,o} \delta_{1,c} \|\xi_c^A\|_{L^2(\mathcal{T}_h^E)}^2 \\
& \quad + \sum_{c=n,p} \frac{C}{\delta_{1,c}} h_S^{2\min(s,k+1)} \left(\left| \frac{\partial \rho_c}{\partial t} \right|_{H^s(\mathcal{T}_h^S)}^2 \right) \\
& \quad + \sum_{c=r,o} \frac{C}{\delta_{1,c}} h_E^{2\min(s,k+1)} \left(\left| \frac{\partial \rho_c}{\partial t} \right|_{H^s(\mathcal{T}_h^E)}^2 \right).
\end{aligned} \tag{4.5.23}$$

After using the continuity of the bilinear forms (Lemma 4.4.1) on T_2 we have,

$$T_2 \leq \sum_{c=n,p} 2K_c \|\xi_c^A\|_{\text{DG,S}} \|\xi_c^I\|_{\text{DG,S}} + \sum_{c=r,o} 2K_c \|\xi_c^A\|_{\text{DG,E}} \|\xi_c^I\|_{\text{DG,E}}. \tag{4.5.24}$$

Using Young's inequality (Lemma 4.1.2) and the projection properties (4.5.11) and (4.5.12) yields the following bound on T_2 ,

$$\begin{aligned}
T_2 &\leq \sum_{c=n,p} K_c \delta_{2,c} \|\xi_c^A\|_{\text{DG,S}}^2 + \sum_{c=r,o} K_c \delta_{2,c} \|\xi_c^A\|_{\text{DG,E}}^2 \\
&\quad + \sum_{c=n,p} \frac{CK_{c,S}}{\delta_{2,c}} h_S^{2\min(s,k+1)-2} (|\rho_c|_{H^s(\mathcal{T}_h^S)}^2) \\
&\quad + \sum_{c=r,o} \frac{CK_{c,S}}{\delta_{2,c}} h_E^{2\min(s,k+1)-2} (|\rho_{c,h}|_{H^s(\mathcal{T}_h^E)}^2). \quad (4.5.25)
\end{aligned}$$

T_4 can be bounded by using using the Cauchy-Schwarz (Theorem 4.1.8), the Lipschitz property of the recombination function (Theorem 4.1.1) and Young's inequality (Lemma 4.1.2),

$$\begin{aligned}
T_4 &= 2 \left| \left(\xi_n^A, \tilde{R}(\rho_n, \rho_p) - \tilde{R}(\rho_{n,h}, \rho_{p,h}) \right)_{\Omega_S} \right|, \\
&\leq 2 \|\xi_n^A\|_{L^2(\mathcal{T}_h^S)} \|\tilde{R}(\rho_n, \rho_p) - \tilde{R}(\rho_{n,h}, \rho_{p,h})\|_{L^2(\mathcal{T}_h^E)}, \\
&\leq 2 C_R \|\xi_n^A\|_{L^2(\mathcal{T}_h^S)} \left(\|\rho_n - \rho_{n,h}\|_{L^2(\mathcal{T}_h^S)} + \|\rho_p - \rho_{p,h}\|_{L^2(\mathcal{T}_h^S)} \right), \\
&\leq 2 C_R \|\xi_n^A\|_{L^2(\mathcal{T}_h^S)} \sum_{c=n,p} \left(\|\xi_c^A\|_{L^2(\mathcal{T}_h^S)} + \|\xi_c^I\|_{L^2(\mathcal{T}_h^S)} \right), \quad (4.5.26) \\
&= 2 C_R \|\xi_n^A\|_{L^2(\mathcal{T}_h^S)}^2 + 2 C_R \|\xi_n^A\|_{L^2(\mathcal{T}_h^S)} \|\xi_p^A\|_{L^2(\mathcal{T}_h^S)} \\
&\quad + 2 C_R \|\xi_n^A\|_{L^2(\mathcal{T}_h^S)} \|\xi_n^I\|_{L^2(\mathcal{T}_h^S)} + 2 C_R \|\xi_n^A\|_{L^2(\mathcal{T}_h^S)} \|\xi_p^I\|_{L^2(\mathcal{T}_h^S)}, \\
&\leq (2 + \delta_{41} + \delta_{42} + \delta_{43}) C_R \|\xi_n^A\|_{L^2(\mathcal{T}_h^S)}^2 + \frac{C_R}{\delta_{41}} \|\xi_p^A\|_{L^2(\mathcal{T}_h^S)}^2 + \\
&\quad + \frac{C_R}{\delta_{42}} \|\xi_n^I\|_{L^2(\mathcal{T}_h^S)}^2 + \frac{C_R}{\delta_{43}} \|\xi_p^I\|_{L^2(\mathcal{T}_h^S)}^2,
\end{aligned}$$

Where $C_R = \max(\frac{1}{\tau_n}, \frac{1}{\tau_p})$. We can then use the projection properties (4.5.9) and (4.5.10) to obtain the estimate,

$$\begin{aligned} &\leq (2 + \delta_{41} + \delta_{42} + \delta_{43}) C_R \|\xi_n^A\|_{L^2(\mathcal{T}_h^S)}^2 + \frac{C_R}{\delta_{41}} \|\xi_p^A\|_{L^2(\mathcal{T}_h^S)}^2 \\ &\quad + \frac{CC_R}{\delta_{42}} h_S^{2\min(s, k+1)} \left(|\rho_n|_{H^s(\mathcal{T}_h^S)}^2 \right) + \frac{CC_R}{\delta_{43}} h_S^{2\min(s, k+1)} \left(|\rho_p|_{H^s(\mathcal{T}_h^S)}^2 \right), \end{aligned} \quad (4.5.27)$$

Similarly for T_5 we have,

$$\begin{aligned} T_5 &= 2 \left| \left(\xi_p^A, \tilde{R}(\rho_n, \rho_p) - \tilde{R}(\rho_{n,h}, \rho_{p,h}) \right)_{\Omega_S} \right| \\ &\leq 2 \|\xi_p^A\|_{L^2(\mathcal{T}_h^S)} \|\tilde{R}(\rho_n, \rho_p) - \tilde{R}(\rho_{n,h}, \rho_{p,h})\|_{L^2(\mathcal{T}_h^E)} \\ &\leq 2 C_R \|\xi_p^A\|_{L^2(\mathcal{T}_h^S)} \left(\|\rho_n - \rho_{n,h}\|_{L^2(\mathcal{T}_h^S)} + \|\rho_p - \rho_{p,h}\|_{L^2(\mathcal{T}_h^S)} \right) \\ &\leq 2 C_R \|\xi_p^A\|_{L^2(\mathcal{T}_h^S)} \sum_{c=n,p} \left(\|\xi_c^A\|_{L^2(\mathcal{T}_h^S)} + \|\xi_c^I\|_{L^2(\mathcal{T}_h^S)} \right) \\ &= 2 C_R \|\xi_p^A\|_{L^2(\mathcal{T}_h^S)}^2 + 2 C_R \|\xi_n^A\|_{L^2(\mathcal{T}_h^S)} \|\xi_p^A\|_{L^2(\mathcal{T}_h^S)} \\ &\quad + 2 C_R \|\xi_p^A\|_{L^2(\mathcal{T}_h^S)} \|\xi_n^I\|_{L^2(\mathcal{T}_h^S)} + 2 C_R \|\xi_p^A\|_{L^2(\mathcal{T}_h^S)} \|\xi_p^I\|_{L^2(\mathcal{T}_h^S)} \quad (4.5.28) \\ &\leq 2 C_R \|\xi_p^A\|_{L^2(\mathcal{T}_h^S)}^2 + 2 C_R \|\xi_n^A\|_{L^2(\mathcal{T}_h^S)} \|\xi_p^A\|_{L^2(\mathcal{T}_h^S)} \\ &\quad + 2 C_R \|\xi_p^A\|_{L^2(\mathcal{T}_h^S)} \|\xi_n^I\|_{L^2(\mathcal{T}_h^S)} + 2 C_R \|\xi_p^A\|_{L^2(\mathcal{T}_h^S)} \|\xi_p^I\|_{L^2(\mathcal{T}_h^S)}, \\ &\leq (2 + \delta_{51} + \delta_{52} + \delta_{53}) C_R \|\xi_p^A\|_{L^2(\mathcal{T}_h^S)}^2 + \frac{C_R}{\delta_{51}} \|\xi_n^A\|_{L^2(\mathcal{T}_h^S)}^2 \\ &\quad + \frac{C_R}{\delta_{52}} \|\xi_n^I\|_{L^2(\mathcal{T}_h^S)}^2 + \frac{C_R}{\delta_{53}} \|\xi_p^I\|_{L^2(\mathcal{T}_h^S)}^2, \end{aligned}$$

Using the projection properties (4.5.9) and (4.5.10) we obtain the estimate,

$$\begin{aligned}
T_5 \leq & (2 + \delta_{51} + \delta_{52} + \delta_{53}) C_R \|\xi_p^A\|_{L^2(\mathcal{T}_h^S)}^2 + \frac{C_R}{\delta_{51}} \|\xi_n^A\|_{L^2(\mathcal{T}_h^S)}^2 + \\
& + \frac{CC_R}{\delta_{52}} h_S^{2\min(s,k+1)} \left(|\rho_n|_{H^s(\mathcal{T}_h^S)}^2 \right) + \frac{CC_R}{\delta_{53}} h_S^{2\min(s,k+1)} \left(|\rho_p|_{H^s(\mathcal{T}_h^S)}^2 \right). \tag{4.5.29}
\end{aligned}$$

Combining the terms $T_{45} = T_4 + T_5$ we have,

$$\begin{aligned}
T_{45} \leq & (2 + \delta_{41} + \delta_{42} + \delta_{43} + \frac{1}{\delta_{51}}) C_R \|\xi_n^A\|_{L^2(\mathcal{T}_h^S)}^2 \\
& + (2 + \delta_{51} + \delta_{52} + \delta_{53} + \frac{1}{\delta_{41}}) C_R \|\xi_p^A\|_{L^2(\mathcal{T}_h^S)}^2 \\
& + CC_R h_S^{2\min(s,k+1)} \left(\left(\frac{1}{\delta_{42}} + \frac{1}{\delta_{52}} \right) |\rho_n|_{H^s(\mathcal{T}_h^S)}^2 + \left(\frac{1}{\delta_{43}} + \frac{1}{\delta_{53}} \right) |\rho_p|_{H^s(\mathcal{T}_h^S)}^2 \right). \tag{4.5.30}
\end{aligned}$$

Now we work on T_3 ,

$$\begin{aligned}
T_3 &= 2 |\mathcal{J}(\xi_n^A, \xi_p^A, \xi_r^A, \xi_o^A; \rho_n, \rho_p, \rho_r, \rho_o) - \mathcal{J}(\xi_n^A, \xi_p^A, \xi_r^A, \xi_o^A; \rho_{n,h}, \rho_{p,h}, \rho_{r,h}, \rho_{o,h})|, \\
&= 2 |\langle \xi_n^A, I_{et}(\mathcal{M}(\rho_n - \rho_n^e), \mathcal{M}(\rho_o)) - I_{et}(\mathcal{M}(\rho_{n,h} - \rho_n^e), \mathcal{M}(\rho_{o,h})) \rangle_{\mathcal{E}_\Sigma}| \\
&\quad + 2 |\langle \xi_p^A, I_{ht}(\mathcal{M}(\rho_p - \rho_p^e), \mathcal{M}(\rho_r)) - I_{ht}(\mathcal{M}(\rho_{p,h} - \rho_p^e), \mathcal{M}(\rho_{r,h})) \rangle_{\mathcal{E}_\Sigma}| \\
&\quad + 2 |\langle \xi_r^A, I_{ht}(\mathcal{M}(\rho_p - \rho_p^e), \mathcal{M}(\rho_r)) - I_{ht}(\mathcal{M}(\rho_{p,h} - \rho_p^e), \mathcal{M}(\rho_{r,h})) \rangle_{\mathcal{E}_\Sigma}| \\
&\quad + 2 |\langle \xi_r^A, I_{et}(\mathcal{M}(\rho_n - \rho_n^e), \mathcal{M}(\rho_o)) - I_{et}(\mathcal{M}(\rho_{n,h} - \rho_n^e), \mathcal{M}(\rho_{o,h})) \rangle_{\mathcal{E}_\Sigma}| \\
&\quad + 2 |\langle \xi_o^A, I_{ht}(\mathcal{M}(\rho_p - \rho_p^e), \mathcal{M}(\rho_r)) - I_{ht}(\mathcal{M}(\rho_{p,h} - \rho_p^e), \mathcal{M}(\rho_{r,h})) \rangle_{\mathcal{E}_\Sigma}| \\
&\quad + 2 |\langle \xi_o^A, I_{et}(\mathcal{M}(\rho_n - \rho_n^e), \mathcal{M}(\rho_o)) - I_{et}(\mathcal{M}(\rho_{n,h} - \rho_n^e), \mathcal{M}(\rho_{o,h})) \rangle_{\mathcal{E}_\Sigma}|, \\
&= S_1 + S_2 + S_3 + S_4 + S_5 + S_6. \tag{4.5.31}
\end{aligned}$$

Working on S_1 we can use the Lipschitz property of $I_{ket}(\mathcal{M}(\cdot), \mathcal{M}(\cdot))$ and to obtain,

$$\begin{aligned}
S_1 &= 2 |\langle \xi_n^A, I_{et}(\mathcal{M}(\rho_n - \rho_n^e), \mathcal{M}(\rho_o)) - I_{et}(\mathcal{M}(\rho_{n,h} - \rho_n^e), \mathcal{M}(\rho_{o,h})) \rangle_{\mathcal{E}_\Sigma}|, \\
&\leq 2 \langle \xi_n^A, |I_{et}(\mathcal{M}(\rho_n - \rho_n^e), \mathcal{M}(\rho_o)) - I_{et}(\mathcal{M}(\rho_{n,h} - \rho_n^e), \mathcal{M}(\rho_{o,h}))| \rangle_{\mathcal{E}_\Sigma}, \\
&\leq 2 \langle \xi_n^A, k_{et}M |\rho_n - \rho_{n,h}| \rangle_{\mathcal{E}_\Sigma} + 2 \langle \xi_n^A, k_{et}M |\rho_{o,h} - \rho_{o,h}| \rangle_{\mathcal{E}_\Sigma}, \\
&\leq 2 k_{et}M \|\xi_n^A\|_{L^2(\mathcal{E}_\Sigma)} (\|\rho_n - \rho_{n,h}\|_{L^2(\mathcal{E}_\Sigma)} + \|\rho_o - \rho_{o,h}\|_{L^2(\mathcal{E}_\Sigma)}), \\
&\leq 2 k_{et}M \|\xi_n^A\|_{L^2(\mathcal{E}_\Sigma)}^2 + 2 k_{et}M \|\xi_n^A\|_{L^2(\mathcal{E}_\Sigma)} \|\xi_n^I\|_{L^2(\mathcal{E}_\Sigma)} \\
&\quad + 2 k_{et}M \|\xi_n^A\|_{L^2(\mathcal{E}_\Sigma)} \|\xi_o^A\|_{L^2(\mathcal{E}_\Sigma)} + 2 k_{et}M \|\xi_n^A\|_{L^2(\mathcal{E}_\Sigma)} \|\xi_o^I\|_{L^2(\mathcal{E}_\Sigma)}. \tag{4.5.32}
\end{aligned}$$

Similarly for S_2 ,

$$\begin{aligned}
S_2 &= 2 |\langle \xi_p^A, I_{ht}(\mathcal{M}(\rho_p - \rho_p^e), \mathcal{M}(\rho_r)) - I_{et}(\mathcal{M}(\rho_{p,h} - \rho_p^e), \mathcal{M}(\rho_{r,h})) \rangle_{\mathcal{E}_\Sigma}|, \\
&\leq 2 k_{ht}M \|\xi_p^A\|_{L^2(\mathcal{E}_\Sigma)} (\|\rho_p - \rho_{p,h}\|_{L^2(\mathcal{E}_\Sigma)} + \|\rho_r - \rho_{r,h}\|_{L^2(\mathcal{E}_\Sigma)}), \\
&\leq 2 k_{ht}M \|\xi_p^A\|_{L^2(\mathcal{E}_\Sigma)}^2 + 2 k_{ht}M \|\xi_p^A\|_{L^2(\mathcal{E}_\Sigma)} \|\xi_p^I\|_{L^2(\mathcal{E}_\Sigma)} \\
&\quad + 2 k_{ht}M \|\xi_p^A\|_{L^2(\mathcal{E}_\Sigma)} \|\xi_r^A\|_{L^2(\mathcal{E}_\Sigma)} + 2 k_{ht}M \|\xi_p^A\|_{L^2(\mathcal{E}_\Sigma)} \|\xi_r^I\|_{L^2(\mathcal{E}_\Sigma)}. \tag{4.5.33}
\end{aligned}$$

And S_3 ,

$$\begin{aligned}
S_3 &= 2 |\langle \xi_r^A, I_{ht}(\mathcal{M}(\rho_p - \rho_p^e), \mathcal{M}(\rho_r)) - I_{et}(\mathcal{M}(\rho_{p,h} - \rho_p^e), \mathcal{M}(\rho_{r,h})) \rangle_{\mathcal{E}_\Sigma}|, \\
&\leq 2 k_{ht}M \|\xi_r^A\|_{L^2(\mathcal{E}_\Sigma)} (\|\rho_p - \rho_{p,h}\|_{L^2(\mathcal{E}_\Sigma)} + \|\rho_r - \rho_{r,h}\|_{L^2(\mathcal{E}_\Sigma)}), \\
&\leq 2 k_{ht}M \|\xi_r^A\|_{L^2(\mathcal{E}_\Sigma)} \|\xi_p^A\|_{L^2(\mathcal{E}_\Sigma)} + 2 k_{ht}M \|\xi_r^A\|_{L^2(\mathcal{E}_\Sigma)} \|\xi_p^I\|_{L^2(\mathcal{E}_\Sigma)} \\
&\quad + 2 k_{ht}M \|\xi_r^A\|_{L^2(\mathcal{E}_\Sigma)}^2 + 2 k_{ht}M \|\xi_r^A\|_{L^2(\mathcal{E}_\Sigma)} \|\xi_r^I\|_{L^2(\mathcal{E}_\Sigma)} \tag{4.5.34}
\end{aligned}$$

And S_4 ,

$$\begin{aligned}
S_4 &= 2 |\langle \xi_r^A, I_{et}(\mathcal{M}(\rho_n - \rho_n^e), \mathcal{M}(\rho_o)) - I_{et}(\mathcal{M}(\rho_{n,h} - \rho_n^e), \mathcal{M}(\rho_{o,h})) \rangle_{\mathcal{E}_\Sigma}|, \\
&\leq 2 k_{et} M \|\xi_r^A\|_{L^2(\mathcal{E}_\Sigma)} (\|\rho_n - \rho_{n,h}\|_{L^2(\mathcal{E}_\Sigma)} + \|\rho_o - \rho_{o,h}\|_{L^2(\mathcal{E}_\Sigma)}), \\
&\leq 2 k_{et} M \|\xi_r^A\|_{L^2(\mathcal{E}_\Sigma)} \|\xi_n^A\|_{L^2(\mathcal{E}_\Sigma)} + 2 k_{et} M \|\xi_r^A\|_{L^2(\mathcal{E}_\Sigma)} \|\xi_n^I\|_{L^2(\mathcal{E}_\Sigma)} \\
&\quad + 2 k_{et} M \|\xi_r^A\|_{L^2(\mathcal{E}_\Sigma)} \|\xi_o^A\|_{L^2(\mathcal{E}_\Sigma)} + 2 k_{et} M \|\xi_r^A\|_{L^2(\mathcal{E}_\Sigma)} \|\xi_o^I\|_{L^2(\mathcal{E}_\Sigma)} \tag{4.5.35}
\end{aligned}$$

And S_5 ,

$$\begin{aligned}
S_5 &= 2 |\langle \xi_o^A, I_{ht}(\mathcal{M}(\rho_p - \rho_p^e), \mathcal{M}(\rho_r)) - I_{et}(\mathcal{M}(\rho_{p,h} - \rho_p^e), \mathcal{M}(\rho_{r,h})) \rangle_{\mathcal{E}_\Sigma}|, \\
&\leq 2 k_{ht} M \|\xi_o^A\|_{L^2(\mathcal{E}_\Sigma)} (\|\rho_p - \rho_{p,h}\|_{L^2(\mathcal{E}_\Sigma)} + \|\rho_r - \rho_{r,h}\|_{L^2(\mathcal{E}_\Sigma)}), \\
&\leq 2 k_{ht} M \|\xi_o^A\|_{L^2(\mathcal{E}_\Sigma)} \|\xi_p^A\|_{L^2(\mathcal{E}_\Sigma)} + 2 k_{ht} M \|\xi_o^A\|_{L^2(\mathcal{E}_\Sigma)} \|\xi_p^I\|_{L^2(\mathcal{E}_\Sigma)} \\
&\quad + 2 k_{ht} M \|\xi_o^A\|_{L^2(\mathcal{E}_\Sigma)} \|\xi_r^A\|_{L^2(\mathcal{E}_\Sigma)} + 2 k_{ht} M \|\xi_o^A\|_{L^2(\mathcal{E}_\Sigma)} \|\xi_r^I\|_{L^2(\mathcal{E}_\Sigma)}, \tag{4.5.36}
\end{aligned}$$

And finally S_6 ,

$$\begin{aligned}
S_6 &= 2 |\langle \xi_o^A, I_{et}(\mathcal{M}(\rho_n - \rho_n^e), \mathcal{M}(\rho_o)) - I_{et}(\mathcal{M}(\rho_{n,h} - \rho_n^e), \mathcal{M}(\rho_{o,h})) \rangle_{\mathcal{E}_\Sigma}|, \\
&\leq 2 k_{et} M \|\xi_o^A\|_{L^2(\mathcal{E}_\Sigma)} (\|\rho_n - \rho_{n,h}\|_{L^2(\mathcal{E}_\Sigma)} + \|\rho_o - \rho_{o,h}\|_{L^2(\mathcal{E}_\Sigma)}), \\
&\leq 2 k_{et} M \|\xi_o^A\|_{L^2(\mathcal{E}_\Sigma)} \|\xi_n^A\|_{L^2(\mathcal{E}_\Sigma)} + 2 k_{et} M \|\xi_o^A\|_{L^2(\mathcal{E}_\Sigma)} \|\xi_n^I\|_{L^2(\mathcal{E}_\Sigma)} \\
&\quad + 2 k_{et} M \|\xi_o^A\|_{L^2(\mathcal{E}_\Sigma)}^2 + 2 k_{et} M \|\xi_o^A\|_{L^2(\mathcal{E}_\Sigma)} \|\xi_o^I\|_{L^2(\mathcal{E}_\Sigma)}. \tag{4.5.37}
\end{aligned}$$

Collecting all the terms we have,

$$\begin{aligned}
T_3 \leq & 2M \left(k_{et} \|\xi_n^A\|_{L^2(\mathcal{E}_\Sigma)}^2 + k_{ht} \|\xi_p^A\|_{L^2(\mathcal{E}_\Sigma)}^2 + k_{ht} \|\xi_r^A\|_{L^2(\mathcal{E}_\Sigma)}^2 + k_{et} \|\xi_o^A\|_{L^2(\mathcal{E}_\Sigma)}^2 \right) \\
& + 4M \left(k_{et} \|\xi_n^A\|_{L^2(\mathcal{E}_\Sigma)} \|\xi_o^A\|_{L^2(\mathcal{E}_\Sigma)} + k_{ht} \|\xi_p^A\|_{L^2(\mathcal{E}_\Sigma)} \|\xi_r^A\|_{L^2(\mathcal{E}_\Sigma)} \right) \\
& + 2M (k_{et} + k_{ht}) \|\xi_r^A\|_{L^2(\mathcal{E}_\Sigma)} \|\xi_o^A\|_{L^2(\mathcal{E}_\Sigma)} \\
& + 2M \left(k_{ht} \|\xi_o^A\|_{L^2(\mathcal{E}_\Sigma)} \|\xi_p^A\|_{L^2(\mathcal{E}_\Sigma)} + k_{et} \|\xi_n^A\|_{L^2(\mathcal{E}_\Sigma)} \|\xi_r^A\|_{L^2(\mathcal{E}_\Sigma)} \right) \\
& + 2M k_{et} \|\xi_n^A\|_{L^2(\mathcal{E}_\Sigma)} (\|\xi_n^I\|_{L^2(\mathcal{E}_\Sigma)} + \|\xi_o^I\|_{L^2(\mathcal{E}_\Sigma)}) \\
& + 2M k_{ht} \|\xi_p^A\|_{L^2(\mathcal{E}_\Sigma)} (\|\xi_p^I\|_{L^2(\mathcal{E}_\Sigma)} + \|\xi_r^I\|_{L^2(\mathcal{E}_\Sigma)}) \\
& + 2M (\|\xi_r^A\|_{L^2(\mathcal{E}_\Sigma)} + \|\xi_o^A\|_{L^2(\mathcal{E}_\Sigma)}) \\
& (k_{et} \|\xi_n^I\|_{L^2(\mathcal{E}_\Sigma)} + k_{ht} \|\xi_p^I\|_{L^2(\mathcal{E}_\Sigma)} + k_{ht} \|\xi_r^I\|_{L^2(\mathcal{E}_\Sigma)} + k_{et} \|\xi_o^I\|_{L^2(\mathcal{E}_\Sigma)}) \tag{4.5.38}
\end{aligned}$$

Using Young's inequality (Lemma 4.1.2) yields,

$$\begin{aligned}
T_3 \leq & 2M \left(k_{et} \|\xi_n^A\|_{L^2(\mathcal{E}_\Sigma)}^2 + k_{ht} \|\xi_p^A\|_{L^2(\mathcal{E}_\Sigma)}^2 + k_{ht} \|\xi_r^A\|_{L^2(\mathcal{E}_\Sigma)}^2 + k_{et} \|\xi_o^A\|_{L^2(\mathcal{E}_\Sigma)}^2 \right) \\
& + 2M k_{et} \delta_{31} \|\xi_n^A\|_{L^2(\mathcal{E}_\Sigma)}^2 + \frac{2M k_{et}}{\delta_{31}} \|\xi_o^A\|_{L^2(\mathcal{E}_\Sigma)}^2 \\
& + 2M k_{ht} \delta_{32} \|\xi_p^A\|_{L^2(\mathcal{E}_\Sigma)}^2 + \frac{2M k_{ht}}{\delta_{32}} \|\xi_r^A\|_{L^2(\mathcal{E}_\Sigma)}^2 \\
& + M (k_{et} + k_{ht}) \delta_{33} \|\xi_r^A\|_{L^2(\mathcal{E}_\Sigma)}^2 + \frac{M (k_{et} + k_{ht})}{\delta_{33}} \|\xi_o^A\|_{L^2(\mathcal{E}_\Sigma)}^2 \\
& + M \delta_{34} k_{ht} \|\xi_o^A\|_{L^2(\mathcal{E}_\Sigma)}^2 + \frac{M k_{ht}}{\delta_{34}} \|\xi_p^A\|_{L^2(\mathcal{E}_\Sigma)}^2 \\
& + M k_{et} \delta_{35} \|\xi_n^A\|_{L^2(\mathcal{E}_\Sigma)}^2 + \frac{M k_{et}}{\delta_{35}} \|\xi_r^A\|_{L^2(\mathcal{E}_\Sigma)}^2 \\
& + M k_{et} \delta_{36} \|\xi_n^A\|_{L^2(\mathcal{E}_\Sigma)}^2 + \frac{M k_{et}}{\delta_{36}} \left(\|\xi_n^I\|_{L^2(\mathcal{E}_\Sigma)} + \|\xi_o^I\|_{L^2(\mathcal{E}_\Sigma)} \right)^2 \\
& + M k_{ht} \delta_{37} \|\xi_p^A\|_{L^2(\mathcal{E}_\Sigma)}^2 + \frac{M k_{ht}}{\delta_{37}} \left(\|\xi_p^I\|_{L^2(\mathcal{E}_\Sigma)} + \|\xi_r^I\|_{L^2(\mathcal{E}_\Sigma)} \right)^2 \\
& + M \left(\delta_{38} \|\xi_r^A\|_{L^2(\mathcal{E}_\Sigma)}^2 + \delta_{39} \|\xi_o^A\|_{L^2(\mathcal{E}_\Sigma)}^2 \right) \\
& + \frac{M}{\delta_{38}} \left(k_{et} \|\xi_n^I\|_{L^2(\mathcal{E}_\Sigma)} + k_{ht} \|\xi_p^I\|_{L^2(\mathcal{E}_\Sigma)} + k_{ht} \|\xi_r^I\|_{L^2(\mathcal{E}_\Sigma)} + k_{et} \|\xi_o^I\|_{L^2(\mathcal{E}_\Sigma)} \right)^2 \\
& + \frac{M}{\delta_{39}} \left(k_{et} \|\xi_n^I\|_{L^2(\mathcal{E}_\Sigma)} + k_{ht} \|\xi_p^I\|_{L^2(\mathcal{E}_\Sigma)} + k_{ht} \|\xi_r^I\|_{L^2(\mathcal{E}_\Sigma)} + k_{et} \|\xi_o^I\|_{L^2(\mathcal{E}_\Sigma)} \right)^2
\end{aligned} \tag{4.5.39}$$

Or,

$$\begin{aligned}
T_3 \leq & M k_{et} (2 + 2\delta_{31} + \delta_{35} + \delta_{36}) \|\xi_n^A\|_{L^2(\mathcal{E}_\Sigma)}^2 \\
& + M k_{ht} \left(2 + 2\delta_{32} + \frac{1}{\delta_{34}} + \delta_{37} \right) \|\xi_p^A\|_{L^2(\mathcal{E}_\Sigma)}^2 \\
& + M \left(2k_{ht} + \frac{2k_{ht}}{\delta_{32}} + (k_{et} + k_{ht})\delta_{33} + \frac{k_{et}}{\delta_{35}} + \delta_{38} \right) \|\xi_r^A\|_{L^2(\mathcal{E}_\Sigma)}^2 \\
& + M \left(2k_{et} + \frac{2k_{et}}{\delta_{31}} + \frac{(k_{et} + k_{ht})}{\delta_{33}} + k_{ht}\delta_{34} + \delta_{39} \right) \|\xi_o^A\|_{L^2(\mathcal{E}_\Sigma)}^2 \\
& + \frac{M k_{et}}{\delta_{36}} (\|\xi_n^I\|_{L^2(\mathcal{E}_\Sigma)} + \|\xi_o^I\|_{L^2(\mathcal{E}_\Sigma)})^2 + \frac{M k_{ht}}{\delta_{37}} (\|\xi_p^I\|_{L^2(\mathcal{E}_\Sigma)} + \|\xi_r^I\|_{L^2(\mathcal{E}_\Sigma)})^2 \\
& + \frac{M}{\delta_{38}} (k_{et}\|\xi_n^I\|_{L^2(\mathcal{E}_\Sigma)} + k_{ht}\|\xi_p^I\|_{L^2(\mathcal{E}_\Sigma)} + k_{ht}\|\xi_r^I\|_{L^2(\mathcal{E}_\Sigma)} + k_{et}\|\xi_o^I\|_{L^2(\mathcal{E}_\Sigma)})^2 \\
& + \frac{M}{\delta_{39}} (k_{et}\|\xi_n^I\|_{L^2(\mathcal{E}_\Sigma)} + k_{ht}\|\xi_p^I\|_{L^2(\mathcal{E}_\Sigma)} + k_{ht}\|\xi_r^I\|_{L^2(\mathcal{E}_\Sigma)} + k_{et}\|\xi_o^I\|_{L^2(\mathcal{E}_\Sigma)})^2
\end{aligned} \tag{4.5.40}$$

Using the Theorem 4.1.11, the projection properties (4.5.11) and (4.5.12) yields,

$$\begin{aligned}
T_3 \leq & M k_{et} (C_{\text{tr}}^S)^2 (2 + 2\delta_{31} + \delta_{35} + \delta_{36}) \|\xi_n^A\|_{\text{DG,S}}^2 \\
& + M k_{ht} (C_{\text{tr}}^S)^2 \left(2 + 2\delta_{32} + \frac{1}{\delta_{34}} + \delta_{37} \right) \|\xi_p^A\|_{\text{DG,S}}^2 \\
& + M (C_{\text{tr}}^E)^2 \left(2k_{ht} + \frac{2k_{ht}}{\delta_{32}} + (k_{et} + k_{ht})\delta_{33} + \frac{k_{et}}{\delta_{35}} + \delta_{38} \right) \|\xi_r^A\|_{\text{DG,E}}^2 \\
& + M (C_{\text{tr}}^E)^2 \left(2k_{et} + \frac{2k_{et}}{\delta_{31}} + \frac{(k_{et} + k_{ht})}{\delta_{33}} + k_{ht}\delta_{34} + \delta_{39} \right) \|\xi_o^A\|_{\text{DG,E}}^2 \\
& + M C_\Sigma \max(h_S^{2\min(k+1,s)-2}, h_E^{2\min(k+1,s)-2})
\end{aligned} \tag{4.5.41}$$

Where,

$$C_\Sigma = C \left(k_{et}, k_{ht}, C_{\text{tr}}^S, C_{\text{tr}}^E, |\rho_n|_{H^s(\mathcal{T}_h^S)}, |\rho_p|_{H^s(\mathcal{T}_h^S)}, |\rho_r|_{H^s(\mathcal{T}_h^E)}, |\rho_o|_{H^s(\mathcal{T}_h^E)} \right). \tag{4.5.42}$$

We can combine (4.5.23), (4.5.25), (4.5.41), (4.5.30) to obtain a single bound in (4.5.22),

$$\begin{aligned}
& \frac{d}{dt} \left(\sum_{c=n,p} \|\xi_c^A\|_{L^2(\mathcal{T}_h^S)}^2 + \sum_{c=r,o} \|\xi_c^A\|_{L^2(\mathcal{T}_h^E)}^2 \right) + \sum_{c=n,p} \gamma_c^2 \|\xi_c^A\|_{\text{DG,S}}^2 + \sum_{c=r,o} \gamma_c^2 \|\xi_c^A\|_{\text{DG,E}}^2 \\
& \leq \left(\delta_{1,n} + C_R (2 + \delta_{41} + \delta_{42} + \delta_{43} + \frac{1}{\delta_{51}}) \right) \|\xi_n^A\|_{L^2(\mathcal{T}_h^S)}^2 \\
& \quad + (K_{n,S} \delta_{2,n} + M k_{et} (C_{\text{tr}}^S)^2 (2 + 2\delta_{31} + \delta_{35} + \delta_{36})) \|\xi_n^A\|_{\text{DG,S}}^2 \\
& \quad + \left(\delta_{1,p} + C_R (2 + \delta_{51} + \delta_{52} + \delta_{53} + \frac{1}{\delta_{41}}) \right) \|\xi_p^A\|_{L^2(\mathcal{T}_h^S)}^2 \\
& \quad + \left(K_{p,S} \delta_{2,p} + M k_{ht} (C_{\text{tr}}^S)^2 (2 + 2\delta_{32} + \frac{1}{\delta_{34}} + \delta_{37}) \right) \|\xi_p^A\|_{\text{DG,S}}^2 \\
& \quad + \delta_{1,o} \|\xi_o^A\|_{L^2(\mathcal{T}_h^E)}^2 + \delta_{1,r} \|\xi_r^A\|_{L^2(\mathcal{T}_h^E)}^2 \\
& \quad + \left(K_{r,E} \delta_{2,r} + M (C_{\text{tr}}^E)^2 \left(2k_{ht} + \frac{2k_{ht}}{\delta_{32}} + (k_{et} + k_{ht}) \delta_{33} + \frac{k_{et}}{\delta_{35}} + \delta_{38} \right) \right) \|\xi_r^A\|_{\text{DG,E}}^2 \\
& \quad + \left(K_{o,E} \delta_{2,o} + M (C_{\text{tr}}^E)^2 \left(2k_{et} + \frac{2k_{et}}{\delta_{31}} + \frac{(k_{et} + k_{ht})}{\delta_{33}} + k_{ht} \delta_{34} + \delta_{39} \right) \right) \|\xi_o^A\|_{\text{DG,E}}^2 \\
& \quad + C_1 \max \left(h_S^{2 \min(k+1,s)}, h_E^{2 \min(k+1,s)} \right) + C_2 \max \left(h_S^{2 \min(k+1,s)-2}, h_E^{2 \min(k+1,s)-2} \right)
\end{aligned} \tag{4.5.43}$$

Choosing $\delta_{1,n} = \delta_{1,p} = C_R$, $\delta_{1,r} = \delta_{1,o} = 1$, $\delta_{41} = \delta_{51} = 1$ and $\delta_{42} = \delta_{43} = \delta_{52} = \delta_{53} = \frac{1}{2}$. As well as,

$$\delta_{2,c} = \frac{\gamma_c^2}{4K_{c,S}}, \quad \text{for } c = \{n, p\}, \tag{4.5.44}$$

$$\delta_{2,c} = \frac{\gamma_c^2}{4K_{c,E}}, \quad \text{for } c = \{r, o\}. \tag{4.5.45}$$

Taking $\delta_{31} = \delta_{35} = \delta_{36} = \delta_{32} = \delta_{34} = \delta_{37} = \delta_{33} = 1$ and $\delta_{38} = \delta_{39} = k_{ht} + k_{ket}$

yields,

$$\begin{aligned}
& \frac{d}{dt} \left(\sum_{c=n,p} \|\xi_c^A\|_{L^2(\mathcal{T}_h^S)}^2 + \sum_{c=r,o} \|\xi_c^A\|_{L^2(\mathcal{T}_h^E)}^2 \right) \\
& + \left(\frac{3\gamma_n^2}{4} - 6Mk_{et}(C_{\text{tr}}^S)^2 \right) \|\xi_n^A\|_{\text{DG,S}}^2 + \left(\frac{3\gamma_p^2}{4} - 6Mk_{ht}(C_{\text{tr}}^S)^2 \right) \|\xi_p^A\|_{\text{DG,S}}^2 \\
& + \left(\frac{3\gamma_r^2}{4} - M(6k_{ht} + 3k_{et})(C_{\text{tr}}^E)^2 \right) \|\xi_r^A\|_{\text{DG,E}}^2 \\
& + \left(\frac{3\gamma_o^2}{4} - M(3k_{ht} + 6k_{et})(C_{\text{tr}}^E)^2 \right) \|\xi_o^A\|_{\text{DG,E}}^2 \\
& \leq 5C_R \left(\sum_{c=n,p} \|\xi_c^A\|_{L^2(\mathcal{T}_h^S)}^2 \right) + \sum_{c=r,o} \|\xi_c^A\|_{L^2(\mathcal{T}_h^E)}^2 \\
& + C_1 \max \left(h_S^{2 \min(k+1,s)}, h_E^{2 \min(k+1,s)} \right) \\
& + C_2 \max \left(h_S^{2 \min(k+1,s)-2}, h_E^{2 \min(k+1,s)-2} \right)
\end{aligned} \tag{4.5.46}$$

For some constants C_1 and C_2 independent of h . If the coercivity constants satisfy,

$$\gamma_n^2 \geq 24Mk_{et}(C_{\text{tr}}^S)^2 \tag{4.5.47}$$

$$\gamma_p^2 \geq 24Mk_{ht}(C_{\text{tr}}^S)^2 \tag{4.5.48}$$

$$\gamma_r^2 \geq 8M(3k_{ht} + k_{et})(C_{\text{tr}}^E)^2 \tag{4.5.49}$$

$$\gamma_o^2 \geq 8M(k_{ht} + 3k_{et})(C_{\text{tr}}^E)^2 \tag{4.5.50}$$

Then (4.5.46) becomes,

$$\begin{aligned}
& \frac{d}{dt} \left(\sum_{c=n,p} \|\xi_c^A\|_{L^2(\mathcal{T}_h^S)}^2 + \sum_{c=r,o} \|\xi_c^A\|_{L^2(\mathcal{T}_h^E)}^2 \right) \\
& + \sum_{c=n,p} \frac{\gamma_c^2}{2} \|\xi_c^A\|_{\text{DG,S}}^2 + \sum_{c=r,o} \frac{\gamma_c^2}{2} \|\xi_c^A\|_{\text{DG,E}}^2 \\
& \leq 6C_R \left(\sum_{c=n,p} \|\xi_c^A\|_{L^2(\mathcal{T}_h^S)}^2 \right) + \sum_{c=r,o} \|\xi_c^A\|_{L^2(\mathcal{T}_h^E)}^2 \\
& + C_1 \max \left(h_S^{2 \min(k+1,s)}, h_E^{2 \min(k+1,s)} \right) \\
& + C_2 \max \left(h_S^{2 \min(k+1,s)-2}, h_E^{2 \min(k+1,s)-2} \right). \tag{4.5.51}
\end{aligned}$$

Integrating from $(0, T)$ we have

$$\begin{aligned}
& \sum_{c=n,p} \|\xi_c^A(T)\|_{L^2(\mathcal{T}_h^S)}^2 + \sum_{c=r,o} \|\xi_c^A(T)\|_{L^2(\mathcal{T}_h^E)}^2 + \sum_{c=n,p} \frac{\gamma_c^2}{2} \int_0^T \|\xi_c^A(t)\|_{\text{DG,S}}^2 dt \\
& + \sum_{c=r,o} \frac{\gamma_c^2}{2} \int_0^T \|\xi_c^A(t)\|_{\text{DG,E}}^2 dt \\
& \leq \sum_{c=n,p} \|\xi_c^A(0)\|_{L^2(\mathcal{T}_h^S)}^2 + \sum_{c=r,o} \|\xi_c^A(0)\|_{L^2(\mathcal{T}_h^E)}^2 \\
& + 6C_R \sum_{c=n,p} \int_0^T \|\xi_c^A(t)\|_{L^2(\mathcal{T}_h^S)}^2 dt + \sum_{c=r,o} \int_0^T \|\xi_c^A(t)\|_{L^2(\mathcal{T}_h^E)}^2 dt \\
& + C_1 T \max \left(h_S^{2 \min(k+1,s)}, h_E^{2 \min(k+1,s)} \right) \\
& + C_2 T \max \left(h_S^{2 \min(k+1,s)-2}, h_E^{2 \min(k+1,s)-2} \right). \tag{4.5.52}
\end{aligned}$$

Using the fact the initial conditions are the L^2 projection on to the the DG

basis and Gronwall's inequality (Theorem 4.1.5) yields,

$$\begin{aligned}
& \sum_{c=n,p} \|\xi_c^A(T)\|_{L^2(\mathcal{T}_h^S)}^2 + \sum_{c=r,o} \|\xi_c^A(T)\|_{L^2(\mathcal{T}_h^E)}^2 \\
& + \sum_{c=n,p} \frac{\gamma_c^2}{2} \int_0^T \|\xi_c^A(t)\|_{\text{DG,S}}^2 dt + \sum_{c=r,o} \frac{\gamma_c^2}{2} \int_0^T \|\xi_c^A(t)\|_{\text{DG,E}}^2 dt \\
& \leq C_{L^2} \max \left(h_S^{2 \min(k+1,s)}, h_E^{2 \min(k+1,s)} \right) \\
& + C_{\text{DG}} \max \left(h_S^{2 \min(k+1,s)-2}, h_E^{2 \min(k+1,s)-2} \right).
\end{aligned} \tag{4.5.53}$$

Where,

$$\begin{aligned}
C_{L^2} &= C \left(T, \tau_n, \tau_p, \max_{c \in \{n,p\}} \left(|\rho_c|_{H^s(\mathcal{T}_h^S)} \right), \max_{c \in \{n,p\}} \left(\left| \frac{\partial \rho_c}{\partial t} \right|_{H^s(\mathcal{T}_h^S)} \right), \right. \\
&\quad \left. \max_{c \in \{r,o\}} \left(|\rho_c|_{H^s(\mathcal{T}_h^E)} \right), \max_{c \in \{r,o\}} \left(\left| \frac{\partial \rho_c}{\partial t} \right|_{H^s(\mathcal{T}_h^E)} \right) \right), \\
C_{\text{DG}} &= C \left(T, M, k_{et}, k_{ht}, C_{\text{tr}}^S, C_{\text{tr}}^E, \max_{c \in \{n,p\}} \left(|\rho_c|_{H^s(\mathcal{T}_h^S)} \right), \max_{c \in \{r,o\}} \left(|\rho_c|_{H^s(\mathcal{T}_h^E)} \right), \right. \\
&\quad \left. \max_{c \in \{n,p,r,o\}} (K_c) \right).
\end{aligned} \tag{4.5.54}$$

We can then use the triangle inequality,

$$\|\rho_c - \rho_{c,h}\|_{L^2} \leq \|\xi_c^A\|_{L^2} + \|\xi_c^I\|_{L^2}, \tag{4.5.55}$$

for $c = \{n, p, r, o\}$ to obtain the desired results.

□

Chapter 5

Numerical Results

In this chapter we discuss the performance of the numerical algorithms proposed in Chapter 3 as well as present some results from numerical simulations of photoelectrochemical solar cells. We first conduct a convergence study on the spatial discretization strategies that we employed. The purpose of this study is for code verification purposes as well as to validate the convergence rates that were proven in Chapter 4. We then conduct a study on performance of the proposed time stepping algorithms from Chapter 3 as well as present results on parallel implementation of one specific algorithm. Finally, we discuss some preliminary results from numerical experiments conducted on photoelectrochemical solar cells in one and two dimensions.

5.1 Study On Discretizations Convergence Rates

In order to verify the accuracy of our codes we conduct a convergence study on the individual solvers, i.e. the mixed finite element (MFEM) solver on Poisson's equation and the local discontinuous Galerkin (LDG) solver on the drift-diffusion equation. We show that the individual solvers have convergence rates which are consistent with what their theoretical rates predict. We then

investigate the convergence properties of the spatial discretizations applied to the semiconductor-electrolyte interface problem. We present some of the convergence results from test cases in both one and two dimensions to verify that our numerical routines are operating as expected.

5.1.1 One Dimensional Results

We start with a benchmark study on the convergence properties of the spatial discretization schemes, that is, the MFEM scheme for the Poisson equation and the LDG scheme for the drift-diffusion equations, that we employed. We benchmark our MFEM solver for the Poisson equation,

$$-\frac{d^2\Phi}{dx^2} = -20x^3, \text{ in } (0, 1), \quad \Phi(0) = 0, \quad \Phi(1) = 1. \quad (5.1.1)$$

The analytical solution is $\Phi(x) = x^5$. We use Raviart-Thomas elements for the electric field and discontinuous Legendre elements for the potential. We test the code with basis functions of order 1 and 2 and with meshes that have numbers of elements ranging from 4 to 1024. The L^2 error plots for this test case can be seen in Figure 5.1 (a). We benchmark our LDG solver for the stationary drift-diffusion equation,

$$\frac{1}{\pi}u_x + u_{xx} = 0, \text{ in } (0, \pi), \quad u(0) = 0, \quad u(\pi) = 1. \quad (5.1.2)$$

The analytical solution for this problem solution is $u(x) = \frac{1.0 - e^{-x/\pi}}{1.0 - e^{-1}}$. We use discontinuous Legendre elements to approximate both the density and current. We test the code with basis functions of order 1 and 2 and with meshes that have numbers of elements ranging from 4 to 1024. The L^2 error plots for this

test case can be observed in Figure 5.1 (b). The results show that we achieve optimal convergence rates for both the MFEM and LDG solvers.

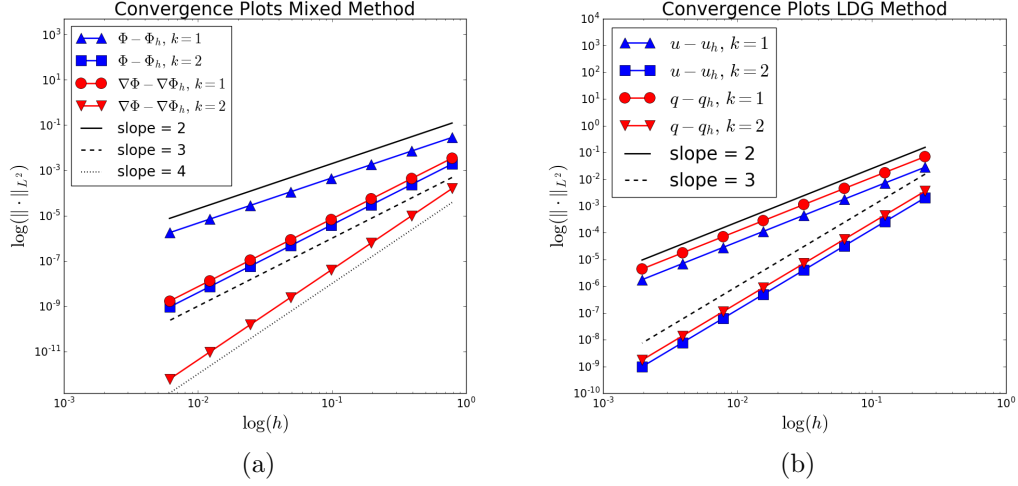


Figure 5.1: 1D L^2 error plots for (a) MFEM on Poisson's equation and (b) LDG on the drift-diffusion equation.

To benchmark the algorithms for the semiconductor-electrolyte interface simulation, we plot L^2 errors in the steady-state electron densities in Figure 5.2. Note that since we do not have a manufactured analytical solution here, we use the numerical solution on an extremely fine mesh in place of the true solution. In Figure 5.2 we show the results for linear and quadratic LDG approximations. The results show that we obtain optimal convergence rates.

5.1.2 Two Dimensional Results

We break the verification for the two dimensional code into three cases:

1. Testing the MFEM and LDG solvers independently.

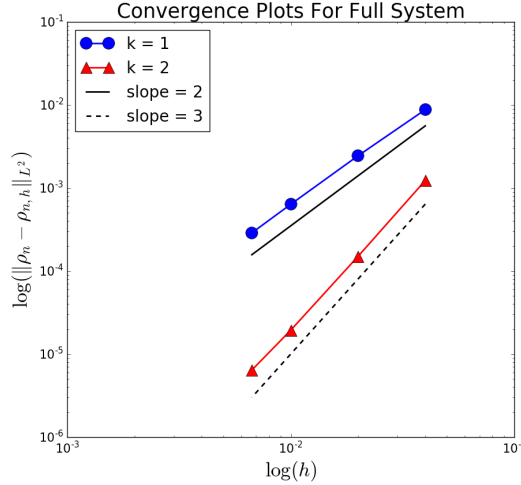


Figure 5.2: L^2 error plots for steady-state electron densities.

2. Testing the coupling of the MFEM solver and the LDG solver.
3. Testing the coupling of two LDG solvers across a reactive interface.

These cases test all the individual components and coupling procedures that will be used in simulations of the semiconductor-electrolyte interface. To be specific case 1 verifies that each individual solver is operating properly. In case 2 we use two meshes: one for the MFEM and one for the LDG method. This test problem not only verifies that the coupling between MFEM and LDG solvers is operating correctly, but also that the mappings between the Poisson mesh and the semiconductor or electrolyte mesh are constructed properly. In case 3 we again use two meshes: one for the semiconductor and one for the electrolyte. This test problem not only verifies that the coupling of two LDG solvers across a reactive interface is operating correctly, but also that

the mapping between the semiconductor and electrolyte interface mesh faces is constructed properly.

5.1.2.1 Decoupled Tests

We test the mixed finite element solver in two dimensions on the Poisson equation,

$$\begin{aligned} -\Delta\Phi(\mathbf{x}) &= f(\mathbf{x}) && \text{in } [0, 1] \times [0, 1], \\ \mathbf{n} \cdot (-\nabla\Phi(\mathbf{x})) &= 0 && \text{on } [0, 1] \times \{y = 0, 1\}, \\ \Phi(\mathbf{x}) &= \Phi_D(\mathbf{x}) && \text{on } \{x = 0, 1\} \times [0, 1]. \end{aligned} \quad (5.1.3)$$

We use the manufactured solution,

$$\Phi(x, y) = \cos(2\pi y) - \sin(2\pi x) - x, \quad (5.1.4)$$

which has a corresponding right hand side function,

$$f(x, y) = 4\pi^2 (\cos(2\pi y) - \sin(2\pi x)). \quad (5.1.5)$$

We use the solution $\Phi(x, y)$ to prescribe the Dirichlet data values $\Phi_D(x, y)$ on the boundary. The L^2 errors for the mixed method using $k = 1$ and $k = 2$ can be seen in Figure 5.3. We see that we achieve optimal convergence for the approximations of Φ and super convergence for the approximation of $-\nabla\Phi$.

To test the LDG-IMEX method on the time-dependent linear drift-

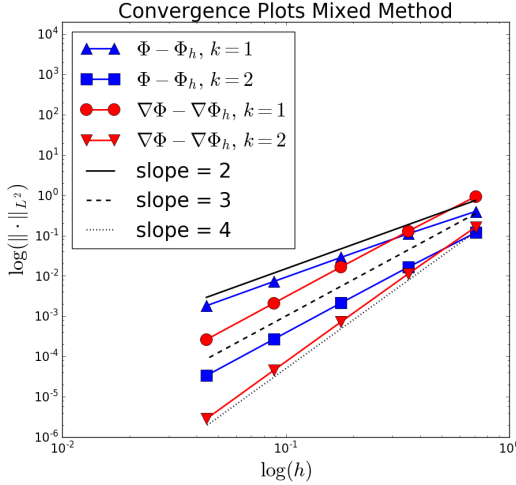


Figure 5.3: 2D L^2 error plots for MFEM for the problem (5.1.3).

diffusion equation we solve the problem,

$$\begin{aligned}
 u_t + \nabla \cdot (\mathbf{E}u - \nabla u) &= f(\mathbf{x}, t) && \text{in } \Omega \times (0, T), \\
 \mathbf{n} \cdot (\mathbf{E}u - \nabla u) &= g_I(\mathbf{x}, t) && \text{on } \Gamma_I \times (0, T), \\
 \mathbf{n} \cdot (\mathbf{E}u - \nabla u) &= 0 && \text{on } \Gamma_N \times (0, T), \\
 u &= g_D(\mathbf{x}, t) && \text{on } \Gamma_D \times (0, T), \\
 u &= u_0(\mathbf{x}) && \text{in } \Omega \times \{t = 0\}.
 \end{aligned} \tag{5.1.6}$$

We take the domain to be $\Omega = [0, 1] \times [0, 1]$ with boundaries $\partial\Omega = \Gamma_D \cup \Gamma_N \cup \Gamma_I$.

The “reactive interface” is the boundary $\Gamma_I = \{x = 1\} \times [0, 1]$. We break up the other boundaries up into two cases:

- **Case 1:** $\Gamma_D = (\{x = 0\} \times [0, 1]) \cup ([0, 1] \times \{y = 0, 1\})$ and $\Gamma_N = \emptyset$.
- **Case 2:** $\Gamma_D = \{x = 0\} \times [0, 1]$ and $\Gamma_N = [0, 1] \times \{y = 0, 1\}$.

For simplicity we assume $\mathbf{E}(x, y) = \langle 1, 0 \rangle$. The manufactured solution to (5.1.6) for both cases is,

$$u(x, y, t) = e^{-t} + \cos(2\pi x) + \cos(2\pi y). \quad (5.1.7)$$

The corresponding right hand side function is,

$$f(x, y, t) = -e^{-t} + 4\pi^2 \cos(2\pi x) + 4\pi^2 \cos(2\pi y) + 2\pi \sin(2\pi x). \quad (5.1.8)$$

The Dirichlet boundary conditions $g_D(x, y, t)$ are taken to be $u(x, y, t)$ on Γ_D and the interface function is,

$$g_I(x, y, t) = -e^{-t} - \cos(2\pi y) - 1. \quad (5.1.9)$$

The initial condition $u_0(x, y)$ is the L^2 projection of the solution $u(x, y, 0)$ onto the DG basis. To perform time stepping we use a first-order IMEX method and an end time of $T = 1$. In order to obtain the underlying errors of the LDG method we take time steps $\Delta t = h^{k+1}$ for basis functions of order k . The results for Case 1 can be seen in Figure 5.4 (a) and for Case 2 in Figure 5.4 (b). As can be observed the results show that we obtain the theoretical convergence rates of the LDG method.

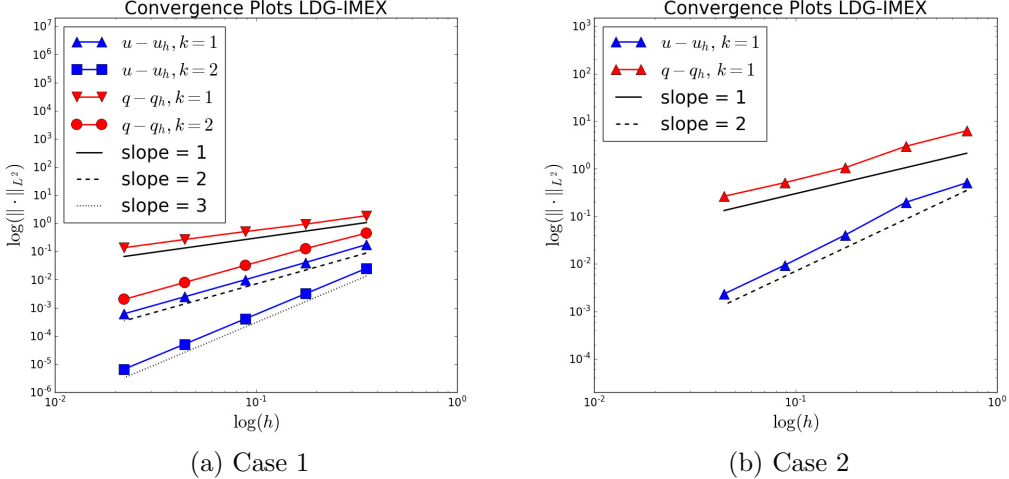


Figure 5.4: 2D L^2 error plots for the LDG-IMEX method for the problem (5.1.6)

5.1.2.2 Coupled MFEM-LDG-IMEX Test

The coupling of the drift-diffusion-Poisson problem using a LDG method and a MFEM is tested on the problem,

$$\begin{aligned}
 -\Delta\Phi &= C(\mathbf{x}, t) - u && \text{in } \Omega \times (0, T), \\
 \Phi &= \Phi_D(\mathbf{x}) && \text{on } \partial\Omega \times (0, T), \\
 u_t + \nabla \cdot (-\nabla\Phi u - \nabla u) &= f(\mathbf{x}, t) && \text{in } \Omega \times (0, T), \quad (5.1.10) \\
 u &= g_D(\mathbf{x}, t) && \text{on } \partial\Omega \times (0, T), \\
 u &= u_0(\mathbf{x}) && \text{in } \Omega \times \{t = 0\}.
 \end{aligned}$$

We take the domain to be $\Omega = [0, 1] \times [0, 1]$. The solutions to (5.1.10) are,

$$\Phi(x, y) = \cos(2\pi y) - \sin(2\pi x) - x, \quad (5.1.11)$$

and,

$$u(x, y, t) = e^{-t} + \cos(2\pi x) + \cos(2\pi y). \quad (5.1.12)$$

The corresponding right hand side functions are,

$$C(x, y, t) = 4\pi^2 (\cos(2\pi y) - \sin(2\pi x)) + e^{-t} + \cos(2\pi x) + \cos(2\pi y), \quad (5.1.13)$$

and,

$$\begin{aligned} f(x, y, t) &= 4\pi^2 (\cos(2\pi y) - \sin(2\pi x)) (e^{-t} + \cos(2\pi x) + \cos(2\pi y)) \\ &\quad - 2\pi (2\pi \cos(2\pi x) + 1) \sin(2\pi x) - 4\pi^2 \sin(2\pi y)^2 \\ &\quad - e^{-t} + 4\pi^2 \cos(2\pi x) + 4\pi^2 \cos(2\pi y). \end{aligned} \quad (5.1.14)$$

The Dirichlet boundary condition $g_D(x, y, t)$ and $\Phi_D(x, y)$ are taken to be the solutions $u(x, y, t)$ and $\Phi(x, y, t)$ respectively on the boundary $\partial\Omega$. The initial condition $u_0(x, y)$ is the L^2 projection of the solution $u(x, y, 0)$ onto the DG basis. To perform time stepping we use a first-order IMEX method and an end time of $T = 1$. In order to obtain the underlying errors of the LDG and mixed method we take time steps $\Delta t = h^{k+2}$ for basis functions of order k . The results for the mixed finite element method can be seen in Figure 5.5 (a) and the local discontinuous Galerkin method can be seen in Figure 5.5 (b). The results show that we obtain the same convergence rates for the MFEM and LDG method as previously discussed.

5.1.2.3 Coupled LDG Reactive Interface Test

To test the coupling of the carriers across a reactive interface (Σ) using and LDG method we take $u : \Omega_S \times [0, T] \rightarrow \mathbb{R}$ and $v : \Omega_E \times [0, T] \rightarrow \mathbb{R}$ and

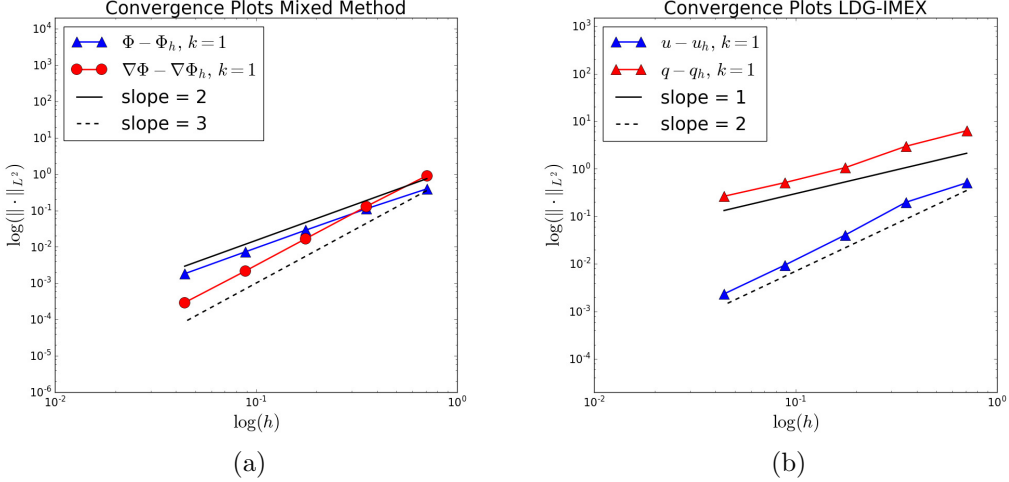


Figure 5.5: 2D L^2 error plots for the MFEM-LDG method for the problem (5.1.6)

solve the coupled parabolic problems,

$$\begin{aligned}
 u_t - \Delta u &= f_1(\mathbf{x}, t) && \text{in } \Omega_S \times (0, T), \\
 \mathbf{n}_{\Sigma^S} \cdot (-\nabla u) \cdot &= u(\mathbf{x}, t)v(\mathbf{x}, t) - I(\mathbf{x}, t) && \text{on } \Sigma \times (0, T), \\
 u &= g_{1,D}(\mathbf{x}, t) && \text{on } \Gamma_{S,D} \times (0, T), \\
 u &= u_0(\mathbf{x}) && \text{in } \Omega_S \times \{t = 0\},
 \end{aligned} \tag{5.1.15}$$

and,

$$\begin{aligned}
 v_t - \Delta v &= f_2(\mathbf{x}, t) && \text{in } \Omega_E \times (0, T), \\
 \mathbf{n}_{\Sigma^E} \cdot (-\nabla v) \cdot &= u(\mathbf{x}, t)v(\mathbf{x}, t) - I(\mathbf{x}, t) && \text{on } \Sigma \times (0, T), \\
 v &= g_{2,D}(\mathbf{x}, t) && \text{on } \Gamma_{E,D} \times (0, T), \\
 v &= v_0(\mathbf{x}) && \text{in } \Omega_E \times \{t = 0\}.
 \end{aligned} \tag{5.1.16}$$

We take the domain to be $\Omega = [0, 1] \times [0, 1]$ with $\Omega_S = [0, 1/2] \times [0, 1]$ and $\Omega_E = [1/2, 1] \times [0, 1]$. The interface is $\Sigma = \{x = 1/2\} \times [0, 1]$ and the

boundaries are $\Gamma_{1,D} = \partial\Omega_S \setminus \Sigma$ and $\Gamma_{2,D} = \partial\Omega_E \setminus \Sigma$. The manufactured solutions for this problem are,

$$u(x, y, t) = v(x, y, t) = e^{-t} + \cos(2\pi x) + \cos(2\pi y). \quad (5.1.17)$$

The corresponding right hand side functions are,

$$f_1(x, y, t) = f_2(x, y, t) = -e^{-t} + 4\pi^2 \cos(2\pi x) + 4\pi^2 \cos(2\pi y) + 2\pi \sin(2\pi x). \quad (5.1.18)$$

The Dirichlet boundary conditions $g_{1,D}(x, y, t)$ and $g_{2,D}(x, y, t)$ are taken to be $u(x, y, t)$ on $\Gamma_{1,D}$ and $v(x, y, t)$ on $\Gamma_{2,D}$ respectively. The interface function is,

$$I(x, y, t) = (e^{-t} + \cos(\pi y) - 1)^2. \quad (5.1.19)$$

The initial conditions $u_0(x, y)$ and $v_0(x, y)$ are taken to be the L^2 projection of the solutions $u(x, y, 0)$ and $v(x, y, 0)$ onto the DG basis. To perform time stepping we use a first-order PS-IMEXEX method and an end time of $T = 1$. In order to obtain the underlying errors of the LDG method we take time step to be $\Delta t = h^{k+1}$ when using basis functions of order k . The results can be seen in Figure 5.6 and show that we obtain optimal convergence rates for the LDG method. We note that h will be the same value for both of the triangulations of Ω_S and Ω_E , that is $h_S = h_E = h$.

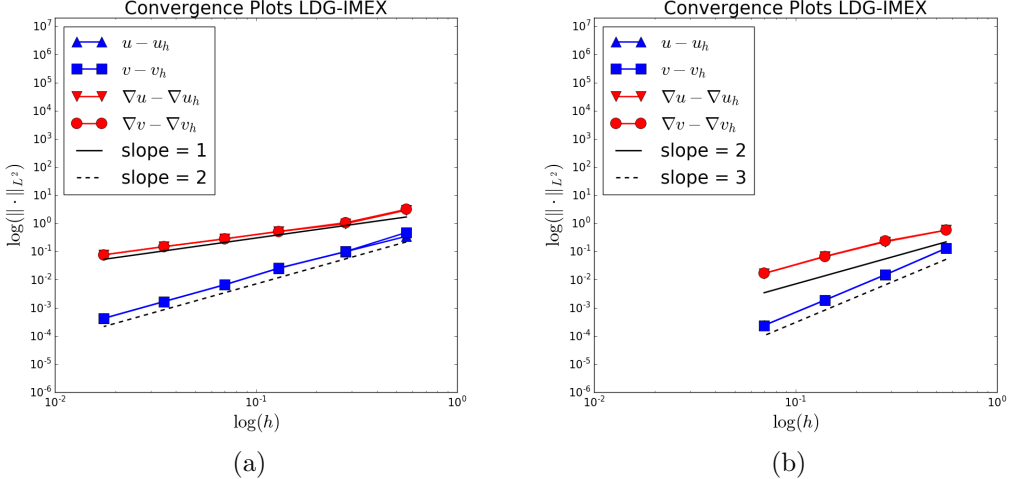


Figure 5.6: 2D L^2 error plots for the LDG-PS-IMEXEX method for the problem (5.1.15) and (5.1.16) for (a) $k = 1$ and (b) $k = 2$.

5.2 Studies On Computational Performance

5.2.1 Study On The Performance Of Time Stepping Algorithms

In this section we discuss the performance of the different time stepping routines on our one dimensional code. In our implementation of the algorithms, we use the SparseLU direct solver provided by the Eigen Library [3] for the inversion of the LDG matrices. We use the GRVY Library [133] to monitor the computational time spent within all the critical subroutines of each algorithm. In Figure. 5.7 we show a typical example of the information provided by the GRVY library.

We now look at the performance of the four time stepping algorithms. Our focus will be on the comparison between the four algorithms. We take the domain $\Omega = (-1, +1)$ where the interface Σ is located at $x = 0$. The semi-

GRVY TIMING - Performance Timings:		Mean	Variance	Count
--> Solve LDG System	: 8.17959e+01 secs (54.6135 %)	[7.97446e-05	1.53082e-09	1025724]
--> Solve Poisson System	: 2.00118e+01 secs (13.3615 %)	[8.75509e-05	5.26597e-09	228574]
--> Assemble Drift Term	: 1.96407e+01 secs (13.1137 %)	[1.91481e-05	1.30040e-10	1025724]
--> Assemble Recombination Term	: 1.63993e+01 secs (10.9495 %)	[7.80914e-05	6.30061e-08	210001]
--> Assemble LDG RHS	: 3.48435e+00 secs (2.3264 %)	[3.39697e-06	1.27820e-10	1025724]
--> Assemble Poisson RHS	: 1.54971e+00 secs (1.0347 %)	[6.77988e-06	1.56398e-12	228574]
--> Print State	: 3.90441e-01 secs (0.2607 %)	[1.34635e-02	3.72972e-07	29]
--> Boiler Plate	: 8.18901e-02 secs (0.0547 %)	[8.18901e-02	0.00000e+00	1]
--> Factorize LDG Matrix	: 4.62532e-03 secs (0.0031 %)	[5.78165e-04	1.19131e-09	8]
--> Assemble LDG Matrix	: 4.31538e-04 secs (0.0003 %)	[5.39422e-05	8.67928e-12	8]
--> Reassemble and refactor	: 3.55244e-05 secs (0.0000 %)	[3.55244e-05	0.00000e+00	1]
--> Check converged	: 0.00000e+00 secs (0.0000 %)	[N/A	0.00000e+00	0]
--> GRVY_Unassigned	: 6.41314e+00 secs (4.2819 %)			
Total Measured Time = 1.49772e+02 secs (100.0000 %)				

Figure 5.7: Run time performance results provided by GRVY.

conductor domain is $\Omega_S = (-1, 0)$ with Γ_S being at $x = -1$. The electrolyte domain is $\Omega_E = (0, 1)$ with Γ_E being at $x = +1$. The simulations were run until steady state using the same fixed time step. We used 100 linear elements on a Dell Precision T1700 Workstation (i5-4590 Processor, Quad Core 3.30GHz).

Table 5.1: Time in seconds spent in the subroutines of each Schwarz method.

	AS-IMIMEX	AS-IMEXEX	PS-IMEXEX	TsPS-IMEXEX
Fact. LDG	2,322	2,421	< 1	< 1
Drift Term	9,133	48	92	51
Recom. Term	307	326	293	286
Sol. LDG	265	265	258	141
Sol. MFEM	73	73	71	7
Run Time	12,498	3,529	766	518

In Table 5.1, we summarize the performance information of the four algorithms provided by GRVY. Besides the total run time of each algorithm, we show, for each algorithm, the portion of the computational time spent on (i) assembling the drift term (first row), (ii) assembling the recombination term (second row), (iii) factorizing the LDG matrices (third row), (iv) inverting the

LDG matrices (fourth row), and (v) inverting the MFEM matrices (fifth row).

In Figure 5.8 we display the percentage of the total run time that each of these operations used.

The difference between the AS-IMIMEX algorithm and the AS-IMEXEX algorithm is that AS-IMIMEX uses implicit density values to assemble the drift term while AS-IMEXEX uses explicit density values to assemble the drift term. Using implicit density values to assemble the drift term is prohibitively expensive. In this case assembling the matrix corresponding to the drift term (3.4.16) in (3.4.10) alone takes up nearly 70% of the run time. We see that the AS-IMEXEX method is approximately 3.5 times faster than the AS-IMIMEX method (in total CPU time). This is because using explicit density values to assemble the drift term we never compute the matrix (3.4.16) that is used in AS-IMIMEX. Instead in the AS-IMEXEX method we assemble a right hand side vector (3.4.29) that includes drift term in (3.4.28) by performing local quadrature over each cell. It should be noted that although we used a fixed time step size in these experiments, the time step size needed to maintain stability for the AS-IMEXEX method was about one half of that needed for the AS-IMIMEX algorithm. This loss of stability is consistent with the choice of an explicit method instead of an implicit method.

We see from Figure 5.8 that the main bottle neck in the AS-IMEXEX algorithm is due to the factorization of the LDG matrices. If we treat all the densities on the interface using explicit density values then the LDG matrices such as (3.4.38) will remain constant in time. With this choice the contri-

butions for the interface face conditions will be added to the linear system for LDG systems in the right hand side vector (3.4.39). All the LDG matrices can then be factorized in the beginning of the simulation and only linear solves must be performed at every time step. This is the reason that the PS-IMEXEX algorithm is approximately 4.6 times faster (in total CPU time) than the AS-IMEXEX algorithm.

Finally, we observe from Tab. 5.1 that using a TsPS-IMEXEX method over PS-IMEXEX method results in a total speed up of approximately 1.5. The faster run time is a result of the reduction in the total number of linear solves performed in TsPS-IMEXEX. As noted previously, this method uses two time steps, one for the semiconductor systems and one for the electrolyte system. In our simulations we found that time step for the electrolyte system, Δt_e , is almost 100 bigger than the time step for the semiconductor system, Δt_s . Therefore the choice of $K \leq 10$ mentioned in Section 3.4.4 could be relaxed and one might obtain even more savings from TsPS-IMEXEX. Overall, the TsPS-IMEXEX has a reduction in CPU time over AS-IMIMEX by a factor of nearly 24.

We see from Table 5.1 that using a parallel Schwarz method over an alternating Schwarz method results in significant savings in CPU time. However, in Figure 5.8 we see that the assembly of coupling terms as contributions to the right hand side vector uses a significant portion of the run time. Since the assembly of these terms occurs on an element-by-element basis this process can easily be parallelized. This is the topic of the next section.

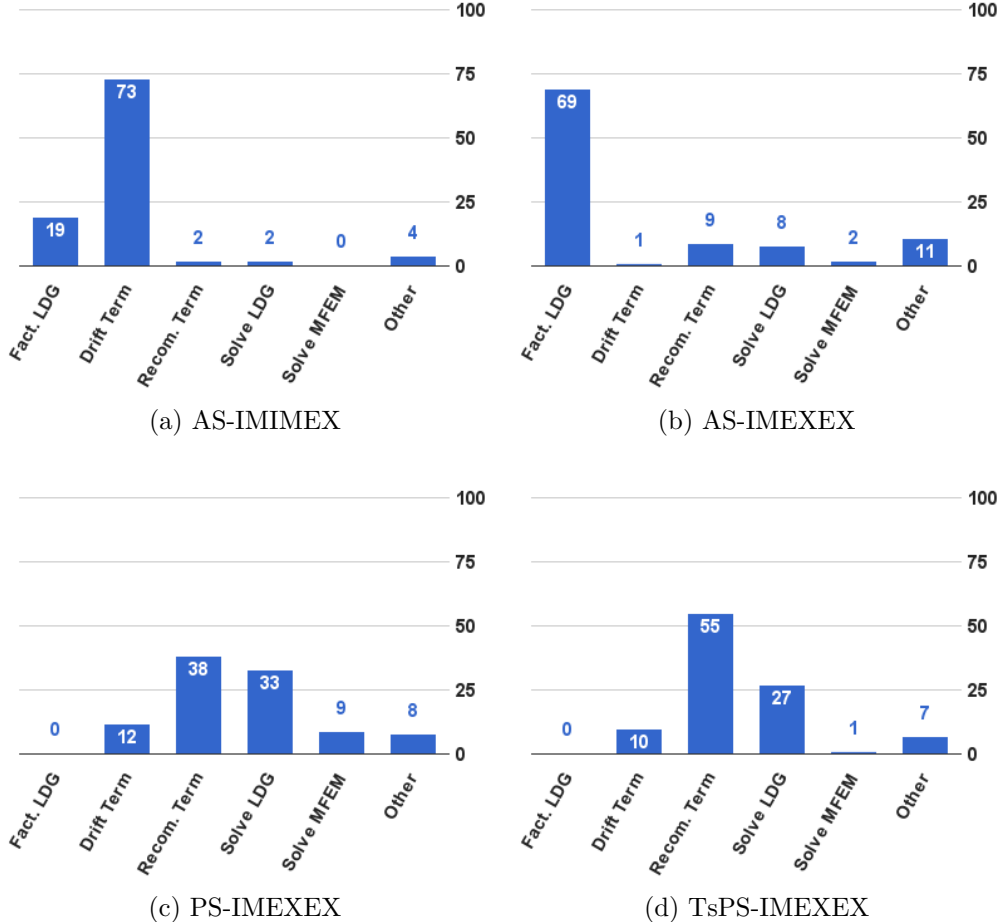


Figure 5.8: Percentage of runtime in subroutines from Table 5.1.

5.2.2 Parallel Implementation

In discussing the parallelization of our codes we focus on the two dimensional code that was developed using the deal.II library [21, 22]. We use the PS-IMEXEX algorithm and the deal.II prepackaged direct solver UMF-PACK [54–57]. The choice of direct solver is justified since each system has less than 100,000 degrees of freedom. The code was parallelized using the Intel

Thread Building Blocks (TBB) [6]. The two procedures that are most suitable for parallelization are,

- Assembling of the MFEM matrix (3.2.9) and LDG matrices of the such as (3.4.38).
- Assembling in the right hand side vectors for the MFEM (3.2.13) and (3.2.14) as well as the right hand side vectors for the LDG systems such as (3.4.39) and (3.4.29).

Additionally we use task-based parallelism through TBB by,

- Assigning the solving of each LDG linear system such as (3.4.38) to an independent task.
- Assigning the printing of the data from the Poisson system, the electron-hole system and the reductant-oxidant system to independent tasks.

Each independent task can be completed at the same time by assigning them to the different available cores. However, the scalability of such procedures is limited. Indeed, one cannot obtain any speed up of the task-based operations by using more than four cores.

We now perform a study on strong the scaling of our two dimensional code using the Stampede supercomputer at the Texas Advanced Computing Center (TACC). The time used by each subroutine and its percentage of the total time was recorded by the deal.II library. An example of the information

provided by deal.II at the end of each simulation is presented in Figure 5.9. We observe from Figure 5.9 that in the case where only one core is used that approximately 75% of the time is spent in solving the linear systems and 25% of the time is spent assembling the right hand side vectors. Since the direct solver UMFPACK is sequential in nature we cannot expect the code to scale well. The results of the scaling study can be seen in Table 5.2.

Total wallclock time elapsed since start		2.52e+03s	
Section	no. calls	wall time	% of total
Allocate Memory	1	0.0737s	0.0029%
Assemble LDG Matrices	1	0.322s	0.013%
Assemble Poisson Matrix	1	0.132s	0.0052%
Assemble Poisson rhs	10000	269s	11%
Assemble electrolyte rhs	10000	163s	6.5%
Assemble semiconductor rhs	10000	183s	7.3%
Build Mappings	1	0.0459s	0.0018%
Factor Matrices	1	2.04s	0.081%
Make Grids	1	0.00656s	0.00026%
Printing	99	36.1s	1.4%
Solve LDG Systems	10000	981s	39%
Solve Poisson system	10000	884s	35%

Figure 5.9: Run time performance results of key subroutines provided by the deal.II library using one core on Stampede.

From Table 5.2 we can see that the mixed method has almost twice as many unknowns as each of the LDG linear systems. Additionally, in Figure 5.9 we see that solving the MFEM linear system takes up a significant percentage of the total run time. Indeed, even with one core solving the linear system resulting from the mixed method uses almost the same amount of time as solving all four LDG linear systems. We expect that if we have a smaller mixed finite element system that we could not only reduce the overall run time

Table 5.2: Run times and speedup ratio of two dimensional code on Stampede. The number of degrees of freedom (DOFS) was 31,040 for the MFEM and 15,360 for each LDG system for a total of 92,480 DOFS.

Cores	Run Time In Seconds	Speedup Ratio
1	2,516	-
2	1,884	1.33
4	1,610	1.56
8	1,532	1.64
12	1,524	1.65
16	1,534	1.64

of our simulations, but also improve its parallel performance. We attempt to accomplish this by using a mixed finite element method that uses a polynomial basis that is one order less than that of the LDG method. Specifically, we use the approximation spaces $W_{h,k-1}^P$ and $\mathbf{RT}_{h,k-1}^P$ for the mixed finite element method and the use the approximation spaces $W_{h,k}^S$, $\mathbf{W}_{h,k}^S$ and $W_{h,k}^E$, $\mathbf{W}_{h,k}^E$ for the semiconductor and electrolyte systems respectively. We note that this choice of approximation spaces will not effect the accuracy of the approximation to the currents. This is because the errors in the electric field and the current are now both $\mathcal{O}(h^k)$. The results from scaling study using the reduced MFEM can be seen in Table 5.3. We observe that while the speed-up ratio has improved, as expected, the scaling of our code is still rather limited due to the sequential nature of the linear solver. Improvements in scaling might be obtained through the use of parallel direct solvers.

Table 5.3: Run times and speedup ratio of two dimensional code on Stampede using the reduced MFEM. The number of degrees of freedom (DOFS) was 7,840 for the MFEM and 15,360 for each LDG system for a total of 69,280 DOFS.

Cores	Run Time In Seconds	Speedup Ratio
1	1,324	-
2	833	1.59
4	584	2.27
8	537	2.47
12	557	2.38
16	580	2.28

5.3 Numerical Experiments

We now present some numerical experiments in one and two dimensions. The physical constants used in these simulations are record in Table 5.4 and come from [139]. We use silicon as our semiconductor material since it is the most commonly used material for terrestrial photovoltaic devices. The bulk properties of the our Silicon crystal are recorded in Table 5.5 and are from [81, 84, 130]. The choice of redox system is rather arbitrary as most simulation studies neglect its interaction with the semiconductors electrode interaction all together. Therefore we choose bulk redox property values record in Table 5.6. These values are computationally convenient, but are still representative of realistic electrolytes [84, 111]. Other physical parameter such as the size [67, 84], doping profile [67] and transfer rates [99] will be introduced when necessary.

Remark 5.3.1. We remark that the choice of our choices of redox charge numbers do not satisfy the requirement of $\alpha_r + \alpha_0 = 1$. These studies were

Table 5.4: Physical constants

Parameter	Value	Unit
q	1.6×10^{-19}	C
k_B	1.38066×10^{-23}	J K ⁻¹
ϵ_0	8.85×10^{-14}	C V ⁻¹ cm ⁻¹
T	300	K
G_0	1.2×10^{17}	cm ⁻² s ⁻¹

Table 5.5: Bulk silicon properties

Parameter	Value	Unit
μ_n	1350	cm ² V ⁻¹ s ⁻¹
μ_p	480	cm ² V ⁻¹ s ⁻¹
α_n	1	-
α_p	-1	-
τ_n	5×10^{-5}	s
τ_p	5×10^{-5}	s
α	1.74974×10^5	cm ⁻¹
ρ_i	2.564×10^9	cm ⁻³
Φ_{SCR}	0.41	V
ϵ_S	11.9	-

Table 5.6: Bulk redox properties

Parameter	Value	Unit
μ_r	1	cm ² V ⁻¹ s ⁻¹
μ_o	1	cm ² V ⁻¹ s ⁻¹
α_r	1	-
α_o	-1	-
Φ^∞	0.0	V
ϵ_E	1000	-

performed on an older model of the semiconductor-electrolyte which did not have this requirement.

5.3.1 One Dimensional Simulations

We are now ready to present some simulation results in one dimension. We aim at studying the dependence of solution on different device parameters and develop a strategy to maximize power output for nanoscale devices. Precisely, we investigate the sensitivity of the device with respect to (i) device size, (ii) minority transfer rates on the interface, and (iii) variations in the semiconductor's doping profile. We then demonstrate how the simulations performed with the Schottky approximation can produce results which deviate from results computed with the full system.

5.3.1.1 Effect Of Device Size

We consider two devices here: (i) D-I, $\Omega = (-1 \times 10^{-4} \text{ cm}, 1 \times 10^{-4} \text{ cm})$ and (ii) D-II, $\Omega = (-0.2 \times 10^{-4} \text{ cm}, 0.2 \times 10^{-4} \text{ cm})$. Besides their sizes, the other model parameters of the two devices are identical and are recorded in Table 5.7. The parameters are chosen to better visualize the effects of illumination. The steady state characteristics of D-I under dark and illuminated conditions are presented in Figure 5.10 and Figure 5.11. The steady state characteristics of D-II under dark and illuminated conditions are presented in Figure 5.12 and Figure 5.13.

Comparing the results of the two devices it is evident that the device characteristics vary greatly depending on its size. Indeed, the size of the device can have significant impact on its energy conversion rates. To see that, we perform simulations on two more devices: (iii) D-III and (iv) D-

Table 5.7: D-I & D-II parameter values.

Parameter	Value	Unit
ρ_n^e	2×10^{16}	cm^{-3}
ρ_p^e	0	cm^{-3}
ρ_r^∞	5×10^{16}	cm^{-3}
ρ_o^∞	4×10^{16}	cm^{-3}
k_{et}	10^{-19}	$\text{cm}^4 \text{ s}^{-1}$
k_{ht}	10^{-16}	$\text{cm}^4 \text{ s}^{-1}$
$\Phi_{\text{app.}}$	0	V

IV. D-III and D-IV have the same dimensions as D-I and D-II respectively. The model parameters, however, are very different; see the values listed in Table 5.8. Devices D-III and D-IV use higher concentrations of reductants and oxidants and also have faster minority transfer rates (k_{ht}). We apply a range of applied biases to the devices and record their steady state currents under illumination. The results of these simulations are displayed in Figure 5.14 and the performance of the devices are summarized in Table 5.8. From Table 5.8 it is observed that device D-IV has a lower efficiency and fill factor than D-III. Figure 5.14 shows that this is because both the short circuit current and the open circuit voltage have been reduced when using a smaller devices.

Table 5.8: D-III & D-IV parameter values (left) and performance (right).

Parameter	Value	Unit	Device	η_{eff}	ff
ρ_n^e	2×10^{16}	cm^{-3}	D-III	4.3%	0.524
ρ_p^e	0	cm^{-3}	D-IV	3.1%	0.411
ρ_r^∞	30×10^{16}	cm^{-3}			
ρ_o^∞	29×10^{16}	cm^{-3}			
k_{et}	10^{-19}	$\text{cm}^4 \text{ s}^{-1}$			
k_{ht}	10^{-14}	$\text{cm}^4 \text{ s}^{-1}$			

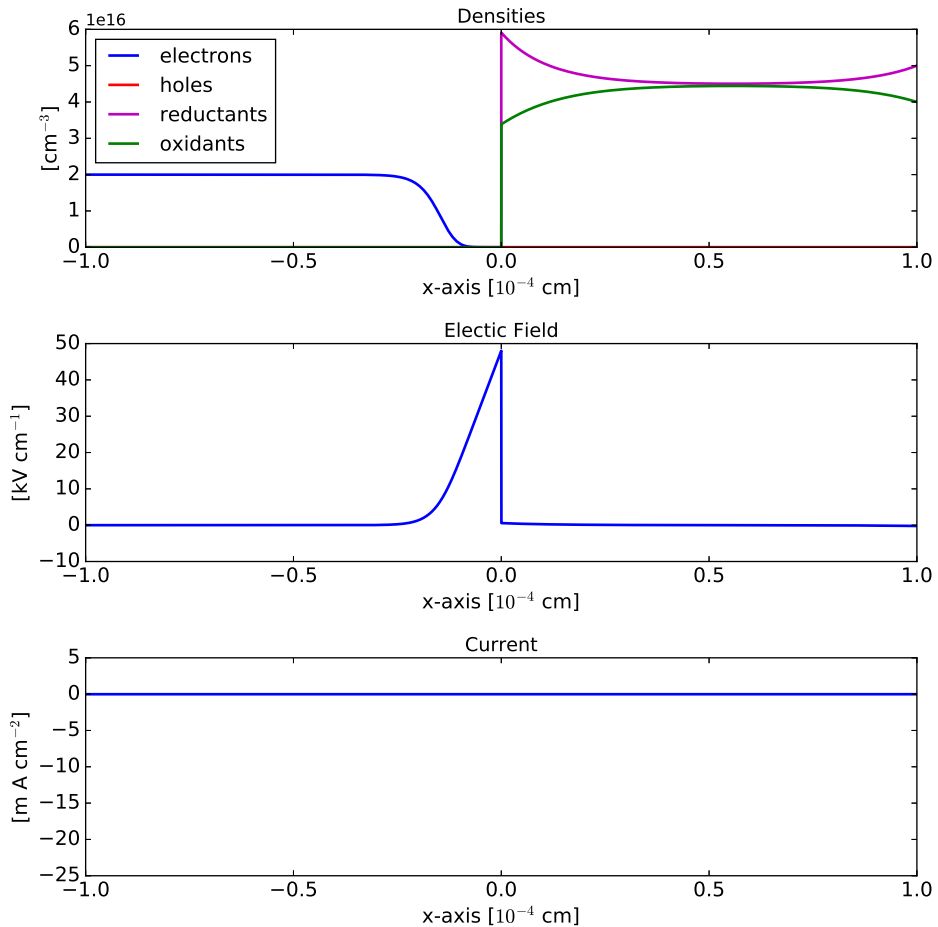


Figure 5.10: Steady state characteristics of D-I in the the dark.

5.3.1.2 Impact Of Interfacial Charge Transfer Rates

The charge transfer dynamics across the semiconductor-electrolyte interface is controlled mainly by the electron and hole transfer rates k_{et} and k_{ht} . There has been tremendous progress in recent years on the theoretical calculation and experimental measurement of these rate constants [66, 97–99, 120].

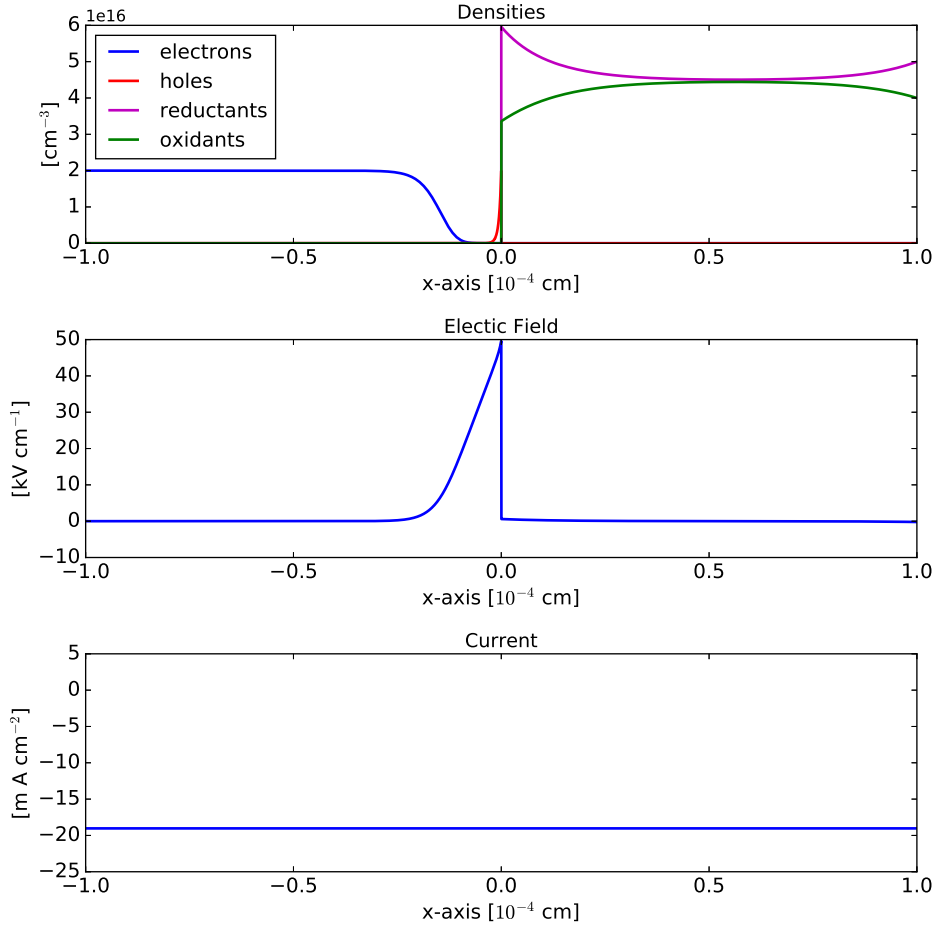


Figure 5.11: Steady state characteristics of D-I in under illumination.

Here we study numerically the impact of these parameters on the performance of the PEC cell.

In Figure 5.15 and Figure 5.16, we show the current-voltage curves of devices D-III and D-IV under different rate constants. For simplicity, we fix the electron transfer rate k_{et} , varying only the hole transfer rate k_{ht} to see its effect. The values of k_{ht} and the corresponding performance indicators for D-III and

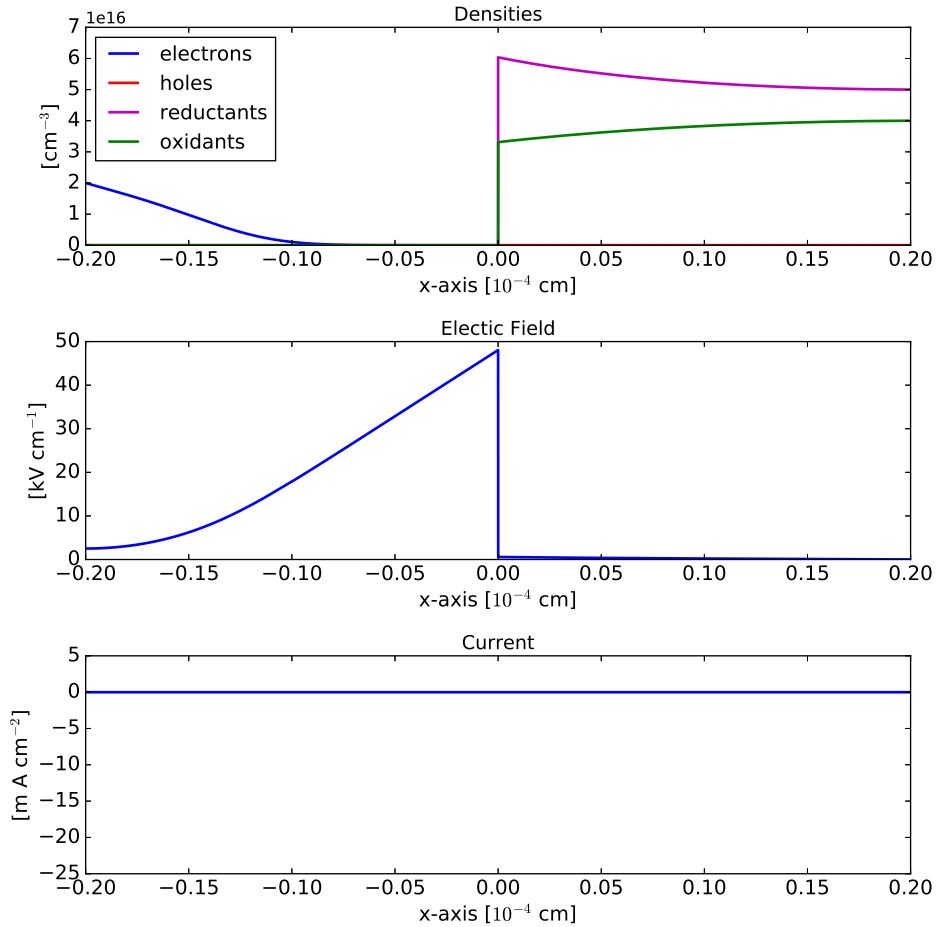


Figure 5.12: Steady state characteristics of D-II in the the dark.

Table 5.9: Performance of D-III (left) & D-IV (right) with various k_{ht} values.

Case	$\eta_{\text{eff.}}$	ff	Case	$\eta_{\text{eff.}}$	ff
$k_{ht} = 10^{-16} [\text{cm}^4 \text{s}^{-1}]$	6.3%	0.671	$k_{ht} = 10^{-14} [\text{cm}^4 \text{s}^{-1}]$	3.1%	0.411
$k_{ht} = 10^{-14} [\text{cm}^4 \text{s}^{-1}]$	4.3%	0.524	$k_{ht} = 10^{-12} [\text{cm}^4 \text{s}^{-1}]$	4.8%	0.561
$k_{ht} = 10^{-12} [\text{cm}^4 \text{s}^{-1}]$	2.2%	0.280			

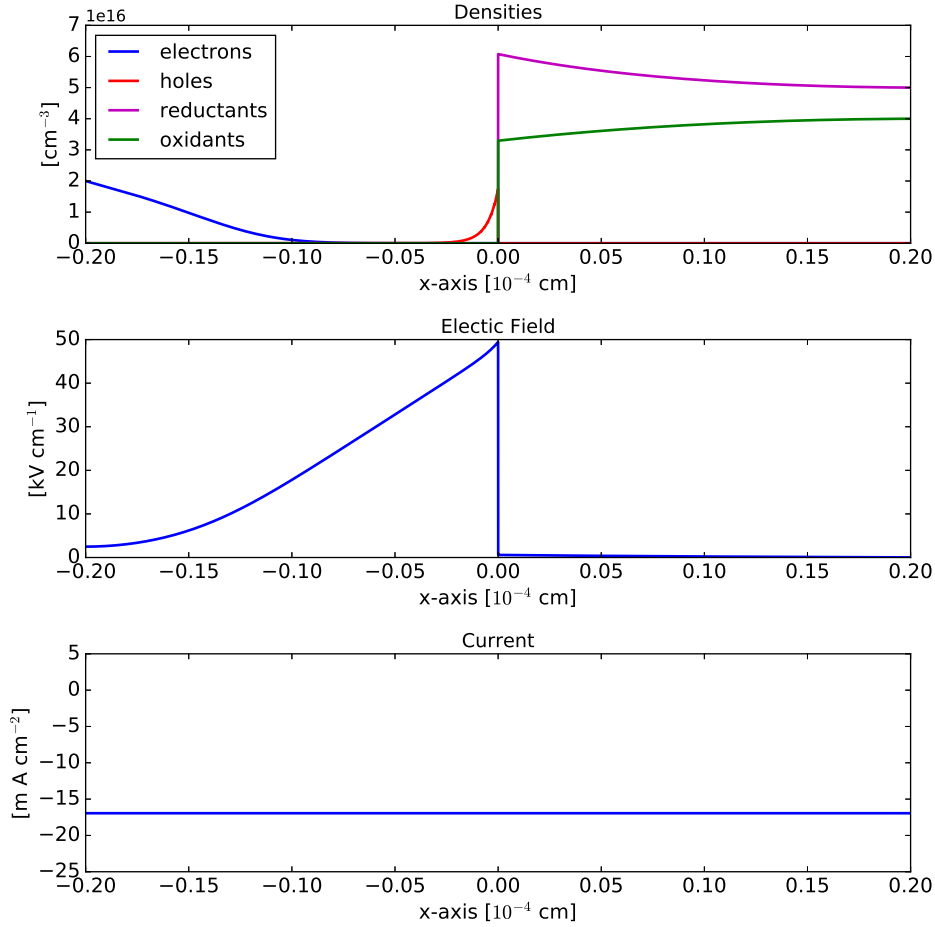


Figure 5.13: Steady state characteristics of D-II in under illumination.

D-IV are summarized in Table 5.9 (left) and Table 5.9 (right) respectively. It is clear from the data that the value of the minority transfer rate greatly effects the efficiency and the fill factor of a PEC solar cell. Specifically it is observed that faster minority rates increase both the solar cell efficiency and fill factor. While the values of k_{ht} that we have used may be relatively high, they are still within the upper limit of its value given in [99]. In fact, the large

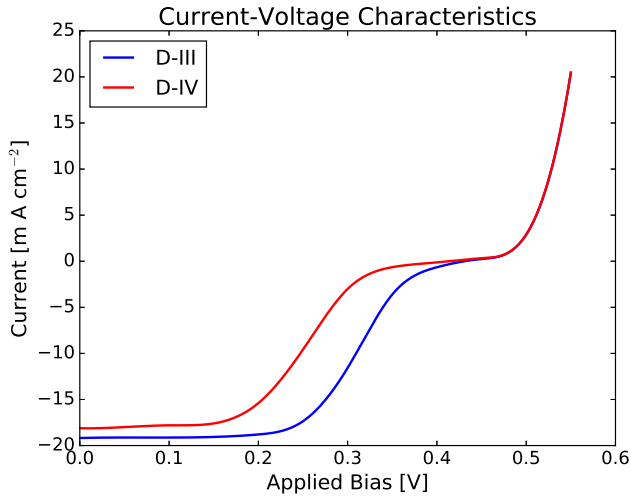


Figure 5.14: Illuminated current-voltage curves for D-III & D-IV.

amount of efforts in practical studies focus on how to select the combination of the semiconductor material and the electrolyte so that the transfer rate is high.

5.3.1.3 Impact Of The Doping Profile

We now study the impact of the doping profile on the performance of PEC cells. We focus on the doping profile of the majority carrier. We perform simulations on device D-V which has the same size as device D-I, that is, $\Omega = (-0.2 \times 10^{-4} \text{ cm}, 0.2 \times 10^{-4} \text{ cm})$, but different model parameters that are listed in Table 5.10 (left). We consider four different majority doping profiles that are given as:

- Doping Profile 1:

$$N_D^1 = 2 \times 10^{16} [\text{cm}^{-3}]$$

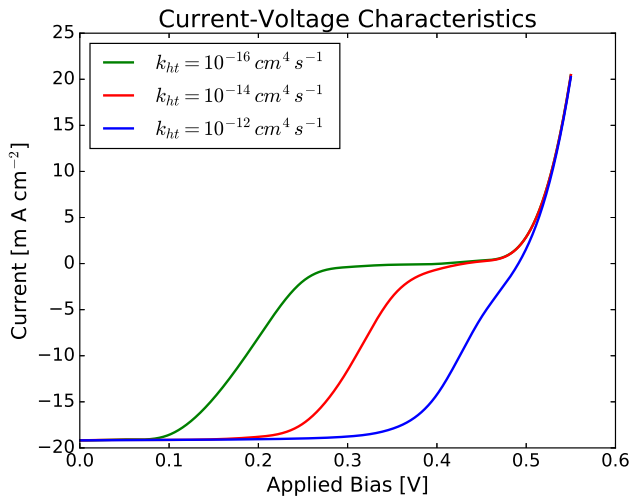


Figure 5.15: Illuminated current-voltage curves for D-III with varying minority transfer rate.

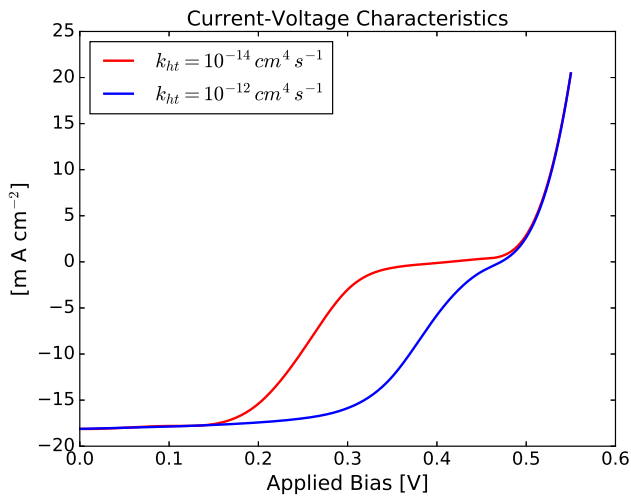


Figure 5.16: Illuminated current-voltage curves for D-IV with varying minority transfer rate.

- Doping Profile 2:

$$N_D^2 = \begin{cases} 10 \times 10^{16} [\text{cm}^{-3}] & -0.2 \times 10^{-4} \text{ cm} \leq x < -0.07 \times 10^{-4} \text{ cm} \\ 2 \times 10^{16} [\text{cm}^{-3}] & -0.07 \times 10^{-4} \text{ cm} < x \leq 0 \text{ cm} \end{cases}$$

- Doping Profile 3:

$$N_D^3 = \begin{cases} 10 \times 10^{16} [\text{cm}^{-3}] & -0.20 \times 10^{-4} \text{ cm} \leq x < -0.13 \times 10^{-4} \text{ cm} \\ 2 \times 10^{16} [\text{cm}^{-3}] & -0.13 \times 10^{-4} \text{ cm} < x \leq 0 \text{ cm} \end{cases}$$

- Doping Profile 4:

$$N_D^4 = \begin{cases} 20 \times 10^{16} [\text{cm}^{-3}] & -0.20 \times 10^{-4} \text{ cm} \leq x < -0.13 \times 10^{-4} \text{ cm} \\ 2 \times 10^{16} [\text{cm}^{-3}] & -0.13 \times 10^{-4} \text{ cm} < x \leq 0 \text{ cm} \end{cases}$$

The values of ρ_n^e is then given as $\rho_n^e = N_D$ since the minority carrier doping profile is set as $N_A = 0$.

Table 5.10: D-V (left) parameter values & performance (right).

Parameter	Value	Unit	Doping Profile.	$\eta_{\text{eff.}}$	ff
ρ_p^e	0	cm^{-3}	N_D^1	4.8%	0.561
ρ_r^∞	30×10^{16}	cm^{-3}	N_D^2	4.9%	0.626
ρ_o^∞	29×10^{16}	cm^{-3}	N_D^3	4.9%	0.617
k_{et}	10^{-19}	$\text{cm}^4 \text{ s}^{-1}$	N_D^4	4.9%	0.634
k_{ht}	10^{-12}	$\text{cm}^4 \text{ s}^{-1}$			

The simulation results are displayed in Figure 5.17 and summarized in Table 5.10 (right). It seems that by adding variations to the doping profile we greatly improve the fill factor. It is evident in Figure 5.17 that the improvement of the fill factor is caused by a decrease in open circuit voltage. We see that a doping profile that has a thin, highly doped layer near the Ohmic contact has the best fill factor of all four cases. Interestingly, in Figure 5.18

the introduction of non-constant doping profiles causes the electric field to switch signs within the semiconductor domain for certain applied biases. This could be the reason for the reduction in the cells' open circuit voltage and the subsequent increase in the cell's fill factor. The phenomenon we observe here are consistent with what is known in the literature; see, for instance the discussions in [67, 114].

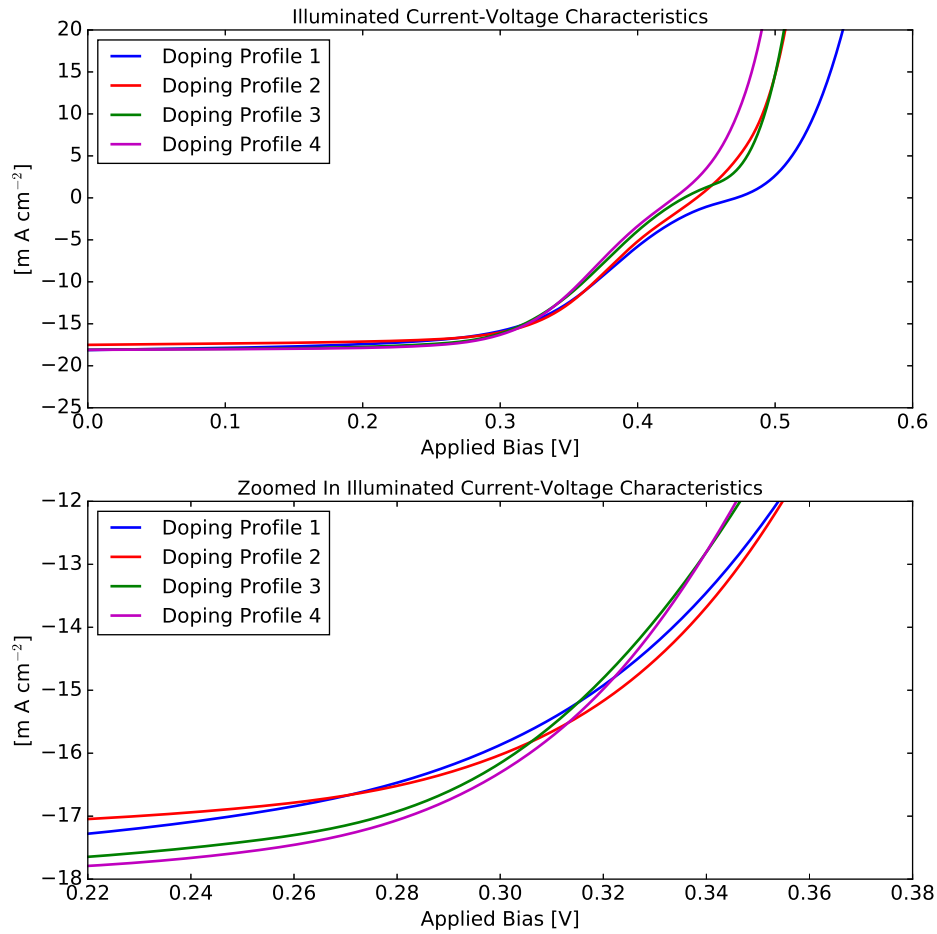


Figure 5.17: Illuminated currents of D-V with different doping profiles.

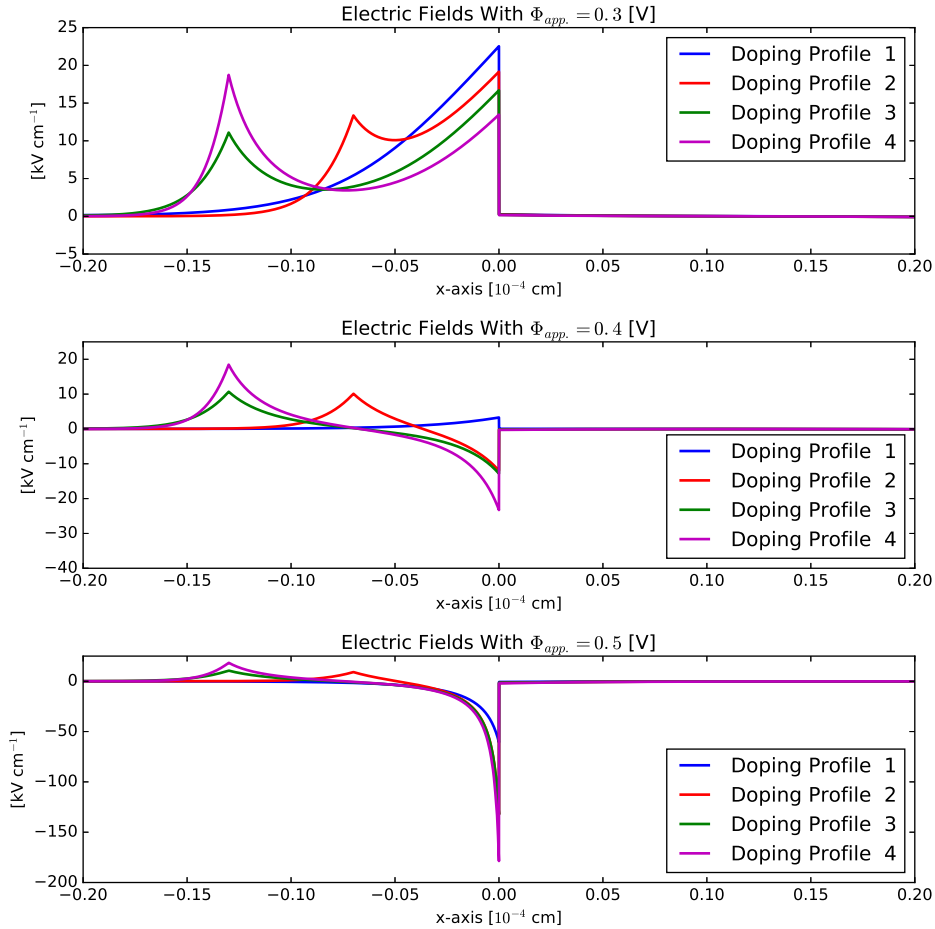


Figure 5.18: Electric field values of D-V with different doping profiles.

5.3.1.4 Comparison With The Schottky Approximation

In most previous simulation-based studies of PECs, the impact of the electrolyte solution on the performance of the system has been modeled in a simpler manner. Essentially, the simulations are only performed on the semiconductor component. The impact of the electrolyte component comes in

from the so-called “Schottky boundary conditions” on the interface [61, 67, 93, 110, 127, 147]. The Schottky boundary conditions on the interface are,

$$\begin{aligned}\mathbf{n}_\Sigma \cdot (-\alpha_n \mu_n \rho_n \nabla \Phi - \mu_n \nabla \rho_n) &= v_n (\rho_n - \rho_n^e), \\ \mathbf{n}_\Sigma \cdot (-\alpha_p \mu_p \rho_p \nabla \Phi - \mu_p \nabla \rho_p) &= v_p (\rho_p - \rho_p^e),\end{aligned}\tag{5.3.1}$$

where v_n [cm s⁻¹] and v_p [cm s⁻¹] are respectively the electron and hole recombination velocities. It is clear that when the densities of the reductants and oxidants do not change over all applied biases, these Schottky boundary conditions are simply the interface conditions (2.4.7) and (2.4.8) with $v_n = k_{et} \rho_o$ and $v_p = k_{ht} \rho_r$. If the densities of the reductants and oxidants change with applied biases, then the Schottky approximation fails to faithfully reflect the impact of the electrolyte system on the performance of the device.

We compare here the simulation results using our model in this dissertation with those using the Schottky approximation. We consider the comparison for a device with $\Omega = (-0.1 \times 10^{-4} \text{cm}, 0.1 \times 10^{-4} \text{cm})$ with two different sets of parameters: D-VI, listed in Table 5.11 (left) and D-VII, listed in Table 5.11 (right). The main difference between the two devices are their redox pair concentrations. The comparison of current densities between simulations of the full system and the Schottky approximation for the two devices are displayed in Figure 5.19.

It can be observed from Figure 5.19 that the Schottky approximation produces results which are acceptable when the concentration of redox species are high compared to the densities of electrons and holes. However, when the redox concentrations are comparable with the density of electrons and

Table 5.11: D-VI (left) & D-VII (right) parameter values.

Parameter	Value	Unit	Parameter	Value	Unit
ρ_p^n	2	cm^{-3}	ρ_p^n	2	cm^{-3}
ρ_p^e	0	cm^{-3}	ρ_p^e	0	cm^{-3}
ρ_r^∞	30×10^{16}	cm^{-3}	ρ_r^∞	5×10^{16}	cm^{-3}
ρ_o^∞	29×10^{16}	cm^{-3}	ρ_o^∞	4×10^{16}	cm^{-3}
k_{et}	10^{-19}	$\text{cm}^4 \text{ s}^{-1}$	k_{et}	10^{-19}	$\text{cm}^4 \text{ s}^{-1}$
k_{ht}	10^{-12}	$\text{cm}^4 \text{ s}^{-1}$	k_{ht}	10^{-12}	$\text{cm}^4 \text{ s}^{-1}$
v_n	3×10^5	$\text{cm}^2 \text{ s}^{-1}$	v_n	3×10^5	$\text{cm}^2 \text{ s}^{-1}$
v_p	2.9×10^{-2}	$\text{cm}^2 \text{ s}^{-1}$	v_p	2.9×10^{-2}	$\text{cm}^2 \text{ s}^{-1}$
$\Phi_{\text{app.}}$	0	V	$\Phi_{\text{app.}}$	0	V

holes the Schottky approximation produces results that deviate appreciably from those computed with the full system. Specifically, in device D-VII, the current density computed with the full system is much smaller than the current density computed with the Schottky approximation. Deviations in current calculations can yield erroneous estimates of solar cell efficiency and fill factors. We demonstrate this as by plotting the current-voltage curves for both devices in Figure 5.20. The Schottky approximation over estimates the efficiency (3.58%) and the fill factor (0.5) compared to the simulation with the full reactive-interface conditions (efficiency = 3.01% and fill factor = 0.42) by over 0.5% and 0.08 respectively. We can see that it would be much more accurate to use the full semiconductor-electrolyte systems in such instances.

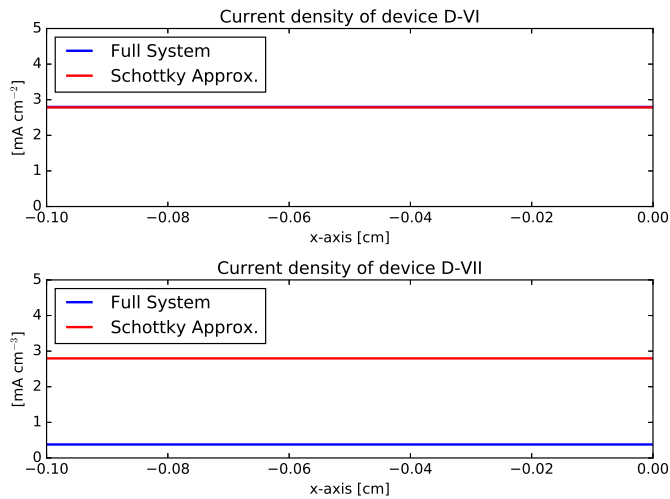


Figure 5.19: Current density as computed with full system and Schottky approximation.

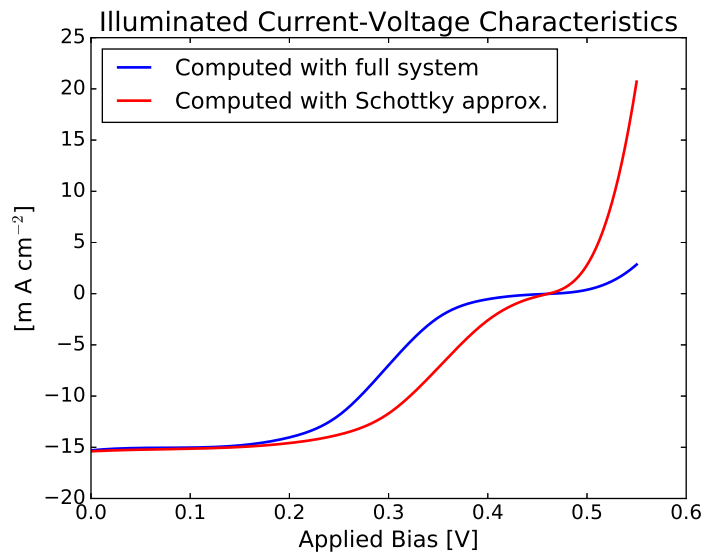


Figure 5.20: Illuminated current-voltage curves for device D-VII.

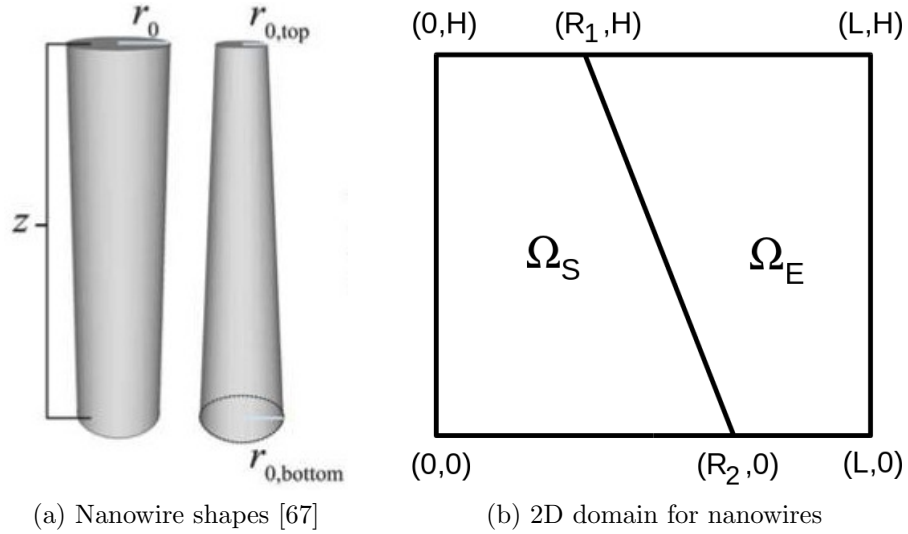


Figure 5.21: The domain for two dimensional nanowire simulations.

5.3.2 Two Dimensional Simulations

We now turn to the two dimensional simulations to investigate the dependence of the numerical solution on the shape of the nanowire as well as the boundary conditions. The simulations for a two dimensional semiconductor-electrolyte interface use the domain in Figure 5.21 (b) to represent a cross section of the nanowires depicted in Figure 5.21 (a). Specifically we aim to investigate the effect the radii lengths R_1 and R_2 as well as the boundary conditions have on a PEC solar cell's characteristics. We refer D-VIII to represent the two dimensional device where the interface is parallel to the vertical boundaries in Figure 5.21 (b). We refer D-IX to be the case where the interface is oblique to the vertical boundaries as depicted in Figure 5.21 (b). The common parameter values that we use in the two dimensional simulations are recorded in Table 5.12. These parameter values were chosen to better visual-

ize the dynamics of the charge densities under illumination. Throughout all the simulations, the top ($y = H$) and bottom ($y = 0$) of the electrolyte domain will always be insulated and the right boundary of the electrolyte domain ($y = L$) will have bulk redox and bulk potential values. That is we define the boundaries of the electrolyte to be,

$$\begin{aligned}\Gamma_{E,D} &= \{x = L\} \times [0, H], \\ \Gamma_{E,N} &= ([R_2, L] \times \{y = 0\}) \cup ([R_1, L] \times \{y = H\}).\end{aligned}\tag{5.3.2}$$

The boundary conditions of the semiconductor are broken up into three cases:

- **Boundary Conditions Case 1:** The top and bottom of the domain are insulating and the left boundary of the domain is an Ohmic contact:

$$\begin{aligned}\Gamma_{S,D} &= \{x = 0\} \times [0, H], \\ \Gamma_{S,N} &= ([0, R_2] \times \{y = 0\}) \cup ([0, R_1] \times \{y = H\}).\end{aligned}\tag{5.3.3}$$

- **Boundary Conditions Case 2:** The top and bottom boundary of the domain are Ohmic contacts and the left boundary of the domain is insulating:

$$\begin{aligned}\Gamma_{S,D} &= ([0, R_2] \times \{y = 0\}) \cup ([0, R_1] \times \{y = H\}), \\ \Gamma_{S,N} &= \{x = 0\} \times [0, H].\end{aligned}\tag{5.3.4}$$

- **Boundary Conditions Case 3:** The top, bottom and left boundary of the domain are all Ohmic contacts:

$$\begin{aligned}\Gamma_{S,D} &= (\{x = 0\} \times [0, H]) \cup ([0, R_2] \times \{y = 0\}) \cup ([0, R_1] \times \{y = H\}), \\ \Gamma_{S,N} &= \emptyset.\end{aligned}\tag{5.3.5}$$

Table 5.12: Parameter values for the two dimensional simulations.

Parameter	Value	Unit
ρ_n^e	2×10^{16}	cm^{-3}
ρ_p^e	0	cm^{-3}
ρ_r^∞	5×10^{16}	cm^{-3}
ρ_o^∞	4×10^{16}	cm^{-3}
k_{et}	10^{-19}	$\text{cm}^4 \text{ s}^{-1}$
k_{ht}	10^{-16}	$\text{cm}^4 \text{ s}^{-1}$
T	5×10^4	ps

Throughout all three cases the top boundary of the semiconductor domain ($y = H$) corresponds to a glass cover where light enters the device and travels straight downwards. Light will not be able to enter the bottom ($y = 0$) or the left boundary ($x = 0$) of the semiconductor domain. We remark that case 2 and case 3 are not realistic boundary conditions in computational electronics since the solutions to these problems are known to have analytical and numerical singularities as well as instability issues [69, 82]. We include these results in this dissertation for completeness.

5.3.2.1 Boundary Conditions Case 1

We first simulate devices that have an Ohmic contact on the left boundary of the semiconductor domain and the top and bottom of the device are insulated. We use the design of device D-VIII to simulate a cylindrical nanowire with dimensions that are summarized in Table 5.13 (left). The other device we investigate, D-IX, is used to simulate a conic nanowire design and its parameter values are summarized in Table 5.13 (right).

The densities of electron, holes, reductants and oxidants under an applied bias $\Phi_{\text{app.}} = 0.0$ [V] and an applied bias of $\Phi_{\text{app.}} = 0.5$ [V] are displayed in Figure 5.22. We can see that under zero applied bias electrons are mostly forced away from the interface and under a large applied bias they are forced toward the interface. This can also be verified from Figure 5.23 (a) and Figure 5.24 (a) which show the electron current density, \mathbf{J}_n , for $\Phi_{\text{app.}} = 0.0$ [V] and $\Phi_{\text{app.}} = 0.5$ [V] respectively. From Figure 5.23 (b) and Figure 5.24 (b), we can see that the photo-generated holes are mostly forced towards the interface for the case of $\Phi_{\text{app.}} = 0.0$ [V] and mostly forced away from the interface for $\Phi_{\text{app.}} = 0.5$ [V].

Table 5.13: D-VIII (left) & D-IX (right) domains.

Parameter	Value	Unit	Parameter	Value	Unit
R_1	0.5×10^{-4}	cm	R_1	0.3×10^{-4}	cm
R_2	0.5×10^{-4}	cm	R_2	0.7×10^{-4}	cm
H	1×10^{-4}	cm	H	1×10^{-4}	cm
L	1×10^{-4}	cm	L	1×10^{-4}	cm

Similarly, we can observe from Figure 5.22, Figure 5.23 and Figure 5.24 that reductants and oxidants are forced towards or away from interface depending on the value of the applied bias. It is important to note that in Figure 5.22 (b) the reductant and oxidant densities at the interface deviate appreciably from their bulk values. Indeed, the bulk density of the oxidants is lower than the bulk density of the reductants, however, at the interface the density of oxidants is higher than the density of reductants. In such instances, the validity of the assumption used for the Schottky approximations that the density or

redox species remains constants is clearly not true.

Finally, the potential distributions throughout the device under three applied biases are displayed in Figure 5.25. We can see that all three cases most of the applied potential drop occurs in the semiconductor region. However, depending on the value of the applied bias, the potential difference from the Ohmic contact to the interface can either be positive or negative. A positive potential difference corresponds to the electrons (holes) being forced away (towards) the interface and negative potential difference corresponds to the electrons (holes) being forced towards (away) the interface.

The densities of electrons, holes, reductants and oxidants of D-IX under illumination with an applied bias $\Phi_{app.} = 0.0$ [V] and $\Phi_{app.} = 0.5$ [V] are displayed in Figure 5.26. We can immediately see the behavior of device D-IX is very different from the behavoir of device D-VIII. The densities values of carriers in D-VIII were uniform y-axis, however, in device D-IX, the densities are not even uniform along the interface. Indeed, in Figure 5.26 we can observe local increases and decreases in the densities of carriers; specifically at the corners ends of the interface, that is the points (R_1, H) and $(R_2, 0)$. Interestingly, in Figure 5.29 we can see that the change in potential distribution remains uniform along the interface.

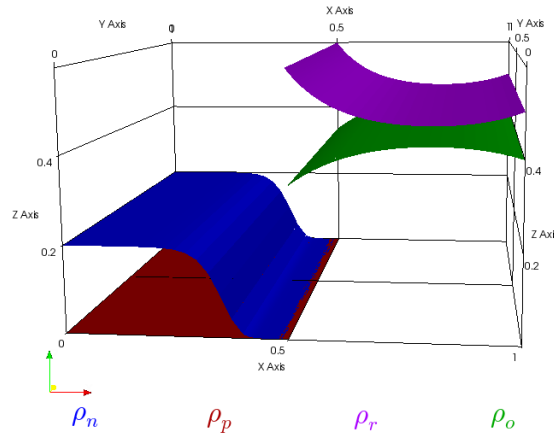
5.3.2.2 Boundary Conditions Case 2

We continue with simulations of device D-VIII, however, we choose the top and bottom of the semicondcutor to have Ohmic contacts and the left

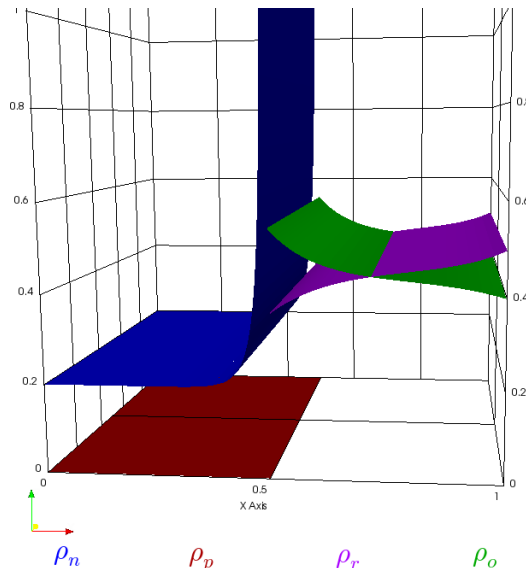
boundary of the domain to be insulating. The choice of applied potential is $\Phi_{\text{app.}} = \Phi_{\text{SCR}}$. However, this choice of boundary conditions does not produce strong currents at the semiconductor-electrolyte interface. As can be observed in Figure 5.30 (a), most of the photo-generated holes are created just below the top Ohmic contact. Figure 5.30 (b) displays the hole current density \mathbf{J}_p . We can see that the majority of these photo-generated holes do not approach the interface; instead they exit the semiconductor through the top Ohmic contact. Furthermore, using a design such as in device D-IX (where interface is slanted) with these boundary conditions leads to instabilities in the numerical solutions. We note that such instabilities are well-known phenomena [69, 82].

5.3.2.3 Boundary Conditions Case 3

Lastly, we have a two dimensional simulation where all of the semiconductor boundaries except for the interface are Ohmic contacts. For this choice of boundary conditions we only simulate a cylindrical nanowire design device D-VIII. We do not apply a potential bias to the device ($\Phi_{\text{app.}} = 0$) and the space charge region potential Φ_{SCR} occurs on the boundary $x = 0$. This choice of boundary conditions does not result in a stable discretization as can be observed in Figure 5.31. We see in Figure 5.31 that there is a break down in the regularity of the numerical solution for electrons near the points $(0, 0)$ and $(0, H)$. Near these two points there are discontinuous spikes in the density of electrons. As mentioned previously, such numerical instability is a well known result [69, 82].



(a)



(b)

Figure 5.22: Densities of charge carriers in D-VIII (parallel interface with case 1 boundary conditions) with (a) $\Phi_{app} = 0.0$ [V] and (b) $\Phi_{app} = 0.0$ [V]. Note: Densities are in 10^{17} [cm^{-3}].

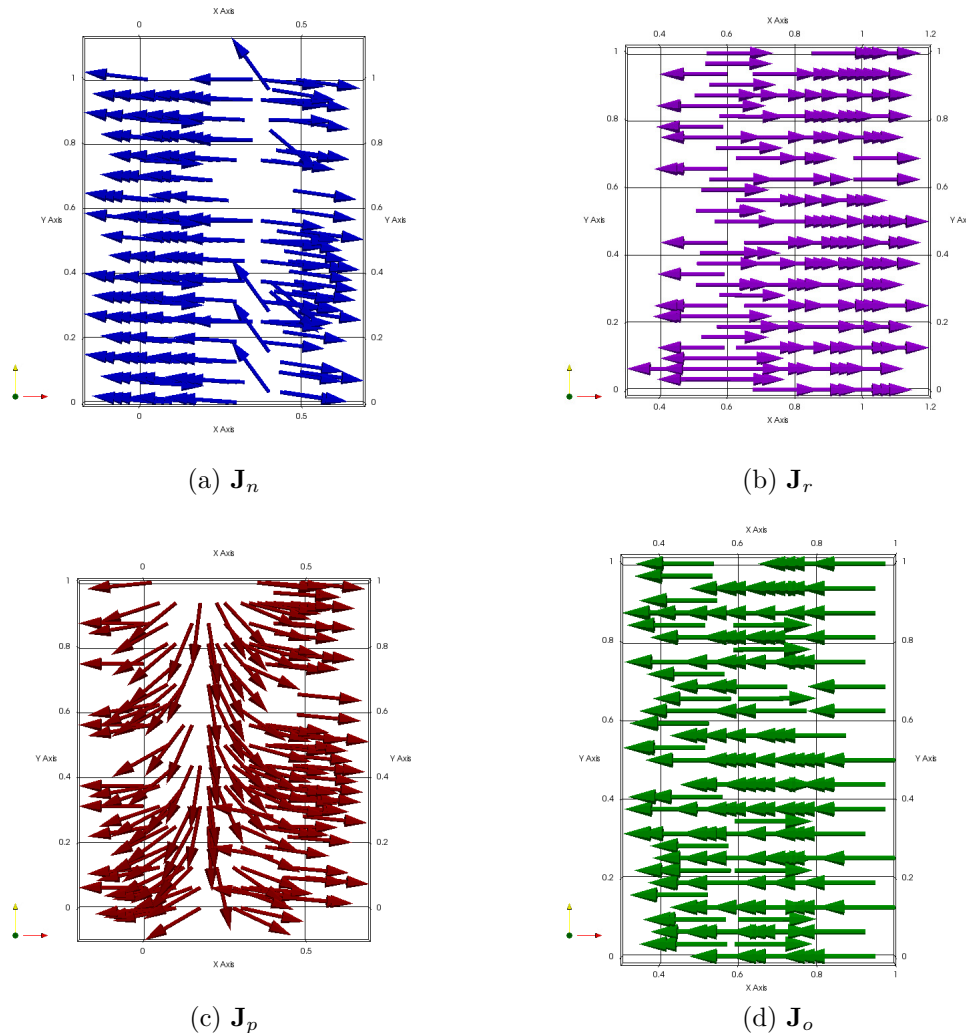


Figure 5.23: Carrier currents in device D-VIII (parallel interface with case 1 boundary conditions) with $\Phi_{app} = 0.0$ [V] for D-VIII.

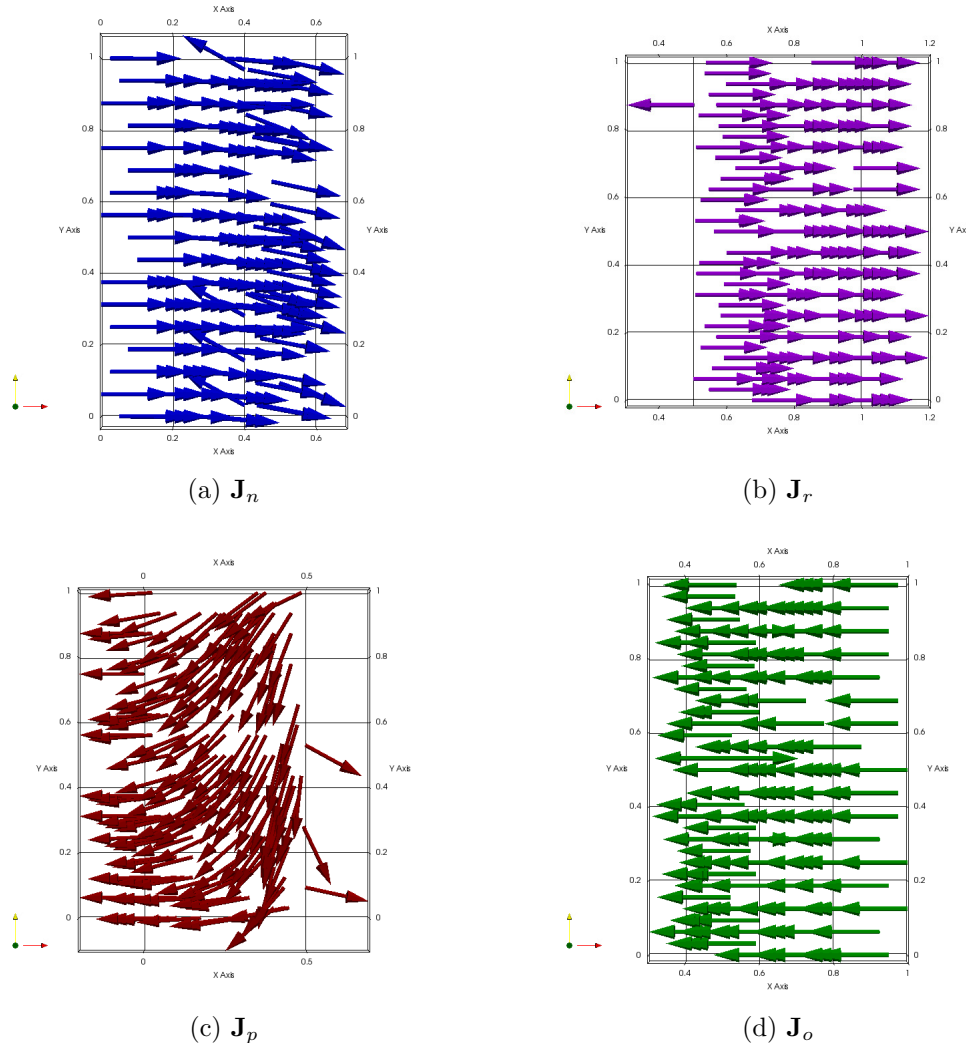


Figure 5.24: Carrier currents in device D-VIII (parallel interface with case 1 boundary conditions) with $\Phi_{app} = 0.5$ [V].

$$\Phi_{app} = 0.0 [V]$$

$$\Phi_{app} = 0.25 [V]$$

$$\Phi_{app} = 0.5 [V]$$

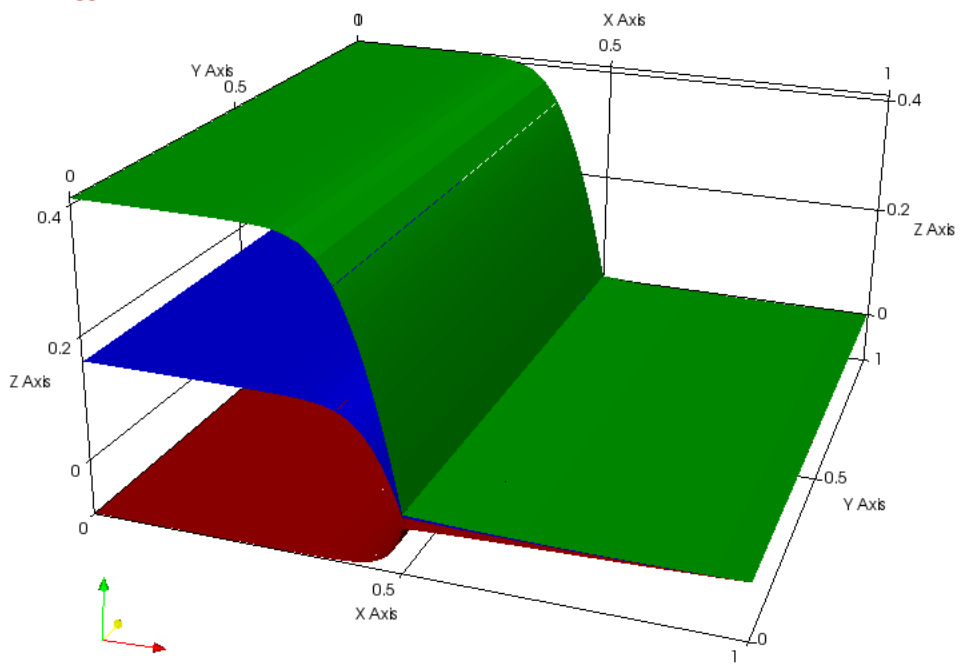
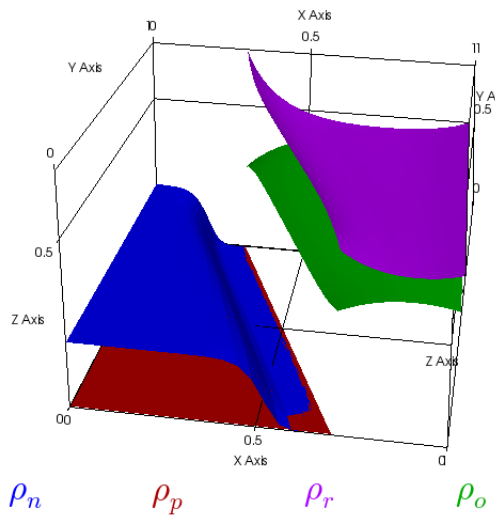
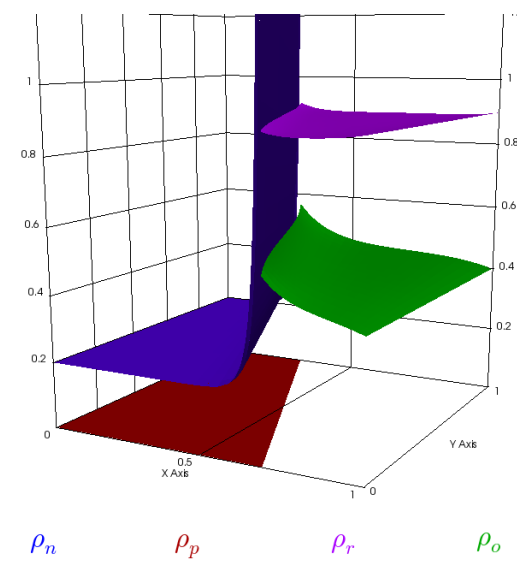


Figure 5.25: The potential distribution of D-VIII (parallel interface with case 1 boundary conditions) with different applied biases.

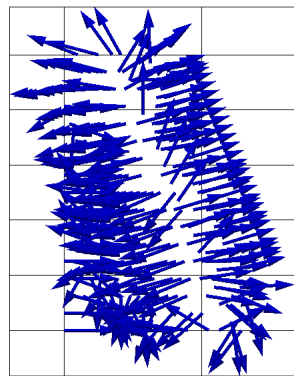


(a)

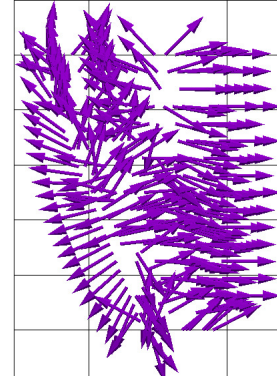


(b)

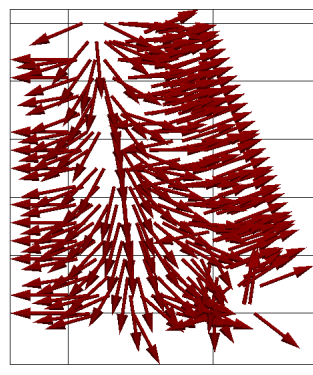
Figure 5.26: Densities of charge carriers in device D-IX (oblique interface with case 1 boundary conditions) with (a) $\Phi_{app} = 0.0$ [V] and (b) $\Phi_{app} = 0.0$ [V]. Note: Densities are in 10^{17} [cm $^{-3}$].



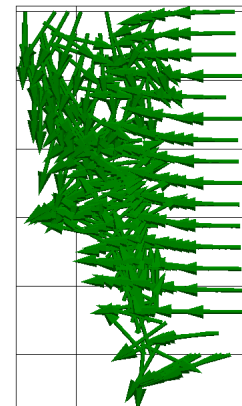
(a) \mathbf{J}_n



(b) \mathbf{J}_r

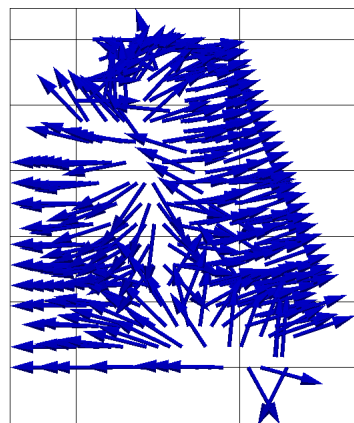


(c) \mathbf{J}_p

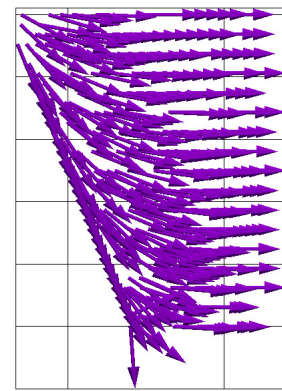


(d) \mathbf{J}_o

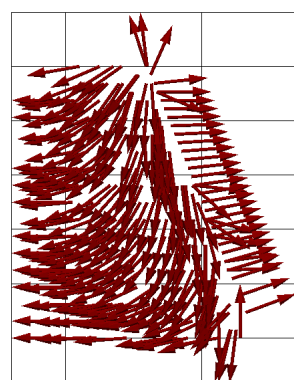
Figure 5.27: Carrier currents for device D-IX (oblique interface with case 1 boundary conditions) with $\Phi_{\text{app}} = 0 \text{ [V]}$.



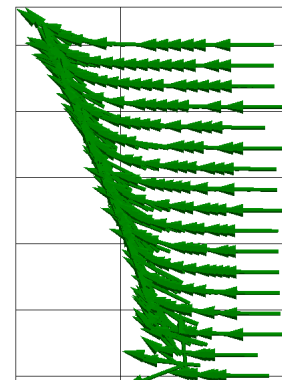
(a) \mathbf{J}_n



(b) \mathbf{J}_r



(c) \mathbf{J}_p



(d) \mathbf{J}_o

Figure 5.28: Carrier currents for device D-IX (oblique interface with case 1 boundary conditions) with $\Phi_{app} = 0.5$ [V].

$$\Phi_{app} = 0.0 [V]$$

$$\Phi_{app} = 0.25 [V]$$

$$\Phi_{app} = 0.5 [V]$$

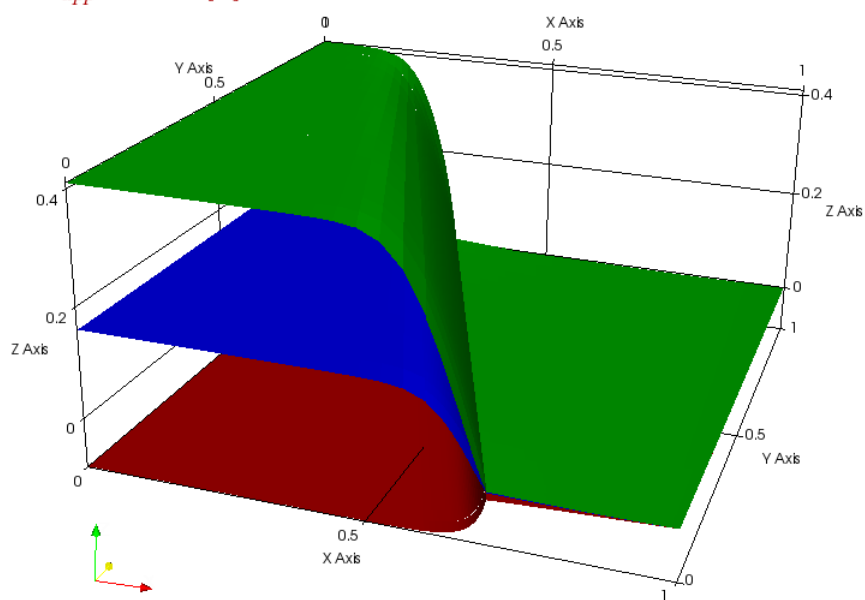
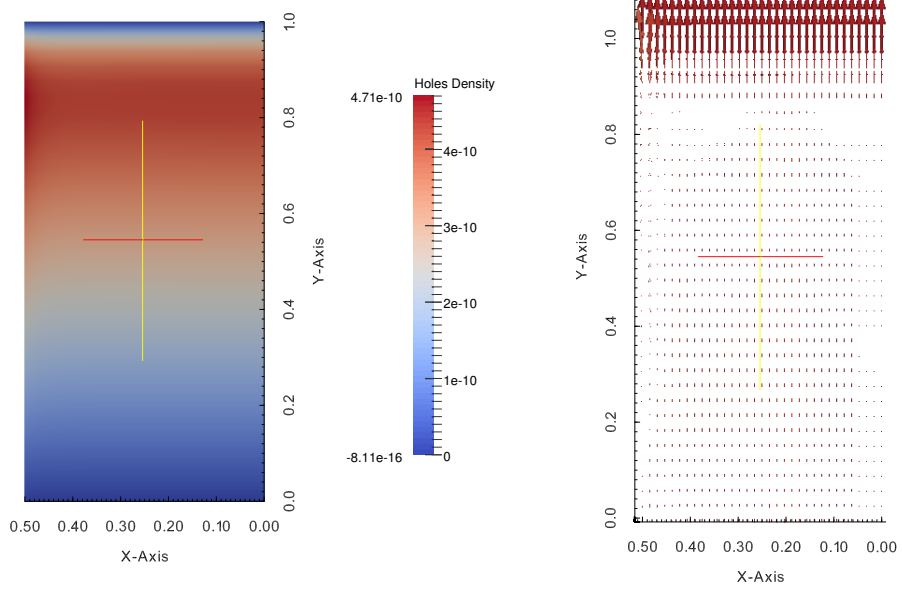


Figure 5.29: The potential distribution of device D-IX (oblique interface with case 1 boundary conditions) with different applied biases.



(a) Photo-generated hole density. Note: Densities are in 10 cm^{-3} . (b) Photo-generated hole current.

Figure 5.30: Results from D-VIII (parallel interface with case 2 boundary conditions).

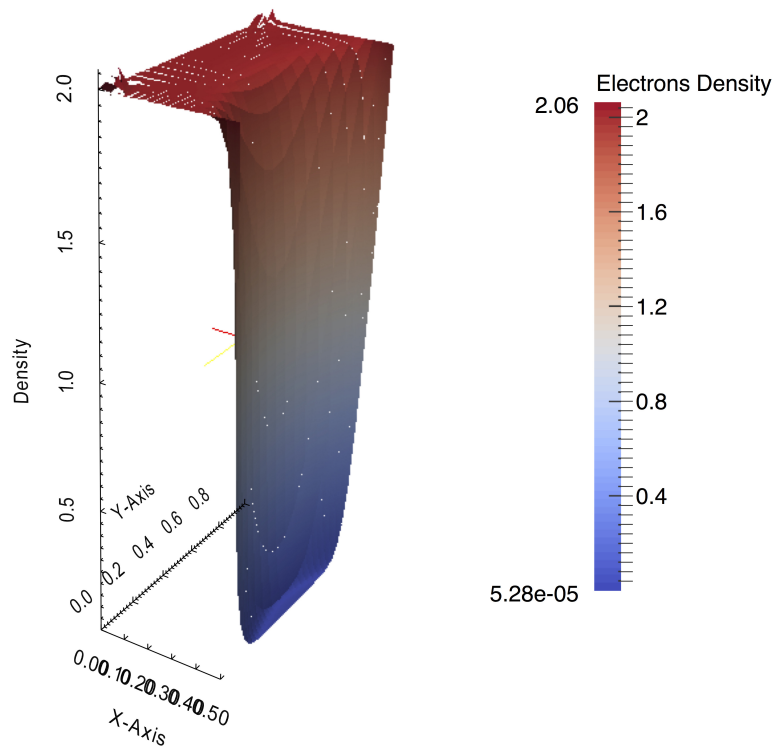


Figure 5.31: Electron densities for D-VIII (parallel interface with case 3 boundary conditions). Note: The density is in 10^{16} [cm $^{-3}$].

Chapter 6

Concluding Remarks And Future Developments

In this dissertation we proposed some numerical algorithms for solving systems of drift-diffusion-Poisson equations that arise from the modeling of charge transport in PEC solar cells with reactive interfaces. In our algorithms we used a mixed finite element discretization for the Poisson equation and a local discontinuous Galerkin discretization for the corresponding drift-diffusion equations. For the temporal variable, we developed some implicit-explicit time stepping methods to alleviate the stability constraints imposed by the Courant-Friedrichs-Lax (CFL) conditions as well as to decouple the equations in the semiconductor domain from the equations in the electrolyte domain. We calibrated our implementation with manufactured solutions and presented numerical simulations to show the impact of various device parameters on the performance of the PEC cells.

The convergence of some of the numerical algorithms was proven in a slightly simplified setting. To do so, we derived the primal form of the semidiscrete LDG method and proved this methods consistency, as well as the coercivity and continuity of its bilinear form. We used these properties

to obtain the semidiscrete error estimates for the LDG approximations to the semiconductor-electrolyte interface problem.

In order to make simulations of this model more relevant for optimizing the design of PEC cells under variations of all material parameters the numerical approximation of solutions to steady state equations should be addressed. In addition, such implementations should be completed on distributed processors for simulations to be conducted in three dimensions. This requires the use of iterative solvers and to determine appropriate preconditioners of the resulting linear systems. On the theoretical side, the question of existence and uniqueness of solutions to the simplified model of the reactive interface needs to be addressed. Finally, one can extend the error estimates derived here to include the MFEM and LDG method for the fully coupled system of drift-diffusion-Poisson equations.

Appendices

Appendix A

Appendix

A.1 LDG Analysis Appendix

A.1.1 Lipschitz Property of Recombination

Proof of Thoerem 4.1.1: The proof of the Lipschitz property of the function (2.2.21) comes from its multilinearity. We write this as a general function,

$$R(x, y) := \frac{A - x y}{C + \alpha x + \beta y}. \quad (\text{A.1.1})$$

Where $x = \rho_n$, $y = \rho_p$, $A = \rho_i^2$, $C = \tau_n \rho_n^t + \tau_p \rho_p^t$, $\alpha = \tau_n$, and $\beta = \tau_p$.

We now look at the difference,

$$\begin{aligned} & R(x_1, y_1) - R(x_2, y_2) \\ &= \frac{A - x_1 y_1}{C + \alpha x_1 + \beta y_1} - \frac{A - x_2 y_2}{C + \alpha x_2 + \beta y_2} \\ &= \frac{(A\alpha + \beta y_1 y_2 + C y_1)(x_2 - x_1) + (A\beta + \alpha x_1 x_2 + C x_2)(y_2 - y_1)}{C^2 + C\alpha(x_1 + x_2) + C\beta(y_1 + y_2) + \alpha\beta(x_1 y_2 + x_2 y_1) + \alpha^2 x_1 x_2 + \beta^2 y_1 y_2} \end{aligned} \quad (\text{A.1.2})$$

Fixing $y_1 = y_2 = y$ then,

$$\lim_{y \rightarrow \infty} |R(x_1, y) - R(x_2, y)| \leq \frac{1}{\alpha} |x_1 - x_2|, \quad (\text{A.1.3})$$

and doing the same for x ,

$$\lim_{x \rightarrow \infty} |R(x, y_1) - R(x, y_2)| \leq \frac{1}{\beta} |y_1 - y_2|. \quad (\text{A.1.4})$$

This gives us,

$$|R(x_1, y_1) - R(x_2, y_2)| \leq \frac{1}{\alpha} |x_1 - x_2| + \frac{1}{\beta} |y_1 - y_2|. \quad (\text{A.1.5})$$

For the case of Shockley-Reed-Hall recombination with the form (2.2.21) we obtain,

$$|R(\rho_n^1, \rho_p^1) - R(\rho_n^1, \rho_p^2)|^2 \leq \frac{1}{\tau_n^2} |\rho_n^1 - \rho_n^2|^2 + \frac{1}{\tau_p^2} |\rho_p^1 - \rho_p^2|^2. \quad (\text{A.1.6})$$

Integrating over the domain Ω_S produces the desired results.

□

A.1.2 Derivation Of Primal Form Of LDG Method

In this section we derive the primal form of the LDG formulation discussed presented in Chapter 4. To simplify the presentation of the discretization, we only consider the drift-diffusion equation for the electrons in the system (4.1.3)- (4.1.6). The primal form of the LDG method for other charge carriers are derived in the same way. The semidiscrete LDG approximation of (4.1.3)- (4.1.6) is,

Find $\rho_{n,h}(\cdot, t) \in W_{h,k}^S$ and $\mathbf{q}_{n,h}(\cdot, t) \in \mathbf{W}_{h,k}^S$ such that,

$$\begin{aligned} (w, \partial_t \rho_{n,h}) + \mathcal{L}_{n,S}(w, \mathbf{w}; \rho_{n,h}, \mathbf{q}_{n,h}) + \langle w, I_{et}(\mathcal{M}(\rho_{n,h} - \rho_n^e), \mathcal{M}(\rho_{o,h})) \rangle_{\mathcal{E}_\Sigma^S} \\ = \left(w, \tilde{R}(\rho_{n,h}, \rho_{p,h}) \right)_{\Omega_S} + \langle w, \sigma_n \rho_n^e \rangle_{\mathcal{E}_D^S} \end{aligned} \quad (\text{A.1.7})$$

$$\mathcal{A}_{n,S}(w, \mathbf{w}; \rho_{n,h}, \mathbf{q}_{n,h}) - (w, \alpha_n D_n^{-1} \mu_n \mathbf{E} \rho_{n,h})_{\Omega_S} = -\langle \mathbf{n} \cdot \mathbf{w}, \rho_n^e \rangle_{\mathcal{E}_D^S} \quad (\text{A.1.8})$$

for all $(w, \mathbf{w}) \in W_{h,k}^S \times \mathbf{W}_{h,k}^S$ and all $t \in (0, T)$. The quadlinear forms $\mathcal{L}_{n,S}$ and $\mathcal{A}_{n,S}$ are defined as,

$$\begin{aligned} \mathcal{L}_{n,S} = & -(\nabla w, \mathbf{q}_{n,h})_{\Omega_S} + \langle [\![w]\!], \sigma_n [\![\rho_{n,h}]\!] \rangle_{\mathcal{E}_h^{i,S}} + \langle [\![w]\!], \{\mathbf{q}_{n,h}\} - [\![\mathbf{q}_{n,h}]\!] \boldsymbol{\beta} \rangle_{\mathcal{E}_h^{i,S}} \\ & + \langle w, \mathbf{n} \cdot \mathbf{q}_{n,h} \rangle_{\mathcal{E}_D^S} + \langle w, \sigma_n \rho_{n,h} \rangle_{\mathcal{E}_D^S}, \end{aligned} \quad (\text{A.1.9})$$

$$\begin{aligned} \mathcal{A}_{n,S} = & (\mathbf{w}, D_n^{-1} \mathbf{q}_{n,h})_{\Omega_S} - (\nabla \cdot \mathbf{w}, \rho_{n,h})_{\Omega_S} + \langle [\![\mathbf{w}]\!], \{\rho_{n,h}\} + \boldsymbol{\beta} \cdot [\![\rho_{n,h}]\!] \rangle_{\mathcal{E}_h^{i,S}} \\ & + \langle w, \rho_{n,h} \rangle_{\mathcal{E}_N^S \cup \mathcal{E}_\Sigma^S}. \end{aligned} \quad (\text{A.1.10})$$

Substituting in (A.1.10) into (A.1.8) we rearrange the terms to obtain the equation,

$$\begin{aligned} & (\mathbf{w}, D_n^{-1} \mathbf{q}_{n,h})_{\Omega_S} - (\mathbf{w}, \alpha_n D_n^{-1} \mu_n \mathbf{E} \rho_{n,h})_{\Omega_S} - (\nabla \cdot \mathbf{w}, \rho_{n,h})_{\Omega_S} \\ & + \langle [\![\mathbf{w}]\!], \{\rho_{n,h}\} + \boldsymbol{\beta} \cdot [\![\rho_{n,h}]\!] \rangle_{\mathcal{E}_h^{i,S}} + \langle \mathbf{n} \cdot \mathbf{w}, \rho_{n,h} \rangle_{\mathcal{E}_N^S \cup \mathcal{E}_\Sigma^S} \quad (\text{A.1.11}) \\ & + \langle \mathbf{n} \cdot \mathbf{w}, \rho_n^e \rangle_{\mathcal{E}_D^S} = 0. \end{aligned}$$

Using Lemma 4.1.7 on the third term in (A.1.11) yields,

$$\begin{aligned} & (\mathbf{w}, D_n^{-1} \mathbf{q}_{n,h})_{\Omega_S} - (\mathbf{w}, \alpha_n D_n^{-1} \mu_n \mathbf{E} \rho_{n,h})_{\Omega_S} + (\mathbf{w}, \nabla_h \rho_{n,h})_{\Omega_S} - \langle [\![\mathbf{w}]\!], \{\rho_{n,h}\} \rangle_{\mathcal{E}_h^{i,S}} \\ & - \langle \{\mathbf{w}\}, [\![\rho_{n,h}]\!] \rangle_{\mathcal{E}_h^{i,S}} - \langle \mathbf{n} \cdot \mathbf{w}, \rho_{n,h} \rangle_{\mathcal{E}_D^S \cup \mathcal{E}_N^S \cup \mathcal{E}_\Sigma^S} \\ & + \langle [\![\mathbf{w}]\!], \{\rho_{n,h}\} + \boldsymbol{\beta} \cdot [\![\rho_{n,h}]\!] \rangle_{\mathcal{E}_h^{i,S}} + \langle \mathbf{n} \cdot \mathbf{w}, \rho_{n,h} \rangle_{\mathcal{E}_N^S \cup \mathcal{E}_\Sigma^S} \\ & + \langle \mathbf{n} \cdot \mathbf{w}, \rho_n^e \rangle_{\mathcal{E}_D^S} = 0. \end{aligned} \quad (\text{A.1.12})$$

Upon simplifying the above we have,

$$\begin{aligned}
& (\mathbf{w}, D_n^{-1} \mathbf{q}_{n,h})_{\Omega_S} - (\mathbf{w}, \alpha_n \mu_n \mathbf{E} \rho_{n,h})_{\Omega_S} + (\mathbf{w}, \nabla_h \rho_{n,h})_{\Omega_S} + \langle [\![\mathbf{w}]\!], \boldsymbol{\beta} \cdot [\![\rho_{n,h}]\!] \rangle_{\mathcal{E}_h^{i,S}} \\
& - \langle \{ \mathbf{w} \}, [\![\rho_{n,h}]\!] \rangle_{\mathcal{E}_h^{i,S}} - \langle \mathbf{n} \cdot \mathbf{w}, (\rho_{n,h} - \rho_n^e) \rangle_{\mathcal{E}_D^S} = 0.
\end{aligned} \tag{A.1.13}$$

Using the lift operators (4.1.27), (4.1.28), and (4.1.29) then (A.1.13) becomes,

$$\begin{aligned}
& (\mathbf{w}, D_n^{-1} \mathbf{q}_{n,h})_{\Omega_S} - (\mathbf{w}, \alpha_n \mu_n \mathbf{E} \rho_{n,h})_{\Omega_S} + (\mathbf{w}, \nabla_h \rho_{n,h})_{\Omega_S} \\
& - (\mathbf{w}, \mathbf{l}^S(\boldsymbol{\beta} \cdot [\![\rho_{n,h}]\!]))_{\Omega_S} - (\mathbf{w}, \mathbf{r}^S([\![\rho_{n,h}]\!]))_{\Omega_S} \\
& - (\mathbf{w}, \mathbf{r}_D^S(\rho_{n,h} - \rho_n^e))_{\Omega_S} = 0.
\end{aligned} \tag{A.1.14}$$

Rearranging terms yields,

$$\begin{aligned}
& (\mathbf{w}, D_n^{-1} \mathbf{q}_{n,h} - \alpha_n \mu_n \mathbf{E} \rho_{n,h} + \nabla_h \rho_{n,h} - \mathbf{r}^S([\![\rho_{n,h}]\!]) - \mathbf{l}^S(\boldsymbol{\beta} \cdot [\![\rho_{n,h}]\!]) \\
& - \mathbf{r}_D^S(\rho_{n,h} - \rho_n^e))_{\Omega_S} = 0.
\end{aligned} \tag{A.1.15}$$

Noting that (A.1.15) holds for all $\mathbf{w} \in \mathbf{W}_{h,k}^S$ then,

$$\begin{aligned}
\mathbf{q}_{n,h} &= \alpha_n \mu_n \mathbf{E} \rho_{n,h} \\
&+ D_n (-\nabla_h \rho_{n,h} + \mathbf{r}^S([\![\rho_{n,h}]\!]) + \mathbf{l}^S(\boldsymbol{\beta} \cdot [\![\rho_{n,h}]\!]) + \mathbf{r}_D^S(\rho_{n,h} - \rho_n^e))
\end{aligned}$$

in Ω_S and all $t \in (0, T)$.

Now we return to (A.1.9). Substituting in the definitions of the lift

operators (4.1.27), (4.1.28), and (4.1.29) into (A.1.9) to obtain,

$$\begin{aligned}
\mathcal{L}_{n,S} &= - \left(\nabla_h w, \mathbf{q}_{n,h} \right)_{\Omega_S} + \langle \llbracket w \rrbracket, \sigma_n \llbracket \rho_{n,h} \rrbracket \rangle_{\mathcal{E}_h^{i,S}} + \langle \llbracket w \rrbracket, \{ \mathbf{q}_{n,h} \} - \llbracket \mathbf{q}_{n,h} \rrbracket \boldsymbol{\beta} \rangle_{\mathcal{E}_h^{i,S}} \\
&\quad + \langle w, \mathbf{n} \cdot \mathbf{q}_{n,h} \rangle_{\mathcal{E}_D^S} + \langle w, \sigma_n \rho_{n,h} \rangle_{\mathcal{E}_D^S} \\
&= - \left(\nabla_h w, \mathbf{q}_{n,h} \right)_{\Omega_S} + \left(\mathbf{r}^S(\llbracket w \rrbracket), \mathbf{q}_{n,h} \right)_{\Omega_S} + \left(\mathbf{l}^S(\boldsymbol{\beta} \cdot \llbracket w \rrbracket), \mathbf{q}_{n,h} \right)_{\Omega_S} \\
&\quad + \langle \mathbf{r}_D^S(w), \mathbf{q}_{n,h} \rangle_{\Omega_S} + \langle \llbracket w \rrbracket, \sigma_n \llbracket \rho_{n,h} \rrbracket \rangle_{\mathcal{E}_h^{i,S}} + \langle w, \sigma_n \rho_{n,h} \rangle_{\mathcal{E}_D^S} \\
&= (-\nabla_h w + \mathbf{r}^S(\llbracket w \rrbracket) + \mathbf{l}^S(\boldsymbol{\beta} \cdot \llbracket w \rrbracket) + \mathbf{r}_D^S(w), \mathbf{q}_{n,h})_{\Omega_S} \\
&\quad + \langle \llbracket w \rrbracket, \sigma_n \llbracket \rho_{n,h} \rrbracket \rangle_{\mathcal{E}_h^{i,S}} + \langle w, \sigma_n \rho_{n,h} \rangle_{\mathcal{E}_D^S}.
\end{aligned}$$

Substituting this in to (A.1.7) yields,

$$\begin{aligned}
&(w, \partial_t \rho_{n,h}) + (-\nabla_h w + \mathbf{r}^S(\llbracket w \rrbracket) + \mathbf{l}^S(\boldsymbol{\beta} \cdot \llbracket w \rrbracket) + \mathbf{r}_D^S(w), \mathbf{q}_{n,h})_{\Omega_S} \\
&\quad + \langle w, I_{et}(\rho_{n,h} - \rho_n^e, \rho_{o,h}) \rangle_{\mathcal{E}_{\Sigma}^S} \\
&= \left(w, \tilde{R}(\rho_{n,h}, \rho_{p,h}) \right)_{\Omega_S} + \langle w, \sigma_n \rho_n^e \rangle_{\mathcal{E}_D^S}
\end{aligned}$$

Now substituting (A.1.16) into the above we arrive at the primal form of (A.1.7)-(A.1.8),

$$\begin{aligned}
&(w, \partial_t \rho_{n,h}) + B_{n,S}(w, \rho_{n,h}) + \langle w, I_{et}(\mathcal{M}(\rho_{n,h} - \rho_n^e), \mathcal{M}(\rho_{o,h})) \rangle_{\mathcal{E}_{\Sigma}^S} \\
&= l \left(w, \tilde{R}(\rho_{n,h}, \rho_{p,h}) \right)_{\Omega_S} + \langle w, \sigma_n \rho_n^e \rangle_{\mathcal{E}_D^S} \\
&\quad - (D_n(-\nabla_h w + \mathbf{r}^S(\llbracket w \rrbracket) + \mathbf{l}^S(\boldsymbol{\beta} \cdot \llbracket w \rrbracket) + \mathbf{r}_D^S(w)), \mathbf{r}_D^S(\rho_n^e))_{\Omega_S}, \tag{A.1.16}
\end{aligned}$$

where we have defined the bilinear form $B_{n,S} : W_{h,k}^S \times W_{h,k}^S \rightarrow \mathbb{R}$ for all

$t \in (0, T)$ as,

$$B_{n,S}(w, \rho_{n,h}) =$$

$$(-\nabla_h w + \mathbf{r}^S(\llbracket w \rrbracket) + \mathbf{l}^S(\boldsymbol{\beta} \cdot \llbracket w \rrbracket) + \mathbf{r}_D^S(w),$$

$$D_n(-\nabla_h \rho_{n,h} + \mathbf{r}^S(\llbracket \rho_{n,h} \rrbracket) + \mathbf{l}^S(\boldsymbol{\beta} \cdot \llbracket \rho_{n,h} \rrbracket) + \mathbf{r}_D^S(\rho_{n,h})))_{\Omega_S} \quad (\text{A.1.17})$$

$$- (\nabla_h w - \mathbf{r}^S(\llbracket w \rrbracket) - \mathbf{l}^S(\boldsymbol{\beta} \cdot \llbracket w \rrbracket) - \mathbf{r}_D^S(w), \alpha_n \mu_n \mathbf{E} \rho_{n,h})_{\Omega_S}$$

$$+ \langle \llbracket w \rrbracket, \sigma_n \llbracket \rho_{n,h} \rrbracket \rangle_{\mathcal{E}_h^{i,S}} + \langle w, \sigma_n \rho_{n,h} \rangle_{\mathcal{E}_D^S}.$$

Bibliography

- [1] *Boost c++ libraries*. <http://www.boost.org>.
- [2] *Cmake: Cross platform make*. <http://www.cmake.org>.
- [3] *Eigen*. <http://www.eigen.tuxfamily.org>.
- [4] *Electrochemical energy lab*. <http://web.mit.edu/eel/people.html>.
- [5] *Gnu scientific library*. <http://www.gnu.org/software/gsl/>.
- [6] *Intel thread building blocks*. <http://www.intel.org>.
- [7] *Openmp*. <http://www.openmp.org>.
- [8] *The visualization toolkit*. <http://www.vtk.org>.
- [9] T. ARBOGAST, S. BRYANT, C. DAWSON, F. SAAF, C. WANG, AND M. F. WHEELER, *Computational methods for multiphase flow and reactive transport problems arising in subsurface contaminant remediation*, J. of Comp. and App. Math., 33 (1996), pp. 19–32.
- [10] T. ARBOGAST, M. JUNTUNEN, J. POOL, AND M. F. WHEELER, *A discontinuous galerkin method for two-phase flow in a porous medium enforcing $h(\text{div})$ velocity and continuous capillary pressure*, Comput. Geosci., 17 (2013), pp. 1055–1078.

- [11] T. ARBOGAST, M. F. WHEELER, AND N.-Y. ZHANG, *A nonlinear mixed finite element method for a degenerate parabolic equation arising in flow in porous media*, Siam J. Numer. Anal., 33 (1996), p. 1996.
- [12] D. ARNOLD, F. BREZZI, B. COCKBURN, AND L. MARINI, *Unified analysis of discontinuous galerkin methods for elliptic problems*, Siam J. Numer. Anal., 339 (2002), pp. 1749–1779.
- [13] U. M. ASCHER, S. J. RUUTH, AND R. J. SPITERI, *Implicit-explicit runge-kutta methods for time-dependent partial differential equations*, Applied Numer. Math., 25 (1997), pp. 151–167.
- [14] U. M. ASCHER, S. J. RUUTH, AND B. T. WETTON, *Implicit-explicit methods for time-dependent partial differential equations*, SIAM J. Numer. Anal., 32 (1995), pp. 797–823.
- [15] B. AYUSO AND L. D. MARINI, *Discontinuous galerkin methods for advection-diffusion-reaction problems*, SIAM J. Numer. Anal., 47 (2009), pp. 1391–1420.
- [16] C.-W. S. B. COCKBURN, *Tvb runge-kutta local projection discontinuous galerkin finite element method for conservation laws iii: One-dimensional systems*, J. Comp. Phys., 84 (1989), pp. 90–113.
- [17] ——, *The runge-kutta local projection discontinuous galerkin finite element method for conservation laws iv: The multidimensional case*, Math. Comp., 54 (1990), pp. 545–581.

- [18] C.-W. S. B. COCKBURN, *The runge-kutta local projection p1-discontinuous galerkin finite element method for scalar conservation laws.*, Math. Anal. Numer, 25 (1991), pp. 337–361.
- [19] C.-W. S. B. COCKBURN, *The runge-kutta local projection discontinuous galerkin finite element method for conservation laws v: Multidimensional systems*, J. Comp. Phys., 141 (1998), pp. 199–224.
- [20] I. BABUSKA, *The finite element method with lagrange multipliers*, Num. Math., 20 (1973), pp. 172–192.
- [21] W. BANGERTH, R. HARTMANN, AND G. KANSCHAT, *deal.II – a general purpose object oriented finite element library*, ACM Trans. Math. Softw., 33 (2007), pp. 24/1–24/27.
- [22] W. BANGERTH, T. HEISTER, L. HELTAI, G. KANSCHAT, M. KRONBICHLER, M. MAIER, AND B. TURCKSIN, *The deal.II library, version 8.3*, preprint, (2015).
- [23] R. E. BANK, D. J. ROSE, AND W. FICHTNER, *Numerical methods for semiconductor device simulation*, SIAM J. Sci and Stat. Comput., 30 (1983).
- [24] A. J. BARD AND L. R. FAULKNER, *Electrochemical Methods*, John Wiley & Sons, 2001.
- [25] A. J. BARD, R. MEMMING, AND B. MILLER, *Terminiology in semiconductor electrochemistry and photoelectrochemical energy conversion*, In-

ternatiional Union Of Pure And Applied Chemistry, 63 (1991), pp. 569–596.

- [26] J. BARNES AND R. LOMAX, *Finite element methods in semiconductor device modeling*, IEEE Trans. Electron. Devices, (1977).
- [27] F. BASSI AND S. REBAY, *A high-order accurate discontinuous galerkin finite element method for then numerical solution of the compressible navier-stokes equations*, J. Comput. Physics, 131 (1997), pp. 267–279.
- [28] S. BAUMGARTNER AND C. HEITZINGER, *A one-level feti method for the dfit-diffusion-poisson system with discontinuities at an interface*, J. Comp. Phys., 243 (2013), pp. 74–86.
- [29] M. Z. BAZANT, K. THORTON, AND A. AJDARI, *Diffuse charge dynamics in electrochemical system*, Phys. Rev. E., 70 (2004).
- [30] E. B. BECKER, G. F. CAREY, AND J. T. ODEN, *Finite Elements: An Introduction*, vol. 1, 1981.
- [31] P. M. BIESCHEUVEL, Y. FU, AND M. Z. BAZANT, *Electrochemistry and capacitance charging of porous electrodes in asymmetric multicomponent electrolytes*, Russian J. Electrochem, 48 (2012), pp. 580–592.
- [32] D. BOFFI, F. BREZZI, AND M. FORTIN, *Mixed Finite Element Methods and Applications*, Springer, 2013.

- [33] S. C. BRENNER AND L. R. SCOTT, *The Mathematical Theory of Finite Element Methods*, Springer, 2008.
- [34] F. BREZZI, *On the existence uniqueness and approximation of saddle-point problems arising from lagrange multipliers*, R.A.I.R.O., 8 (1974), pp. 129–151.
- [35] F. BREZZI, J. DOUGLAS, AND L. D. MARINI, *Two familes of mixed finite elements for second order elliptic problems*, Numerische Mathematik, 47 (1985), pp. 217–235.
- [36] D. BRINKMAN, K. FELLNER, P. A. MARKOWICH, AND M. T. WOLFRAM, *A drift-diffusion reaction model for excitonic photovoltaic bilayers: asymptotic analysis and a 2d hdg finite element scheme*, Math. Model Methods Appl. Sci., 23 (2013), pp. 839–972.
- [37] C. F. C.A. FELIPPA, K.C. PARK, *Partitioned analysis of coupled mechanical systems*, Computer Methods in Applied Mechanics and Engineering, 190 (1998), pp. 3247–3270.
- [38] G. CAREY AND A. L. P. AND. S. W. BOVA, *Advanced numerical methods and software approaches for semiconductor device simulation*, VLSI DESIGN, 10 (2000), pp. 391–414.
- [39] P. CASTILLO, *Performance of discontinuous galerkin methods for elliptic pde's*, SIAM J. Sci. Comput., 24 (2002), pp. 524–547.

- [40] P. CASTILLO, B. COCKBURN, I. PERUGIA, AND D. SCHOTZAU, *An a priori error analysis of the local discontinuous galerkin method for elliptic problems*, SIAM, 38 (2000), pp. 1676–1706.
- [41] ———, *Local discontinuous galerkin methods for elliptic problems*, Communications In Numerical Methods In Engineering, 18 (2002), pp. 69–75.
- [42] P. CASTILLO, B. COCKBURN, D. SCHOTZAU, AND C. SCHWAB, *Optimal a priori error estimates for the hp -version of the local discontinuous galerkin method for convection-diffusion problems.*, Math. Comp., 71 (2002), pp. 455–478.
- [43] Z. CHEN, *Finite element analysis of the one-dimensional full drift-diffusion semiconductor model*, SIAM J. Numer. Anal., 32 (1995), pp. 455–483.
- [44] Z. CHEN AND B. COCKBURN, *Analysis of a finite element method for the drift-diffusion semiconductor device equations: the multidimensional case*, Numer. Math., 71 (1995), pp. 1–28.
- [45] Z. CHEN, G. HUAN, AND B. LI, *An improved impos method for two phase flow in porus media*, Transport in Porous Media, 54 (2004), pp. 361–376.
- [46] K. H. COATS, *A note on impos and some impos-based simulation models*, Society of Petroleum Engineering Journal, 5 (2000), pp. 245–251.
- [47] ———, *Impos stability: Selection of stable timesteps*, Society of Petroleum Engineering Journal, 8 (2003), pp. 181–187.

- [48] B. COCKBURN AND C. DAWSON, *Some extensions of the local discontinuous galerkin method for convection-diffusion equations in multidimensions*, 1999, pp. 225–238.
- [49] B. COCKBURN, G. KANSCHAT, I. PERUGIA, AND D. SCHOTZAU, *Superconvergence of the local discontinuous galerkin method for elliptic problems on cartesian grids*, SIAM J. Numer. Anal., 39 (2002), pp. 264–285.
- [50] B. COCKBURN AND C.-W. SHU, *The local discontinuous galerkin methods for time-dependent convection-diffusion systems*, SIAM J. Numer. Anal., 35 (1998).
- [51] B. COCKBURN AND C. W. SHU, *Runge-kutta discontinuous galerkin methods for convection-dominated problems*, J. of Sci. Comp., 16 (2001).
- [52] J. M. CONNORS, J. S. HOWELL, AND W. J. LAYTON, *Partitioned time stepping for a parabolic two domain problem*, SIAM J. Numer. Anal., 47 (2009), pp. 3526–3549.
- [53] ——, *Decoupled time stepping methods for fluid-fluid interaction*, SIAM J. Numer. Anal., 50 (2012), pp. 1297–1319.
- [54] T. A. DAVIS, *Algorithm 832: Umfpack, an unsymmetric-pattern multifrontal method*, ACM Transactions on Mathematical Software, 30 (2004), pp. 196–199.

- [55] ——, *A column pre-ordering strategy for the unsymmetric-pattern multifrontal method*, ACM Transactions on Mathematical Software, 30 (2004), pp. 165–195.
- [56] T. A. DAVIS AND I. S. DUFF, *An unsymmetric-pattern multifrontal method for sparse lu factorization*, SIAM Journal on Matrix Analysis and Applications, 1 (1997), pp. 140–158.
- [57] ——, *A combined unifrontal/multifrontal method for unsymmetric sparse matricesa*, ACM, 25 (1999), pp. 1–19.
- [58] C. DAWSON, S. SUN, AND M. F. WHEELER, *Compatible algorithms for coupled flow and transport*, Computer Methods in Applied Mechanics and Engineering, 193 (2004), pp. 2565–2580.
- [59] C. N. DAWSON, Q. DU, AND T. DUPONT, *A finite difference domain decomposition algorithm for numerical soluton of the heat equation*, Mathematics of Computation, 57 (1991), pp. 63–71.
- [60] C. N. DAWSON AND T. DUPONT, *Explicit/implicit conservative galerkin domain decomposition procedures for parabolic problems*, Mathematics of Computation, 58 (1992), pp. 21–34.
- [61] A. DEINEGA AND S. JOHN, *Finite difference discretization of semicon- ductor drift-diffusion equations for nanowire soalr cells*, Comput. Phys. Comun., 183 (2012), pp. 2128–2135.

- [62] J. W. DEMMEL, S. C. EISENSTAT, J. R. GILBERT, X. S. LI, AND J. W. H. LIU, *A supernodal approach to sparse partial pivoting*, SIAM J. Matrix Analysis and Applications, 20 (1999), pp. 720–755.
- [63] J. DOUGLAS, D. E. EWING, AND M. F. WHEELER, *A time discretization process for a mixed finite element approximation of miscible displacement in porous media.*, R.A.I.R.O Num. Anal., 17 (1983), pp. 249–265.
- [64] J. DOUGLAS, I. M. GAMBA, AND M. C. J. SQUEFF, *Simulation of the transient behavoir of a one dimensional semiconductor device*, Mat. Apl. Comput., 5 (1986), pp. 103–122.
- [65] B. EISENBERG, *Ionic channels: Natural nanotubes desrcibed by the drift diffusion equations*, Superlattices and Microstructures, 27 (2000), pp. 545–549.
- [66] A. M. FAJARDO AND N. S. LEWIS, *Free energy dependenc of electron-transfer rate constants at si/liquid interfaces*, J. Phys. Chem. B, 101 (1997), pp. 11136–11151.
- [67] J. M. FOLEY, M. J. PRICE, J. I. FELDBLYUM, AND S. MALDONADO, *Analysis of the operation of thin nanowire photoelectrodes for solar energy conversion*, Energy and Environmental Science, 5 (2011), pp. 5203–5220.

- [68] A. FUJISHIMA AND K. HONDA, *Electrochemical photolysis of water at a semiconductor electrode*, Nature, 238 (1972), pp. 37–38.
- [69] I. M. GAMBA, *Asymptotic Behavior at the Boundary of a Semiconductor Device in Two Space Dimensions*, PhD thesis, University of Chicago, 1989.
- [70] I. M. GAMBA AND M. C. J. SQUEFF, *Simulation of the transient behavoir of a one dimensional semicondcutor device ii*, SIAM J. Numer. Anal., 2 (1989), pp. 539–552.
- [71] M. J. GANDER, *Schwarz methods in the course of time*, ETNA, 31 (2008), pp. 228–255.
- [72] Y. GAO, Y. GEORGIEVSKII, AND R. MARCUS, *On the theory of electron transfer reactions at semiconductor electrode/liquid interfaces*, J. Phys. Chem., 112 (2000), pp. 3358–3369.
- [73] Y. GAO AND R. MARCUS, *On the theory of electron transfer reactions at semiconductor electrode/liquid interfaces. ii. a free electron model*, J. Phys. Chem., 112 (2000), pp. 6351–6360.
- [74] H. GERISCHER, *Electrochemical behavoir of semiconductors under illumination*, J. of the Electrochemical Society, 18 (1966), pp. 97–122.
- [75] H. GERISCHER, *On the role of electrons and holes in surface reactions on semiconductors*, Surface Science, 13.1 (1969), pp. 265–278.

- [76] H. GERISCHER, *The impact of semiconductors on the concepts of electrochemistry*, *Electrochimica Acta*, 35 (1990), pp. 1677–1699.
- [77] O. GHATTAS AND X. LI, *A variational finite element method for stationary nonlinear fluidsolid interaction*, *Journal of Computational Physics*, 121 (1995), pp. 347 – 356.
- [78] ——, *Domain decomposition methods for sensitivity analysis of a nonlinear aeroelasticity problem*, *International Journal of Computational Fluid Dynamics*, 11 (1998), pp. 113–130.
- [79] R. GLOWINSKI AND M. F. WHEELER, *Domain decomposition and mixed finite element methods for elliptic problems*, in *First international symposium on domain decomposition methods for partial differential equations*, 1988, pp. 263–290.
- [80] M. GRATZEL, *Photoelectrochemical cells*, *Nature*, 414 (2001), pp. 338–344.
- [81] M. A. GREEN AND M. J. KEEVERS, *Optical properties of intrinsic silicon at 300 k*, *Progress in Photovoltaics: Research and Applications*, 3 (1995), pp. 189 – 192.
- [82] P. GRISVARD, *Elliptic problems in Nonsmooth Domains*, Society for Industrial and Applied Mathematics, 2011.

- [83] H. K. GUMMEL, *A self-consistent iterative scheme for one-dimensional steady state transistor calculations*, IEEE Trans. Electron Devices, 11 (1964), pp. 455–465.
- [84] Y. HE, I. M. GAMBA, H. LEE, AND K. REN, *On the modeling and simulation of semiconductor-electrolyte solar cells*, Accepted for publication in SIAM J. Appl. Math., (2015).
- [85] J. S. HESTHAVEN AND T. WARBURTON, *Nodal Discontinuous Galerkin Methods*, Springer, 2010.
- [86] T. L. HORNG, T. C. LIN, C. LIU, AND B. EISENBERG, *Pnp equations with steric effects: A model of ion flow through channels*, J. Phys. Chem. B., 116 (2012), pp. 11422–11441.
- [87] N. S. HUSH, *Adiabatic theory of outer sphere electron transfer reactions in solutions*, Trans. Faraday Soc., 57 (1961), pp. 557–580.
- [88] J. JEROME AND T. KERKHOVEN, *A finite element approximation theory for the drift-diffusion semiconductor model*, SIAM J. Numer. Anal., 28 (1991), pp. 403–422.
- [89] C. JOHNSON, *Numerical Solution of Partial Differential Equations by the Finite Element Method*, Dover Publications, 1987, (2009 Republished).
- [90] E. L. JOHNSON, *The Texas Instruments Solar Energy System Development*, vol. 27, 1981, pp. 2–5.

- [91] A. JUNGEL, *Transport Equations For Semiconductors*, Springer, 2009.
- [92] G. KANSCHAT, *Preconditioning methods for local discontinuous galerkin methods*, Siam J. Sci. Comput., 25 (2003), pp. 815–831.
- [93] M. KAYES, H. A. ATWATER, AND N. LEWIS, *Comparison of the device physics principles of planar and radial p-n junction nanorod solar cells*, The Journal of Applied Physics, 97 (2005).
- [94] E. KEMPPAINEN, J. HALME, AND P. LUND, *Physical modeling of photoelectrochemical hydroden production devices*, The Journal of Physical Chemistry C, 119 (2015), pp. 21747–21766.
- [95] W. LAYTON AND C. TRENCHEA, *Stability of two imex methods, cnlf and bdf2-ab2, for uncoupling systems of evolution equations*, Applied Numerical Mathematics, 62 (2012), pp. 112–120.
- [96] P. LESAINT AND P. RAVIART., *Mathematical Aspects of Finite Elements in Partial Differential Equations*, Academic Press, 1974, ch. On a finite element method for solving the neutron transport equation, pp. 89–145.
- [97] N. LEWIS, *An analysis of charge transfer rate constants for semconductor/liquid interfaces*, Annu. Rev. Phys. Chem., 42 (1991), pp. 543–580.
- [98] N. S. LEWIS, *Mechanistic studeis of light-induced charge seperatation at semiconductor/liquid interfaces*, Acc. Chem. Res., 23 (1990), pp. 176–183.

- [99] ——, *Progress in understanding electron-transfer reactions at semiconductor/liquid interfaces*, J. Phys. Chem. B, 102 (1998), pp. 4843–4855.
- [100] X. LI, J. DEMMEL, J. GILBERT, L. GRIGORI, M. SHAO, AND I. YAMAZAKI, *SuperLU Users' Guide*, Tech. Rep. LBNL-44289, Lawrence Berkeley National Laboratory, September 1999.
- [101] X. S. LI, *An overview of SuperLU: Algorithms, implementation, and user interface*, ACM Trans. Math. Softw., 31 (2005), pp. 302–325.
- [102] P.-L. LIONS, *On the schwarz alternating method. i.*, in First International Symposium on Domain Decomposition Methods, SIAM, Philadelphia, PA., 1988, pp. 1–42.
- [103] ——, *On the schwarz alternating method. ii. stochastic interpretation and order properties.*, in Domain Decomposition Methods, SIAM, Philadelphia, PA., 1989.
- [104] ——, *On the schwarz alternating method. iii. a variant for non-overlapping subdomains.*, in Third International Symposium on Domain Decomposition Methods for Partial Differential Equations, SIAM, Philadelphia, PA, vol. 6, 1990.
- [105] R. A. MARCUS., *On the theory of oxidation-reduction reactions involving electron transfer 1*, Journal of Chemical Physics, 24 (1956), pp. 966–978.

- [106] R. A. MARCUS, *Chemical and electrochemical electron-transfer theory*, Annual Review of Physical Chemistry, 15 (1964), pp. 155–196.
- [107] P. MARKOWICH, *The Stationary Semiconductor Device Equations*, Springer-Verlag, 1986.
- [108] P. MARKWICH, C. RINGHOFER, AND C. SCHMEISER, *Semiconductor Equations*, Springer-Verlag, 1990.
- [109] T. MATHEW, *Domain Decomposition Methods for the Numerical Solution of Partial Differential Equations*, Springer, 2008.
- [110] J. MCKONE, N. LEWIS, AND H. GRAY, *Will solar-driven water-splitting devices see the light of day?*, Chemistry of Materials, 26 (2013), pp. 407–414.
- [111] R. MEMMING, *Semiconductor electrochemistry*, Wile-VCH, 2015.
- [112] S. MICHELETTI, A. QUARTERONI, AND R. SACCO, *Current-voltage characteristics simulation of semiconductor devices using domain decompositions*, Journal of Computational Physics, 119 (1995), pp. 46–61.
- [113] T. J. MILLS, F. LIN, AND S. W. BOETTCHER, *Theory and simulations of electrocatalyst-coated semiconductor electrodes for solar water splitting*, Phys. Rev. Lett., 112 (2014), p. 148304.
- [114] J. NELSON, *Physics Of Solar Cells*, Imperial College Press, 2003.

- [115] J. NEWMAN AND K. E. THOMAS-ALYEA, *Electrochemical Systems*, Wiley-Interscience, New York, 2004.
- [116] A. J. NOZIK AND R. MEMMING, *Physical chemistry of semiconductors-liquid interfaces*, J. Phys. Chem., 100 (1996), pp. 13061–13078.
- [117] J. H. PARK AND J. W. JEROME, *Qualitative properties of steady-state poisson-nernst-planck systems: Mathematical study*, SIAM J. Appl. Math., 57 (1997), pp. 609–630.
- [118] M. PENNY, T. FARRELL, AND G. WILL, *A mathematical model for the anodic half cell of a dye-sensitised solar cell*, Solar Energy Materials and Solar Cells, 92 (2008), pp. 24 – 37.
- [119] J. PERAIRE AND P.-O. PERSSON, *The compact discontinuous galerkin (cdg) method for elliptic problems*, SIAM J. Sci. Comput., (2008), pp. 1806–1824.
- [120] K. E. POMYKAL, , AND N. S. LEWIS, *Measurement of interfacial charge-transfer rate constants at n-type inp/ch3oh junctions*, The Journal of Physical Chemistry B, 101 (1997), pp. 2476–2484.
- [121] A. QUARTERONI AND A. VALLI, *Domain Decomposition Methods for Partial Differential Equations*, Oxford Science Publications, 1999.
- [122] K. RAJESHWAR, *Encyclopedia of Electrochemistry*, Wiley-VCH Verlag, 2007, ch. Fundamentals of Semiconductor Electrochemistry and Photoelectrochemistry.

- [123] P. RAVIART AND J.-M. THOMAS, *Mathematical aspects of finite element methods*, Springer Berlin Heidelberg, 1977, ch. A mixed finite element method for 2-nd order elliptic problems, pp. 292–315.
- [124] W. REED AND T. HILL, *Triangular mesh methods for the neutron transport equation*, tech. report la-ur-73-479, Los Alamos Scientific Laboratory, 1973.
- [125] B. RIVIERE AND M. F. WHEELER, *Discontinuous galerkin methods for flow and transport problems in porous media*, Comm. in Num. Meth. in Eng., 18 (2001), pp. 63–68.
- [126] B. M. RIVIERE, *Discontinuous Galerkin Methods For Solving Elliptic And parabolic Equations: Theory and Implementation*, SIAM, 2008.
- [127] E. A. SANTORI, N. C. STRANDWITZ, R. L. GRIMM, B. S. BRUN-SCHWIG, H. A. ATWATER, AND N. S. LEWIS, *Operation of lightly doped si microwires under high-level injection conditions.*, Energy and Environmental Science, 7 (2014), pp. 23–29.
- [128] D. L. SCHARFETTER AND H. K. GUMMEL, *Large-signal analysis of a silicon read diode oscillator*, IEEE Transactions on Electron Devices, 16 (1969), pp. 64–77.
- [129] A. SCHWARZ, *Gesammelte mathematische abhadlungen*, Vierteljahrsschrift der naturforschenden gesselschaft in Zurich, (1870).

- [130] S. SELBERHER, *Analysis and Simulation of Semiconductor Devices*, Springer-Verlag, 2001.
- [131] J. SHELDON AND W. C. JR., *One-dimensional, incompressible, non-capillary, two-phase fluid flow in a porous medium*, Trans. SPE AIME, 216 (1959), pp. 290–296.
- [132] W. SHOCKLEY AND W. T. READ, *Statistics of recombination of holes and electrons*, Physical Review, 87 (1952).
- [133] C. S. SIMMONS AND K. W. SCHULZ, *A distributed memory out-of-core method on hpc clusters and its applications to quantum chemistry applications*, no. 1 in XSEDE 2012, ACM, 2012.
- [134] D. SINGH, X. GUO, J. MURTHY, A. ALEXEENKO, AND T. FISHER, *Modeling of subcontinuum thermal transport across semiconductor-gas interfaces*, J. Appl. Phys., 106 (2009).
- [135] C. M. SNOWDEN, *Introduction To Semiconductor Device Modeling*, World Scientific Publishing Co., 1986.
- [136] H. STONE AND A. G. JR., *Analysis of gas-cap or dissolved-gas reservoirs*, Trans. SPE AIME, 222 (1961), pp. 92–104.
- [137] S. SUN, B. RIVIERE, AND M. F. WHEELER, *A combined mixed finite element and discontinuous galerkin method for miscible displacement problem in porous media*, in Recent Progress in computational and applied PDEs, Springer, 2002, pp. 323–351.

- [138] S. SUN AND M. WHEELER, *Discontinuous galerkin methods for coupled flow and reactive transport problems*, Applied Numerical Mathematics, 52 (2002), pp. 273–298.
- [139] S. SZE, *Semiconductor Devices, Physics and Technology*, Bell Telephone Laboratories Inc., 1985.
- [140] A. TOSELLI AND O. B. WIDLUND, *Domain Decomposition Methods - Algorithms and Theory*, Springer-Verlag, 2005.
- [141] C. TRENCHEA, *Stability of partitioned imex methods for systems of evolution equations with skew-symmetric coupling*, submitted to Journal of Computational and Applied Mathematics, (2012).
- [142] W. V. VAN ROOSBECK, *Theory of flow of electrons and holes in germanium and other semiconductors*, tech. rep., Bell Sys. Tech. J., 1950.
- [143] D. VASILESKA AND S. M. GOODNICK, *Computational Electronics*, Morgan & Claypool, 2006.
- [144] M. WALTER, E. WARREN, J. MCKONE, S. BOETTCHER, Q. MI, E. SANTORI, AND N. LEWIS, *Solar water splitting cells*, Chemical Reviews., 110 (2010), pp. 6446–6473.
- [145] H. WANG, C. SHU, AND Q. ZHANG, *Stability and error estimates of local discontinuous galerkin methods with implicit-explicit time-marching for advection-diffusion problems*, SIAM J. Numer. Anal., 53 (2015), pp. 206–227.

- [146] ——, *Stability analysis and error estimates of local discontinuous galerkin methods with implicit-explicit time-marching for nonlinear convection-diffusion problems*, Applied Math. and Computation, 272 (2016), pp. 237–258.
- [147] A. WANGPERAWONG AND S. F. BENT, *Three-dimensional nanojunction device models for photovoltaics*, Applied Physics Review, 98 (2011).

Vita

Michael Harmon was born in Boston, Massachusetts. He graduated from New York University with an associate in the arts in 2005 and a bachelors in the arts in Mathematics in 2007. He graduated from the University of Texas at Austin in 2010 with masters in Computational and Applied Mathematics.

Permanent address: mdh266@gmail.com

This dissertation was typeset with L^AT_EX[†] by ‘the author’.

[†]L^AT_EX is a document preparation system developed by Leslie Lamport as a special version of Donald Knuth’s T_EX Program.